

---

# Advanced modeling for personalized dosimetry in nuclear medicine applications

Alexandra Zvereva

---



München 2017



---

# **Advanced modeling for personalized dosimetry in nuclear medicine applications**

**Alexandra Zvereva**

---

Dissertation  
an der Fakultät für Physik  
der Ludwig–Maximilians–Universität  
München

vorgelegt von  
Alexandra Zvereva  
aus Werchnjaja Salda, Russland

München, den 2. Mai, 2017

Erstgutachter: Prof. Dr. Katia Parodi  
Zweitgutachter: Prof. Dr. Werner Rühm  
Tag der mündlichen Prüfung: 26. Juli, 2017

# Zusammenfassung

Hintergrund und Ziele: Nuklearmedizin wird heutzutage häufig in der Diagnostik und der Therapie angewendet. Hierzu werden radioaktive Tracer mit biologischen Komplexen zu sogenannten Radiopharmaka verbunden, die den Patienten verabreicht werden. Dies führt zur Emission von radioaktiver Strahlung im Körper des Patienten. Die therapeutische Wirkung wird erzielt, indem ein Teil der Energie zum Beispiel in Tumorgewebe deponiert wird. Der Anteil der Strahlung, der den Körper verlässt, kann außerhalb des Patienten detektiert werden und dient zur Erstellung eines funktionellen Bildes des untersuchten Systems. Dosisabsorption im übrigen Teil des Patienten ist ein unvermeidbarer und unerwünschter Nebeneffekt, da hierdurch potentiell das Risiko für Tumor- und Erbkrankheiten steigt und die Bildqualität verschlechtert wird. Diese Dosis muss aus rechtlichen Gründen sowie zur Bewertung von Risiko und Nutzen für den Patienten abgeschätzt werden. Darüber hinaus werden personalisierte Dosisabschätzungen für die Therapie und epidemiologische Studien benötigt. Nach der gängigen Lehrmeinung benötigt man zur personalisierten Dosimetrie patientenspezifische pharmakokinetische Modelle, die die Verteilung und Ausscheidung des verabreichten Radiopharmakons beschreiben, sowie personalisierte anatomische Modelle, die die Simulation des Strahlentransportes im menschlichen Körper für die interne Dosimetrie ermöglichen. Aufgrund des hohen Zeitaufwandes kommen diese Modelle allerdings in der klinischen Routine nicht zum Einsatz. Infolgedessen werden in der Regel Referenzdosen angewendet, welche sich stark von personalisierten Dosen unterscheiden können. Die vorliegende Arbeit hat das Ziel zu untersuchen, wie die Zuverlässigkeit von internen Dosisabschätzungen des individuellen Patienten mit praktikablen Methoden erhöht werden kann.

Material und Methoden: Personalisierte pharmakokinetische Kompartimentmodelle wurden für fünf gesunde Probanden erstellt und deren interindividuelle Variabilität in der Pharmakokinetik analysiert. Der Einfluss der Aktivität im Blut auf Organdosen wurde untersucht, indem die Organdosen auf zwei verschiedene Arten berechnet wurden: mit und ohne Blut als individuelle Strahlungsquelle. Ein Referenz-Polygonnetzphantom wurde auf ausgesuchte Körpermaße eines schlanken und eines übergewichtigen Menschen skaliert. Die skalierten Körpermaße umfassten den Abstand zwischen Beckenkamm und Schlüsselbein, Körpergröße und Tiefe und Breite des Brustkorbes. Anschließend wurde untersucht, ob die durch interindividuelle Abweichungen hervorgerufenen Dosisdifferenzen durch die entwickelte Skalierung abgebildet werden können. Zum Abschluss wurde eine Varianz-basierte Sensitivitätsanalyse erstmalig auf die interne Dosimetrie angewendet. Dadurch wurde es möglich, die Varianzen in den Organdosen zu quantifizieren, die durch interindividuelle Unterschiede in Pharmakokinetik und Anatomie hervorgerufen werden. Die implementierte Sensitivitätsanalyse ermöglicht zudem die Bewertung der Inputfaktoren nach ihrem Einfluss auf diese Varianzen.

Ergebnisse: Es wurde gezeigt, dass die Aktivität im Blut einen erheblichen Einfluss hat auf die absorbierte Dosis von gut durchbluteten Regionen, die keine Strahlungsquellen sind. Die Anpassung des Referenz-Polygonnetzphantomes ermöglichte es, die interindividuellen anatomischen Unterschiede teilweise abzubilden und folglich den Fehler in den Organdosen aufgrund von unterschiedlicher Anatomie zu reduzieren. Die Ergebnisse der Sensitivitätsanalyse zeigen, dass die genaue Bestimmung der zeitlich integrierten Aktivitätskoeffizienten zusammen mit der Bestimmung der individuellen Masse der Strahlenquellenregionen und der Benutzung von geeigneten Blutverteilungen im Patientenkörper

großes Potential haben, die Varianz in den internen Dosen zu reduzieren. Für Organe, die sich in direkter Umgebung zu Strahlenquellregionen befinden, spielen auch spezifische, durch sogenanntes Cross-fire beeinflusste absorbierte Fraktionen eine Rolle.

Schlussfolgerungen: Messprotokolle für pharmakokinetische und dosimetrische Studien sollten die Auswertung der Aktivität in Blutproben beinhalten. Blut sollte im Anschluss als eigenständige Strahlenquellregion in die Berechnung der internen Dosen eingehen. Es ist möglich und auch im Klinikbetrieb realisierbar, die Dosisabschätzung durch Anpassung von ausgewählten Körpermaßen des Referenz-Polygonnetzphantoms zu verbessern. Alternativ könnten die ausgewählten Körpermaße benutzt werden, um das am besten passende Phantom zu bestimmen. In dieser Arbeit wurde die leistungsfähige varianz-basierte Sensitivitätsanalyse an die Anforderungen für die interne Dosimetrie in der Nuklearmedizin angepasst. Sie ermöglicht die Identifizierung der Inputfaktoren, die den größten Einfluss auf die Varianz der Dosiskoeffizienten haben. Eine genaue Bestimmung dieser Inputfaktoren hat das große Potential, die Unsicherheiten in den Organdosiskoeffizienten in der Nuklearmedizin auf höchst effiziente Weise zu reduzieren. Die implementierten und ausgewerteten Methoden sowie die entwickelten Programme können dafür eingesetzt werden, die Zuverlässigkeit der individuellen Organdosensbestimmung für Patienten der Nuklearmedizin zu verbessern.

# Abstract

Purpose: Nuclear medicine applications are extensively used for diagnostic and therapeutic purposes nowadays. In these modalities radioactive tracers labeled with biological compounds, so-called radiopharmaceuticals, are internally administered to the patients. Subsequently, radiation is emitted by the radiopharmaceuticals in the patient's body. Therapeutic function is achieved by depositing a fraction of energy in e.g. tumor tissue. The fraction of radiation that leaves the patient's body can be detected externally and is employed to obtain a functional image of a studied system. The dose absorption in the rest of the patient's body is an unavoidable and undesirable side process, since it can potentially increase the risk of induction of cancer and heritable diseases and it decreases the image quality. This dose needs to be estimated for regulatory purposes and for an assessment of patient's risks and benefits. Moreover, therapeutic nuclear medicine procedures and epidemiological studies require personalized dose estimations. According to the commonly used framework, personalized internal dosimetry requires the development of individual-specific pharmacokinetic models, which describe the distribution and excretion of the administered radiopharmaceutical, as well as personalized anatomical models, which facilitate radiation transport simulations in the human body for internal dosimetry. These models are usually not viable in clinical routine though, due to high time and effort requirements. Consequently, reference doses, which can be substantially different from personalized doses, are typically applied to individuals. This thesis aims at investigating how the reliability of internal dose estimates for individual patients can be increased by practically viable methods.

Methods: Personalized compartmental pharmacokinetic models were established for five healthy volunteers and the inter-individual variability in pharmacokinetics was analyzed. The effect of blood activity on organ doses was evaluated by computing organ doses in two ways – with and without blood as a distinct source region. A reference polygon-surface phantom was scaled to fit a set of selected dimensions of one slim and one overweight individual. The scaled dimensions comprised the distance between the iliac crest and the clavicles, total height, front-to-back distance and width of the rib cage. It was subsequently investigated whether the dose differences originating from inter-individual variations in anatomy can be captured by the developed scaling. Finally, variance-based sensitivity analysis was applied for the first time to internal dosimetry. This allowed to quantify the variances in organ doses caused by inter-individual differences in pharmacokinetics and anatomy. The implemented sensitivity analysis facilitated ranking of the input factors according to their impact on these variances.

Results: A substantial effect of blood activity on absorbed doses for highly vascular non-source regions was shown. Adjusting the reference polygon-surface phantom enabled partly capturing inter-individual anatomic variability and, consequently, decreasing the error in estimated organ doses caused by differences in anatomy. Based on the results of the sensitivity analysis it follows that the accurate determination of the time-integrated activity coefficients accompanied by the estimation of individual source region masses and the usage of an appropriate blood distribution in a patient's body have great potential to decrease the variance of internal doses. For organs located in close proximity to the source regions the cross-fire specific absorbed fractions have an impact as well.

Conclusion: Measurement protocols for pharmacokinetic and dosimetric studies should include the assessment of activity in blood samples and blood should subsequently be considered as a distinct source region in internal dose calculations. It is feasible and

practically achievable to improve dose estimates by scaling the reference polygon-surface phantom to selected dimensions of individuals. Alternatively, these dimensions could be considered in selecting the phantom that best matches to the individual patient. In this thesis the powerful variance-based sensitivity analysis was successfully adapted to internal dosimetry in nuclear medicine applications. It allows to identify the input factors, which have the highest impact on the variance of dose coefficients. An accurate determination of these input factors has the great potential to reduce the uncertainties of organ dose coefficients in nuclear medicine in the most effective way. The implemented and evaluated methods as well as the developed programs can be used to enhance the reliability of organ dose assessment for individual patients in nuclear medicine applications.

# Contents

<b>Introduction</b>	<b>3</b>
<b>Structure and outline of the thesis</b>	<b>7</b>
<b>I. Fundamentals of nuclear medicine techniques</b>	<b>9</b>
<b>1. Nuclear medicine modalities</b>	<b>13</b>
1.1. Intra-operative probes, organ uptake probes and gamma cameras . . . . .	14
1.2. Single photon emission computed tomography (SPECT) . . . . .	15
1.3. Positron-emission-tomography (PET) . . . . .	15
1.3.1. Operating principles of PET imaging . . . . .	15
1.3.2. Interaction of emitted radiation with matter . . . . .	16
1.3.3. Radiation detection in PET imaging . . . . .	20
<b>2. Dosimetry in nuclear medicine</b>	<b>23</b>
<b>II. Pharmacokinetic modeling</b>	<b>27</b>
<b>3. Fundamentals of pharmacokinetic modeling</b>	<b>31</b>
3.1. Input data to establish a personalized pharmacokinetic model . . . . .	32
3.2. Simulation, Analysis, and Modeling Software II (SAAM II) . . . . .	32
3.3. Blood in pharmacokinetic modeling . . . . .	33
<b>4. Clinical investigations and pharmacokinetic model development</b>	<b>35</b>
4.1. Patients . . . . .	35
4.2. Measurements . . . . .	35
4.3. Development of personalized pharmacokinetic models . . . . .	36
4.4. Proposed method for modeling blood contents of organs and tissues . . . . .	40
<b>5. Developed pharmacokinetic models and blood effect</b>	<b>43</b>
5.1. Developed individual pharmacokinetic models . . . . .	43
5.2. Effect of blood activity on dosimetric calculations . . . . .	47
<b>III. Anatomical modeling</b>	<b>53</b>
<b>6. Three generations of anatomical models, their construction and applications</b>	<b>57</b>
6.1. General methods to construct a human computational phantom . . . . .	57
6.1.1. Stylized mathematical phantoms . . . . .	57

6.1.2. Voxel phantoms . . . . .	58
6.1.3. Phantoms based on boundary representation geometries . . . . .	60
6.2. Reference human computational phantoms . . . . .	62
6.2.1. Reference voxel ICRP adult male phantom . . . . .	63
6.2.2. Reference polygon-surface ICRP adult male phantom . . . . .	63
6.3. Rationale for individual anatomical models . . . . .	64
<b>7. Adjustment of reference model to individuals and Monte Carlo calculations of specific absorbed fractions</b>	<b>67</b>
7.1. Adjustment of reference phantom to individual-specific characteristics . . . . .	68
7.1.1. Selected individuals . . . . .	68
7.1.2. Adjusted dimensions . . . . .	70
7.2. Monte Carlo radiation transport calculations . . . . .	72
7.2.1. EGSnrc . . . . .	73
7.2.2. Geometry, radiation types and energies . . . . .	74
7.3. Voxelization of polygon-surface models . . . . .	75
7.4. Internal dosimetry for the developed anatomical models . . . . .	76
7.4.1. Mass-correction of specific absorbed fractions . . . . .	76
7.4.2. Considered target regions . . . . .	77
7.4.3. Special case of urinary bladder dosimetry . . . . .	78
<b>8. Developed anatomical models and comparison of their organ doses</b>	<b>81</b>
8.1. Developed anatomical models . . . . .	81
8.2. Performed Monte Carlo calculations . . . . .	83
8.3. Comparison of organ doses for developed anatomical models . . . . .	83
8.3.1. Self-absorption component of absorbed dose coefficients . . . . .	84
8.3.2. Cross-fire component of absorbed dose coefficients . . . . .	84
8.4. Synopsis of performed anatomical modeling . . . . .	90
<b>IV. Uncertainty and sensitivity analysis</b>	<b>93</b>
<b>9. Fundamentals of uncertainty and sensitivity analysis</b>	<b>97</b>
9.1. Objectives of uncertainty and sensitivity analysis . . . . .	97
9.2. Methods of uncertainty and sensitivity analysis . . . . .	97
9.2.1. Uncertainty propagation . . . . .	97
9.2.2. Local approach to sensitivity analysis . . . . .	99
9.2.3. “One-factor-at-a-time” sensitivity analysis . . . . .	99
9.2.4. Global variance-based sensitivity analysis . . . . .	100
<b>10. Application of uncertainty and global sensitivity analysis to internal dosimetry</b>	<b>103</b>
10.1. Uncertainties in internal dosimetry . . . . .	103
10.2. Evaluated model and considered sources of uncertainty . . . . .	104
10.3. Monte Carlo approach for variance-based sensitivity analysis . . . . .	105
10.4. Input factors used in sensitivity analysis . . . . .	106
10.5. Sampling of input factors . . . . .	108
10.6. Sobol’ low discrepancy sequence . . . . .	108
10.7. Number of model executions and convergence . . . . .	111

<b>11. Effect of input factor variabilities on computed uncertainties of organ dose coefficients</b>	<b>113</b>
11.1. Uncertainty of computed dose coefficients . . . . .	113
11.2. Convergence of sensitivity indices . . . . .	116
11.3. Effect of input factors on variability of dose coefficients . . . . .	118
<b>V. Summary and conclusion</b>	<b>125</b>
12. Summary	127
13. Conclusion	129
<b>VI. Appendix</b>	<b>131</b>
<b>A. Comparison of organ dose coefficients for employed anatomical models</b>	<b>133</b>
A.1. Self-absorption component of absorbed dose coefficients . . . . .	133
A.2. Cross-fire component of absorbed dose coefficients . . . . .	138
<b>B. Total effect sensitivity indices for all considered outputs</b>	<b>143</b>
<b>List of Figures</b>	<b>145</b>
<b>List of Tables</b>	<b>147</b>
<b>List of Abbreviations and Acronyms</b>	<b>149</b>
<b>List of Symbols</b>	<b>151</b>
<b>Bibliography</b>	<b>153</b>



# Introduction



Many diagnostic and therapeutic procedures in medicine rely on the application of ionizing radiation. This radiation can be emitted by external sources, i.e. those located outside the patient’s body, or it can be ejected by internally administered radioactive substances. An example of the modalities with externally applied radiation is the usage of X-ray sources for a widely known diagnostic modality like computed tomography (CT). Another example is the external beam radiotherapy – application of electrons, X-rays,  $\gamma$ -radiation (e.g.  $^{60}\text{Co}$ ), protons or ions for cancer treatment. Diagnostic and therapeutic procedures, which employ radioactive substances, are commonly combined under the term “nuclear medicine”. These substances are administered to the patient in form of radiopharmaceuticals – radioactive tracers labeled with biological compounds. The biochemical properties of the latter define the clinical purpose of the radiopharmaceutical. As a result of the administration of radiopharmaceuticals, the patient’s body emits photon radiation, which is externally detected. In contrast to CT, which is applied to visualize the anatomy of the patient, nuclear medicine modalities are employed to investigate the physiological function of organs, tissues or other studied systems. For this reason the nuclear medicine diagnostic applications are often called functional imaging. To enable an external radiation detection in diagnostic nuclear medicine applications, radiation that can penetrate substantial soft-tissue thicknesses is used. Thus, X- and  $\gamma$ -emitting radionuclides are employed in such imaging. The therapeutic applications in nuclear medicine are commonly denoted as radionuclide therapy. Radionuclide therapy is used for treatment of cancer, metastatic bone pain and neuroendocrine tumors, for radiosynovectomy (a treatment of synovial inflammation and related arthritis) etc. To locally sterilize cancer cells by self-irradiation and avoid the irradiation of surrounding normal tissues, in radionuclide therapy radionuclides emitting short range radiation such as electrons,  $\beta$ -rays or  $\alpha$ -particles are used [1–3]. Nuclear medicine applications are available nowadays in many clinics worldwide and are extensively used for both, diagnostics and therapy.

As mentioned above, the use of nuclear medicine modalities is associated with an administration of radiation to the patient. The administered radiation deposits energy in a patient’s body. Consequently, besides the patient’s benefit from the diagnosis or therapy, these procedures are associated with undesirable radiation doses, which could potentially increase the risk of inducing cancer and heritable diseases. For the regulatory purpose and to facilitate an assessment of risks and benefits for a patient, these doses need to be estimated. Due to the operating principles of nuclear medicine applications, the associated doses cannot be determined by direct measurements. Thus the internal dosimetry relies on computational methods.

The commonly used framework of internal dosimetry was developed and formulated by the Committee on Medical Internal Radiation Dose (MIRD) [4]. It relies on the knowledge of the spatial distribution of an injected radiopharmaceutical in the patient’s body and the values called specific absorbed fractions (SAFs) [5]. The spatial distribution, metabolism and excretion of the administered substance in the patient’s body is often described mathematically by pharmacokinetic models [6–8]. Alternatively, it can be given as integrated activities, accumulated in source regions – anatomical regions that accumulate considerable amount of activity, higher than the general level of activity in the body. Integrated activities, normalized by the injected activity, are given in units of time and often called time-integrated activity coefficients  $\tilde{a}(r_S)$ . The specific absorbed fraction  $\Phi(r_T \leftarrow r_S, E)$  is defined as a fraction of energy  $E$  emitted from the source region  $r_S$ , which is absorbed in the target region  $r_T$ , normalized by the target region mass. It is specific

to a radiation type and energy and the combination of the source  $r_S$  and the target  $r_T$  regions. If  $r_T = r_S$ , i.e. the dose is deposited in a target region from radiation contained in the target region itself, the corresponding dose is called the self-absorption dose. The dose from the cross-fire denotes a dose deposited in a tissue  $r_T$  from radiation coming from the radionuclides contained in another tissue  $r_S$  ( $r_T \neq r_S$ ). Specific absorbed fractions  $\Phi(r_T \leftarrow r_S, E)$  are usually derived by Monte Carlo calculations. For a certain type of radiation and energy the amount of radiation released by a source region and deposited in a target region is affected by the relative locations and compositions of the source and the target. Thus the geometries where the Monte Carlo radiation transport is to be simulated should mimic the patient's anatomy. For this purpose digital models of the human anatomy, called anatomical models or human computational phantoms, are developed. In summary, the determination of internal organ doses involves several modeling steps: pharmacokinetic modeling, anatomical modeling with subsequent radiation transport simulations and the dose computation according to the model promulgated by the MIRDC committee.

Some situations, mainly radionuclide therapy and epidemiological studies, require personalized medical dosimetry [9–11]. For example, even the same radiopharmaceutical activities administered to different patients may result in different doses delivered to the regions of interest. Since the delivered doses define the therapeutic success, their individual estimation and adjustment, if needed, potentially increase the success of the therapy. Individualized dosimetry can affect the outcome of epidemiological studies and, therefore, it is also important in this case. Personalized dose assessment in diagnostics can facilitate the reduction of late negative effects of the radiation. However, it is often omitted, due to the relatively low associated doses. Individualized dosimetry is required for a proper treatment planning, which is a routine practice in e.g. external beam radiation therapy, but is often disregarded in radionuclide therapy. To this end, the framework described above would require personalized modeling at each step. The collection of human data, required for the calculation of individual time-integrated activity coefficients  $\tilde{a}(r_S)$ , is not always done in the clinical routine though. With a lack of robust automatic segmentation tools, the construction of individual-specific anatomical model is not viable for each patient due to the very time-consuming manual work required. Consequently, personalized modeling is often neglected and reference pharmacokinetic models along with anatomical models that mimic a reference standard anatomy are applied to individuals instead. In fact, doses computed in this way correspond to the used model and not to the investigated individual. The neglect of the inter-individual variability in pharmacokinetics and anatomy, which can potentially amount to a high value [12–16], can lead to substantial uncertainties of the estimated doses in nuclear medicine applications. The importance of the quantification of these uncertainties is recognized by various authors [17–19]. Besides the uncertainty analysis, a key procedure used to assess the quality of a model-based study is sensitivity analysis [20]. It is a study of the relative importance of a variability of different input factors on the uncertainty of model output. In some works, e.g. [21], sensitivity analysis is applied to pharmacokinetic models only. Whereas little work has been done to apply it to all modeling steps involved in internal dosimetry.

The objective of this thesis is to evaluate and apply advanced modeling procedures required for personalized internal dosimetry, to analyze the inter-individual variability in the pharmacokinetics and anatomy, to quantify the uncertainties in the organ doses caused by this variability and to investigate the effect of input factors on the output doses by the application of a variance-based global sensitivity analysis. As a practical outcome, the

global sensitivity analysis of this thesis will reveal what substantially affects the variance of the organ doses and, consequently, how this variance can be reduced in the most effective way. The main steps taken to fulfill the aim of this thesis are outlined in the following section.



# Structure and outline of the thesis

This section summarizes the main steps taken to fulfill the aim of this thesis – to investigate the viability and accuracy of personalized dosimetry in nuclear medicine applications in practice of clinical PET. Throughout this thesis various types of advanced modeling for personalized dosimetry in nuclear medicine applications were implemented and evaluated. This is subdivided into six parts as follows:

- Part I “**Fundamentals of nuclear medicine techniques**” summarizes operating principles and applications of nuclear medicine modalities in general and positron-emission tomography in particular in chapter 1. Chapter 2 recapitulates the main concepts of internal dosimetry. These include the systems formulated by the Committee on Medical Internal Radiation Dose for the computation of absorbed dose coefficients from internally administered radiopharmaceuticals. Two formalisms are presented in chapter 2: the general framework of internal dosimetry and the special case of urinary bladder dosimetry.
- Part II “**Pharmacokinetic modeling**” presents the first type of advanced modeling needed for internal dosimetry. Its fundamentals and mathematical formalism are summarized in chapter 3. The inputs required to establish a pharmacokinetic model along with the challenging aspect of considering blood in such a model are also introduced in chapter 3. Experimental data employed in this thesis for establishing pharmacokinetic models, the used methods and the proposed approach to model blood contents of organs and tissues are described in chapter 4. The developed pharmacokinetic models and the evaluated effect of blood on the internal organ doses are presented and discussed in chapter 5.
- Part III “**Anatomical modeling**” presents the second type of modeling required in the framework of internal dosimetry. The background of the development of digital models mimicking human anatomy, their construction and applications are given in chapter 6. The method proposed, implemented and evaluated in the scope of this thesis to capture the inter-individual differences in anatomy for the purpose of internal dosimetry is described in chapter 7. Chapter 8 presents the newly developed anatomical models and evaluates the feasibility to reduce the inter-individual anatomic differences with less effort than that needed for the segmentation of an individual anatomical model.
- Part IV “**Uncertainty and sensitivity analysis**” deals with two key procedures required for the evaluation of a model-based study – uncertainty and sensitivity analyses. The fundamentals of these procedures are summarized in chapter 9. The details of the global variance-based sensitivity analysis implemented in this thesis, along with an uncertainty analysis, are provided in chapter 10. Chapter 11 presents the computed uncertainties of organ dose coefficients. As an outcome of the sensitivity analysis, the effect of input factors on the variance of organ dose coefficients is shown

in chapter 11. The main results, obtained using the materials and methods of Part I – Part IV are presented and discussed here.

- Part V “**Summary and conclusion**” summarizes this thesis in chapter 12 and gives its outcomes and conclusions in chapter 13.
- Part VI “**Appendix**” contains additional figures from sections 8.3 and 11.3 not included in the main text of the thesis. It is followed by the lists of figures and tables, the lists of abbreviations, acronyms and symbols as well as the bibliography, the list of publications, the acknowledgment and the curriculum vitae.

## **Part I.**

# **Fundamentals of nuclear medicine techniques**



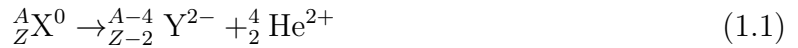
This part recapitulates the commonly used nuclear medicine modalities and the main principles of their work in chapter 1. Since the clinical data employed in this work correspond to a radiopharmaceutical used in positron-emission-tomography, this particular modality is described in detail in section 1.3. In chapter 2 the main concepts of internal dosimetry are recapitulated. The formalism is originally presented in the pamphlet 21 [4] of the Committee on Medical Internal Radiation Dose. A special case of the internal dose computation is the urinary bladder dosimetry. The Committee on Medical Internal Radiation Dose developed and promulgated in the revised pamphlet 14 [22] a dynamic model to be used for the urinary bladder dosimetry. The main concepts of this model are also summarized in chapter 2.



# 1. Nuclear medicine modalities

Radioactive decay modes are recapitulated in the following. Principles of intra-operative probes, organ uptake probes and gamma cameras are summarized in the following section 1.1. The most common nuclear medicine modalities are Single Photon Emission Computed Tomography (SPECT) and Positron Emission Tomography (PET). The main principles of SPECT are outlined in section 1.2. The description of PET is given in detail in section 1.3. This chapter is partly based on the book “Clinical nuclear medicine” by H.-J. Biersack and L.M. Freeman [1]. As it is discussed in the following sections, nuclear medicine images can be planar or represent a three-dimensional geometry, depending on the modality and the used instrumentation. All these applications are based on the concept of administration of radioactive substances (radiopharmaceuticals) to a patient and subsequent external detection of radiation emitted by the administered substances.

Radioactivity of some atomic nuclei is caused by their structural instability [1]. The process by which a structurally unstable nucleus transforms to a more stable nucleus is called radioactive decay. The typical radioactive decay mode for nuclei of elements with high atomic number  $Z$  is an emission of an  $\alpha$ -particle (a nucleus of  ${}^4_2\text{He}$ ):



Nuclei with low  $Z$  increase their stability via  $\beta^-$ -,  $\beta^+$ -decay or electron capture.  $\beta^-$ -decay occurs for the nuclei that have a high neutron-to-proton ratio  $N/Z$ . During this process a neutron is converted to a proton and an electron, and an anti-neutrino  $\bar{\nu}$  is ejected:



where  $A$  is the mass number,  $A = Z + N$ . Small nuclei with a low  $N/Z$  ratio transform to structurally more stable nuclei by a  $\beta^+$ -decay, i.e. a conversion of a proton to a neutron and generating a positron  $e^+$  and a neutrino  $\nu$ :



Alternatively to a  $\beta^+$ -decay, an electron capture can occur:



Another type of radioactive decay is  $\gamma$ -decay. In this process a nucleus makes a transition from a higher energy state to a lower energy state. The energy difference is released in a form of a  $\gamma$ -ray.  $\gamma$ -decay often follows an  $\alpha$ - or  $\beta$ -decay, if a proton or a neutron inside the daughter nucleus jumps to an excited state and subsequently relaxes back down to ground state via a  $\gamma$ -decay. The number of protons  $Z$  and neutrons  $N$  ( $N = A - Z$ ) remains the same in this process:



where  $\text{X}^*$  and  $\text{X}$  are the excited atom and the relaxed state of the initial excited atom, respectively.

## 1. Nuclear medicine modalities

A number of radioactive decays per unit time is described by the physical quantity activity. It is usually given in units “becquerel” Bq. 1 Bq corresponds to one decay per second. An important property of nuclear medicine images is the possibility or impossibility of their accurate quantification. Quantification of images in nuclear medicine means the determination of e.g. activity concentrations e.g., in [kBq·cm<sup>-3</sup>] from the reconstructed images. Quantitative images facilitate dosimetric calculations and the accuracy of the image quantification limits the accuracy of the computed doses. To generate quantitative data in nuclear medicine, it is necessary to compensate for the attenuation of the radiation emitted by the administered radiopharmaceutical, which occurs between the emission point and the detector (mainly in the patient’s body), and to correct the detected data for scatter. The latter means to consider that the radiation detected in nuclear medicine imaging undergoes scattering, mainly Compton scattering [23], and, as a result, it changes direction and loses energy. Various scatter correction techniques are described e.g. by H. Zaidi [23].

### 1.1. Intra-operative probes, organ uptake probes and gamma cameras

**Intra-operative probes** are portable hand-held devices with a relatively small field-of-view that are mainly used to detect tumors or metastases in regional lymphatic nodes during a surgical treatment of cancer. These devices are commonly employed for identification of sentinel lymph nodes and, thus, assist in decision making regarding the volume of operative intervention. Intra-operative probes are usually either scintillation- or semiconductor-detector-based [1].

**Organ uptake probes** are used for measuring the uptake of radionuclides in body organs, mainly in thyroid. These are portable systems that consist of a wide-aperture, a gantry, a collimator, a scintillator crystal thallium-doped sodium iodine (NaI(Tl)), a photomultiplier tube, an energy discriminator and associated electronics [1]. Measurements with such systems are usually accompanied by a measurement of a standard known activity to facilitate an automatic radioactive decay correction.

**Gamma cameras** or scintillation cameras are devices employed to measure X- and  $\gamma$ -radiation emitted by radionuclides. In contrast to intra-operative probes or organ uptake probes, gamma cameras have a large detector area that enables simultaneous and fast data collection over a large body region. One or more flat crystal detectors of various thicknesses coupled to a two-dimensional (2D) array of photomultiplier tubes are used in gamma cameras. The principle of mechanical collimation is utilized in these systems. Predominantly only radiation traveling perpendicular to the detector surface can pass through the parallel-hole, diverging hole or pinhole collimator and reach the crystal. Any radiation falling to e.g. parallel-hole collimator at an oblique angle will be stopped by the collimator septa (walls between the holes of the collimator) usually composed of lead [1]. Gamma camera collimators can be designed to be more sensitive to certain photon energies. The location of the scintillation within a crystal is determined from the voltage signals from the 2D array of photomultipliers, since the intensity of the signal inversely varies with the distance between the scintillation and the photomultiplier [1].

## 1.2. Single photon emission computed tomography (SPECT)

Besides the standard scintigraphy examinations gamma cameras are employed for a specific nuclear medicine procedure called radionuclide angiography. The latter is applied for testing of the heart function. In this application a radioactive tracer, e.g.  $^{99m}\text{Tc}$ , is used to label red blood cells. The purpose of radionuclide angiography is the evaluation of blood flow and organ function and it is specifically used for cardiac imaging. A gamma camera is used in this case to obtain a series of heart images at different phases of the cardiac cycle.

All nuclear medicine modalities described above, i.e. intra-operative probes, organ uptake probes and gamma cameras allow obtaining planar (2D) images. In contrast to these modalities, tomographic SPECT and PET scanners are used to get a three-dimensional (3D) data. Main principles of their functionality are outlined in the following sections 1.2 and 1.3.

## 1.2. Single photon emission computed tomography (SPECT)

SPECT imaging is based on the detection of radiation released by single-photon-emitting ( $\gamma$ -rays and X-rays) radionuclides. The typical radionuclides used in SPECT include  $^{99m}\text{Tc}$ ,  $^{67}\text{Ga}$ ,  $^{123}\text{I}$ ,  $^{131}\text{I}$  and  $^{111}\text{In}$  [24]. They are usually administered via an injection into the bloodstream and are labeled with biological compounds, whose biochemical properties define the distribution of the administered substance. SPECT systems are usually based on a gamma camera rotating around a patient. Thus the mechanical collimation principle described in section 1.1 for gamma cameras is also applied here. As in a typical tomographic modality, in SPECT multiple projection images are acquired at various angles around the patient with usually  $360^\circ$  of arc (except for cardiac studies, where typically a  $180^\circ$  data collection is used). The projection images are subsequently reconstructed to transverse tissue-section images (slices) with filtered backprojection or iterative reconstruction methods [25]. SPECT images are usually not absolutely quantitative in practice, since the correction for photon attenuation and scattering is challenging for this modality and is often omitted. Nonetheless, recent developments show the possibility to obtain a quantitative SPECT image in the combined systems like e.g. SPECT and computed tomography – SPECT/CT [26]. Bailey and Willowson [26] describe the main challenges of applying the correction for photon attenuation in SPECT, the requirements for quantitative emission tomography and the proposed steps needed for quantitative SPECT reconstruction.

## 1.3. Positron-emission-tomography (PET)

### 1.3.1. Operating principles of PET imaging

The following outline of the main principles of Positron Emission Tomography (PET) imaging is partly based on the book “PET: physics, instrumentation and scanners” by M.E. Phelps [27] and a review article by P. Zanzonico [28]. PET is a widely used nuclear medicine imaging technique. It involves the use of radiation administered in a form of radiopharmaceuticals [28]. These radiopharmaceuticals are positron-emitting radionuclides labeled with biological compounds [27]. Often intravenous administration is used, in some rare cases, e.g. in the studies of gastrointestinal drug absorption with  $^{18}\text{F}$ -labeled fluorodeoxyglucose ( $^{18}\text{F}$ -FDG) – oral administration. The clinical purpose of a radiopharmaceutical depends on

the biochemical properties of the biological compound. The radionuclides commonly used in PET imaging include  $^{18}\text{F}$ ,  $^{11}\text{C}$ ,  $^{15}\text{O}$ ,  $^{124}\text{I}$ ,  $^{13}\text{N}$ ,  $^{82}\text{Rb}$  and some others which are usually produced in a cyclotron. These radionuclides have a neutron-to-proton ratio  $N/Z$  smaller than that of the stable nuclides, i.e. they are “proton rich”. The excess of protons can be eliminated either via  $\beta^+$ -decay, or via electron capture. Electron capture is the dominant process in nuclides with high  $Z$  while  $\beta^+$ -decay is the dominant process in low  $Z$  nuclides. In case of electron capture, a proton in the nucleus is transformed into a neutron by capturing an orbital electron (usually  $K$  shell electrons) and emitting a neutrino  $\nu$  (see equation 1.4 on page 13). An emission of a positron  $e^+$  is needed for the basic principle of PET imaging (described later in this subsection). Since it does not occur as a result of electron capture, in PET imaging usually those radionuclides that decay predominantly by  $\beta^+$ -emission are used. In this case a proton transforms into a neutron by ejecting a positron  $e^+$  and a neutrino  $\nu$ . As an example, the  $\beta^+$ -decay of  $^{18}\text{F}$  is given in the following equation:



The fraction of decays that occur for  $^{18}\text{F}$  by  $\beta^+$ -emission is approximately 97 %. The emitted positrons  $e^+$  are not monoenergetic, since the released energy is shared between the daughter nucleus,  $\nu$  and  $e^+$ . The maximum kinetic energy of  $e^+$  is radionuclide-specific. For  $^{18}\text{F}$  the maximum kinetic energy of  $e^+$  is equal to 633.5 keV.

After losing the kinetic energy in inelastic interactions with atomic electrons and almost at rest, the emitted  $e^+$  annihilates with an electron  $e^-$  of the tissue. The spatial distance between the emission of  $e^+$  and the annihilation depends on positron range, which is in order of a few mm in human tissue [29]. Thus the annihilation occurs in a very short distance from the place where the  $\beta^+$ -emission took place. During the annihilation, the mass of the electron and the positron is converted into electromagnetic energy, which is released (in the vast majority of cases) in the form of two so-called annihilation photons. Due to the conservation of momentum and energy the annihilation photons carry an energy of 511 keV each and are emitted simultaneously in almost opposite directions. The high energy of the emitted photons allows them to escape from the body with a high probability and thus, enables the detection of these coincidence photons outside the body of the patient. This is the main principle of PET imaging. It is schematically shown in figure 1.1. The interaction of the emitted radiation with tissue as well as the detection principle are discussed in sections 1.3.2 and 1.3.3, respectively.

### 1.3.2. Interaction of emitted radiation with matter

Two types of radiation are to be considered in PET imaging: positrons ejected in  $\beta^+$ -decay of the used radionuclide and high-energy photons emitted as a result of annihilation of the positron with an electron of the tissue. Positrons quickly lose their kinetic energy in inelastic interactions with atomic electrons. The annihilation occurs when the kinetic energy is almost zero, i.e. when the positron is almost at rest. The distance that positrons travel in tissue prior to annihilation, also called positron range, depends on the energy of the ejected  $e^+$  and is, thus, radionuclide-specific. For  $^{18}\text{F}$  the maximum positron range in water is  $\approx 0.2$  cm [30]. The calculation of positron range for common PET radionuclides was done by e.g. C.S. Levin and E.J. Hoffman [29]. Due to multiple scattering the trajectories of positrons are not straight and, therefore, the Continuous Slowing Down Approximation (CSDA) range is always higher than the projected range. The CSDA range of positrons

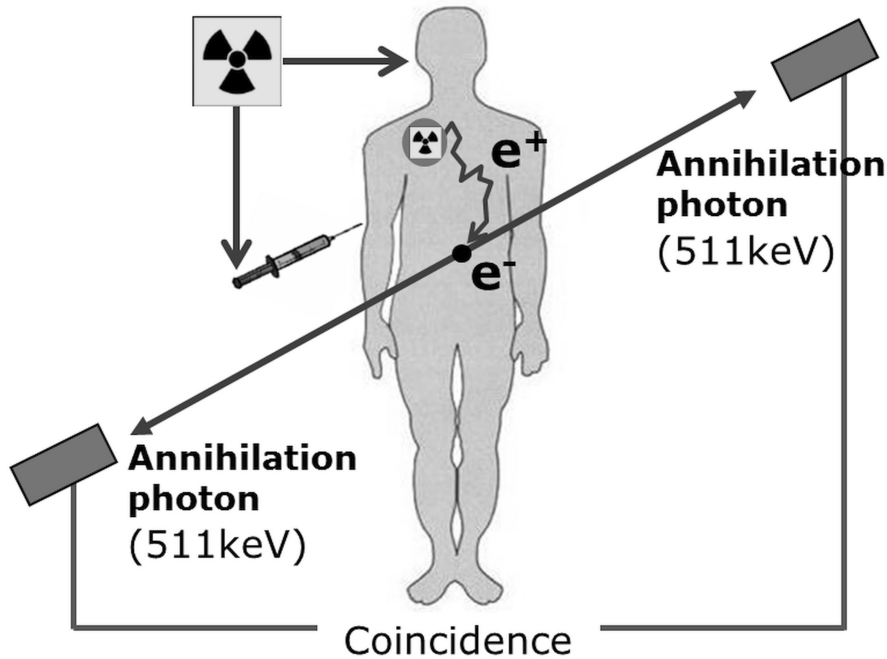


Figure 1.1. Concept of PET imaging: administration of  $\beta^+$ -emitting radionuclide, its decay, annihilation of the emitted  $e^+$  with  $e^-$  and the subsequent external detection of the coincidence annihilation photons. The range of  $e^+$  is not to scale but for clear illustration.

with kinetic energy of 600 keV in water is equal to  $0.2265 \text{ g/cm}^2$  (the data are taken from <http://physics.nist.gov/PhysRefData/Star/Text/ESTAR.html>). The  $e^+$  range effect is one of the factors limiting the resolution of the PET image. Other limiting factors are discussed in section 1.3.3.

In contrast to the energy of the emitted  $e^+$ , the energy of annihilation photons does not depend on the radionuclide, since the annihilation occurs almost at rest and the masses of  $e^+$  and  $e^-$  are converted to the energy of the photons. This energy is equal to the rest mass of  $e^-$  (or  $e^+$ ), which is 511 keV. The annihilation photons subsequently travel in tissue and interact with it. The quantity related to the probability  $dW$  of a particle moving perpendicularly in a thin layer of tissue  $dx$  to undergo a certain type of interaction is called cross section  $\sigma$  [31]:

$$dW = dx \frac{n}{V} \sigma = dx N \sigma \quad (1.7)$$

where  $n$  is the number of scattering centers in an arbitrary volume  $V$  of material and  $N$  is the concentration of scattering centers per unit volume in material. Cross sections that correspond to a particular interaction type are called partial cross sections, whereas the sum of all partial cross sections is denoted as the total cross section  $\sigma_{\text{tot}}$ . A beam of particles loses intensity as it traverses material. This intensity loss is referred as attenuation. Often a simple exponential attenuation law is applied to describe an attenuation of a narrow beam of monoenergetic uncharged particles that incidents perpendicularly on material. “Narrow-beam” geometry means that any scattered or secondary radiation is not considered. For the change  $dI$  in the beam intensity  $I$  after passing thickness  $dx$  of material it can be

## 1. Nuclear medicine modalities

written:

$$dI = -\mu I dx \quad (1.8)$$

where the coefficient of proportionality  $\mu$  is the probability that an individual particle undergoes interaction in a unit thickness of material. After dividing both sides of equation 1.8 by intensity  $I$ , integrating it and solving the resulting equation with respect to  $I$  one gets:

$$I_x = I(x) = \text{Const } e^{-\mu x} \quad (1.9)$$

Assuming the initial beam intensity  $I_0 = I(x = 0)$ , from equation 1.9 it follows that  $\text{Const} = I_0$ :

$$I_x = I_0 e^{-\mu x} \quad (1.10)$$

Equation 1.10 is called exponential attenuation law and  $\mu$  is the linear attenuation coefficient, e.g. in  $[\text{cm}^{-1}]$  if  $dx$  is in  $[\text{cm}]$ . Linear attenuation coefficient  $\mu$  divided by density  $\rho$  of the attenuating material is denoted as mass attenuation coefficient  $\mu/\rho$ , e.g. in  $[\text{cm}^2/\text{g}]$ . From the definition of  $\mu/\rho$  and equation 1.7 it follows:

$$\frac{\mu}{\rho} = \frac{1}{\rho} \frac{n}{V} \sigma_{\text{tot}} = \frac{1}{\rho} \frac{\rho V}{V} \frac{\sigma_{\text{tot}}}{N_A} = \frac{N_A}{A} \sigma_{\text{tot}} \quad (1.11)$$

where  $N_A \approx 6.02 \cdot 10^{23} \text{ mol}^{-1}$  is Avogadro's number and  $A$  is the atomic mass number of the attenuator.

The mass attenuation coefficients for photons in water are shown in figure 1.2. At the photon energy  $E = 511 \text{ keV}$  the interactions to be considered are incoherent (Compton) scattering, coherent (Rayleigh) scattering and photoelectric absorption (effect). The mean free path, i.e. the average distance between two sequential interactions, of 511 keV photons in water  $\lambda$  is 10.42 cm.

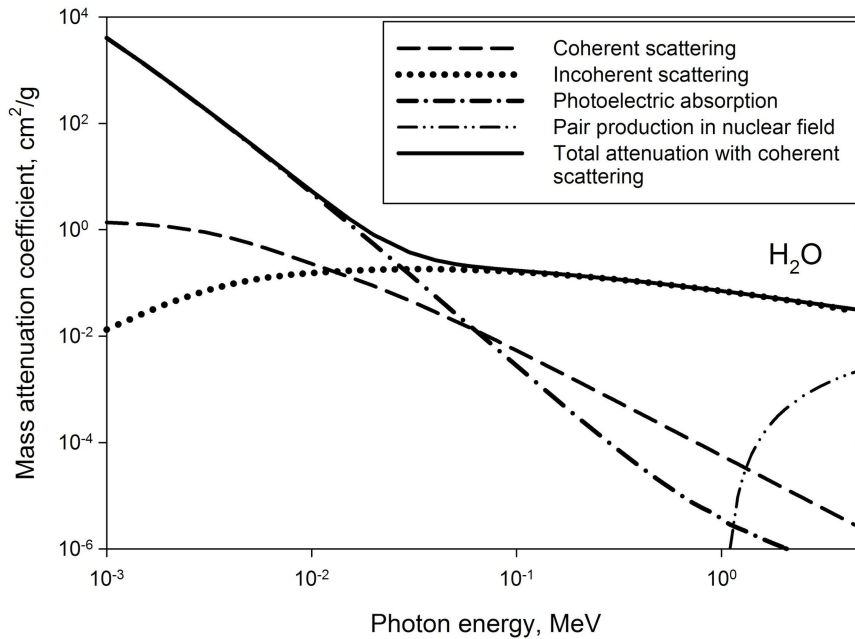


Figure 1.2. Photon mass attenuation coefficients in water,  $[\text{cm}^2/\text{g}]$ . The mass attenuation coefficients data are taken from [www.nist.gov](http://www.nist.gov).

**Compton scattering** Incoherent (Compton) scattering is an inelastic scattering of a photon on a free electron. An electron is considered to be free, if the energy of the photon is much higher than the binding energy of the electron. As a result of this scattering the photon deflects from its original direction and a fraction of its energy is transferred to a kinetic energy of the recoiling electron  $E_e$ :

$$E_e = E_\gamma - E'_\gamma = \frac{E_\gamma}{1 + \frac{m_e c^2}{2E_\gamma \sin^2(\theta/2)}} \quad (1.12)$$

In equation 1.12  $E_\gamma$  is the initial energy of the photon and  $E'_\gamma$  is the energy of the photon after the Compton scattering,  $m_e$  and  $c$  are the electron mass and the speed of light, respectively, and  $\theta$  is the angle at which the photon is scattered.

The anisotropy of the scattering increases with increasing initial energy of the incident photon  $E_\gamma$ . The electronic cross section of the Compton scattering does not depend on the characteristics of the medium. The corresponding atomic cross section  $\sigma_C$  is proportional to atomic number  $Z$  and is inversely proportional to the energy of the photon:

$$\sigma_C \propto \frac{Z}{E_\gamma} \quad (1.13)$$

**Rayleigh scattering** Coherent (Rayleigh) scattering is a scattering of photons by bounded atomic electrons. In this process the atom is not ionized or excited, so no energy transfer occurs. The probability of Rayleigh scattering is higher at low energies of the photons and for materials with high atomic number  $Z$ :

$$\sigma_R \propto \frac{Z^2}{E_\gamma^2} \quad (1.14)$$

**Photoelectric effect** In the photoelectric effect a photon is absorbed by the atom, a part of the photon energy is spent on the binding energy of the electron shell and the rest of the energy of the photon is entirely transferred to an orbital electron. This process is possible if the energy of the incident photon is higher than the binding energy of the electron shell. The electron gets enough energy to escape the atom and is called a photoelectron. The kinetic energy of the photoelectron ( $T_e$ ) can be written as:

$$T_e = E_\gamma - I_i - E_n \quad (1.15)$$

where  $E_\gamma$  is the energy of the incident photon,  $I_i$  is the ionization energy of the electron shell  $i$  ( $i = K, L, M, \dots$ ) and  $E_n$  is the recoil energy of the nucleus, which is usually negligible.

The photoelectric effect is more probable for the electron shell closest to the nucleus, i.e.  $K$  shell ( $\approx 80\%$ ), and due to the conservation of momentum the photoelectron is emitted in almost the same direction as that of the incident photon. The cross section of the photoelectric effect  $\sigma_\tau$  strongly depends on the atomic number  $Z$  of the absorbing material and the energy of the incident photon  $E_\gamma$ , which is equal to 511 keV for annihilation photons:

$$\sigma_\tau \propto \frac{Z^n}{E_\gamma^{7/2}} \quad (1.16)$$

with  $n$  varying from 3 to 5.

## 1. Nuclear medicine modalities

After the photoelectron is emitted, the vacancy in the electron shell of the atom is filled with an electron from a higher electron shell. The energy difference is typically ejected as a characteristic  $X$ -ray photon. This process is called  $X$ -ray “fluorescence”. The typical energies of the  $K$ -shell fluorescence  $X$ -rays range from a few keV (for the elements with atomic numbers 11–30, i.e. from  $_{11}\text{Na}$  to  $_{30}\text{Zn}$ ) to a few tens of keV for heavier atoms. For the elements from  $_4\text{Be}$  to  $_{10}\text{Ne}$  the corresponding energies amount to a few hundreds of eV. Thus the characteristic  $X$ -rays are rapidly absorbed in the medium as well as the photoelectrons. Another process, which is a competing process to the ejection of the characteristic  $X$ -rays, is the Auger effect. When the vacancy in the electron shell is filled with an electron from a higher energy level, the excess of energy can be transferred to another electron. As a result, this electron, called Auger electron, is ejected from the atom. The kinetic energy of the Auger electron is equal to the difference between the electron transition into the vacancy and the binding energy of the electron shell, from which the Auger electron was ejected.

### 1.3.3. Radiation detection in PET imaging

Due to the high energy of annihilation photons, they can leave the body of the patient with a high probability and thus can be detected externally. As it was mentioned above, the annihilation photons are emitted with an angle of approximately  $180^\circ$  to each other. Therefore, if the detected photons can be localized, the line joining the detection points goes through the annihilation site. Since the annihilation occurs almost locally, this event line also approximately goes through the location where the atom of the radionuclide was in the body. To localize exactly where the radioactive nucleus was in the body, the principle of computed tomography is used. According to it, the annihilation photon pairs along the lines that traverse the patient (lines of response) at various angles are measured. The set of lines of response is resorted and re-binned into the projection dataset [1,23]. Subsequently, filtered back-projection or iterative image reconstruction algorithms are employed to compute the transverse tissue-section images. The contiguosness of the transverse-section images in PET (as well as in SPECT) enables a rearrangement of the reconstructed voxels, so that coronal, sagittal, or oblique images can be obtained.

In fact  $e^+$  and  $e^-$  are not completely at rest when they annihilate. Consequently, due to the conservation of momentum, the annihilation photons are emitted not exactly at  $180^\circ$  to each other. This is called non-collinearity and it results in a small error in locating the line of annihilation. Along with the positron range effect mentioned in section 1.3.2, non-collinearity limits the spatial resolution achievable in PET and causes a blurring in the reconstructed image.

The energy of the annihilation photons is independent of the used radionuclide and is always equal to 511 keV. Due to this property PET scanners are optimized to efficiently detect 511 keV photons. The detectors must also localize the annihilation site with good accuracy. The latter is one of the important factors that define the spatial resolution of the resulting image. The detectors with an energy resolution ability, e.g. inorganic scintillating detectors with an energy resolution of about 10–15% are used in PET scanners, so that the photons, which scattered in the body and lost some of their energy in these inelastic interactions can be identified and typically rejected. Since coincident photon pairs need to be detected, an important property of the detectors is their time resolution. This is the ability to estimate the time interval between the detection of two photons. In order to avoid

the undesirable rejection of annihilation photon pairs, a time window in PET scanners is usually set higher than the time resolution of the detectors and is typically 4–18 ns [27]. Because each annihilation photon has always the energy of 511 keV and one pair of annihilation photons corresponds to one  $\beta^+$ -decay, the coincidence detection of this photon pair facilitates the quantification of PET imaging. Applying necessary corrections makes PET imaging absolutely quantitative. The required corrections include e.g. normalization (correction for non-uniformity of measured count rates for the same activity), calibration of the detection efficiency, correction for the count loss due to a deadtime of scintillators, subtraction of randoms from the detected coincidence counts, scatter and attenuation corrections [1]. Thus, activity concentrations of the injected radiopharmaceutical can be determined from the PET image.

As mentioned above, the most frequently used detectors in PET scanners are scintillation detectors. These detectors convert a part of the particles' (in case of PET imaging – annihilation photons) energy deposited in the material of the scintillator into visible light. How much of the deposited energy is converted to scintillation photons is defined by the scintillation efficiency. Scintillators typically used in PET imaging are inorganic crystalline scintillators. Their relatively large effective  $Z$  and density yield a high stopping power of photons in the material of the scintillator. Typical scintillation crystals utilized in the design of current PET systems are e.g. BGO ( $\text{Bi}_4\text{Ge}_3\text{O}_{12}$ ) or LSO ( $\text{Lu}_2\text{SiO}_5$ ). The densities of BGO and LSO are 7.13 and 7.4 g/cm<sup>3</sup>, respectively, whereas effective  $Z$  is 75 for BGO and 66 for LSO [23]. The latter crystal is usually doped with cerium Ce. Consequently, in the Ce-doped LSO additional electron orbitals (activation centers) between the valence and the conduction bands of molecular orbitals are created. The incident photons interact with the material of the scintillator and secondary electrons are produced. These electrons excite and ionize the atoms of the scintillator. Some of the electrons have sufficient energy to jump through the forbidden gap to the conduction band, where they migrate till they drop to the excited-state orbitals of the activation center. The holes in the valence band also effectively migrate to the ground-state orbitals of the activation center. Eventually, an electron from the excited-state orbital of the activation center drops down and fills the hole at the ground-state orbital of the activation center. The excess energy is released in a form of a scintillation photon, which passes through the crystal and strikes a photocathode. As a result of a photoelectric effect in the material of the photocathode, an electron is ejected into a vacuum space of a photo-multiplier tube. The electrons in the photo-multiplier tube are accelerated by the voltage and knock out from a set of dynodes a number of other electrons, which create a measurable electronic signal at the anode of the photo-multiplier. The height of the generated pulse is proportional to the energy absorbed in the scintillator. Usually a whole ring of scintillators (detector elements) is used in PET scanners. According to the principle described above, each photon striking a detector element results in a pulse, generated by the detector element. The timed pulse sequences generated by each detector element are compared and those occurred within a short time-window are considered to be coincident. The number of coincidence events correspond to the number of detected  $\beta^+$ -decays and the underlying radionuclide activity can be reconstructed and quantified with the data correction and image reconstruction techniques above mentioned.



## 2. Dosimetry in nuclear medicine

The standard model of organ absorbed dose computation proposed by the Committee on Medical Internal Radiation Dose (MIRD) is described in reference [4] and summarized in the following text. According to this model, the absorbed dose coefficient  $d(r_T)$  in the target region  $r_T$  is calculated as:

$$d(r_T, T_D) = \sum_{r_S} \int_0^{T_D} a(r_S, t) S(r_T \leftarrow r_S, t) dt \quad (2.1)$$

where  $a(r_S, t)$  denotes the fraction of administered activity in the source regions  $r_S$  at time  $t$  after administration of a radiopharmaceutical, normalized to a unit of administered activity  $A_0$ . The values of  $a(r_S, t)$  are usually calculated by numeric solution of a system of differential equations, defined by an employed pharmacokinetic model (cf. section 4.3).  $T_D$  is the dose-integration period which is theoretically infinite.

The values  $S(r_T \leftarrow r_S, t)$  are specific to the radionuclide and to the considered human computational phantom. They are defined as:

$$S(r_T \leftarrow r_S, t) = \sum_i E_i Y_i \Phi(r_T \leftarrow r_S, E_i, t) \quad (2.2)$$

with

$$\Phi(r_T \leftarrow r_S, E_i, t) = \frac{\phi(r_T \leftarrow r_S, E_i, t)}{M_{r_T}} \quad (2.3)$$

$E_i$ ,  $Y_i$  are mean energy and yield of radiation  $i$ ;  $\phi(r_T \leftarrow r_S, E_i, t)$  and  $\Phi(r_T \leftarrow r_S, E_i, t)$  are absorbed fraction and specific absorbed fraction (SAF) [5], respectively.  $\phi(r_T \leftarrow r_S, E_i, t)$  is defined as the fraction of radiation  $i$  with energy  $E_i$  emitted from  $r_S$  at time  $t$  that is absorbed in  $r_T$ .  $M_{r_T}$  denotes the mass of the target region, which in general can also be time-dependent ( $M_{r_T}(t)$ ). The time-dependence of the mass  $M_{r_T}(t)$  is to be considered if e.g.  $r_T$  is a tumor region, since  $M_{r_T}(t)$  varies during the irradiation period.

For  $\beta$ -emitters, where the continuous  $\beta$ -spectrum is to be considered, the summation in equation 2.2 is replaced by the following integral:

$$S(r_T \leftarrow r_S, t) = \int_0^{E_0} P(E) E \Phi(r_T \leftarrow r_S, E, t) dE \quad (2.4)$$

In equation 2.4  $E_0$  is the maximum (end-point) energy of the  $\beta$ -spectrum;  $P(E)$  is the number of  $\beta$ -particles emitted at the energy  $E$  per MeV per nuclear transformation. If for the combination of  $r_S$  and  $r_T$ , where  $r_S \neq r_T$ ,  $\phi(r_T \leftarrow r_S, E_0, t)$  is negligible, equation 2.2 for the mean energy of  $\beta$ -spectrum can be used instead of equation 2.4.

If the time-dependence of  $S(r_T \leftarrow r_S, t)$  can be neglected, equation 2.1 can be written as:

$$\begin{aligned} d(r_T, T_D) &= \sum_{r_S} S(r_T \leftarrow r_S) \int_0^{T_D} a(r_S, t) dt \\ &= \sum_{r_S} S(r_T \leftarrow r_S) \tilde{a}(r_S, T_D) \end{aligned} \quad (2.5)$$

## 2. Dosimetry in nuclear medicine

where  $\tilde{a}(r_S, T_D)$  is the time-integrated activity coefficient in the source region  $r_S$ , given in units of time.

In dosimetric calculations for radiopharmaceuticals the list of source regions usually includes the so-called rest of body (RoB).  $r_{RoB}$  comprises the total body, excluding other source regions, which are explicitly considered in a pharmacokinetic model. Thus, for different agents that have various mechanisms of distribution in a human body and, consequently, different lists of source regions,  $r_{RoB}$  does not remain the same anatomical region. Therefore, it is not robust to derive the values  $S(r_T \leftarrow r_{RoB})$  via direct Monte Carlo calculations for this source region. The common practice is to compute  $S(r_T \leftarrow r_{RoB})$  from the corresponding values for the total body as a source ( $r_{TB}$ ) and other  $r_S \neq r_{RoB}$ :

$$S(r_T \leftarrow r_{RoB}) = \frac{M_{r_{TB}} S(r_T \leftarrow r_{TB}) - \sum_{r_S \neq r_{RoB}} M_{r_S} S(r_T \leftarrow r_S)}{M_{r_{RoB}}} \quad (2.6)$$

where  $M_{r_S}$  and  $M_{r_{TB}}$  denote the masses of source regions and total body, respectively.  $M_{r_{RoB}}$  is the mass of rest of body  $r_{RoB}$ . The definition of  $r_{RoB}$  results in the following equation for  $M_{r_{RoB}}$ :

$$M_{r_{RoB}} = M_{r_{TB}} - \sum_{r_S \neq r_{RoB}} M_{r_S} \quad (2.7)$$

Using equations 2.5 and 2.6 for the case of time-independent  $S(r_T \leftarrow r_S)$  the absorbed dose coefficient in the target region  $r_T$  is computed as follows:

$$d(r_T, T_D) = \sum_{r_S \neq r_{RoB}} \tilde{a}(r_S, T_D) S(r_T \leftarrow r_S) + \tilde{a}(r_{RoB}, T_D) \left( \frac{M_{r_{TB}} S(r_T \leftarrow r_{TB}) - \sum_{r_S \neq r_{RoB}} M_{r_S} S(r_T \leftarrow r_S)}{M_{r_{RoB}}} \right) \quad (2.8)$$

A special case in internal dosimetry is the reconstruction of absorbed dose to the urinary bladder wall. For renally excreted radiopharmaceuticals a notable fraction of the injected activity is accumulated in urinary bladder content. Thus a high contribution to the dose absorbed in urinary bladder wall comes from the radiation emitted by urinary bladder contents. It was demonstrated elsewhere [32] that absorbed dose to urinary bladder wall depends on the volume of bladder content and the thickness of the bladder wall. The phantom-specific values of  $\Phi(UB_{\text{wall}} \leftarrow UB_{\text{cont}})$  are derived with Monte Carlo calculations in the geometry of the respective phantoms. They correspond to the bladder volume segmented in the phantom and to the thickness of the bladder wall, which is often limited by the voxel size. Hence, the changes in the volume of the bladder content and the corresponding thickness of the wall with bladder filling and emptying are neglected, if computing the absorbed dose according to equation 2.5. To account for these limitations a dynamic urinary bladder model was developed in [22].

According to the dynamic bladder model [22], the volume of bladder contents  $V(t)$  is defined as (time  $t = 0$  correspond to the time when the radiopharmaceutical was administered):

$$V(t) = \begin{cases} V_0 + \int_0^t U(t') dt', & \text{for } 0 \leq t < T_1 \\ V_r + \int_{T_{n-1}}^t U(t') dt', & \text{for } T_{n-1} \leq t < T_n \end{cases} \quad (2.9)$$

$V_0$  [ml] and  $V_r$  [ml] are, respectively, the initial bladder-content volume and the residual bladder-content volume after the voiding.  $T_i$  [min] is the time between the administration of the radiopharmaceutical and the  $i$ -th voiding, e.g.  $T_1$  [min] is that of the first voiding.  $U(t)$  [ml/min] stands for the urine production rate.

Thomas et al. [22] define the activity of the bladder contents normalized to the injected activity  $A_0$  as follows:

$$a(UB_{\text{cont}}, t) = \frac{A(t)}{A_0} = e^{-\lambda t} \sum_{j=1}^m \alpha_j (1 - e^{-\lambda_j t}) - \sum_{i=1}^n \left(1 - \frac{V_r}{V(T_i)}\right) A(T_i) e^{-\lambda(t-T_i)} \quad (2.10)$$

where  $\lambda$  is the physical decay constant,  $n$  is the number of voidings,  $V(T_i)$  and  $A(T_i)$  denote the bladder volume and the activity in the bladder contents right before the  $i$ -th voiding at  $t = T_i$ , respectively.  $\alpha_j$  and  $\lambda_j$  are biologic parameters for the bladder contents, which are radiopharmaceutical-specific. The values of  $\alpha_j$  and  $\lambda_j$  for commonly used radiopharmaceuticals are summarized in reference [22]. Thomas et al. [22] stated that for radiopharmaceuticals that are excreted solely via the urinary path,  $\alpha_j$  and  $\lambda_j$  can be estimated from the total body retention data. These data are fitted to a sum of exponential functions, where the number of the exponential functions (= parameter  $m$  in equation 2.10) is defined by the modeler based on the retention data. For example, if total body time-activity data are in agreement with a double-exponential function, it can be written:

$$a(r_{TB}, t) = e^{-\lambda t} (\alpha_1 e^{-\lambda_1 t} + \alpha_2 e^{-\lambda_2 t}) \quad (2.11)$$

and  $m = 2$  in this case. From equations 2.10 and 2.11 it can be seen that the first term of equation 2.10 represents the input of activity from the total body to the bladder content. Whereas the second term of equation 2.10 is the voided bladder content activity, i.e. this term corrects the activity accumulated in the bladder contents for the activity that is excreted at each voiding time  $T_i$ .

$S(UB_{\text{wall}} \leftarrow UB_{\text{cont}}, t)$  is dependent on  $V(t)$  and can be derived by Monte Carlo calculations for various volumes of the bladder contents  $V(t)$ . Such simulations were done by Andersson et al. [33] for photon and electron sources. Knowing the time-dependent activity of bladder contents from equation 2.10 and the time-dependent bladder-content volume from equation 2.9, the absorbed dose coefficient for urinary bladder wall from activity accumulated in bladder contents can be calculated according to equation 2.1:

$$d(UB_{\text{wall}}, T_D) = \int_0^{T_D} a(UB_{\text{cont}}, t) S(UB_{\text{wall}} \leftarrow UB_{\text{cont}}, V(t)) dt \quad (2.12)$$

To compute the bladder-wall dose from all considered sources, equations 2.12 and 2.8 are to be used for the contributions from bladder content and other source regions, respectively.

For comparison values similar to effective dose were computed in this thesis. For the sake of convenience, they are denoted as effective dose (or effective dose coefficients). The effective doses calculated in section 5.2 are not age- and sex-averaged, in contrast to the definition of effective dose given by the International Commission on Radiological Protection (ICRP) [34]. They were computed for individual phantoms as weighted average of the individual organ equivalent dose conversion coefficients using tissue weighting factors from ICRP Publication 103 [34].



## **Part II.**

# **Pharmacokinetic modeling**



In chapter 3 a short summary of the classes of mathematical models used in kinetic studies as well as the general equations describing a lumped deterministic model (compartmental model) are given. It is followed by the description in chapter 4 of materials and methods used for the development of compartmental pharmacokinetic models in this work. In chapter 5 the newly developed compartmental pharmacokinetic models along with the model predictions are presented with emphasis on the effect of blood activity on internal organ doses. Materials, methods and results of this part were also summarized and published by Zvereva et al. [35] in the paper related to one specific issue in internal dosimetry – the way of considering blood activities in dosimetric studies.



### 3. Fundamentals of pharmacokinetic modeling

The material in this chapter is recapitulated partly based on the books of Godfrey [36], Phelps, Mazziotta and Schelbert [37] and Carson, Cobelli and Finkelstein [38].

Carson, Cobelli and Finkelstein [38] review the commonly used classes of mathematical models describing kinetic and metabolic processes. The models can be lumped or distributed. Both of these model classes can be linear or nonlinear, stochastic or deterministic. In a linear model the variables and their derivatives are present only in a linear combination. Stochastic models include probabilistic effects, when e.g. describing some processes on a cellular level. In the lumped models the distributed entity is assumed to be homogeneous, e.g. a metabolite in plasma. In fact a metabolite in plasma has gradients of concentration, but in a lumped model it is considered to be one compartment with homogeneously distributed substance. Mathematically a lumped model leads to ordinary differential equations. Such a simplified representation is adequate in many cases. Where it is not appropriate to neglect the distribution effects like, e.g. blood flow, diffusion, chemical reactions, the distributed models are employed. Mathematically the distributed effects are usually described by partial differential equations.

An example of a lumped deterministic model frequently used in kinetic or metabolic studies is a compartmental model. Such model consists of a finite number of well-mixed homogeneous subsystems (compartments) that exchange with each other and with the environment [36]. The kinetics of substances in a compartmental model is usually described by a system of first-order differential equations. The general form of compartmental equations is based on mass-balance equations for such system and the flux of an investigated entity from each compartment to other sites. Godfrey [36] gives these equations for a system with  $p$  compartments as follows:

$$\frac{dx_i}{dt} = f_{i0} + \sum_{\substack{j=1 \\ j \neq i}}^p f_{ij} - \sum_{\substack{j=1 \\ j \neq i}}^p f_{ji} - f_{0i}, \quad i = 1, 2, \dots, p \quad (3.1)$$

In this equation  $x_i$  is the amount (or concentration) of the substance of interest in compartment  $i$ ,  $f_{ij}$  is the flow rate to compartment  $i$  from compartment  $j$ . The flow rates  $f_{i0}$  and  $f_{0i}$  are from the environment to compartment  $i$  and from compartment  $i$  to the environment, respectively. In pharmacokinetic studies for radiopharmaceuticals used for PET imaging  $f_{i0}$  and  $f_{0i}$  correspond to injection and excretion, respectively.

The most commonly used compartmental models are linear and time-invariant [36]. In such models the flow rates are proportional to the amount of substance in a compartment from which the substance flows to other sites. The constant of proportionality is often

### 3. Fundamentals of pharmacokinetic modeling

denoted as a rate constant. Considering this assumption, equation 3.1 can be written as:

$$\frac{dx_i}{dt} = u_i(t) + \sum_{\substack{j=1 \\ j \neq i}}^p k_{ij}x_j - \sum_{\substack{j=1 \\ j \neq i}}^p k_{ji}x_i - k_{0i}x_i, \quad i = 1, 2, \dots, p \quad (3.2)$$

The rate constants  $k_{ij}$  represent parameters of a compartmental model and “establishing” a compartmental model means the estimation of the rate constants.

## 3.1. Input data to establish a personalized pharmacokinetic model

In PET imaging pharmacokinetic models describe the distribution of the injected radiopharmaceutical in the body of the patient over time and the excretion of the injected substance. In the compartmental equations 3.2 used for describing these processes,  $x_i$  is the activity accumulated in the source region  $i$ . Since PET imaging is absolutely quantitative, as it is discussed in section 1.3, these activities can be obtained from the PET image. Radiopharmaceuticals in PET imaging are usually administered intravenously. Thus, the parameter  $u_i(t)$  in equations 3.2 is present usually only in the corresponding equation for the blood compartment. The exact shape of the input function  $u_i(t)$  is defined by the type of administration, e.g. bolus (instant injection) or infusion (prolonged administration), and is, therefore, usually known. Since the distribution of the injected substance in the human body is a dynamic process, the activity values in the considered compartments need to be determined over time to allow the estimation of the model parameters. This practically means that for the set up of a personalized pharmacokinetic model a series of activity measurements in various regions of interest has to be done for the patient. The number and the frequency of the measurements as well as the list of regions of interest to be measured depends on the expected complexity of the compartmental model. For this reason usually the development of the measurement protocol is accompanied by the evaluation of the model identifiability. The model is globally identifiable if a unique solution of the system of equations 3.2 exists under the assumption that noise is not present.

## 3.2. Simulation, Analysis, and Modeling Software II (SAAM II)

Simulation, Analysis, and Modeling Software II (SAAM II) [39] is a software package for tracer and pharmacokinetic analysis. Compartmental and numerical modules are available in SAAM II. The compartmental module can be used to create a visual representation of a model in the graphical user interface. The program creates subsequently a system of ordinary differential equations from the graphically specified compartmental model structure. The numerical module allows direct specification of algebraic equations describing the model. Three integration methods are implemented in SAAM II. This includes the Rosenbrock integrator, the Runge-Kutta integrator as well as the Pade integrator. In this thesis the Rosenbrock integrator was employed. Depending on the investigated problem, one of these integrators can be specified by the user. The values of unknown model parameters are estimated by minimizing the objective function, which in SAAM II is the extended

least-squares maximum likelihood function [39]. A detailed description of SAAM II package is given by Barrett et al. [39] and in the SAAM II User's Guide.

### 3.3. Blood in pharmacokinetic modeling

As described in section 3.1, the input data, required for setting up a compartmental pharmacokinetic model, include time-resolved activities in the considered organs and tissues. Since most of radiopharmaceuticals in nuclear medicine are administered intravenously, they are distributed to other body tissues via blood. Right after the injection a large amount of tracer activity is contained in the blood and might remain in the blood during a substantial time, depending on the speed of the clearance of the injected agent from the blood. To consider the fraction of activity in the ROI that is associated with the circulating blood, ICRP [7] and Legget and Williams [40] recommend using the blood distribution model. ROI activities are obtained from registered PET and CT images. For each organ or tissue the measured radiotracer activity represents the sum of the activity in the organ or tissue parenchyma and the activity in the blood content of this organ or tissue. The blood is distributed throughout the organs in vessels. The diameters of the vessels go down to 4–9 micrometres for capillary [41], which is much smaller than the spatial resolution of both PET and CT. Therefore, the activity in organ parenchyma and organ blood cannot be discriminated. Only the total activity in organ parenchyma and organ blood is measurable. Consequently, usually these aggregate values, i.e. the measured activities in organ parenchyma and organ blood together, are used to establish a pharmacokinetic model. Aggregate measured activities might substantially differ from the corresponding activities in organ parenchyma for highly vascular organs and tissues. This circumstance might considerably affect the estimated model parameters.

Activities in blood contents of body organs and tissues were employed in some established pharmacokinetic models for various purposes. For example, pharmacokinetic models of some short-lived radionuclides summarized in ICRP publication 53 [7], were derived based on the blood distribution model. Sgouros [42] corrected the activity of red bone marrow biopsy samples for blood contamination. Bigler and Sgouros [43] derived cumulated activities of oxygen in blood in various tissues according to the blood volume of each tissue. Little work has been done though to sub-divide the aggregate activities obtained from PET images into activities in organ parenchyma and organ blood in pharmacokinetic models. Such sub-division of the measured activities facilitates the calculation of activity in organ parenchyma and organ blood, which, as described above, cannot be obtained by direct measurements.

Knowing activities in organ parenchyma and organ blood, two concepts of organ dose computation can be applied. According to concept-1, activities in source organ parenchyma, with blood as a distinct source region are to be used. In concept-2 blood is not considered to be a distinct source region and the aggregate measured activities in perfused organs, i.e. in organ parenchyma and organ blood content together, are employed. Concept-2 is the conventional one. The majority of the recent publications, related to dosimetric characterisation of new diagnostic and therapeutic agents [44–46], derive the dosimetry using the computer program OLINDA/EXM [47]. OLINDA/EXM does not utilize specific absorbed fractions for blood as a source  $\Phi(r_T \leftarrow r_{Blood}, E, t)$ . Thus the computed doses in this case correspond to the concept-2. It is of a high interest to evaluate and compare concept-1 and concept-2, since the way of considering blood activity in the dose calculation might

### *3. Fundamentals of pharmacokinetic modeling*

considerably influence the resulting organ doses. This is true even for relatively low activity concentrations in the blood because they can amount to high integral activity due to the large blood volumes (5300 ml and 3900 ml for reference male and female, respectively) [48].

In this thesis a new method for modeling separately activities in parenchyma and blood contents of source regions was proposed, implemented and evaluated. The dosimetric influence of defining blood as a distinct source region, i.e. blood contents of various organs and blood vessels, was also examined. The related findings are presented later in sections 4.4 and 5.2, respectively.

# 4. Clinical investigations and pharmacokinetic model development

## 4.1. Patients

In this work five sets of activity data were used. They were obtained from five healthy volunteers (three women, two men) administered with a radiopharmaceutical for PET/CT imaging. The employed radiopharmaceutical (S)-4-(3-<sup>18</sup>F-fluoropropyl)-L-glutamic acid (<sup>18</sup>F-FSPG) is designated for the diagnosis of cancer. This novel agent was recently described by Smolarz et al. [44] and is not yet clinically approved. For convenience, the following nomenclature for naming the volunteers will be used here and in the consecutive text: 1101/94, 1102/94, 1103/94, 1104/94, 1105/94. Non-image information (age, height, weight of the volunteers) and the injected activities (IA) are presented in table 4.1.

	1101/94 female	1102/94 female	1103/94 male	1104/94 female	1105/94 male
Age, years	58	64	57	63	51
Height, cm	170	170	189	160	168
Weight, kg	90	95	106	65	65
IA, MBq	283	316	275	330	295

Table 4.1. Volunteers details and injected activities (IA) [35].

## 4.2. Measurements

The PET images, blood and urine samples were acquired at the Nuclear Medicine Department of Klinikum rechts der Isar of Technische Universität München as part of the characterization of this agent [44]. The ethics committee approval had been granted. <sup>18</sup>F-FSPG was administered intravenously via a catheter placed in the antecubital vein. Another catheter was placed in the antecubital vein of the other arm to allow blood sampling. PET scans were obtained with Biograph 64 TruePoint PET/CT scanner (Siemens Medical Solutions). The imaging protocol comprised seven sequential scans. The description of it is given by Zvereva et al. [35] and Smolarz et al. [44]. The frequency of the scans was higher at the beginning in order to resolve the high-gradient part of the time-activity curves. The total body scan started instantly after the tracer administration and the other six scans were done from the top of the head to the mid-thigh starting at approximately 15, 20, 30, 40, 150 and 240 minutes after injection. The first scan comprised 12 bed positions, with each bed position being one minute long. It was followed by four scans of seven bed positions (one minute per bed position). The two last scans comprised a total of seven bed positions, four minutes long each. Blood samples were collected at approximately 5, 10, 15, 20, 30, 45, 60, 90, 180 and 240 minutes after injection. Blood samples of volunteer 1102/94 were not

#### 4. Clinical investigations and pharmacokinetic model development

taken because of technical reasons. Activities of the blood samples were measured with a well counter detector (Wallac) with respect to a reference, which was calibrated in the well counter (Capintec). To do the cross calibration between the imaging system and the well counter, a phantom filled with a known activity measured in the well counter (Capintec) was included in the PET scans. Smolarz et al. [44] compensated the off-image activity in the partial body scans. Urine samples were collected at approximately 50, 125, 180, 225 and 265 minutes after the tracer administration. Individual voiding times and the volumes of the voided urine were recorded. Various regions of interest (ROI) were considered: kidneys, urinary bladder contents, heart, thyroid, salivary glands, pancreas, stomach wall, liver and spleen [44]. The activity concentrations for the ROIs were determined from the PET images. After segmenting the registered CT images, Smolarz et al. [44] defined the organ volumes and, subsequently, calculated absolute activity values in these regions.

### 4.3. Development of personalized pharmacokinetic models

The activity data used in this work to establish a compartmental pharmacokinetic model for radiopharmaceutical  $^{18}\text{F}$ -FSPG included the physical decay of  $^{18}\text{F}$ . Half-life of  $^{18}\text{F}$  is  $T_{1/2} = 109.771$  min. The activities obtained from PET images corresponded to the times at which the respective PET scans were obtained, and not to the injection time. The measured activities in blood corresponded to the times at which the blood samples were taken. Therefore it was necessary to account for the radioactive decay of  $^{18}\text{F}$  in the model. For this purpose an additional loss from each compartment in the model equal to the decay constant  $\lambda$  of  $^{18}\text{F}$  was included. The compartmental pharmacokinetic model structure proposed in this work for  $^{18}\text{F}$ -FSPG is presented in figure 4.1. Note that the transfer rates mimicking the physical decay of  $^{18}\text{F}$  are not shown in figure 4.1, since they are not the unknown model parameters. Their values were fixed to  $\lambda = \frac{\ln 2}{T_{1/2}} = 0.0063 \text{ min}^{-1}$ .

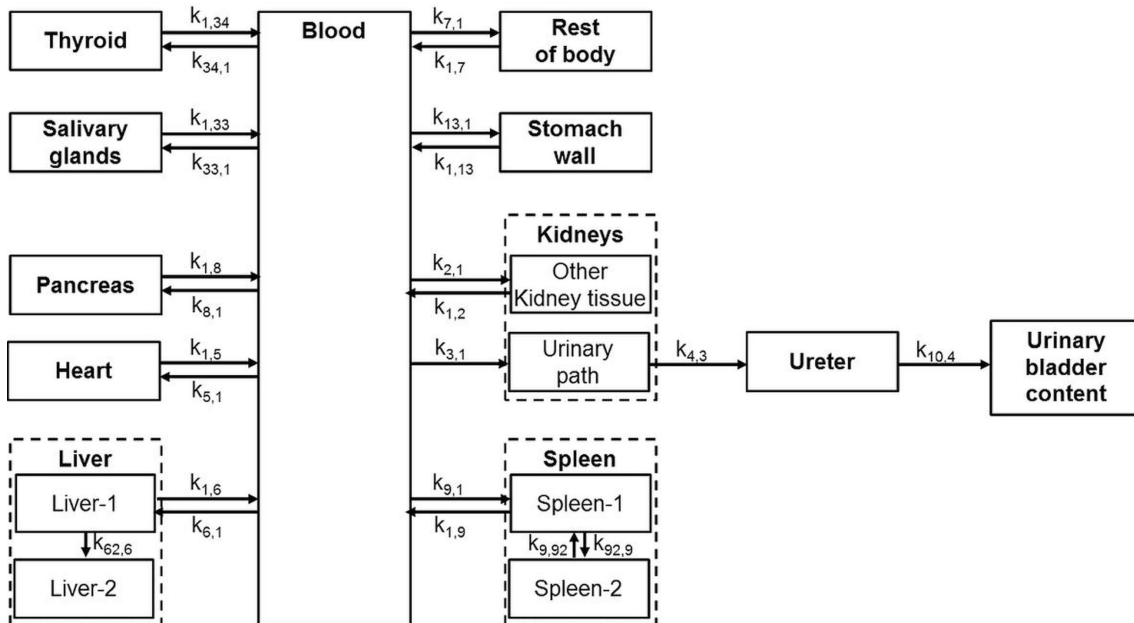


Figure 4.1. Compartmental pharmacokinetic model structure for  $^{18}\text{F}$ -FSPG [35].

### 4.3. Development of personalized pharmacokinetic models

To establish the compartmental model shown in figure 4.1 relative activities in % of injected activity were employed, i.e. activity in Bq normalized to the injected activity in Bq and given in %. These values are denoted as activity coefficients in the following text. A system of first-order linear ordinary differential equations was used to describe the distribution and the excretion of  $^{18}\text{F}$ -FSPG. Model structural identifiability was tested against the measured data (PET images, blood samples) using the computer program DAISY (Differential Algebra for Identifiability of SYstems) [49]. The model is globally identifiable if a unique solution of the system of differential equations describing the model can be found with the available input and output data under a condition that noise is not present. The considered ROIs included kidneys, bladder, heart, thyroid, salivary glands, pancreas, stomach wall, liver and spleen [44]. These organs were initially implemented into the proposed model as compartments connected to the central blood compartment. In addition to the mentioned ROIs Smolarz et al. [44] considered bone marrow for two volunteers. For the other three volunteers the uptake by the bone marrow was not above the general activity level in the body and was not measured. To keep the same consistent model structure, bone marrow was not considered as a distinct source region in this work. Sub-compartments for liver and spleen were added to the model to better fit the measured data, analogously to, e.g., ICRP [50] and Giussani et al. [51], who introduced two liver sub-compartments. Sub-compartments 1 and 2 represent, respectively, short- and long-term retention of  $^{18}\text{F}$ -FSPG. Liver-2 and spleen-2 are defined on a kinetic rather than a biological basis. To describe the urinary excretion of  $^{18}\text{F}$ -FSPG initially the kidney-bladder model reported by the ICRP [50] was adopted. It includes the direct transfer from blood to the urinary bladder and the slower transfer to the bladder through the urinary path. During the model fit, the transfer rate representing the direct flow from the blood to the bladder content could not resolve the relatively slow experimentally measured uptake of  $^{18}\text{F}$ -FSPG by bladder. Thus, for  $^{18}\text{F}$ -FSPG the fast transfer from blood to bladder was removed. To model the observed fast renal clearance and the slow uptake by bladder, an additional compartment was introduced between kidneys and bladder. Physiologically it represents the urine flow through the ureter (figure 4.1). The activity of  $^{18}\text{F}$ -FSPG in ureter can be also seen in the PET images in figure 4.2.

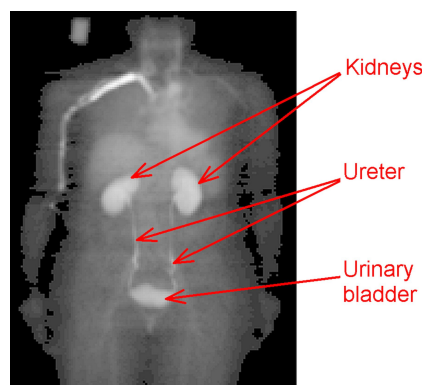


Figure 4.2. PET image of volunteer 1104/94 showing activity of  $^{18}\text{F}$ -FSPG in urine, which is produced in kidneys and flows through ureter to bladder content.  $^{18}\text{F}$ -FSPG was injected via an intravenous catheter placed in the antecubital vein of the right arm. Since this image corresponds to the PET scan obtained right after the administration of  $^{18}\text{F}$ -FSPG, a large amount of activity can still be seen in the blood vessels of the right arm.

#### 4. Clinical investigations and pharmacokinetic model development

One compartment, defined as rest of body (RoB), was added to the model to account for the radiotracer activity transported to the organs and tissues that were not explicitly considered in the compartmental pharmacokinetic model. The activity coefficients of RoB were calculated via the subtraction of organ activity coefficients from the total body data. One common model structure was used for all volunteers; however, personalized model parameter sets were estimated based on the individual PET images and measured blood samples. A system of linear first-order ordinary differential equations was used to mathematically describe the kinetics of  $^{18}\text{F}$ -FSPG. All necessary nomenclature is given in table 4.2. The system of differential equations 4.2 for the model developed in this work (see figure 4.1) is given in the end of this section.

Activity coefficient in respective compartment of the model	Symbol		Measured activity coefficient <sup>†</sup>	Symbol
Blood	$x_1$		Blood-per-ml	$y_1$
Other kidney tissue	$x_2$	}	Kidneys	$y_2$
Urinary path	$x_3$			
Ureter	$x_4$		—	—
Heart	$x_5$		Heart	$y_5$
Liver-1	$x_6$	}	Liver	$y_6$
Liver-2	$x_{62}$			
Rest of body	$x_7$		Rest of body*	$y_7$
Pancreas	$x_8$		Pancreas	$y_8$
Spleen-1	$x_9$	}	Spleen	$y_9$
Spleen-2	$x_{92}$			
Urinary bladder content	$x_{10}$		Urinary bladder content	$y_{10}$
Stomach wall	$x_{13}$		Stomach wall	$y_{13}$
Salivary glands	$x_{33}$		Salivary glands	$y_{33}$
Thyroid	$x_{34}$		Thyroid	$y_{34}$
			Known injected activity coefficient <sup>‡</sup>	$u_1$

Table 4.2. Symbols used in the system of differential equations for the model shown in figure 4.1. Kidneys, liver and spleen are represented by two sub-compartments, which were defined on a kinetic rather than a biological or anatomical basis. Thus the separate determination of the activity in the sub-compartments was not possible and the whole organs were measured instead. This represented by one entry in the two rightmost columns for kidney, liver and spleen.

<sup>†</sup>Activity coefficient is a measured activity given in % of injected activity.

\*Rest of body data were not measured, but calculated instead.

<sup>‡</sup>Normalized to injected activity, it is always equal to 100 %.

Exact voiding times of the volunteers were recorded. This enables a volunteer-specific modeling of the urinary excretion. The volume and the activity of the collected urine samples were also measured, however, the available data for the activities in the urine samples were not conclusive and, therefore, analogously to [44], not used in the modeling. In this work the bladder-content activities determined from the PET images were employed instead. Some published bladder models [22] account for the residual urine volume following voiding. To account for the residual urine volume in this work, an additional equation was included at every time-point of the voiding cycle:

$$x_{10}^{after} = x_{10}^{before} (1 - fr_i) \quad (4.1)$$

### 4.3. Development of personalized pharmacokinetic models

where  $x_{10}^{before}$  denotes the activity coefficient in the urinary bladder-content compartment right before the voiding and  $x_{10}^{after}$  – right after the voiding;  $fr_i$  is the voiding fraction of voiding  $i$  with  $0 \leq fr_i \leq 1$ . The values  $fr_i$  were included as additional unknown parameters into the compartmental pharmacokinetic model. Although the amount of voided activity could be determined from the total measured activities in the urine samples, these were not used in the modeling due to the above mentioned reasons.

$$\left\{ \begin{array}{l}
 \frac{dx_1}{dt} = u_1 - (k_{34,1} + k_{33,1} + k_{2,1} + k_{3,1} + k_{9,1} + k_{6,1} + k_{8,1} + k_{5,1} + k_{13,1} + k_{7,1}) x_1 \\
 \quad + k_{1,34}x_{34} + k_{1,33}x_{33} + k_{1,2}x_2 + k_{1,9}x_9 + k_{1,6}x_6 + k_{1,8}x_8 + k_{1,5}x_5 + k_{1,13}x_{13} \\
 \quad + k_{1,7}x_7 - \lambda x_1 \\
 \frac{dx_2}{dt} = k_{2,1}x_1 - k_{1,2}x_2 - \lambda x_2 \\
 \frac{dx_3}{dt} = k_{3,1}x_1 - k_{4,3}x_3 - \lambda x_3 \\
 \frac{dx_4}{dt} = k_{4,3}x_3 - k_{10,4}x_4 - \lambda x_4 \\
 \frac{dx_5}{dt} = k_{5,1}x_1 - k_{1,5}x_5 - \lambda x_5 \\
 \frac{dx_6}{dt} = k_{6,1}x_1 - k_{1,6}x_6 - k_{62,6}x_6 - \lambda x_6 \\
 \frac{dx_{62}}{dt} = k_{62,6}x_6 - \lambda x_{62} \\
 \frac{dx_7}{dt} = k_{7,1}x_1 - k_{1,7}x_7 - \lambda x_7 \\
 \frac{dx_8}{dt} = k_{8,1}x_1 - k_{1,8}x_8 - \lambda x_8 \\
 \frac{dx_9}{dt} = k_{9,1}x_1 - k_{1,9}x_9 + k_{9,92}x_{92} - k_{92,9}x_9 - \lambda x_9 \\
 \frac{dx_{92}}{dt} = k_{92,9}x_9 - k_{9,92}x_{92} - \lambda x_{92} \\
 \frac{dx_{10}}{dt} = k_{10,4}x_4 - \lambda x_{10} \\
 \frac{dx_{13}}{dt} = k_{13,1}x_1 - k_{1,13}x_{13} - \lambda x_{13} \\
 \frac{dx_{33}}{dt} = k_{33,1}x_1 - k_{1,33}x_{33} - \lambda x_{33} \\
 \frac{dx_{34}}{dt} = k_{34,1}x_1 - k_{1,34}x_{34} - \lambda x_{34}
 \end{array} \right. \tag{4.2}$$

The duration of the measurements covered 4.5 hours, and not the entire modeled time-period of 1000 minutes ( $\approx 17$  hours). To account for the urinary excretion of activity after the last recorded voiding, a scheme used by the MIRD committee [22] was considered:

3-hours voiding intervals following the last measured voiding and a 6-hours nighttime gap beginning at midnight with an extra voiding right before midnight. Due to the absence of experimental data later than 4.5 hours after the injection these later voidings were assumed to be complete, i.e. the values  $fr_i = 1$  were fixed. Since the bladder-content activities were determined from the PET images, they were available at the time-points when the PET scans were taken. If more than one voiding took place between the two sequential PET scans, it was possible to estimate only the latest voiding fraction  $fr_i$  in this time-period. The indeterminable  $fr_i$  in this time-period were fixed to one (complete voiding).

The coefficient  $\lambda$  in the system of differential equations 4.2 is the decay constant of  $^{18}\text{F}$ , as described on page 36. The system of differential equations 4.2 was numerically solved in the software SAAM II (Simulation, Analysis, and Modeling Software II) [39] described in section 3.2. The equation 4.1 describing the bladder voiding, i.e. full or partial emptying of compartment  $x_{10}$  at the voiding times, was added as a “change conditions” option of SAAM II. The fitting was done simultaneously for all transfer rates. All transfer rates were adjustable.

## 4.4. Proposed method for modeling blood contents of organs and tissues

To consider that aggregate activities obtained from the PET images comprise the activities of organ parenchyma and organ blood, each measured organ activity was associated with the respective organ compartment and a fraction of the blood compartment. For each source organ and tissue the attributed blood fraction was equal to the blood content of the respective organ or tissue given as a fraction of the total blood volume. The remaining blood activity was included into the RoB. The blood compartment was associated with the measured activity coefficients-per-ml in blood samples multiplied by the total blood volume (5300 ml and 3900 ml for reference male and female [48], respectively). Thus for each source region except blood in concept-1 (see section 3.3) the measured activity coefficients were considered as follows:

$$y_{r_{S_i}}^{\text{measured}} = y_{r_{S_i}}^{\text{parench}} + RBF_{r_{S_i}} y_1^{\text{measured,ml}} TBV \quad (4.3)$$

where  $y_{r_{S_i}}^{\text{measured}}$  is the activity coefficient (in % of IA) obtained from the PET images in the source region  $r_{S_i}$ ;  $y_{r_{S_i}}^{\text{parench}}$  is the activity coefficient in the parenchyma of  $r_{S_i}$  (in % of IA);  $RBF_{r_{S_i}}$  is the regional blood fraction in  $r_{S_i}$ , i.e. blood content of  $r_{S_i}$  given as fraction of the total blood;  $y_1^{\text{measured,ml}}$  and  $TBV$  are the measured activity coefficient in blood-per-ml (in % of IA/ml) and the total blood volume (in ml), respectively. Reference values of regional blood fractions  $RBF_{r_{S_i}}$  and total blood volumes  $TBV$  reported by ICRP [48] were used (see table 4.3), because individual data for the studied volunteers were not available. ICRP publication 89 [48] does not provide the blood contents for salivary glands. Mass fractions of blood in salivary glands were evaluated as average of the mass fractions of blood in some other tissues (namely: fat, brain, stomach/oesophagus, small intestine, large intestine, kidneys, liver, skeletal muscle, pancreas, red marrow, skin, thyroid, lymph nodes, gonads, adrenals, and urinary bladder). Blood contents for salivary glands were evaluated from the mass of salivary glands, mass fractions of blood in salivary glands and the total mass of blood.

#### 4.4. Proposed method for modeling blood contents of organs and tissues

Regions of interest for $^{18}\text{F}$ -FSPG	Adult female	Adult male
Kidneys	2.000%	2.000%
Heart*	8.950%	9.078%
Bladder content	0.000%	0.000%
Spleen	1.400%	1.400%
Pancreas	0.600%	0.600%
Liver	10.000%	10.000%
Stomach wall	1.000%	1.000%
Thyroid	0.060%	0.060%
Salivary glands <sup>‡</sup>	0.244%	0.257%
Rest of body	75.746%	75.605%
Total body	100.000%	100.000%
Blood	100.000%	100.000%

Table 4.3. Reference blood contents of considered regions of interest (in % of total blood volume  $TBV$ ) from ICRP publication 89 [48].

$TBV$  is equal to 3900 ml and 5300 ml for reference adult female and reference adult male, respectively [48].

\*Mainly heart content. Includes the inner part of the heart wall, though.

<sup>‡</sup>Is not taken from ICRP [48], but calculated as described in the text.

Using the nomenclature from table 4.2 on page 38 and the values of  $RBF_{r_{S_i}}$  from table 4.3 as an example for reference adult female, equations 4.3 for  $^{18}\text{F}$ -FSPG can be written as follows:

$$\left\{ \begin{array}{l} y_1 = \frac{x_1}{3900} \\ y_2 = x_2 + x_3 + 2.00 \cdot 10^{-2} x_1 \\ y_5 = x_5 + 8.95 \cdot 10^{-2} x_1 \\ y_6 = x_6 + x_{62} + 10.00 \cdot 10^{-2} x_1 \\ y_7 = x_7 + x_4 + 75.74 \cdot 10^{-2} x_1 \\ y_8 = x_8 + 0.60 \cdot 10^{-2} x_1 \\ y_9 = x_9 + x_{92} + 1.40 \cdot 10^{-2} x_1 \\ y_{10} = x_{10} \\ y_{13} = x_{13} + 1.00 \cdot 10^{-2} x_1 \\ y_{33} = x_{33} + 0.24 \cdot 10^{-2} x_1 \\ y_{34} = x_{34} + 0.06 \cdot 10^{-2} x_1 \end{array} \right. \quad (4.4)$$

For male volunteers the values of  $RBF_{r_{S_i}}$  for reference adult male were employed. The available sets of time-activity coefficients  $y_{r_{S_i}}$  were used as an input in the SAAM II software. In the graphical user interface of the SAAM II,  $y_{r_{S_i}}$  were associated with the corresponding compartment, with a fraction of the compartment or with several compartments (see figure 4.3). Based on this visual graphical representation, the equations 4.4 were created by the SAAM II software, analogously to the system of differential equations 4.2. Equation 4.1 (see page 38) was used as “change conditions” for bladder-content compartment  $x_{10}$ .

The resulting pharmacokinetic model fits along with the estimated model parameters and the computed internal organ doses are presented in the next chapter 5.

#### 4. Clinical investigations and pharmacokinetic model development

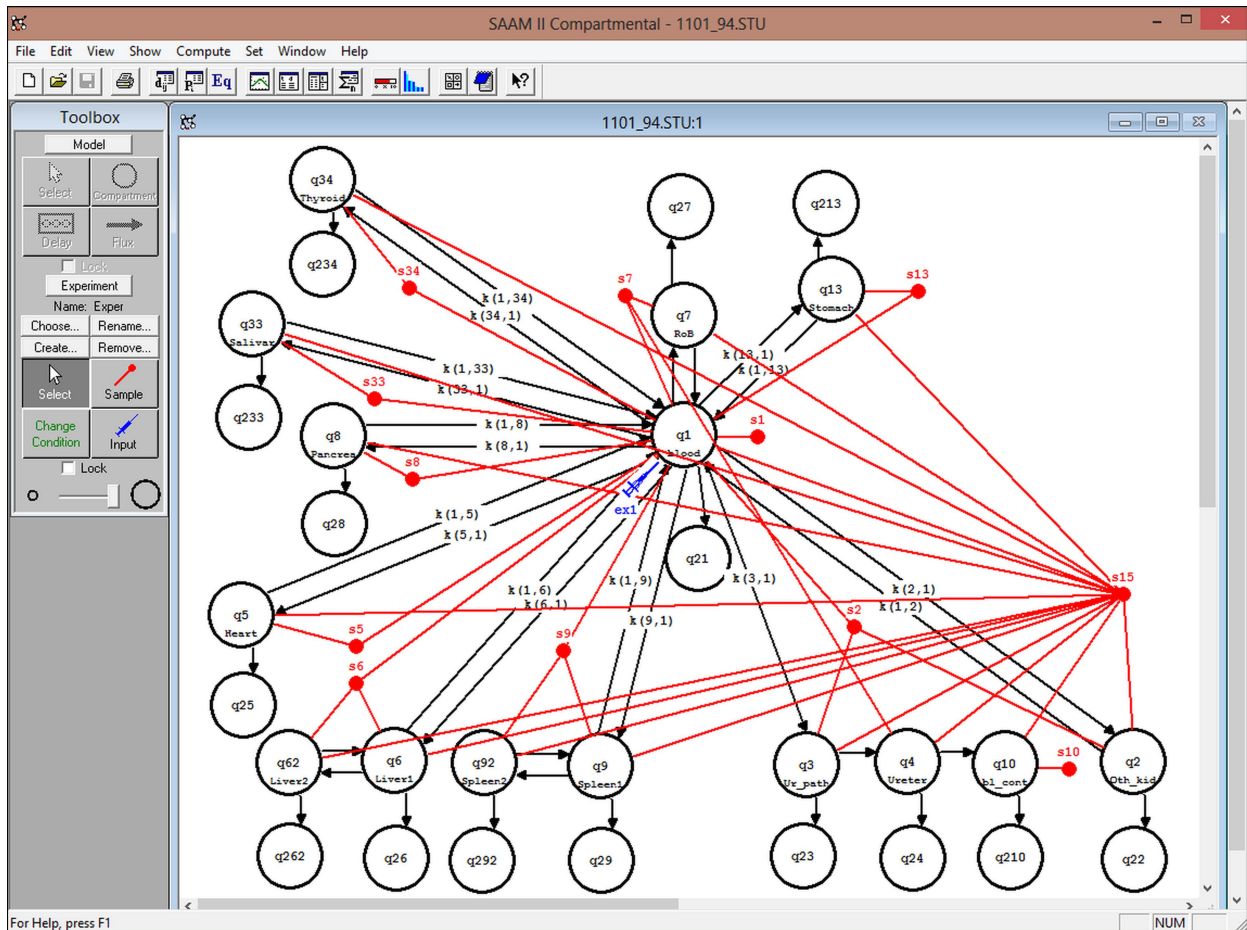


Figure 4.3. Graphical user interface of SAAM II. Black circles and arrows represent the model compartments and the considered transfer ways of  $^{18}\text{F}$ -FSPG, respectively. Red circles show how experimentally measured data were associated with the compartments in the pharmacokinetic model.

# 5. Developed pharmacokinetic models and blood effect

## 5.1. Developed individual pharmacokinetic models

The developed model structure for the considered radiopharmaceutical  $^{18}\text{F}$ -FSPG [44] was presented in figure 4.1 on page 36. With the available experimental data the model structure was globally identifiable – as tested with the software DAISY (Differential Algebra for Identifiability of SYstems) [49]. Table 5.1 shows estimated model parameters for five volunteers. Voiding fractions  $fr_i$  were also estimated with the SAAM II software [39] as explained in section 4.3. They are summarized in table 5.2.

A subset of the resulting compartmental pharmacokinetic model predictions along with the measured data is presented in figure 5.1 [35]. It was assumed that at  $t = 0$  (injection time) 100% of the injected activity was distributed in blood. A fraction of blood activity, corresponding to regional blood volumes, was attributed to the source regions (except the urinary bladder contents), resulting in non-zero activities in these regions at  $t = 0$ . Although such immediate uptake is physiologically not entirely meaningful, this does not have a notable influence on the time-integrated activity coefficients  $\tilde{a}(r_S, T_D)$  due to the fast experimentally observed uptake. Within a few minutes after the tracer administration the uptake of  $^{18}\text{F}$ -FSPG reached its maximum in all source regions except the urinary bladder contents. Hence these assumptions are considered to be appropriate and not critical for the resulting model fits.

The retention of activity in the liver of volunteer 1102/94 was considerably higher compared to the other volunteers. The uptake in pancreas for volunteers 1102/94, 1104/94 and 1105/94 was similar, while for volunteer 1103/94 the maximum uptake in pancreas was approximately only half of that value, followed by a slower decline of activity in this organ. Different accumulation and release of activity in the stomach walls of the volunteers was observed (see figure 5.1). It can be seen that the model prediction for spleen of volunteer 1105/94 does not describe the experimental data precisely. The probable reason of this is the variability in the blood fractions  $RBF_{\text{spleen}}$  in the spleen. The reference fraction of blood attributed to the spleen of volunteer 1105/94 was higher than the respective individual  $RBF_{\text{spleen}}^{1105/94}$ . Consequently, the model could not be precisely fitted to the experimental data at the earlier times, at which the amount of  $^{18}\text{F}$ -FSPG in the blood was still substantial.  $^{18}\text{F}$ -FSPG showed relatively fast release from the body via the urinary excretion pathway. After the first voiding, 30–40 % of the injected activity was excreted. However, such a renal clearance results in substantial doses from  $^{18}\text{F}$ -FSPG for kidneys and urinary bladder wall.

Besides the model predictions for the perfused organs, shown in figure 5.1, the model predictions for the organ parenchyma were also obtained. An example of the time-activity curves derived for the organ parenchyma is presented in figure 5.2.

By the integration under the modeled time-activity curves the time-integrated activity coefficients  $\tilde{a}(r_S, T_D)$  were computed for all considered source regions  $r_S$ . The activity in

## 5. Developed pharmacokinetic models and blood effect

Parameter <sup>*,†</sup>	Compartmental pharmacokinetic model parameters, [min <sup>-1</sup> ]					
	1101/94 f	1102/94 f	1103/94 m	1104/94 f	1105/94 m	Mean ± SD
$k_{1,2}$ Other kidney tissue→Blood	4.20E-02	1.70E-02	4.00E-02	5.80E-02	4.50E-02	4.0E-02 ± 1.3E-02
$k_{1,5}$ Heart <sup>†</sup> →Blood	4.30E-02	1.40E-02	3.60E-02	8.40E-02	1.30E-02	3.8E-02 ± 2.6E-02
$k_{1,6}$ Liver <sub>1</sub> →Blood	3.30E-02	5.40E-03	3.90E-02	8.50E-02	6.70E-03	3.4E-02 ± 2.9E-02
$k_{1,7}$ Rest of body→Blood	2.50E-02	0.00E+00	2.20E-02	2.10E-02	1.10E-02	1.6E-02 ± 9.1E-03
$k_{1,8}$ Pancreas→Blood	1.50E-02	1.10E-02	2.00E-02	1.70E-02	1.50E-02	1.5E-02 ± 3.1E-03
$k_{1,9}$ Spleen <sub>1</sub> →Blood	8.30E-02	2.00E-02	8.40E-02	1.70E-01	0.00E+00	7.2E-02 ± 6.1E-02
$k_{1,13}$ Stomach wall→Blood	2.00E-02	4.30E-02	5.10E-02	1.80E-01	1.20E-02	6.1E-02 ± 6.1E-02
$k_{1,33}$ Salivary glands→Blood	4.40E-02	1.50E-02	4.40E-02	3.90E-02	1.40E-02	3.1E-02 ± 1.4E-02
$k_{1,34}$ Thyroid→Blood	8.90E-02	3.10E-02	4.80E-01	1.00E-01	2.40E-01	1.9E-01 ± 1.6E-01
$k_{2,1}$ Blood→Other kidney tissue	3.70E-02	2.80E-02	3.40E-02	4.40E-02	2.50E-02	3.3E-02 ± 6.8E-03
$k_{3,1}$ Blood→Urinary path	5.30E-02	7.60E-02	5.60E-02	5.70E-02	4.60E-02	5.8E-02 ± 1.0E-02
$k_{4,3}$ Urinary path→Ureter	9.30E-01	9.40E-01	1.00E+00	1.00E+00	4.40E-01	8.7E-01 ± 2.2E-01
$k_{5,1}$ Blood→Heart <sup>†</sup>	3.70E-03	2.20E-03	4.90E-03	2.40E-03	2.50E-04	2.7E-03 ± 1.6E-03
$k_{6,1}$ Blood→Liver <sub>1</sub>	1.10E-02	8.20E-03	1.00E-02	1.60E-02	2.00E-03	9.4E-03 ± 4.6E-03
$k_{7,1}$ Blood→Rest of body	7.00E-02	6.40E-03	8.10E-02	6.50E-02	1.70E-02	4.8E-02 ± 3.0E-02
$k_{8,1}$ Blood→Pancreas	4.50E-03	4.20E-03	2.70E-03	5.60E-03	3.10E-03	4.0E-03 ± 1.0E-03
$k_{9,1}$ Blood→Spleen <sub>1</sub>	2.40E-03	1.20E-03	2.00E-03	4.00E-03	1.20E-05	1.9E-03 ± 1.3E-03
$k_{10,4}$ Ureter→Bladder content	8.80E-02	2.90E-02	6.80E-02	1.50E-01	1.20E-01	9.1E-02 ± 4.2E-02
$k_{13,1}$ Blood→Stomach wall	2.10E-03	1.90E-03	1.90E-03	1.30E-02	4.60E-04	4.0E-03 ± 4.8E-03
$k_{33,1}$ Blood→Salivary glands	5.40E-04	1.90E-04	5.30E-04	3.70E-04	1.00E-04	3.5E-04 ± 1.8E-04
$k_{34,1}$ Blood→Thyroid	8.00E-04	2.30E-04	3.50E-03	7.30E-04	7.60E-04	1.2E-03 ± 1.2E-03
$k_{62,6}$ Liver <sub>1</sub> →Liver <sub>2</sub>	2.90E-03	0.00E+00	1.80E-03	5.70E-03	9.30E-04	2.3E-03 ± 2.0E-03
$k_{92,9}$ Spleen <sub>1</sub> →Spleen <sub>2</sub>	1.40E-03	1.20E-03	0.00E+00	3.40E-03	0.00E+00	1.2E-03 ± 1.2E-03

Table 5.1. Estimated model parameters [min<sup>-1</sup>] [35].

SD is standard deviation.

\*Parameter  $k_{9,92}$  (Spleen<sub>2</sub> → Spleen<sub>1</sub>) is not shown in table 5.1 because the estimated value of it was equal to zero for all five volunteers. This can be explained by too long retention of the radiopharmaceutical <sup>18</sup>F-FSPG in the compartment Spleen<sub>2</sub> compared to the time of the measurements ( $\approx$  4 hours).

‡Blood volumes were not estimated, but fixed to the reference values, reported in ICRP Publication 89 [48] – 3900 ml and 5300 ml for reference female and male, respectively.

†The source region Heart comprised the heart content and only the inner part of the heart wall.

Serial number of voiding fraction	1101/94 f	1102/94 f	1103/94 m	1104/94 f	1105/94 m
1	1.0*	1.0*	1.0*	1.0*	1.0*
2	1.0	0.9	0.8	1.0*	1.0*
3	1.0*	1.0*	0.6	0.1	0.8
4	0.9	1.0	1.0*	1.0*	0.8
5	—	1.0*	—	0.1	—
6	—	—	—	1.0*	—

Table 5.2. Estimated<sup>‡</sup> voiding fractions [35].

‡Where it was not possible to estimate the voiding fractions, they were fixed to the value one – complete voiding. The fixed voiding fractions are marked\*.

5.1. Developed individual pharmacokinetic models

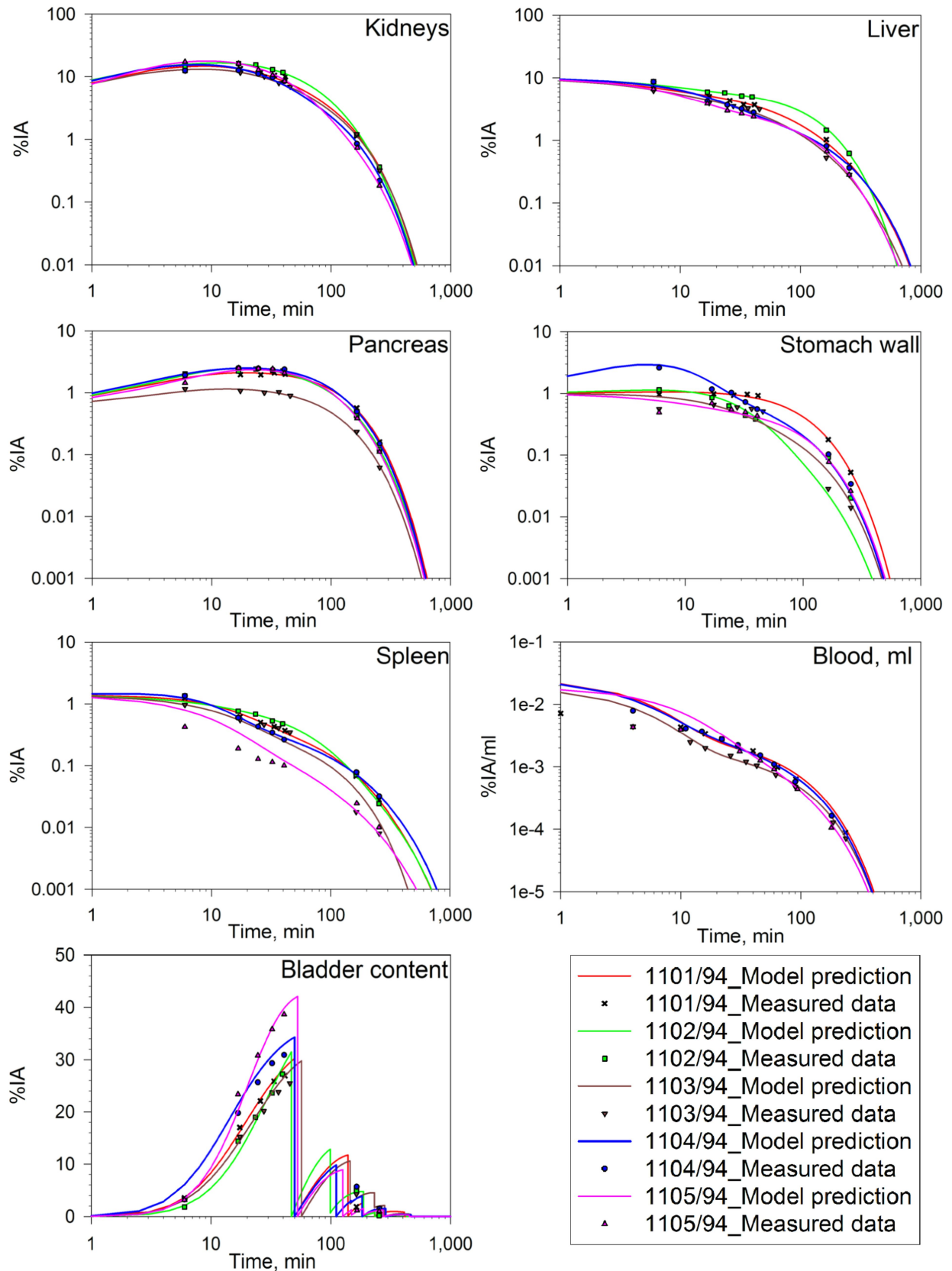


Figure 5.1. Resulting compartmental pharmacokinetic model fits for subjects 1101/94-1105/94. The lines are model predictions, discrete points are measured data. For kidneys, liver, pancreas, stomach wall and spleen measured data, obtained from PET images, represent activity coefficients of organs along with the activity coefficients of blood flowing through them [35].

## 5. Developed pharmacokinetic models and blood effect

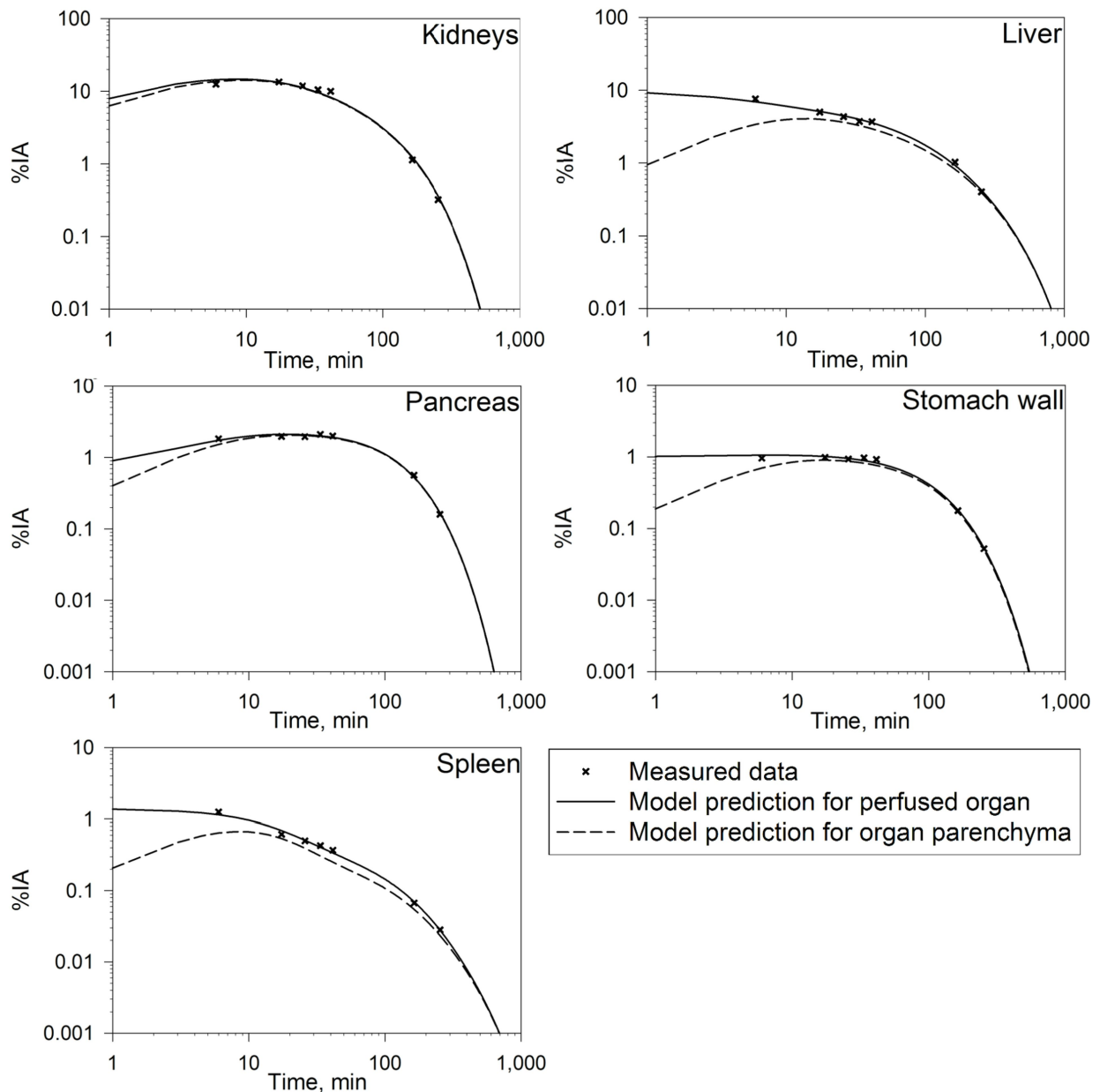


Figure 5.2. Example of resulting compartmental pharmacokinetic model fits for perfused organs and organ parenchyma of subject 1101/94. The solid lines correspond to activity coefficients of perfused organs, i.e. to activity coefficients of organs along with the activity coefficients of blood flowing through them. The dashed lines correspond to the activity coefficients of organ parenchyma.

the ureter compartment was attributed to the rest of body  $r_{RoB}$ . The ureter was hence a part of the source  $r_{RoB}$ . For each source region except urinary bladder content, blood and total body, two sets of the time-integrated activity coefficients  $\tilde{a}(r_S, T_D)$  were computed. They correspond to the organ parenchyma and to the perfused organ, i.e. including the activity of the regional blood content. Specifically, to compute the values of  $\tilde{a}(r_S, T_D)$  for perfused organs, the integration was done under the time-activity curves shown in figure 5.1. To obtain the corresponding values of  $\tilde{a}(r_S, T_D)$  for organ parenchyma, the dashed time-activity curves, e.g. for volunteer 1101/94 those from figure 5.2, were employed.

All computed  $\tilde{a}(r_S, T_D)$  are summarized in table 5.3.

The integration period  $T_D$  was set to 1000 min despite it theoretically being infinite. For the kinetics of  $^{18}\text{F}$ -FSPG considering 1000 minutes was sufficient because at the time  $t = 1000$  min after the tracer administration only 0.001 %–0.015 % of injected activity remained in the body. To test how the time-integrated activity coefficients  $\tilde{a}(r_S, T_D)$  change with increasing the modeled time-period  $T_D$ , their values were recalculated with  $T_D = 10^5$  min. The values of  $\tilde{a}(r_S, T_D)$  increased by 0.25 % at most for spleen of one of the volunteers, if employing  $T_D = 10^5$  min instead of  $T_D = 1000$  min.  $\tilde{a}(r_S, T_D)$  for most source regions remained unaffected by the increase of the integration time. Since  $\tilde{a}(r_S, T_D) = \tilde{a}(r_S, T_D = 1000)$ , the following notation will be used from now on:  $\tilde{a}(r_S)$ .

## 5.2. Effect of blood activity on dosimetric calculations

Organ doses were computed according to the formalism described in chapter 2. To evaluate the effect of blood activity on the organ doses, the calculations were done according to two concepts. The definition of the concepts is given in section 3.3 on page 33. In concept-1 activities of organ parenchyma were employed, i.e. organs without blood content, and blood was a distinct source region. According to concept-2, activities in perfused organs were used, i.e. with their blood contents, the rest of blood activity (besides the part distributed in the source organs) was attributed to the rest of body  $r_{RoB}$ . Thus the organ doses were computed with the two sets of activity data summarized in tables 5.4 and 5.5 for concept-1 and concept-2, respectively.

The source region “Heart” comprised the heart content and only the inner part of the heart wall. When considering a distinct blood source (concept-1), the heart content (being pure blood) is part of this source and should not be considered separately in addition. Therefore the heart source in concept-1 is only the heart wall, and, consequently, the specific absorbed fractions for the heart wall are to be used. When considering perfused organs (concept-2), the heart source should consist of both the heart wall source and the heart content source. This means that two different sets of the specific absorbed fractions are to be used – for the heart wall and for the heart content. The heart contents comprise 481 ml and 349 ml of blood for reference male and female, respectively. Therefore the time-integrated activity coefficient of the heart content  $\tilde{a}(\text{heart content})$  can be calculated by multiplying the known  $\tilde{a}(\text{blood-per-ml})$  by 481 ml (for male volunteers) or 349 ml (for female volunteers).  $\tilde{a}(\text{heart wall})$  is then calculated by subtracting  $\tilde{a}(\text{heart content})$  from the time-integrated activity coefficients for the entire heart.

In this section the values of specific absorbed fractions  $\Phi(r_T \leftarrow r_S, E)$  of ICRP reference voxel phantoms [52–54] were used for computation of the dose.  $\Phi$  (for convenience the argument is omitted in the following) were not adjusted to organ masses of the volunteers to keep the computations consistent, i.e. to use the reference values for both, regional blood volumes and organ volumes/masses. This is a source of uncertainty, though. The inter-individual differences in organ volumes and regional blood volumes may enhance or reduce the investigated effect of blood.

The employed values of  $\Phi$  summarized in the studies [52–54] were originally simulated for organs with blood –  $\Phi_w$ . This corresponds to concept-2. The values of  $\Phi$  corresponding to organ parenchyma –  $\Phi_{w/o}$  – are needed for concept-1. These can be deduced from  $\Phi_w$  considering the following. The probability that a particle is absorbed in any constituent of an organ is proportional to its mass and its mass-energy absorption coefficient  $\mu_{en}/\rho$  for photons

5. Developed pharmacokinetic models and blood effect

Source region	Time-integrated activity coefficients $\bar{a}(r_S)$ , [s]											
	1101/94 f		1102/94 f		1103/94 m		1104/94 f		1105/94 m			
	Value	SD	Value	SD	Value	SD	Value	SD	Value	SD		
Kidneys	5.90E+02	2.74E+01	7.33E+02	2.29E+01	5.30E+02	1.01E+01	5.13E+02	2.51E+01	5.51E+02	1.52E+01		
Kidneys with blood	6.05E+02	2.74E+01	7.45E+02	2.30E+01	5.43E+02	1.00E+01	5.27E+02	2.52E+01	5.70E+02	1.52E+01		
Heart	5.40E+01	3.07E+00	6.09E+01	6.07E+00	7.68E+01	4.01E+00	1.81E+01	4.75E+00	1.18E+01	3.95E+00		
Heart with blood	1.19E+02	1.50E+00	1.13E+02	4.83E+00	1.38E+02	3.84E+00	8.01E+01	3.55E+00	9.69E+01	4.06E+00		
Bladder content	1.17E+03	5.54E+00	9.75E+02	1.68E+01	1.35E+03	2.64E+01	1.15E+03	1.53E+01	1.24E+03	1.96E+00		
Spleen	2.36E+01	1.11E+00	2.97E+01	1.53E+00	1.45E+01	2.12E+00	2.29E+01	9.86E-01	1.71E+00	1.97E+00		
Spleen with blood	3.37E+01	1.02E+00	3.78E+01	1.42E+00	2.39E+01	2.10E+00	3.25E+01	8.29E-01	1.48E+01	4.95E+00		
Pancreas	1.51E+02	4.15E+00	1.46E+02	3.53E+00	6.88E+01	2.05E+00	1.64E+02	2.50E+00	1.42E+02	4.95E+00		
Pancreas with blood	1.56E+02	4.16E+00	1.49E+02	3.57E+00	7.29E+01	2.04E+00	1.68E+02	2.52E+00	1.47E+02	4.95E+00		
Liver	2.66E+02	1.04E+01	4.05E+02	1.14E+01	1.87E+02	1.18E+01	2.18E+02	1.21E+01	1.51E+02	2.55E+00		
Liver with blood	3.39E+02	9.93E+00	4.63E+02	1.04E+01	2.54E+02	1.18E+01	2.87E+02	1.15E+01	2.45E+02	1.91E+00		
Stomach wall	5.71E+01	1.95E+00	2.26E+01	2.11E+00	2.21E+01	4.31E+00	4.98E+01	4.90E+00	2.39E+01	3.47E+00		
Stomach wall with blood	6.44E+01	1.93E+00	2.84E+01	2.45E+00	2.88E+01	4.30E+00	5.67E+01	4.88E+00	3.33E+01	3.46E+00		
Thyroid	6.11E+00	3.91E-01	3.55E+00	4.59E-01	4.85E+00	5.37E-01	4.58E+00	2.35E-01	2.91E+00	4.22E-01		
Thyroid with blood	6.55E+00	3.90E-01	3.90E+00	4.58E-01	5.25E+00	5.36E-01	4.99E+00	2.34E-01	3.47E+00	4.22E-01		
Salivary glands	7.83E+00	2.11E-01	5.11E+00	4.15E-01	7.20E+00	3.15E-01	5.59E+00	6.21E-01	4.65E+00	5.53E-01		
Salivary glands with blood	9.61E+00	1.94E-01	6.53E+00	5.17E-01	8.93E+00	3.11E-01	7.28E+00	6.57E-01	7.06E+00	5.51E-01		
Rest of body	2.02E+03	4.38E+01	1.81E+03	4.59E+01	2.46E+03	5.86E+01	1.89E+03	5.26E+01	1.24E+03	3.75E+01		
Rest of body with blood	2.58E+03	3.61E+01	2.25E+03	2.72E+01	2.97E+03	5.67E+01	2.41E+03	5.02E+01	1.95E+03	3.39E+01		
<sup>a</sup> Blood, ml	1.86E-01	8.52E-03	1.49E-01	1.14E-02	1.27E-01	3.10E-03	1.77E-01	9.69E-03	1.77E-01	2.43E-03		
<sup>a</sup> Blood, total	7.27E+02	3.32E+01	5.79E+02	4.43E+01	6.73E+02	1.65E+01	6.92E+02	3.78E+01	9.38E+02	1.29E+01		
Total body	5.07E+03	2.18E+01	4.77E+03	1.71E+01	5.39E+03	2.98E+01	4.72E+03	3.57E+01	4.31E+03	1.82E+01		

Table 5.3. Time-integrated activity coefficients for perfused organs “with blood” and for organ parenchyma derived from compartmental pharmacokinetic models for the volunteers 1101/94–1105/94 (<sup>18</sup>F-FSPG).

SD is the standard deviation.

<sup>a</sup>Blood samples of the volunteer 1102/94 were not taken because of technical issues, however the total body activities and the activities in the considered source regions were sufficient to determine all parameters of the pharmacokinetic model, which – in turn – allowed the estimation of the blood activity for this volunteer.

The activity in the ureter compartment is not given because the ureter was not considered an explicit source region, but was a part of the source region rest of body instead.

## 5.2. Effect of blood activity on dosimetric calculations

Source region	Time-integrated activity coefficients $\tilde{a}(r_S)$ , [s]				
	1101/94 f	1102/94 f	1103/94 m	1104/94 f	1105/94 m
Kidneys	5.90E+02	7.33E+02	5.30E+02	5.13E+02	5.51E+02
*Heart wall	5.40E+01	6.09E+01	7.68E+01	1.81E+01	1.18E+01
Bladder content	1.17E+03	9.75E+02	1.35E+03	1.15E+03	1.24E+03
Spleen	2.36E+01	2.97E+01	1.45E+01	2.29E+01	1.71E+00
Pancreas	1.51E+02	1.46E+02	6.88E+01	1.64E+02	1.42E+02
Liver	2.66E+02	4.05E+02	1.87E+02	2.18E+02	1.51E+02
Stomach wall	5.71E+01	2.26E+01	2.21E+01	4.98E+01	2.39E+01
Thyroid	6.11E+00	3.55E+00	4.85E+00	4.58E+00	2.91E+00
Salivary glands	7.83E+00	5.11E+00	7.20E+00	5.59E+00	4.65E+00
Rest of body	2.02E+03	1.81E+03	2.46E+03	1.89E+03	1.24E+03
Blood, total	7.27E+02	5.79E+02	6.73E+02	6.92E+02	9.38E+02

Table 5.4. Time-integrated activity coefficients used in the dosimetry according to concept-1 for volunteers 1101/94-1105/94 ( $^{18}\text{F}$ -FSPG).

Concept-1: source organs parenchyma, blood is a separated source.

\*This source region comprised the heart content and only the inner part of the heart wall. The way it was considered in concept-1 is described in the text.

Source region	Time-integrated activity coefficients $\tilde{a}(r_S)$ , [s]				
	1101/94 f	1102/94 f	1103/94 m	1104/94 f	1105/94 m
Kidneys	6.05E+02	7.45E+02	5.43E+02	5.27E+02	5.70E+02
*Heart content	6.50E+01	5.18E+01	6.11E+01	6.19E+01	8.51E+01
*Heart wall	5.41E+01	6.09E+01	7.69E+01	1.81E+01	1.18E+01
Bladder content	1.17E+03	9.75E+02	1.35E+03	1.15E+03	1.24E+03
Spleen	3.37E+01	3.78E+01	2.39E+01	3.25E+01	1.48E+01
Pancreas	1.56E+02	1.49E+02	7.29E+01	1.68E+02	1.47E+02
Liver	3.39E+02	4.63E+02	2.54E+02	2.87E+02	2.45E+02
Stomach wall	6.44E+01	2.84E+01	2.88E+01	5.67E+01	3.33E+01
Thyroid	6.55E+00	3.90E+00	5.25E+00	4.99E+00	3.47E+00
Salivary glands	9.61E+00	6.53E+00	8.93E+00	7.28E+00	7.06E+00
Rest of body	2.58E+03	2.25E+03	2.97E+03	2.41E+03	1.95E+03

Table 5.5. Time-integrated activity coefficients used in the dosimetry according to the concept-2 for the volunteers 1101/94-1105/94 ( $^{18}\text{F}$ -FSPG).

Concept-2: perfused source organs, i.e. with their blood contents, circulating blood is included into rest of body.

\*This source region ‘‘Heart’’ comprised the heart content and only the inner part of the heart wall. The way it was considered in concept-2 is described in the text.

or continuous slowing down approximation (CSDA) ranges for electrons. This is valid for the self-absorption and the cross-fire. The self-absorption and the cross-fire are defined in the introduction (see part on page 4). The National Institute of Standards and Technology (NIST) provides  $\mu_{en}/\rho$  and CSDA ranges in various materials (<http://www.nist.gov>). According to these data,  $\mu_{en}^{Blood}/\rho \approx \mu_{en}^{Tissue,Soft}/\rho$  (equal within the precision accuracy of  $10^{-5}$ ) for the photon energy of 500 keV. The percent differences between CSDA<sup>Blood</sup> and CSDA<sup>Tissue,Soft</sup> amount to 0.75 % and 0.70 % for the electron energies of 250 and 600 keV, respectively. Thus the differences in  $\mu_{en}/\rho$  and CSDA ranges between perfused organs and organ parenchyma are negligible in the considered energy range. Note the relation between the specific absorbed fraction  $\Phi$  and the absorbed fraction  $\phi$ :  $\Phi = \phi/M_{rT}$ . Therefore

## 5. Developed pharmacokinetic models and blood effect

assuming a homogeneous mixture of blood and parenchyma in source regions, for the absorbed fraction  $\phi$  it can be written:

$$\frac{\phi_{w/o}}{\phi_w} \approx \frac{M_{r_{T_{w/o}}}}{M_{r_{T_w}}} \quad (5.1)$$

According to the definition of  $\Phi$  it follows that:

$$\Phi_{w/o} = \frac{\phi_{w/o}}{M_{r_{T_{w/o}}}} \approx \frac{\phi_w}{M_{r_{T_{w/o}}}} \cdot \frac{M_{r_{T_{w/o}}}}{M_{r_{T_w}}} = \frac{\phi_w}{M_{r_{T_w}}} = \Phi_w \quad (5.2)$$

Thus  $\Phi$  for all combinations of source and target regions, except source region rest of body, are approximately the same for both concepts, i.e. for organs with and without blood.

To calculate organ doses, an in-house software “Esoterik”, developed at the Helmholtz Zentrum München (HMGU), was used. It utilizes pre-calculated  $\Phi$  for several gamma-ray energies and for detailed beta spectra from ICRP Publication 107 [55].  $^{18}\text{F}$  is a positron-emitter with mean energy of 249.8 keV. The pre-calculated  $\Phi$  for the corresponding electron energies and a photon energy of 511 keV (annihilation photons) were used. Values defined in chapter 2 on page 25 and denoted as effective dose coefficients were also computed in this thesis. The resulting absorbed dose coefficients, effective dose coefficients and the corresponding relative differences of concept-1 compared to concept-2 are given in table 5.6.

For all source organs, except heart and spleen, no substantial differences between the two concepts were observed with maximum differences of 6.6 % and 4.6 % for liver and thyroid, respectively. The doses for heart wall and spleen slightly increased in concept-1 compared to concept-2 (18.5 % and 11.3 % at maximum, respectively). For most of the target organs, that are not sources, absorbed dose coefficients were higher in concept-1 (up to 92 % for lungs). Consequently, the effective dose coefficients in concept-1 were higher for all volunteers with a mean difference of 5.2 % (median 4.4 %, maximum 10.0 %).

The comparison of organ absorbed dose coefficients between concept-1 and concept-2 revealed notably higher doses in concept-1 for many organs. This was mostly observed for target organs with substantial blood fraction that are not sources, i.e. they are part of  $r_{RoB}$ . For these target regions, the blood activity being attributed to the organs, according to regional blood fractions  $RBF_{r_{S_i}}$  (see table 4.3 on page 41) (concept-1), leads to a higher dose than if the blood activity would be homogeneously distributed in the rest of body  $r_{RoB}$  (concept-2).

For most of the source organs no substantial differences between the two concepts were noticed. This was expected because, on the one hand,  $\tilde{a}(r_S)$ , and, therefore, the self-absorption (see page 4 for the definition), decreased in concept-1 due to the subtraction of the activities in organ blood contents. On the other hand, a blood activity corresponding to  $RBF_{r_{S_i}}$  was present in concept-1 in all source organs. Thus, the subtracted activities were effectively “placed back” to the source organs, compensating the self-absorption and leading to the same dose as for concept-2, disregarding other cross-fire (see page 4 for the definition), i.e. not considering the contribution to the absorbed dose from the radiation contained in another region. The observed differences in absorbed dose coefficients for heart wall and spleen are due to the cross-fire from the blood being inside the neighboring non-source organs, e.g. lungs (for heart wall and spleen), oesophagus (for heart wall), colon and small intestine (for spleen).

The greatest impact of considering blood as a source region in dosimetry of  $^{18}\text{F}$ -FSPG was observed for lungs, small intestine, colon, oesophagus, thymus and extrathoracic airways.

5.2. Effect of blood activity on dosimetric calculations

Target region	1101/94-female			1102/94-female			1103/94-male			1104/94-female			1105/94-male		
	C-1	C-2	%Diff	C-1	C-2	%Diff	C-1	C-2	%Diff	C-1	C-2	%Diff	C-1	C-2	%Diff
Red marrow	8.30E-03	8.26E-03	0.60	7.79E-03	7.78E-03	0.20	7.76E-03	7.78E-03	-0.30	7.73E-03	7.66E-03	1.00	6.55E-03	6.18E-03	6.00
Colon	1.19E-02	1.06E-02	12.00	1.06E-02	9.67E-03	9.90	1.03E-02	9.30E-03	10.40	1.13E-02	1.01E-02	12.40	1.01E-02	7.93E-03	27.00
Lungs	9.57E-03	6.36E-03	50.40	8.62E-03	6.18E-03	39.60	7.82E-03	5.85E-03	33.70	8.73E-03	5.63E-03	54.90	8.27E-03	4.31E-03	91.90
Stomach wall*	2.87E-02	2.87E-02	0.00	1.89E-02	1.89E-02	0.00	1.37E-02	1.38E-02	-0.30	2.58E-02	2.57E-02	0.20	1.51E-02	1.48E-02	1.90
Bladder wall	6.29E-02	6.32E-02	-0.50	5.27E-02	5.29E-02	-0.50	6.83E-02	6.87E-02	-0.60	6.17E-02	6.19E-02	-0.40	6.16E-02	6.20E-02	-0.60
Oesophagus	9.10E-03	7.21E-03	26.20	8.36E-03	6.92E-03	20.70	7.94E-03	6.74E-03	17.90	8.09E-03	6.26E-03	29.40	7.52E-03	4.93E-03	52.60
Liver*	2.13E-02	2.08E-02	2.30	2.68E-02	2.65E-02	1.30	1.38E-02	1.36E-02	1.90	1.85E-02	1.80E-02	2.80	1.39E-02	1.31E-02	6.60
Thyroid*	1.89E-02	1.87E-02	1.10	1.21E-02	1.20E-02	1.20	1.36E-02	1.36E-02	0.20	1.49E-02	1.47E-02	1.60	9.45E-03	9.03E-03	4.60
S-glands*	7.93E-03	7.98E-03	-0.60	5.78E-03	5.84E-03	-1.10	6.20E-03	6.35E-03	-2.40	6.35E-03	6.38E-03	-0.40	4.85E-03	4.80E-03	1.10
Heart wall*	1.62E-02	1.53E-02	5.80	1.69E-02	1.63E-02	4.10	1.57E-02	1.53E-02	2.90	9.28E-03	8.41E-03	10.50	7.51E-03	6.33E-03	18.50
Kidneys*	1.16E-01	1.16E-01	0.20	1.41E-01	1.41E-01	0.10	9.22E-02	9.19E-02	0.30	1.02E-01	1.01E-01	0.30	9.64E-02	9.58E-02	0.70
Adrenals	1.98E-02	1.87E-02	5.90	2.20E-02	2.12E-02	3.90	1.77E-02	1.70E-02	4.10	1.78E-02	1.67E-02	6.50	1.81E-02	1.64E-02	10.10
Pancreas*	7.29E-02	7.27E-02	0.30	7.17E-02	7.12E-02	0.70	3.27E-02	3.25E-02	0.80	7.66E-02	7.61E-02	0.70	5.88E-02	5.77E-02	1.90
Small intestine	1.57E-02	1.43E-02	10.10	1.44E-02	1.33E-02	8.20	1.17E-02	1.07E-02	9.10	1.49E-02	1.35E-02	10.40	1.15E-02	9.32E-03	23.30
Spleen*	2.10E-02	2.04E-02	3.00	2.27E-02	2.22E-02	2.00	1.39E-02	1.35E-02	3.00	1.97E-02	1.91E-02	3.20	1.11E-02	9.95E-03	11.30
Extrathoracic airways	4.54E-03	4.24E-03	7.10	3.91E-03	3.70E-03	5.40	3.88E-03	3.72E-03	4.20	4.22E-03	3.91E-03	8.00	3.09E-03	2.48E-03	24.60
Thymus	6.62E-03	5.45E-03	21.30	5.86E-03	4.99E-03	17.50	5.67E-03	5.04E-03	12.60	5.94E-03	4.80E-03	23.80	4.94E-03	3.43E-03	44.20
Endosteum	5.73E-03	6.00E-03	-4.50	5.21E-03	5.44E-03	-4.40	5.34E-03	5.60E-03	-4.60	5.37E-03	5.61E-03	-4.20	4.08E-03	4.19E-03	-2.60
Gonads	1.70E-02	1.70E-02	0.00	1.44E-02	1.44E-02	-0.20	5.31E-03	5.63E-03	-5.60	1.64E-02	1.64E-02	0.20	3.90E-03	4.10E-03	-4.80
Breast	5.12E-03	4.91E-03	4.30	4.79E-03	4.64E-03	3.00	4.40E-03	4.41E-03	-0.20	4.64E-03	4.41E-03	5.20	3.55E-03	3.26E-03	9.10
Brain	3.54E-03	3.89E-03	-9.00	3.11E-03	3.40E-03	-9.30	3.45E-03	3.76E-03	-8.30	3.31E-03	3.62E-03	-8.60	2.25E-03	2.48E-03	-9.30
Skin	3.88E-03	4.08E-03	-4.70	3.52E-03	3.69E-03	-4.60	3.53E-03	3.77E-03	-6.40	3.63E-03	3.80E-03	-4.30	2.55E-03	2.71E-03	-5.80
Gall bladder	1.84E-02	1.74E-02	5.80	2.04E-02	1.96E-02	3.80	1.15E-02	1.10E-02	4.90	1.69E-02	1.58E-02	6.40	1.28E-02	1.14E-02	12.10
Lymph nodes	1.01E-02	1.02E-02	-0.50	9.58E-03	9.63E-03	-0.60	9.55E-03	9.66E-03	-1.10	9.48E-03	9.49E-03	-0.10	8.37E-03	8.17E-03	2.40
Muscle	5.57E-03	6.00E-03	-7.10	5.11E-03	5.46E-03	-6.90	5.06E-03	5.46E-03	-7.20	5.22E-03	5.61E-03	-6.80	3.70E-03	4.06E-03	-8.80
Oral mucosa	3.96E-03	4.41E-03	-10.10	3.48E-03	3.85E-03	-10.50	3.65E-03	4.08E-03	-10.70	3.66E-03	4.06E-03	-9.90	2.29E-03	2.72E-03	-15.90
Prostate	—	—	—	—	—	—	2.82E-02	2.81E-02	0.30	—	—	—	2.52E-02	2.46E-02	2.30
Uterus	2.83E-02	2.78E-02	1.80	2.38E-02	2.34E-02	1.50	—	—	—	2.76E-02	2.71E-02	1.90	—	—	—
Effective dose coefficient	1.68E-02	1.61E-02	4.40	1.47E-02	1.42E-02	3.70	1.24E-02	1.20E-02	3.20	1.55E-02	1.48E-02	4.80	1.18E-02	1.07E-02	10.00

Table 5.6. Computed organ absorbed-dose coefficients [mGy/MBq] and effective-dose coefficients [mSv/MBq].

C-1 (concept-1): activities in source organs parenchyma, blood is a distinct source.

C-2 (concept-2): aggregate activities in perfused source organs, without blood as a source.

Differences expressed in percentages of concept-2.

\*These are the source regions for <sup>18</sup>F-FSPG.

## 5. Developed pharmacokinetic models and blood effect

These organs are considered in the computation of effective dose. The aforementioned organs were not source regions, though. They received the dose as cross-fire contribution, which for  $^{18}\text{F}$  is expected to be lower than the self-absorption because the low-energy  $e^+$  are predominantly absorbed in source regions themselves. Consequently, the difference of the two approaches on effective dose was found to be up to 10 %. Due to high mass fractions of blood in liver, kidneys and spleen, a substantial impact of blood activity in dosimetric calculations for these organs is expected in case of other radiopharmaceuticals as well, if liver, kidneys and spleen are not sources. The effect of blood on dosimetric calculations is expected to be even more pronounced for radiopharmaceuticals with slower clearance from the blood than the one of  $^{18}\text{F}$ -FSPG.

A considerable influence of the blood even for a radiopharmaceutical with a rapid clearance from the blood, such as  $^{18}\text{F}$ -FSPG, was shown (see table 5.6). This suggests that blood should be introduced as a separate compartment in most compartmental pharmacokinetic models and considered as a distinct source region in dosimetric calculations. Hence, blood samples should be included in all pharmacokinetic and dosimetric studies for radiopharmaceuticals if possible.

**Part III.**  
**Anatomical modeling**



This part describes the development of models mimicking human anatomy and needed for internal dosimetry. Specifically, the feasibility of reducing the difference in the estimated doses in nuclear medicine caused by anatomical differences between a patient and the reference person was evaluated. Three existing generations of anatomical models, their construction and application are presented in chapter 6. This is followed by the description of the proposed method of reducing the difference in internal doses between the patient and the reference phantom in chapter 7. The steps taken to obtain the new anatomical models are also described in chapter 7. Chapter 8 presents the newly developed phantoms and the results of the evaluation of the proposed approach aimed at the development of non-personalized anatomical models which facilitate overall reliable dose estimates for individual patients.



## 6. Three generations of anatomical models, their construction and applications

Models of human anatomy along with radiation transport codes are extensively used for the computation of radiation doses in medical imaging, radiotherapy, nuclide therapy and radiation protection. A detailed review of the developments in computational phantom research is given in e.g. reference [56]. There are three distinct generations of these phantoms currently in use: stylized mathematical models, voxel models and models based on boundary representation (BREP) geometries. The latest include the phantoms defined with Non-Uniform Rational B-Splines (NURBS) and polygon surfaces. The models mimicking the human anatomy are used in radiation protection for the reconstruction of radiation doses to workers or public. In medical imaging (radiology and nuclear medicine) they are used for estimation of the doses associated with these modalities and for the optimization of these procedures. Whereas in radiation therapy, especially in radionuclide therapy, anatomical models are employed for computing the dose distributions inside the patient's body. The latter is especially important, since the therapeutic procedures are associated with high doses and these doses cannot be determined by direct measurements. The dose calculation in the patient's body is essential for treatment planning. As a routine procedure in external radiotherapy, the dose distributions are computed based on the tomographic images of the patient and thus they represent an individual anatomy of the patient. This is usually not the case in nuclide therapy though. In nuclide therapy the anatomy of a patient is approximated by an employed anatomical model, which theoretically can be individual. In routine nuclide therapy and nuclear medicine applications in general the personalized anatomical models are not frequently used due to the complexity of the construction of these models. This will be discussed in more detail in the following sections.

### 6.1. General methods to construct a human computational phantom

The construction of stylized mathematical phantoms, voxel phantoms and BREP phantoms, their advantages and drawbacks are given in the following subsections 6.1.1, 6.1.2 and 6.1.3, respectively.

#### 6.1.1. Stylized mathematical phantoms

This is the first and the oldest generation of human computational phantoms. Stylized mathematical phantoms are based on the surfaces defined by quadratic equations (planar, cylindrical, conical, elliptical, toroidal, spherical surfaces). They were first developed for

internal dosimetry of workers and patients. This is a very simplified representation of human anatomy, since the used mathematical equations can capture only the most general features of organ shapes and positions. The first mathematical model of an average adult man was developed at Oak Ridge National Laboratory (ORNL) and adopted by the MIRDC committee [57]. It is shown in figure 6.1. Based on this model, Cristy and Eckerman [58] created a family of stylized mathematical models, which is included in the clinically used software for internal dosimetry - OLINDA/EXM [47]. All currently available stylized mathematical phantoms are described in the review paper by Xu [56].

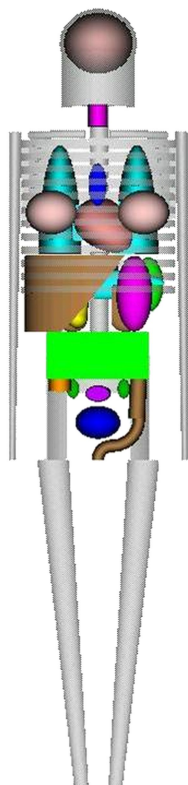


Figure 6.1. First stylized mathematical phantom MIRDC-5 [57].

The main advantage of these models is their simplicity. They facilitated the first Monte Carlo radiation transport simulations in geometry mimicking human anatomy. The lack of anatomical realism limited the use of the stylized models though, and resulted in the development of the next generation of anatomically realistic phantoms.

### 6.1.2. Voxel phantoms

Voxel phantoms are composed of three-dimensional arrays of voxels and are segmented from individual tomographic images, i.e. CT images or magnetic resonance (MR) images. Since these models are constructed based on the tomographic data of real persons, the human anatomy is mimicked very realistically. One of the first voxel phantoms was constructed at the HMGU for pediatric patients [59] and currently the HMGU model library includes various voxel models of adult males, adult females and children [60]. An example of a voxel model of seven years old female individual constructed at HMGU is given in figure 6.2.

The methods of constructing a voxel model from tomographic images are described in detail elsewhere [56, 61] and recapitulated here. Tomographic data consist of a set of slices,

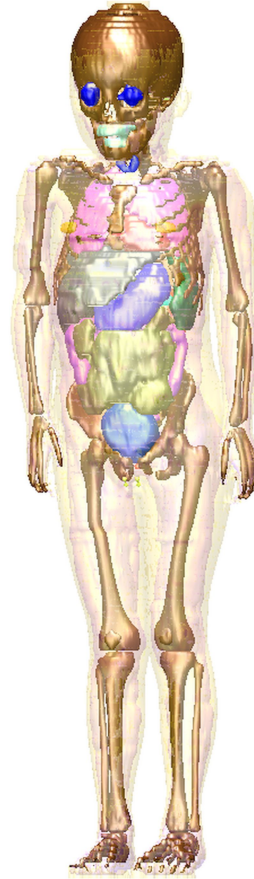


Figure 6.2. Voxel phantom of the seven years old female individual “Child” from HMGU model library (courtesy of Helmut Schlattl).

where each slice is a two-dimensional representation of the anatomy in a transverse (most commonly), coronal or sagittal “cut”. Being interpolated between two sequential slices, each pixel of the tomographic data forms a three-dimensional voxel. The user needs to identify for each voxel the anatomical structure, where it belongs to. This process is called segmentation. It is the most time-consuming step in the construction of a voxel model, because the user needs to define the anatomical boundaries between all organs and tissues of interest based on the original two-dimensional slices and with a lack of robust automatic segmentation tools this process is usually done manually. As a result of the segmentation step, binary files of the considered organs and tissues are created and each structure is assigned with a unique organ identification number (OIN). Subsequently, all binary files are combined to a complete model. Each voxel in the model is identified as belonging to a specific anatomical structure according to the value of its OIN. For Monte Carlo calculations, the density and the elemental composition are specified for each organ or tissue.

From the described procedure it can be seen that it is very time-consuming. Additionally, the construction of a voxel model for the individual patient requires individual CT or MR images of sufficiently large body coverage and adequate resolution to realistically represent even small organs and tissues.

Voxel-based computational phantoms provide a high level of anatomic realism. They are limited in their flexibility though. Such phantoms can be modified only by increasing or decreasing the dimensions of each voxel or adding or removing voxel layers comprising an

organ or e.g. adipose tissue. Selective adjustment or scaling of various body parts of a voxel phantom by different factors cannot be easily done. Thus, despite realistically mimicking human anatomy, they are limited in representing individuals and various body postures, unless segmented from individual tomographic images of the desired posture. Xu [56] summarized the majority of voxel phantoms currently developed by various institutions.

### 6.1.3. Phantoms based on boundary representation geometries

Phantoms based on boundary representation (BREP) geometries belong to the latest third generation of human computational models. They are based upon NURBS or polygon surfaces – the methods widely used in the computer graphics community for creating 3D graphical objects or for movie animation.

**NURBS** models consist of anatomical structures defined with Non-Uniform Rational B-Spline surfaces. This method offers a common mathematical representation of the shapes of different complexity. The main features and properties of NURBS curves are recapitulated in the following, partly based on the book “The *NURBS* book” by Piegl and Tiller [62]. NURBS surfaces are described by a tensor product of two NURBS curves. For the sake of simplicity the mathematical definition is explicitly given here only for NURBS curves.

A NURBS curve is defined by three main element groups: a set of weighted control points, knots and basis functions, which are defined for each control point. A NURBS curve of degree  $k$  is mathematically defined as follows:

$$C(u) = \frac{\sum_{i=0}^n N_{i,k}(u) \omega_i \mathbf{P}_i}{\sum_{i=0}^n N_{i,k}(u) \omega_i}, \quad u \in [a, b] \quad (6.1)$$

where  $\mathbf{P}_i$  ( $i = 0, 1, \dots, n$ ) are the control points,  $\omega_i$  are the weights and  $N_{i,k}(u)$  are the B-spline basis functions of degree  $k$ .

Denote a sequence of real numbers sorted from the smallest to the highest value by  $\mathbf{u}$ . The vector  $\mathbf{u}$  and its elements  $u_i$  are the knot vector and knots, respectively.  $\mathbf{u}$  is used to specify where exactly the control point  $\mathbf{P}_i$  affects the curve  $C(u)$ . It effectively splits  $C(u)$  into intervals where the respective control points have an effect on the curve. In NURBS curves these intervals are not equal in length. Moving  $\mathbf{P}_i$  or changing the weight  $\omega_i$  influences the shape of only a part of the curve  $C(u)$  on the interval  $u \in [u_i, u_{i+k+1}]$ . This property facilitates the localized deformation of the NURBS curve by changing the positions of selected control points. The basis functions determine for each control point how strongly it influences the curve. The  $i$ -th B-spline basis function  $N_{i,k}(u)$  of degree  $k$  is defined as follows [62]:

$$N_{i,k}(u) = \frac{u - u_i}{u_{i+k} - u_i} N_{i,k-1}(u) + \frac{u_{i+k+1} - u}{u_{i+k+1} - u_{i+1}} N_{i+1,k-1}(u) \quad (6.2)$$

with

$$N_{i,0}(u) = \begin{cases} 1, & \text{if } u_i \leq u < u_{i+1} \\ 0, & \text{otherwise} \end{cases} \quad (6.3)$$

### 6.1. General methods to construct a human computational phantom

Knowing  $N_{i,k}(u)$  from equations 6.2 and 6.3 and the weights  $\omega_i$ , rational basis functions  $R_{i,k}(u)$  can be calculated:

$$R_{i,k}(u) = \frac{N_{i,k}(u) \omega_i}{\sum_{j=0}^n N_{j,k}(u) \omega_j} \quad (6.4)$$

Equation 6.1 then becomes:

$$C(u) = \sum_{i=0}^n R_{i,k}(u) \mathbf{P}_i, \quad u \in [a, b] \quad (6.5)$$

NURBS surfaces are continuous in the first derivative, which provides “smooth” surfaces, in contrast to polygon meshes (see next paragraph). This fact potentially allows easier deformation of NURBS surfaces compared to polygon surfaces. NURBS surfaces can form various complex objects. This facilitates the accurate representation of organs and tissues in such phantoms and can realistically mimic human anatomy. The relatively easy deformation facilitates the modeling of various body postures or movements with NURBS surfaces. Figure 6.3 shows widely used NURBS-based 4D XCAT phantoms of adult male and adult female [63].

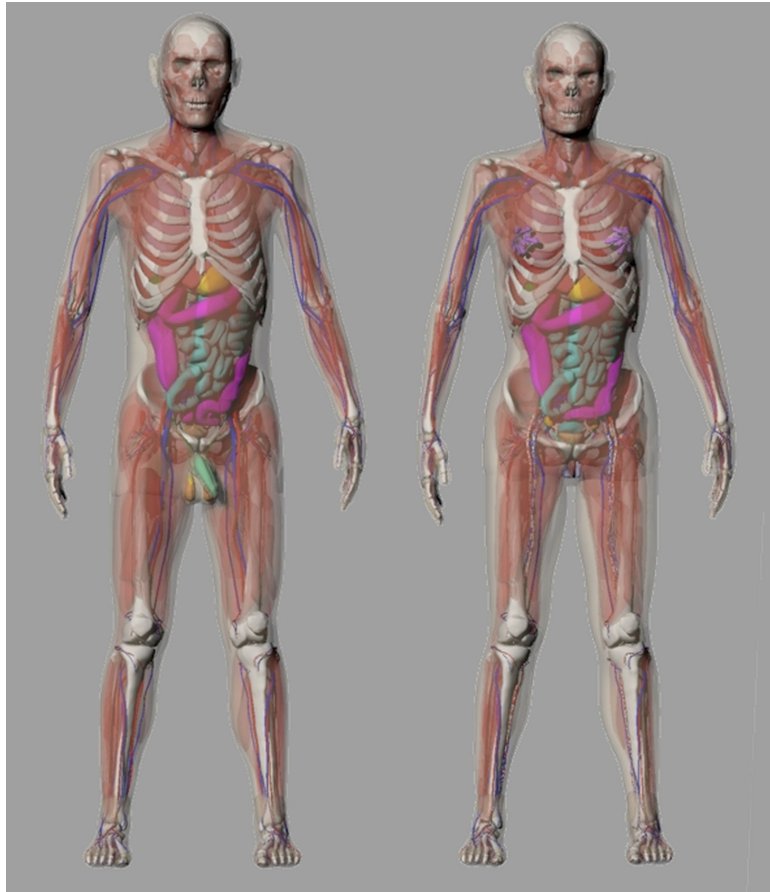


Figure 6.3. Anterior views of the male (left) and the female (right) 4D XCAT phantoms [63]. Image courtesy of Paul Segars.

**Polygon surfaces** or polygon meshes are another BREP modeling method, alternative to the NURBS surfaces described above. A polygon mesh consists of three types of fundamental entities: vertices, edges and faces. The vertices are points in space defined by their coordinates. The connections between two vertices are denoted as edges. The face is defined either as a closed set of the edges or as a connection of several vertices together (clockwise or counter-clockwise). Each face has a minimum of three vertices. Those faces with only three vertices form triangular faces, which are commonly used in the polygon-mesh modeling. Figure 6.4 shows a triangular torso mesh (with vertices) of a polygon-surface adult male phantom. Polygon meshes are very robust and can be used to represent geometries of arbitrary complexity. This makes the polygon meshes beneficial and more convenient compared to the NURBS surfaces for realistic modeling of very complex structures, e.g. human skeletal system or muscles. At the same time, analogously to the NURBS, these models keep the ability to be relatively easily deformed, scaled or adjusted.

In literature BREP models are sometimes denoted as hybrid models, since they preserve the flexibility of the simple stylized mathematical models and the anatomical realism of the voxel models. These properties make this generation of human computational phantoms the current state-of-the-art of anatomical modeling.

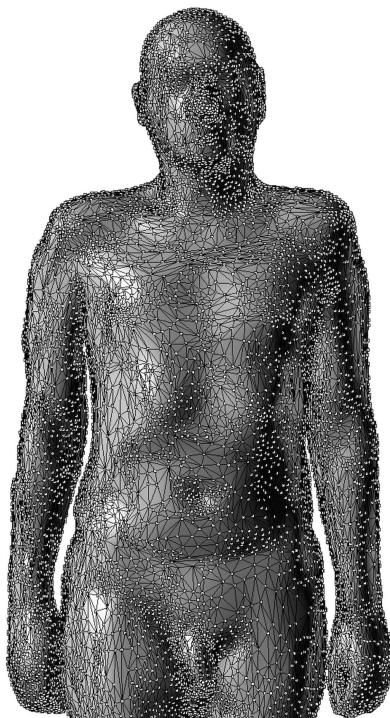


Figure 6.4. Triangular torso mesh of a polygon-surface adult male phantom. The displayed white points are the vertices of the polygon mesh.

## 6.2. Reference human computational phantoms

Reference computational phantoms of adult male and adult female [53] were adopted by the ICRP and the International Commission on Radiation Units and Measurements (ICRU) as standard benchmarked models of adults. These models are consistent with reference organ and tissue masses, body dimensions and body masses given in ICRP [48]. The reference

ICRP phantoms [53] are widely used in dosimetric calculations from different types of internal and external exposures for the purpose of radiation protection. These voxel models were developed from the computed tomographic data of real persons by M. Zankl and colleagues [53, 64] at the HMGU. One of the main motivations for the development of these phantoms was to adopt the models that realistically mimic human anatomy, compared to the employed at that time stylized mathematical phantoms. The over-simplified representation of the human anatomy in the stylized models resulted in deviations in the doses computed based on these models, as reported by various researches [65, 66]. The voxel phantoms described in the ICRP publication 110 [53] are currently the official models of reference adults. Lately the limitations of these models were recognized though [67]. The limitations are caused by relatively big voxel dimensions, which e.g. for the reference computational phantom of adult male are equal to  $2.137 \times 2.137 \times 8.000 \text{ mm}^3$ . Thus the small anatomical structures cannot be realistically represented with such voxel size. This drawback can be overcome with the latest generation of human computational phantoms – BREP-based models. Additionally, the BREP phantoms offer high flexibility and facilitate the modeling of different body postures and movements, needed in some specific situations for the reconstruction of the radiation doses. Hence, the ICRP committee decided to convert the reference voxel models of adult male and adult female to the polygon-surface format. This is an ongoing project at the Department of Nuclear Engineering of Hanyang University in Seoul. The development of various anatomical structures in the polygon-surface format is described in the publications [67–70]. The original voxel ICRP reference computational phantom of adult male and the currently available polygon-surface version of this model are described in the following subsections 6.2.1 and 6.2.2, respectively.

### 6.2.1. Reference voxel ICRP adult male phantom

Voxel ICRP adult male reference computational phantom, denoted as RCP-AM, was constructed from another whole-body voxel phantom Golem [71], which closely resembled the height and the weight of reference adult male, given by ICRP [48]. The height and the weight of Golem were equal to 176 cm and 69 kg, respectively, compared to the corresponding reference values of 176 cm and 73 kg. Various minor adjustments were applied to Golem to fit the individual organ masses and the total body mass to the reference values from ICRP publication 89 [48]. It was achieved by voxel scaling and adding or subtracting voxels from individual organs and adipose tissue. The detailed procedure is described elsewhere [53, 64]. A total number of 138 regions were segmented in RCP-AM.

### 6.2.2. Reference polygon-surface ICRP adult male phantom

Polygon-surface ICRP adult male reference computational phantom, denoted analogously to RCP-AM, as P-RCP-AM, was constructed from its voxel counterpart by Yeom and colleagues [67]. P-RCP-AM [67], used in this thesis, is not the final version, since it is currently under development [68–70]. For this reason some complex structures, e.g. muscles, are not present in P-RCP-AM. In total 111 regions were segmented in this phantom. Figure 6.5 shows the two ICRP reference models of adult male – the voxel phantom RCP-AM and the polygon-surface phantom P-RCP-AM.

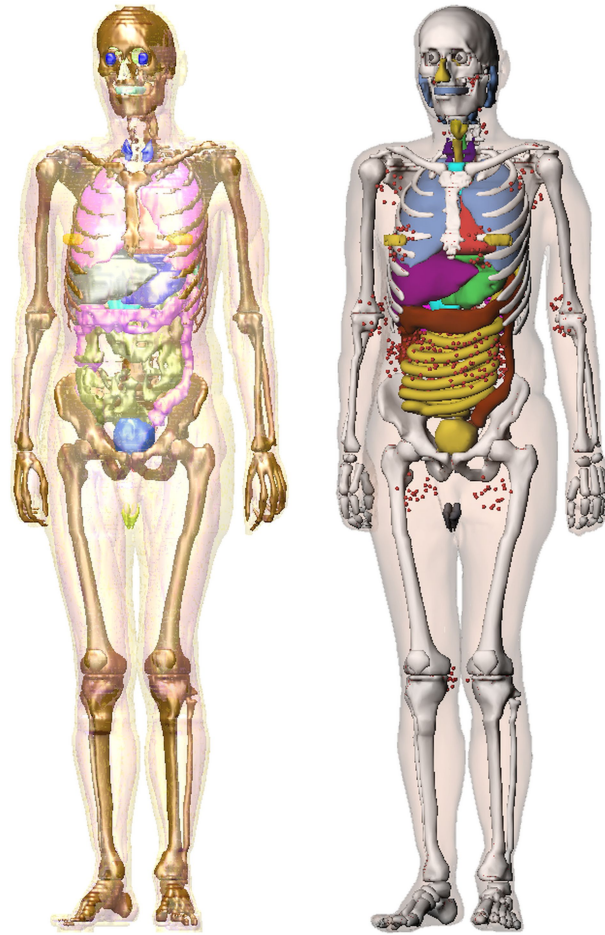


Figure 6.5. Two reference phantoms of adult male: voxel (left) and polygon-surface (right). Note that the image on the left is a surface rendered representation of RCP-AM (courtesy of Helmut Schlattl).

### 6.3. Rationale for individual anatomical models

The reference computational phantoms, described in section 6.2, were originally developed for the purpose of prospective radiation protection. Various authors, e.g. in the publications [13, 56], recognized the need for individualized dosimetry for medical dose tracking. The use of reference anatomical models is limited in medical imaging and therapy applications, because anatomical variations among individuals are disregarded if reference phantoms are employed. These anatomical variations can notably contribute to the uncertainty of the estimated organ doses [13].

To account for anatomical differences between individuals, many groups created families of human computational phantoms. They are constructed via segmentation from available individual tomographic data (voxel phantoms) or obtained via scaling the BREP phantoms in terms of body height and weight [60, 65, 72–85]. To match an individual with a library of available phantoms for the purpose of dosimetric calculations often such parameters as total body height, weight or body mass index (BMI) are used. This usually does not reflect the organ topology of the investigated individual though. Thus it could cause high differences between the real person-specific doses and the ones obtained for the available not-person-specific computational phantom. Zhang et al. [86] investigated the differences

in organ doses, effective doses, and risk indices in CT examinations for adults, caused by the employment of four types of computational phantoms for dose reconstruction. This included the extended cardiac-torso (XCAT) family [63], the reference voxel phantoms described in the ICRP Publication 110 [53] and two stylized mathematical phantoms. The study of Zhang et al. [86] revealed considerable differences in organ doses from CT even in case of closely matched weight, height and organ masses of the investigated phantoms. Other authors also quantified and showed notable differences in some individual organ dose conversion coefficients for external irradiation [60, 65] and specific absorbed fractions or organ absorbed dose coefficients for internal irradiation [14–16], caused by the variations in organ masses and locations in different computational phantoms.

The application of individualized phantoms has the potential to improve the accuracy of medical dosimetric calculations. This is especially important for medical dose estimation in therapeutic applications. Individualized anatomical models can be constructed via a direct segmentation from tomographic data. There are factors precluding this though. As described in detail in subsection 6.1.2, the accurate segmentation of an individual-specific phantom in nuclear medicine is difficult due to the very time-consuming manual work necessary. Another shortcoming of the segmentation of individual phantoms is the need of individual tomographic images of sufficient resolution and body coverage, which are usually not available in routine nuclear medicine procedures.

The objective of this part of the thesis was to study the second modeling step needed for the personalized dosimetry in nuclear medicine applications – anatomical modeling. Specifically, the aim was to investigate whether the differences between the patient-specific absorbed doses and those evaluated for non-personalized models can be efficiently reduced with less effort than would be required were the modelers to segment an individual-specific phantom.



## 7. Adjustment of reference model to individuals and Monte Carlo calculation of specific absorbed fractions

As it is discussed in chapter 6, the goal of anatomical modeling is to develop models mimicking human anatomy, which facilitate simulations of radiation transport in the geometry of human body. These simulations enable the modelers to calculate the specific absorbed fractions  $\Phi(r_T \leftarrow r_S, E)$  defined on page 23 and needed for internal dosimetry (see chapter 2). Since  $\Phi(r_T \leftarrow r_S, E)$  are phantom-specific, it follows that only individualized anatomical models facilitate personalized internal dosimetry. The accuracy of dosimetry in general and the accuracy of mimicking individual patient anatomy in particular depend on the application and on the available resources. As it was mentioned in the introduction (page 4), the accurate segmentation of a complete individual-specific phantom is difficult and most commonly not viable for each patient in the routine nuclear medicine practice. The limiting factors for this were discussed in section 6.3. In this thesis an approach, alternative to the segmentation of an individual-specific model, was proposed and applied. The approach is that an anatomical model is developed not by the segmentation from individual tomographic data, but it is derived by the adjustment of a reference phantom to some individual-specific characteristics instead. The proposed approach has a potential to overcome two main shortcomings of the segmentation of the patient-specific phantom or the direct dosimetry on the patient-specific CT. First, only the source regions are to be contoured, in contrast to the contouring all regions of interest needed for patient-specific dosimetry. With a lack of automated segmentation tools, the latter is difficult and requires an experienced radiologist to be involved. Additionally, most soft tissues are difficult to distinguish in PET/CT images. Doses for not contoured regions cannot be calculated. The second shortcoming of the patient-specific methodology is the need of individual CT or MR images of sufficiently large body coverage and adequate resolution to realistically represent even small organs and tissues. Such tomographic data are not always available. Therefore, the proposed approach can be useful in those scenarios where the segmentation of the patient-specific phantom or the direct dosimetry on the patient-specific CT is not possible. The viability and the accuracy of the proposed approach are evaluated in chapters 7–8. Since in this thesis the human computational phantoms are employed for internal dosimetry, the goodness of the adjusted phantom is evaluated depending on how accurate the computed doses are and how close they are to the real personalized doses.

In nuclear medicine investigations, patient's organs and tissues receive radiation doses due to the accumulation of an administered radiopharmaceutical in the source regions, defined on page 3. There are two components of an organ absorbed dose: the self-absorption dose (for source regions only) and the dose from the cross-fire from other source regions.

The self-absorption and the cross-fire are defined in the introduction (page 4). Organ self-absorption is dominated by organ mass, as demonstrated in the MIRDO Pamphlet 11 [87], which provides a guidance on how patient-specific scaling of  $\Phi(r_T \leftarrow r_S, E)$  is to be done. This scaling requires only the mass of the target (= source) region and is, hence, otherwise independent of the organ topology of an individual. The cross-fire (except the cross-fire from blood and total body), on the contrary, is influenced by the organ topology. To distinguish the impact of the individual organ topology on the computed absorbed dose coefficients, the self-absorption and the cross-fire components of the respective organ absorbed dose coefficients are given and compared separately in this thesis.

### 7.1. Adjustment of reference phantom to individual-specific characteristics

As it is described in subsection 6.1.2, voxel-based computational phantoms are limited in their flexibility. Thus, as a base model in this work the polygon-surface ICRP male reference phantom [67], described in subsection 6.2.2 was used. As a BREP model (see subsection 6.1.3), the polygon-surface phantom can be relatively easily modified and deformed. As mentioned in subsection 6.2.2, the polygon-surface ICRP male reference phantom (P-RCP-AM) used here is not the final version and various complex anatomical structures of this model are currently under development [68–70].

#### 7.1.1. Selected individuals

Two voxel models were selected from the HMGU model library to represent individual target patients. The biggest available model Visible Human [65] and the smallest available model Irene [65, 72, 88] were chosen to test the approach on the individuals with potentially large differences in the anatomy. These models are shown in figure 7.1.

**Overweight individual** The Visible Human model used here was segmented from the CT images obtained from the National Library of Medicine’s Visible Human Project. This phantom is a partial-body phantom covering the head to mid-thigh. It is described in detail by Zankl et al. [65]. The BMI of Visible Human is equal to 31.9 kg/m<sup>2</sup>. The Visible Human phantom has been constructed from an individual who had only one testicle. This circumstance resulted in a testes mass lower than the reference value (25.5 g compared to 35 g). However, for the radiopharmaceutical under consideration (see chapter 4) the testes are not a source region. Hence, the testes dose is only due to cross-fire irradiation. Consequently, this lower target region mass does not have an impact on the estimated doses.

**Slim individual** Irene has been constructed from the CT images of a patient, covering the whole body. The BMI of Irene is equal to 19.2 kg/m<sup>2</sup>. The detailed description of this phantom is given elsewhere [65, 72]. Despite the employed polygon-surface reference model being male, the female model Irene was chosen since no male model with similarly small BMI is available in the HMGU model library. Thus the doses for gender-specific organs could not be compared between Irene and the polygon-surface reference model adjusted

## 7.1. Adjustment of reference phantom to individual-specific characteristics

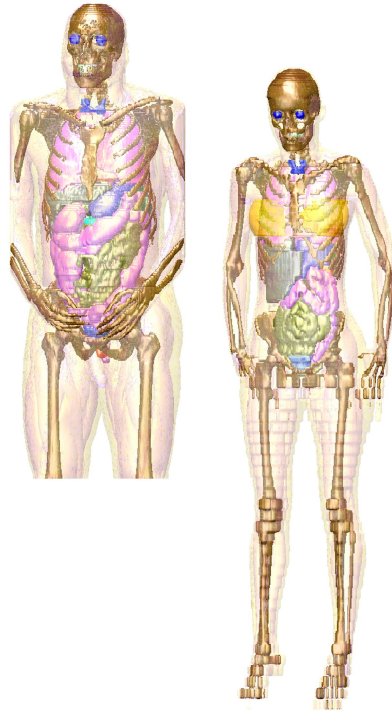


Figure 7.1. Voxel phantoms Visible Human (left) [65] and Irene (right) [65, 72, 88], denoted here as Pat1 and Pat2, respectively. Images courtesy of Helmut Schlattl.

to Irene. The comparison of the doses for other target regions appears to be appropriate though.

For the sake of simplicity and to emphasize that Visible Human and Irene represent individual patients in this thesis, they were denoted in the consecutive text as Pat1 and Pat2, respectively. The height, body weight, number of segmented regions and voxel dimensions of Pat1 and Pat2 are given in table 7.1.

Phantom	Height, [cm]	Weight, [kg]	Number of segmented regions	Voxel dimensions, [mm <sup>3</sup> ]
Pat1 (=Visible Human)	180.0 (125.0)*	103.2 (89.1)*	131	0.908×0.941×5.000
Pat2 (=Irene)	163.0	51.1	62	1.875×1.875×5.000

Table 7.1. Selected properties of employed individual phantoms Pat1 and Pat2.

\*Pat1 is a partial-body phantom. The values in parentheses correspond to the available part of the phantom, without parentheses to the actual height and weight of the individual they were based on.

For each selected individual (Pat1 and Pat2), three models approximating the individual anatomy were considered. These included the voxel (RCP-AM) and the polygon-surface (P-RCP-AM) ICRP adult male reference phantoms (see section 6.2) and the adjusted reference model P-RCP-AM.

### 7.1.2. Adjusted dimensions

The following dimensions of P-RCP-AM were adjusted to the corresponding individual characteristics of Pat1 and Pat2: distance between the iliac crest and the clavicles, total height, front-to-back distance and width of the rib cage (both on the level of the xiphoid process). These dimensions are shown in figure 7.2. The dimensions of the rib cage correspond to those of the skeleton, not the external body dimensions. It is expected that the dimensions of the skeleton correlate with the relative locations of the organs inside the rib cage better than those of the external body, especially for overweighed individuals with a thick layer of subcutaneous fat. The front-to-back distance and the width of the rib cage (skeleton) can be estimated by subtraction of the approximate thickness of the subcutaneous fat from the corresponding external body dimensions. Alternatively, the rib cage dimensions can be determined easily from a CT or MR scan which usually accompanies the actual PET diagnosis. The two new phantoms, matched to Pat1 and Pat2, are indicated as Pat1M and Pat2M, respectively. Table 7.2 summarizes all abbreviations used for naming the phantoms in this thesis.

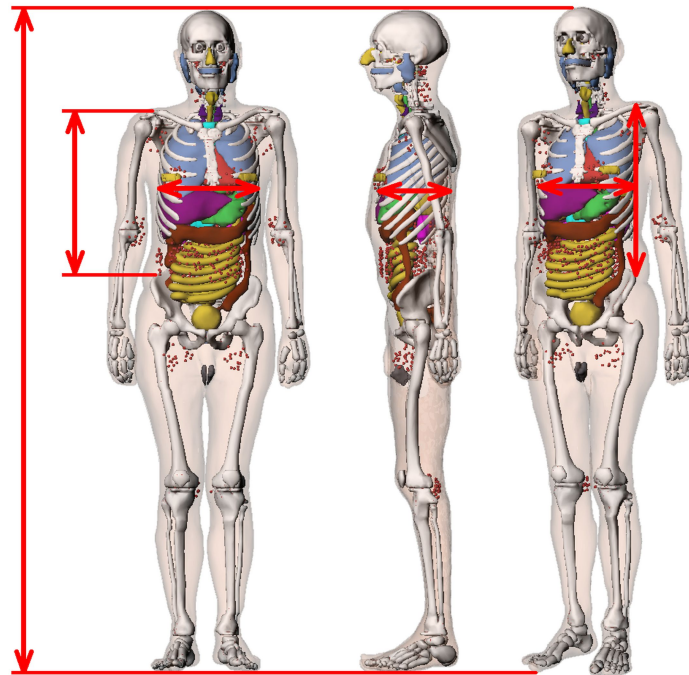


Figure 7.2. Adjusted dimensions of polygon-surface ICRP adult male reference computational phantom P-RCP-AM.

The selected set of adjustments was restricted to individual characteristics which are usually relatively easily measurable in real persons. The head of the phantoms was not scaled in any dimension. The expected variability in the size of a head is not high. In this feasibility study only the dimensions with high expected variability are considered. Since the female individual Pat2 is represented by the male model Pat2M with only limited set of adjustments made, waist to hip ratio is not matched, bone size and muscle distribution are different. Additionally, gender-specific organs as uterus, gonads or prostate are excluded from the analysis.

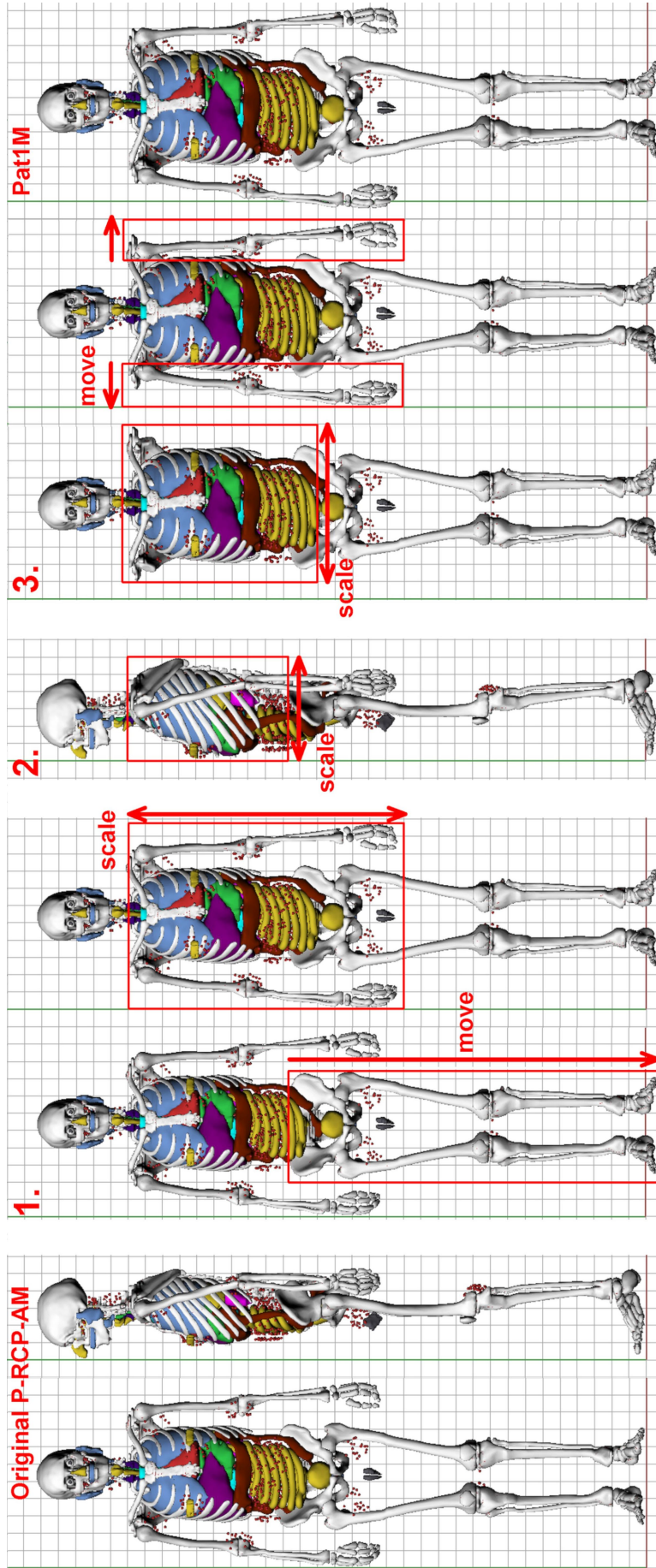


Figure 7.3. Three main steps of the adjustments of P-RCP-AM to fit selected dimensions of Pat1. After matching the distance between the iliac crest and the clavicles at the first step the phantom was re-unified. The adjustments applied to P-RCP-AM to fit Pat2 were similar to those of Pat1 and thus are not shown here.

## 7. Adjustment of reference model and Monte Carlo calculations of SAF

Description	Used abbreviations
Voxel ICRP adult male reference computational phantom [53]	RCP-AM
Polygon-surface ICRP adult male reference computational phantom [67]	P-RCP-AM
Visible Human [65]	(patient 1) Pat1
Irene [65, 72, 88]	(patient 2) Pat2
Phantom obtained via adjustments of polygon-surface ICRP adult male reference computational phantom to fit selected characteristics of Visible Human	Pat1M
Phantom obtained via adjustments of polygon-surface ICRP adult male reference computational phantom to fit selected characteristics of Irene	Pat2M

Table 7.2. Abbreviations used for indicating the computational models in this thesis.

All adjustments were made in the 3D modeling software Rhinoceros<sup>®</sup> 4.0 (McNeel North America, Seattle, WA), which provides powerful tools for, e.g., creating and editing NURBS curves, surfaces and polygon meshes. The adjustments were applied in three main steps, which are schematically shown in figure 7.3. At the first step the distance between the iliac crest and the clavicles and the total height were matched. This was achieved by scaling the rib cage, the spine, the clavicles, the sternum, the scapulae, the arms and all the organs inside the rib cage on the level of thoracic and lumbar spine, including the small intestine and the colon in superior-inferior directions by a factor needed to match the distance between the iliac crest and the clavicles. For convenience, prior to the first scaling step, the pelvis along with the legs, the bladder, the prostate, the testes and the inguinal lymphatic nodes were moved in inferior direction, as shown in figure 7.3. After matching the distance between the iliac crest and the clavicles the phantom was re-unified. If needed, the first scaling step was followed by a scaling of the legs in inferior direction to match the total height. At the second step all the aforementioned organs, except the arms, were scaled together with the rib cage in anterior-posterior direction to fit the outer front-to-back distance of the rib cages of Pat1 and Pat2. At the third step the scaling in lateral dimension was applied to match the outer width of the rib cages of the target individuals. The arms were not scaled at this step, but moved laterally to fit the scaled thorax. The scaling was done with the Scale 1D command. Organ intersections were then found with the MeshIntersect command (Rhinoceros<sup>®</sup> 4.0) and eliminated by applying some minor adjustments of the intersecting organs with the Smooth command and/or Mesh Edit and Mesh Repair Tools of Rhinoceros<sup>®</sup> 4.0. The scaling and the repair of the skin mesh required more manual manipulations, which are not shown in figure 7.3. Scale 1D command, Mesh Edit and Mesh Repair Tools along with Smooth command were employed to scale and repair the skin mesh. No further adjustments of individual organ positions and sizes of Pat1M and Pat2M to match the corresponding values of Pat1 and Pat2 were applied.

## 7.2. Monte Carlo radiation transport calculations

It is generally difficult to analytically solve the radiation transport equation (Boltzmann's transport equation) in an arbitrary medium and geometry. Consequently, stochastic Monte Carlo methods are commonly used to solve it numerically. In Monte Carlo simulations each particle ejected at a given position and with a given momentum and energy by the source is followed step-wise from one interaction to another until either the particle leaves the

considered medium or the energy of the particle becomes smaller than the user-specified minimum energy (cut-off energy) and the particle is locally absorbed. Thus in Monte Carlo simulations each particle's history is a random sequence of interactions. The probabilities of various interaction types are defined by the cross-sections of the corresponding processes. Based on these probabilities the type of interaction is randomly defined for each interaction event. As a result, the particle can lose its kinetic energy, it can be absorbed or deflected from its original direction or secondary particles can be produced. The state of the particle after the underwent interaction is described by its energy, position and direction of flight. All these variables are defined from the corresponding probability density functions. Using Monte Carlo techniques various values, e.g. the energy deposited in the medium, can be scored. Due to the random nature of this method, the results are affected by statistical uncertainties. The latter decreases with  $1/\sqrt{N_{\text{hist}}}$  with increasing number of simulated particles  $N_{\text{hist}}$ . Thus the number of followed particles is usually very high, e.g.  $N_{\text{hist}} \sim 10^7$  for photons and electrons in this thesis (see subsection 7.2.2 for more details). The value of  $N_{\text{hist}}$  is usually selected based on the acceptable statistical uncertainty, which depends on the geometry as well as type and energy of the simulated particles. With  $N_{\text{hist}} \rightarrow \infty$  the scored value converges to its true value.

### 7.2.1. EGSnrc

The Monte Carlo code EGSnrc [89] with a user code developed at the HMGU was employed in this work to calculate the specific absorbed fractions (SAFs) for homogeneous volume sources of monoenergetic photons and electrons. The radiation transport code EGSnrc [89] is an updated version of the EGS4 code, described by Nelson et al. [90]. It facilitates the Monte Carlo simulation of electron and photon transport in various materials. The detailed description of EGSnrc is given elsewhere [89]. The main elements and features are recapitulated here.

EGSnrc is written in Mortran3 [89] – a string processor that produces Fortran77 code. The dynamic range of photon energies in EGSnrc lies between 1 keV and several hundred GeV. The corresponding values for electron kinetic energies are between a few tens of keV and a few hundred GeV. An improved condensed history algorithm for simulation of electron transport was implemented in EGSnrc [91]. Several other features were provided or improved in EGSnrc compared to the original EGS4 code. These included the production and transport of fluorescence photons from K, L, M shells and Auger electrons, bound Compton scattering as well as the Compton scattering on “free” electrons [89]. The cross-sections for photoelectric effect, Rayleigh scattering and pair production used in the EGSnrc code are in accordance to the NIST/XCOM database [92] (<https://www.nist.gov/pml/xcom-photon-cross-sections-database>). Note that pair production is not a possible process for the photon energy of 511 keV (the energy of annihilation photons in PET) considered in this thesis (see subsection 7.2.2).

The user code is a program written to employ EGSnrc for the simulations of radiation transport in the specific defined geometry and for the case-specific source. The user code consists of a MAIN program and three subroutines: HOWFAR, HOWNEAR and AUSGAB. The MAIN program calls two subroutines, HATCH and SHOWER that are part of the EGSnrc code itself. The HATCH subroutine does all necessary initializations and reads the material data. The latest are created by PEGS4 code, which is a stand alone utility program used in EGSnrc. PEGS4 prepares the material dependent cross section datasets

needed for the simulations, according to the user-specified media list and the elemental compositions of the considered organs and tissues. After the call to HATCH, MAIN calls the subroutine SHOWER. One call to SHOWER generates one particle history with the specified parameters. MAIN can also include macros to control functions in EGSnrc. The subroutines HOWFAR and HOWNEAR determine the problem-specific geometry, AUSGAB is used to score and save the results. The user code along with necessary parts of EGSnrc are converted with the Mortran3 string processor to a large complete Fortran77 program. This needs to be compiled to create an executable program. The user code employed in this thesis has been previously utilized and benchmarked in various works to compute dose conversion coefficients for public, occupational and medical exposures [73,88]. The photon cut-off energy was set to 2 keV. The electron cutoff energy was equal to 20 keV, except for initial kinetic energies less than 50 keV, which were followed down to 2 keV.

### 7.2.2. Geometry, radiation types and energies

SAFs for monoenergetic photons and electrons were calculated in the geometry of the six computational phantoms from table 7.2 on page 72. A total of 18 electron energies, ranging from 10 keV to 1 MeV, and one photon energy of 511 keV were considered. The simulated energies were selected to cover the beta spectra of  $^{11}\text{C}$ - and  $^{18}\text{F}$ -labeled compounds, which are commonly used in PET, and the energy of annihilation photons. For photon internal sources and for electron internal sources in the energy range of 10 keV – 600 keV,  $4 \cdot 10^7$  histories were simulated per source region and energy. For electron energies of 800 keV and higher the number of simulated histories was reduced to  $10^7$  for the sake of computational time. The considered internal sources were homogeneously distributed in the source regions of the radiopharmaceutical employed in this thesis –  $^{18}\text{F}$ -FSPG (see chapter 4 on page 35). These included total blood, heart wall, heart contents, kidneys, liver, pancreas, salivary glands, spleen, stomach wall, total body, thyroid and urinary bladder content. Target regions included all organs and tissues segmented in the phantoms. The source region “total blood” comprised blood vessels, if present in the phantom, and blood contents of organs and tissues.

As it was shown in section 5.2 and in the paper by Zvereva et al. [35], blood is an important source region in the internal organ dose calculation. The available Mortran3 programs for the phantoms Pat1 and Pat2 were modified to include organ blood contents into the total blood. For this purpose mass fractions of blood in different organs and tissues are required. Nadler’s formula [93] was applied to calculate the total blood volumes for Pat1 and Pat2. Total blood masses were computed with the blood density from ICRU Report 46 [94] and ICRP Publication 110 [53] ( $1.06 \text{ g/cm}^3$ ). Using the resulting total blood masses, reference blood fractions in various anatomical regions from ICRP Publication 89 [48] and the organ masses of Pat1 and Pat2, mass fractions of blood were calculated for organs and tissues of the aforementioned phantoms.

Media elemental compositions and densities from ICRP Publication 110 [53] were used for organs and tissues of P-RCP-AM, Pat1M and Pat2M. Since muscles were not present in the phantom P-RCP-AM and, consequently, in Pat1M and Pat2M, subcutaneous fat and skeletal muscle were considered together as only one tissue (residual tissue) in these phantoms. The elemental composition and the density of the residual tissue were adjusted to correspond to a mixture of muscles and adipose (66 % and 34 %, respectively, for the parenchyma mass fractions).

### 7.3. Voxelization of polygon-surface models

Since the EGSnrc user code utilizes a voxel geometry, all considered polygon-surface phantoms had to be voxelized. Using the software Binvov developed by Patrick Min, all polygon-surface organs have been transferred into individual organ voxel models with  $1 \times 1 \times 1 \text{ mm}^3$  voxel size. The Binvov software is an open source program and is available at <http://www.patrickmin.com/binvox/>. It is a command-line program and utilizes the parity-count and the ray-stabbing methods developed and described by Nooruddin and Turk [95] for turning the polygonal 3D models into the voxelized format. The parity-count method facilitates the production of the true interiors of the voxel models. In the parity-count algorithm multiple parallel rays going through the polygon-surface model are produced. For instance, for a model with dimensions  $N \times N \times N$  voxels,  $N \times N$  rays, each passing through  $N$  voxel centers, are needed. The algorithm counts the number of times each ray intersects the polygons of the model. According to the number of intersections, each voxel is classified as being located inside or outside of the model. The parity-count algorithm works well for watertight manifold models. For the models with cracks or holes in the surfaces it might have limitations, though. It might lead to unexpected results and holes in the model interior, if the chosen rays do not intersect the polygons of the model, while passing through the holes or cracks in its surface. Increasing the number of projections for the employed rays can solve this issue [95]. The successful voxelization of models with several inter-penetrating subparts is difficult with parity-count method. For this reason, Nooruddin and Turk [95] proposed the ray-stabbing algorithm. Analogously to the parity-count algorithm, the orthographic projections of the polygon-surface model are used here. According to the ray-stabbing algorithm, only the first and the last intersections of the rays with the polygons of the model are kept. The voxels lying between these two extreme intersection depth are interpreted as located inside the model, and otherwise they are stored as located outside of the model. The combination of these algorithms is utilized in Binvov software.

Various formats of the input 3D models are supported by Binvov, the most common format is Wavefront OBJ. The input polygon-surface model is first normalized in the Binvov, so that it fits to a unit cube with an origin at (0.0, 0.0, 0.0) in Cartesian coordinates. The unit cube is subsequently voxelized. The voxelized output models are provided in `.binvox` file format. It has a short ASCII header, followed by the binary data. The header gives the dimensions of the voxel grid along with the scaling and translation factors needed to fit the model to a unit cube with an origin at (0.0, 0.0, 0.0). The binary data consists of pairs of *value* byte and *count* byte. The *value* byte can have values equal to 0 or 1, where the value 1 means the presence of a voxel belonging to the model, and the value 0 otherwise. The *count* byte provides the number of times the preceding *value* byte is repeated.

By executing Binvov for each considered anatomical structure, given in the polygon-surface format, the binary file with the voxelized version of the corresponding organ or tissue is produced. The resulting individual organ voxel models were subsequently combined to complete phantoms using an in-house IDL-based (IDL<sup>®</sup>, Exelis Visual Information Solutions, Inc., version 8.2.1) program. For the sake of simplicity, here and in the following the same abbreviations are used for denoting the polygon-surface models and their voxelized versions, since only the latter were employed for the Monte Carlo calculations. The voxel size of  $1 \times 1 \times 1 \text{ mm}^3$  was selected as a trade-off between the realism of the resulting voxelized anatomical structures and the memory required to store the voxel model.

## 7.4. Internal dosimetry for the developed anatomical models

Five sets of time-integrated activity coefficients  $\tilde{a}(r_S)$ , derived in part II were employed here to compute absorbed organ dose coefficients for the six computational phantoms shown in table 7.2 on page 72. The dose calculations were done according to the formalism described in chapter 2 and concept-1 defined in section 3.3, i.e. for the case of blood being a distinct source region. The used sets of activity data are given in table 5.4 on page 49.

Absorbed-dose coefficients were calculated five times (i.e. once for each set of activity data of five volunteers) for each of the models Pat1, RCP-AM, P-RCP-AM and Pat1M. The specific absorbed fractions SAFs of RCP-AM, P-RCP-AM and Pat1M were mass-scaled to correspond to the organ masses of Pat1. The mass scaling is described in details in the next subsection. For each set of activity data the dose differences between RCP-AM, P-RCP-AM and Pat1M relative to Pat1 were computed. Average, maximum and minimum values of these differences are reported. The same procedure was done for the models Pat2, RCP-AM, P-RCP-AM and Pat2M with SAF scaled to the masses of Pat2. The healthy volunteers (see table 4.1) were the source of the activity data only, i.e. their activity data served as surrogate for Pat1 and Pat2.

In the scope of this thesis a MATLAB-based (MATLAB, version 8.0.0.783 (R2012b), The MathWorks, Inc., Natick Massachusetts, 2012) program was developed to calculate organ absorbed-dose coefficients, according to the MIRD system [4] recapitulated in chapter 2. The detailed  $\beta$ -spectrum of  $^{18}\text{F}$  from ICRP Publication 107 [55] and a single photon energy at 511 keV (annihilation photons) were considered for the dosimetric calculations. The SAFs for the considered radiation types and energies were derived with the Monte Carlo calculations, as described in section 7.2.

### 7.4.1. Mass-correction of specific absorbed fractions

#### Whole-body anatomical models

The MIRD formalism [4] assumes reference mass values for the organs (source and target) and the total body. MIRD Pamphlet 11 [87] provides guidance on how patient-specific scaling of reference radionuclide  $S$  values (and eventually specific absorbed fractions SAFs) is to be done for the electron and photon component of the emission spectrum. Based on this guidance and results of extensive analysis of the mass dependences of photon [16] and electron [52] SAFs, the SAFs derived for RCP-AM, P-RCP-AM, Pat1M and Pat2M were mass-corrected. This was done to transfer the simulated values to the investigated patients (Pat1 and Pat2), who have organ masses differing from those of RCP-AM, P-RCP-AM, Pat1M and Pat2M. The mass-dependences of the SAFs for whole-body phantoms, demonstrated by Petoussi-Henss et al. [16] and Zankl et al. [52], include the self-irradiation ( $r_T = r_S$ ) for both, photons and electrons, and the case of total body  $r_{TB}$  source of electrons with the target  $r_T$  being a part of it. If  $r_T = r_S$ , the SAFs for electrons are inversely proportional to the mass of the target  $M_{r_T}$  ( $= M_{r_S}$ ) and the SAFs for photons are proportional to the  $(M_{r_T})^{-\frac{2}{3}}$  ( $= (M_{r_S})^{-\frac{2}{3}}$ ). The corresponding mass-corrections of SAFs were applied in this case to account for the differences in  $M_{r_T}$  ( $= M_{r_S}$ ) between Pat1 and Pat2 and the models approximating them. Before the SAFs for electrons were explicitly derived from particle transport calculations, an approximation given by ICRP publication 30

[96] was commonly used. According to it, the SAFs for all internal organs as targets and a total body source  $r_{TB}$  are approximately equal to the inverse of the total body mass  $M_{r_{TB}}$  [96]. The validity of this approximation has also been demonstrated by Zankl et al. [52]. The SAFs derived for a total body source of electrons and internal organs as targets were corrected in this way to account for differences in  $M_{r_{TB}}$  of RCP-AM, P-RCP-AM, Pat1M (Pat2M) relative to Pat1 (Pat2).

### Partial-body anatomical model

As mentioned in subsection 7.1.1, the Visible Human phantom (Pat1) is a partial-body phantom, from head to mid-thigh. Thus the SAFs simulated for this model had to be adjusted to correspond to a whole-body model. The above summarized corrections of the SAFs derived for partial-body phantoms are based on the analysis done by Maria Zankl (private communication). Several cases had to be considered. If  $r_S$  and  $r_T$  are both entirely inside the partial-body model, the SAFs of the whole-body model would not differ from those of the partial-body model. Hence, the same mass-correction as for the whole-body models was applied in this case. The second case is for total body  $r_{TB}$  as a source and  $r_T$  being entirely inside the partial-body model. As mentioned above, the electron SAFs in this case are approximately equal to  $1/M_{r_{TB}}$  [52, 96]. Hence, the SAFs evaluated with a phantom comprising only a part of the body are overestimated and should be corrected, so that they correspond to the inverse mass of the total body of the whole person, rather than to the mass of the phantom only. The same is applied here for photons. If the source is another extended region ( $\neq r_{TB}$ ) that is partly outside the partial-body phantom, e.g. total blood or muscles, and the target is entirely inside the phantom, the SAFs are inversely proportional to the total mass of  $r_S$ . Thus, the SAFs simulated for partial-body phantoms should be corrected in this case to account for the missing mass of the extended source region. If  $r_S$  is entirely inside the phantom and  $r_T$  is an extended region that is only partly inside the available part of the phantom, e.g. total body, skin and muscles, the reciprocity principle, introduced by Cristy and Eckerman [58] for photons and confirmed for electrons by Zankl et al. [52], suggests that the situation is the same as when  $r_T$  is entirely inside the partial-body phantom and  $r_S$  is not. Hence, the SAFs are inversely proportional to the total mass of  $r_T$ . The SAFs evaluated for partial-body phantoms should be corrected for the missing target mass. If both,  $r_S$  and  $r_T$  extend beyond the phantom, electron and photon SAFs are inversely proportional to the highest mass ( $r_S$  or  $r_T$ ). Thus, the SAFs simulated for a partial-body phantom had to be corrected for the missing mass of a heavier region ( $r_S$  or  $r_T$ ). All the aforementioned cases of mass-correction of the SAFs were implemented in the in-house MATLAB-based program developed in the scope of this thesis and applied for internal dosimetry in the following.

### 7.4.2. Considered target regions

Absorbed organ dose coefficients were computed simultaneously for all target regions segmented in the considered phantoms. In Pat1 breast was not segmented. Hence for breast in Pat1 the total breast of the RCP-AM was used. Heart wall of Pat1 and Pat2 was surrogated by heart (wall and content). Pat2 is a computational phantom representing a female individual whereas P-RCP-AM and, consequently, Pat2M represent male individuals. Thus, the doses for gonads, uterus or prostate cannot be compared. As it was mentioned in subsection 7.2.2, subcutaneous fat and skeletal muscle were considered together as one

tissue in P-RCP-AM, Pat1M and Pat2M. Thus the skeletal muscle in these models was surrogated by residual tissue in the dose computation.

### 7.4.3. Special case of urinary bladder dosimetry

The dynamic bladder model developed by Thomas et al. [22] and described in chapter 2 was used to compute the absorbed dose coefficient for bladder wall from the source region bladder content. For applying this model, SAFs for the bladder content as source and bladder wall as target are required for different bladder content volumes. However, the SAFs simulated for the computational phantoms in this work correspond to a fixed volume of the bladder contents (e.g. 39.3 and 24.3 cm<sup>3</sup> for Pat1 and Pat2, respectively). Thus they do not reflect the dependence of the absorbed dose to urinary bladder wall on the bladder-contents volume as demonstrated by Smith et al. [32]. Hence, for the urinary bladder dosimetry the SAF values obtained from the models were not used. The values calculated by Andersson et al. [33] were employed instead.

The application of the dynamic bladder model [22] requires the following parameters: biologic parameters for the bladder contents –  $\alpha_j$  and  $\lambda_j$ , which are radiopharmaceutical-specific (see chapter 2 for more details), initial bladder-content volume  $V_0$  [ml], residual bladder-content volume  $V_r$  [ml], the voiding schedule and the urine production rate  $U(t)$  [ml/min]. Since <sup>18</sup>F-FSPG, used in this thesis, is a novel radiopharmaceutical, the aforementioned biologic parameters for <sup>18</sup>F-FSPG are not available in the literature. Hence, the volunteer- and radiopharmaceutical-specific  $\alpha_j$  and  $\lambda_j$  were estimated in the scope of this work. The values of  $\alpha_j$  and  $\lambda_j$  were derived from the total body retention curves. The latter were obtained via the regression of the available activity data for <sup>18</sup>F-FSPG to a double-exponential function (see equation 2.11 on page 25) using SigmaPlot<sup>®</sup> (SigmaPlot<sup>®</sup> Version 12.3, Systat Software Inc., San Jose, CA). The estimated volunteer-specific values of  $\alpha_j$  and  $\lambda_j$  are summarized in table 7.3.

	1101/94 female	1102/94 female	1103/94 male	1104/94 female	1105/94 male
$\alpha_1$	5.86E-01	1.44E-01	7.50E-01	6.09E-01	4.18E-01
$\lambda_1$	5.50E-03	7.00E-04	6.30E-03	6.00E-03	5.90E-03
$\alpha_2$	4.17E-01	8.92E-01	2.69E-01	4.00E-01	6.31E-01
$\lambda_2$	2.06E-02	1.46E-02	2.92E-02	3.39E-02	3.16E-02

Table 7.3. Estimated volunteer-specific biologic parameters  $\alpha_j$  and  $\lambda_j$  of dynamic bladder model formulated by Thomas et al. [22], with radiopharmaceutical <sup>18</sup>F-FSPG.

Thomas et al. [22] used various initial bladder-content volumes, ranging from 10 ml to 500 ml. The initial bladder-content volumes for the volunteers, to whom <sup>18</sup>F-FSPG was administered, were not defined within the study of Smolarz et al. [44]. Thus the values  $V_0 = 10$  ml, analogously to Andersson et al. [33], and  $V_r = 10$  ml as in the study of Thomas et al. [22] were used here. Smolarz et al. [44] recorded the exact voiding times and the volumes of the voided urine at every time-point of the voiding cycle. This facilitated the estimation of  $U(t)$  and the usage of the volunteer-specific voiding schedules in the implemented dynamic bladder model. Smolarz et al. [44] followed the volunteers up to 4.5 hours after the administration of <sup>18</sup>F-FSPG, whereas in this thesis a dose integration period of  $\approx 18.0$  hours was used. In the time period 4.5-18.0 hours post administration a regular 3-hours voiding intervals were assumed with an extra voiding just

before midnight, a night-time gap between midnight and 06:00 o'clock and urine production rates, corresponding to the normal hydration state (1.0 and 0.5 ml/min during the day and the night, respectively), analogously to Thomas et al. [22]. The estimated volunteers-specific urine production rates  $U(t)$  are given in table 7.4.

Volunteer	$U_1(t)$	$U_2(t)$	$U_3(t)$	$U_4(t)$	$U_5(t)$	$U_6(t)$	$U_7(t)$	$U_8(t)$	$U_9(t)$	$U_{10}(t)$	$U_{11}(t)$
1101/94	11.7	2.2	7.3	8.8	1.0	1.0	0.5	1.0	1.0	—	—
1102/94	2.9	1.0	0.2	2.2	0.7	1.0	0.5	1.0	1.0	—	—
1103/94	6.2	3.3	3.4	6.6	1.0	1.0	0.5	1.0	1.0	—	—
1104/94	6.4	3.0	4.9	7.2	3.8	3.4	1.0	1.0	0.5	1.0	1.0
1105/94	3.2	4.2	15.6	10.1	6.8	1.0	0.5	1.0	1.0	—	—

Table 7.4. Estimated volunteer-specific urine production rates  $U_i(t)$  [ml/min], before voiding  $i$ .

A MATLAB-based program was developed in the scope of this thesis to compute the absorbed dose coefficient for urinary bladder wall. The program accounts for the dependence of SAF on the bladder content volume by employing the SAF calculated by Andersson et al. [33] for different volumes of bladder contents. It uses the activity accumulated in urinary bladder contents, according to the dynamic bladder model, as described above. This dose was summed with the bladder wall dose coefficient from other source regions to obtain the total absorbed dose coefficient for urinary bladder wall from all source regions.



# 8. Developed anatomical models and comparison of their organ doses

## 8.1. Developed anatomical models

Two phantoms were developed in this work via adjustments of polygon-surface ICRP adult male reference computational phantom P-RCP-AM [67] to fit selected dimensions of one overweight (Pat1) and one slim individual (Pat2), as described in subsection 7.1.2. The resulting phantoms, matched to Pat1 and Pat2, are denoted as Pat1M and Pat2M, respectively. Figure 8.1 shows P-RCP-AM along with Pat1M and Pat2M. It can be seen from figure 8.1 that the adjusted phantoms Pat1M and Pat2M retain their anatomic realism. The adjusted dimensions are summarized in table 8.1. Table 8.2 contains selected properties of the six employed phantoms.

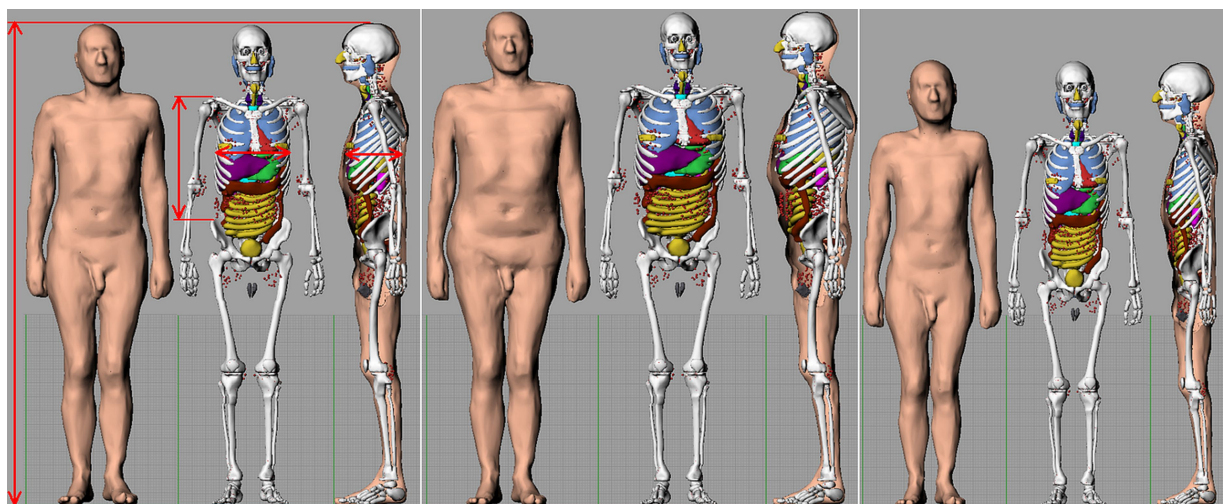


Figure 8.1. P-RCP-AM with the selected dimensions and the result of its adjustment to Pat1 and Pat2 (from left to right).

As discussed in section 7.3, P-RCP-AM, Pat1M and Pat2M were converted to voxel models with  $1 \times 1 \times 1 \text{ mm}^3$  voxel size. The voxelization of the polygon-surface models potentially introduces the limitation of the voxelized models to realistically represent very small ( $< 1 \text{ mm}$  in at least one dimension) anatomical structures. Nonetheless, the used voxel size is notably smaller than in the models segmented directly from the tomographic images (see e.g. table 8.2) and was sufficient for retaining the anatomical realism of most of the organs. This can be seen in figure 8.2, which shows a representable subset of four slices of the voxelized P-RCP-AM. The grey values in the images correspond to the organ identification numbers of the phantom P-RCP-AM. The contours of the organs of P-RCP-AM are smooth (see figure 8.2) and the voxel size of  $1 \times 1 \times 1 \text{ mm}^3$  is sufficient for realistic representations of most of the organs, i.e. those where no dimension is smaller than 1 mm. This can also

## 8. Developed anatomical models and comparison of their organ doses

Adjusted dimension	Pat1	Pat1M	Difference, %	Pat2	Pat2M	Difference, %
Distance between the iliac crest and clavicles	46.0	46.2	0.4%	40.0	39.7	-0.8%
Front-to-back distance of the rib cage	23.6	23.7	0.3%	15.0	15.1	0.5%
Width of the rib cage	32.7	32.7	0.1%	23.6	23.6	0.2%
Height	180.0	180.2	0.1%	163.0	162.4	-0.4%

Table 8.1. Selected dimensions of Pat1 and Pat2 [cm] and the corresponding matched dimensions of Pat1M and Pat2M [cm]. The differences are given in % of the original dimensions of Pat1 and Pat2.

Phantom	Height, [cm]	Weight, [kg]	Number of segmented regions	Voxel dimensions, [mm <sup>3</sup> ]
Pat1	180.0 (125.0) <sup>‡</sup>	103.2 (89.1) <sup>‡</sup>	131	0.908×0.941×5.000
Pat2	163.0	51.1	62	1.875×1.875×5.000
RCP-AM	176.0	73.0	138	2.137×2.137×8.000
P-RCP-AM	176.4	73.6	111	1.000×1.000×1.000
Pat1M	180.2	95.6	111	1.000×1.000×1.000
Pat2M	162.4	51.1	111	1.000×1.000×1.000

Table 8.2. Selected properties of all considered computational phantoms.

<sup>‡</sup>Pat1 is a partial-body phantom. The values in parentheses correspond to the available part of the phantom, without parentheses to the actual height and weight of the individual.

be seen in figure 8.3 showing the rendered voxelized P-RCP-AM, Pat1M and Pat2M. The voxelization can be theoretically done with even smaller voxel sizes. The limiting factors in this case are the available computer RAM to store the phantom and the increasing calculation time of the Monte Carlo simulations when decreasing the voxel size.

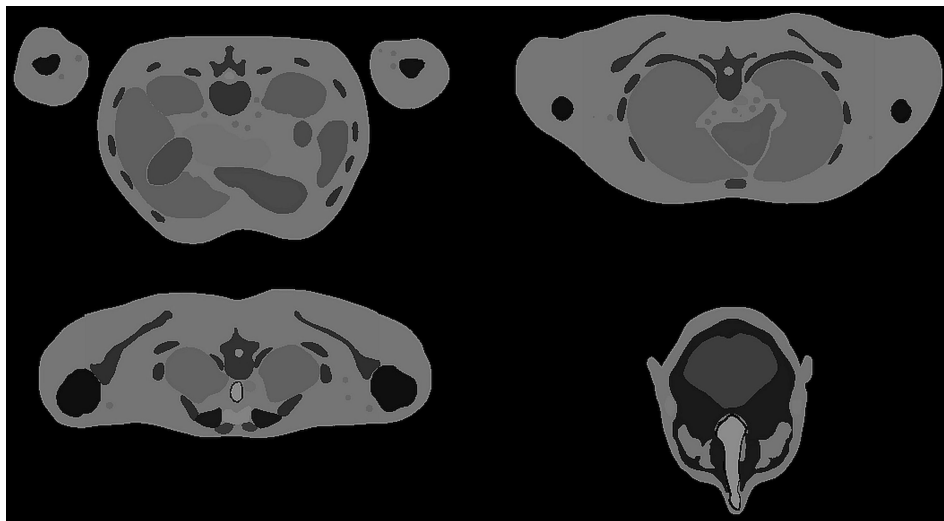


Figure 8.2. A subset of four slices of P-RCP-AM. The voxel size is  $1 \times 1 \times 1$  mm<sup>3</sup>. Grey values correspond to the organ identification numbers.

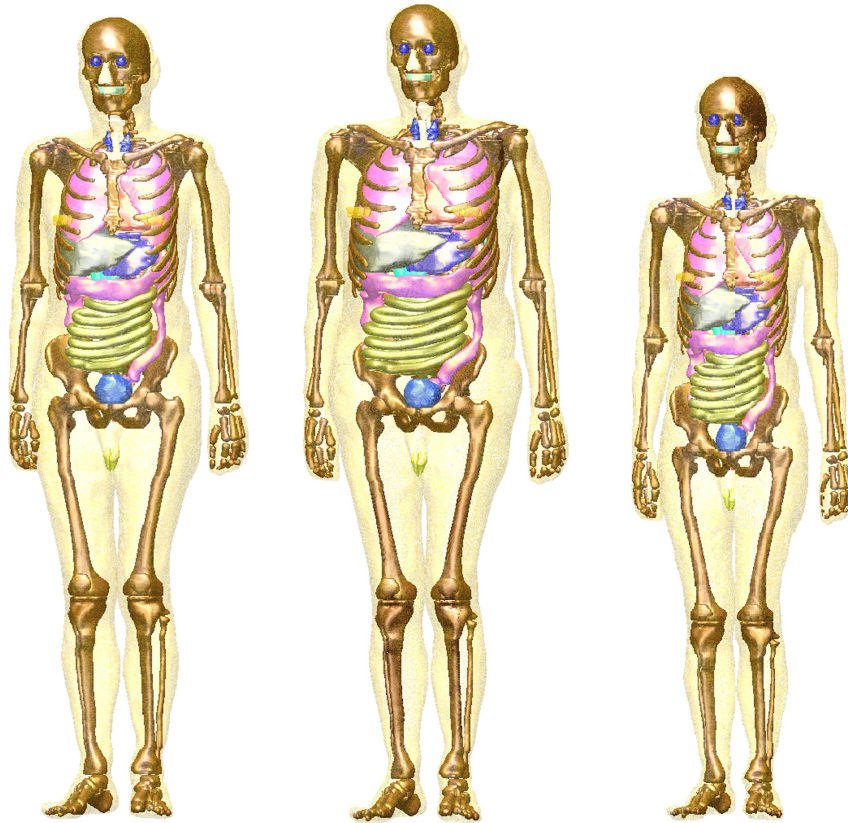


Figure 8.3. Rendered voxelized models P-RCP-AM, Pat1M and Pat2M (from left to right). The models preserved their anatomical realism after the applied voxelization.

## 8.2. Performed Monte Carlo calculations

The number of simulated particle histories for different energies and radiation type was previously given in subsection 7.2.2. Since the probability to hit a target organ is decreasing with increasing source-to-target distance and decreasing target volume, the statistical uncertainties of the performed Monte Carlo calculations notably depend on the absolute values of the absorbed fractions (AF). For the target regions located distant from the source only a small fraction of energy released from the source can reach the target. This results in low AF and higher statistical uncertainties. For the calculations done here, the coefficients of variation for  $AF \geq 10^{-3}$  were below 0.5 %, in most cases even below 0.25 %. For the values  $10^{-4} \leq AF < 10^{-3}$ , the coefficients of variation were below 1.5 %, for  $10^{-5} \leq AF < 10^{-4}$  the coefficients of variation amounted to 2.5 % at most, and for  $10^{-6} \leq AF < 10^{-5}$  they were below 10 %.

## 8.3. Comparison of computed organ doses between selected individuals and the developed matched models

To distinguish the impact of the individual organ topology on the computed organ absorbed dose coefficients, the self-absorption and the cross-fire components of the respective organ

absorbed dose coefficients are given separately in the following. For each set of activity data from the five volunteers the dose differences between RCP-AM, P-RCP-AM and Pat1M relative to Pat1 and RCP-AM, P-RCP-AM and Pat2M relative to Pat2 were computed. Average, minimum and maximum values of these relative differences for the cross-fire components of the organ dose coefficients were calculated. Note that this part of the thesis focuses on the cross-fire absorbed dose coefficients, since only they are affected by the relative positions of organs in the anatomical models.

As described in subsection 7.4.3, for the bladder wall dosimetry the initial bladder content volume was set to  $V_0 = 10$  ml. The absorbed dose coefficient for bladder wall from the cross-fire from bladder content decreases with increasing  $V_0$ . The bladder wall absorbed dose coefficients were computed in this thesis in addition with  $V_0 = 200$  ml. They decreased by 4–22 %, if employing an initial bladder content volume  $V_0 = 200$  ml instead of  $V_0 = 10$  ml. The relative differences in the bladder wall absorbed dose coefficients between the patients and the models approximating them are not substantially affected by the different initial bladder content volumes. The results summarized in the following subsections 8.3.1 and 8.3.2 refer to  $V_0 = 10$  ml, since this presents the conservative approach.

### 8.3.1. Self-absorption component of absorbed dose coefficients

The source regions for the radiopharmaceutical  $^{18}\text{F}$ -FSPG comprise stomach wall, liver, thyroid, salivary glands, heart wall, kidneys, urinary bladder-contents, pancreas, spleen and blood. Due to the accumulation of activity in these regions and relatively low energies of the emitted radiation in case of  $^{18}\text{F}$  ( $E_{\max}(\beta^+) = 633.5$  keV and  $E(\gamma) = 511$  keV), the doses received by the source regions are predominately due to the self-absorption. The calculated absorbed dose coefficients due to the self-absorption along with the deviation in % from the respective values calculated for Pat1 and Pat2 and the absolute contributions of the self-absorption to the total organ absorbed dose coefficients are presented in figure 8.4. Note that the absorbed dose coefficients from figure 8.4 are computed with one set of activity data, i.e. with that for volunteer 1101/94 (see table 5.4 on page 49). The corresponding figures obtained using the four sets of activity data for volunteers 1102/94–1105/94 are similar and hence not presented here but included in appendix A.1 instead. Except for heart wall and stomach wall, no substantial differences in the self-absorption dose coefficients are observed. The expected high contribution of self-absorption to total absorbed dose coefficients, especially for kidneys and pancreas can be seen in figure 8.4.

### 8.3.2. Cross-fire component of absorbed dose coefficients

The subset of the calculated absorbed dose coefficients from cross-fire along with the deviations in % from those calculated for Pat1 and Pat2 employing one set of activity data for volunteer 1101/94 are presented in figure 8.5 and figure 8.6, respectively. The corresponding figures for the four sets of activity data for volunteers 1102/94–1105/94 are similar to those of figure 8.5 and figure 8.6 and, therefore, are not presented here but included in appendix A.2 instead. Note that the same set of activity data is used for figure 8.4, figure 8.5 and figure 8.6. The total absorbed dose coefficients for source organs include the contribution from the self-absorption in addition to the corresponding dose coefficients shown in figures 8.5 and 8.6. The self-absorption is dominated by the organ mass and is otherwise independent of the anatomy of an individual. For the target regions that

8.3. Comparison of organ doses for developed anatomical models

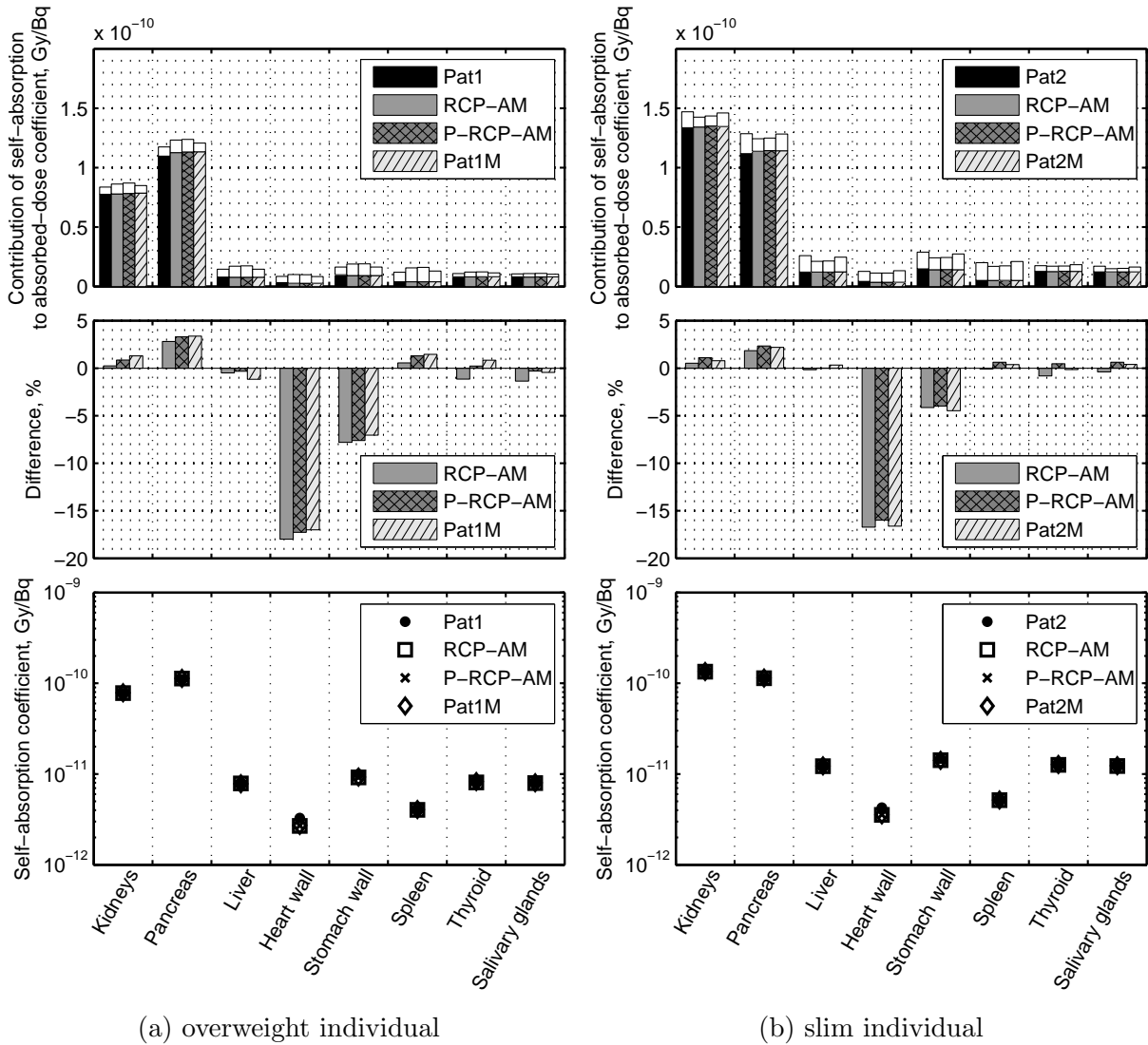


Figure 8.4. Calculated self-absorption components of absorbed dose coefficients, differences in % relative to the corresponding values for Pat1 (a) and Pat2 (b) and absolute contributions of the self-absorption to the total absorbed dose coefficients. The total height of the bars on the upper row corresponds to the total organ absorbed dose coefficients, the filled areas to the self-absorption components. The SAFs estimated with RCP-AM, P-RCP-AM and Pat1M (Pat2M) for organs where source is equal to target were adjusted according to the masses of the patient Pat1 (Pat2), as described in subsection 7.4.1.

are not sources the absorbed dose coefficients in figures 8.5 and 8.6 are the total absorbed dose coefficients for these regions.

Tables 8.3 and 8.4 show the differences in the calculated absorbed dose coefficients from cross-fire for Pat1 and Pat2, respectively, and the models approximating Pat1 and Pat2. The values given in tables 8.3 and 8.4 are computed as average, minimum and maximum within dose differences calculated for five sets of activity data. For the majority of organs of Pat1M (table 8.3) and Pat2M (table 8.4) the deviations in cross-fire absorbed dose coefficients from the ones calculated for Pat1 and Pat2 are lower than the respective dose differences between

the target phantoms Pat1 and Pat2 and the reference phantoms (RCP-AM, P-RCP-AM).

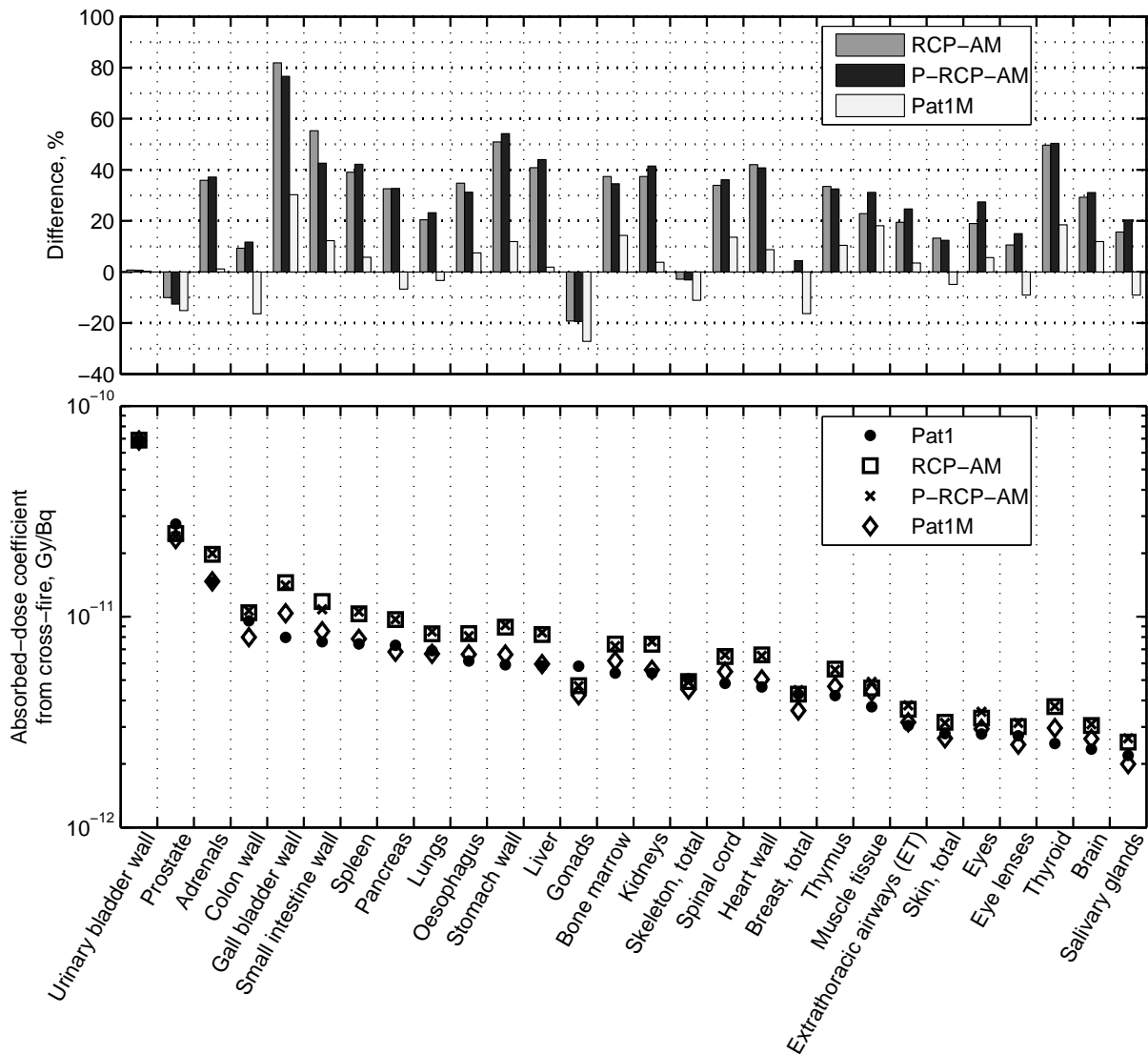


Figure 8.5. Calculated cross-fire components of the organ absorbed dose coefficients for Pat1 and different models approximating it. The dose differences in the upper panel are given relative to Pat1.

The computed differences are similar for all activity datasets of the volunteers. No substantial differences in absorbed dose coefficients for urinary bladder wall were observed. The breast of RCP-AM was used as a surrogate for the breast of Pat1. Hence, no differences between Pat1 and RCP-AM befall in this case, while the differences between Pat1 and Pat1M are below 18.1 %. For Pat1 the relative differences in cross-fire absorbed dose coefficients of liver, extrathoracic airways, kidneys, pancreas and eyes decreased from about 30.0–40.0 % for the reference phantoms RCP-AM and P-RCP-AM to less than 10.0 % for the matched phantom Pat1M. For oesophagus, brain, adrenals, heart wall, spleen, thymus and spinal cord the cross-fire dose differences between Pat1 and the reference phantoms amount to approximately 40.0 %, while the corresponding differences between Pat1 and Pat1M are below 15.0 %. For Pat1 the relative differences in absorbed dose coefficients of gall bladder wall amount to 80.6 % and 75.5 % on average with respect to RCP-AM

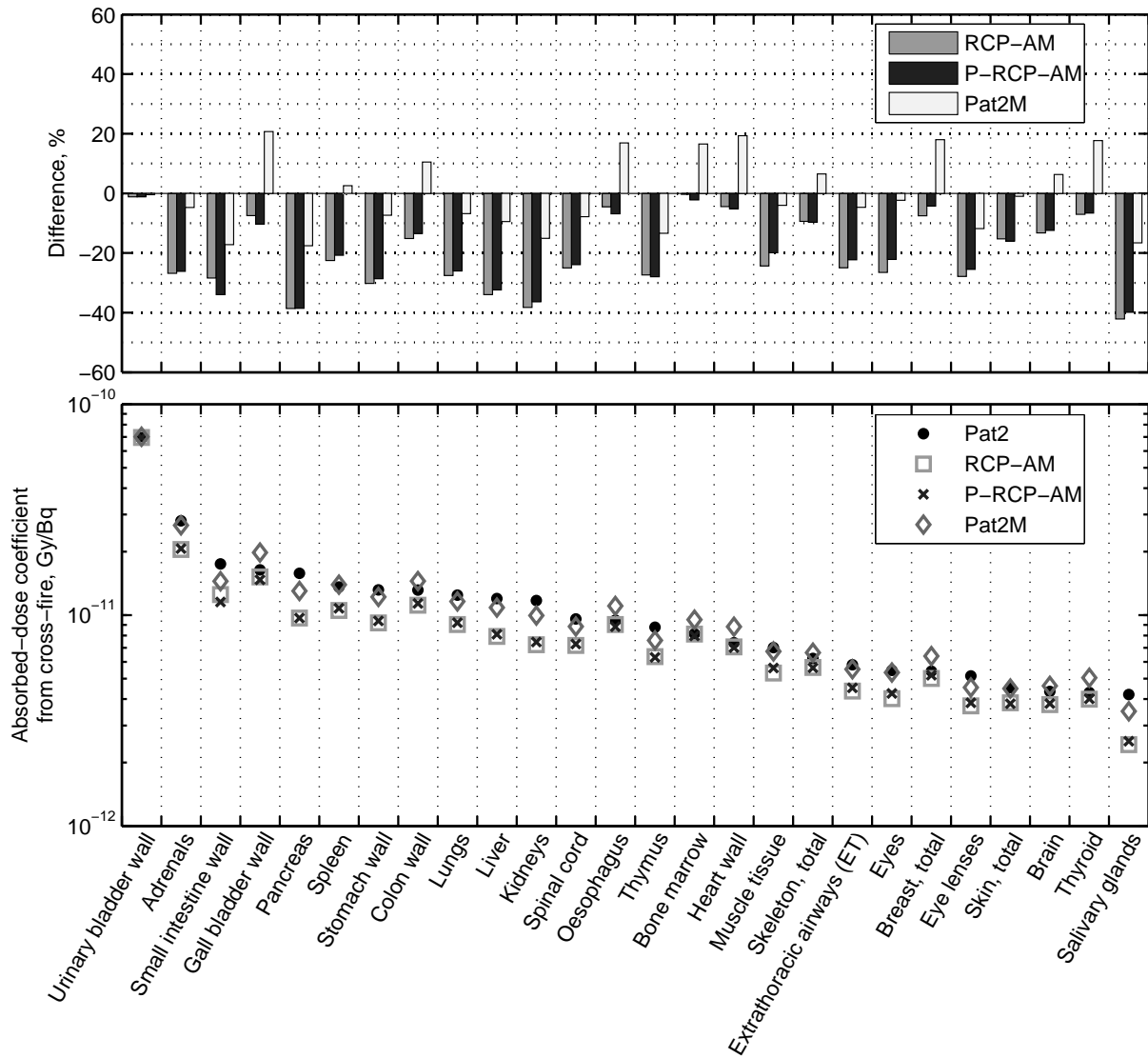


Figure 8.6. Calculated cross-fire components of the organ absorbed dose coefficients for Pat2 and different models approximating it. The dose differences in the upper panel are given relative to Pat2.

and P-RCP-AM, respectively. The corresponding differences relative to Pat1M are below 30.0 % on average. For active bone marrow, thyroid and salivary glands the calculated relative dose differences between Pat1M and Pat1 are only half of those between reference phantoms and Pat1. For lungs the computed dose differences decreased on average from 21–24 % between Pat1 and reference phantoms to -3 % between Pat1 and Pat1M. The relative differences in the calculated cross-fire absorbed dose coefficients for stomach wall and small intestine wall amount, respectively, to 12.4 % and 14.0 % on average between Pat1 and Pat1M. The corresponding differences between Pat1 and both reference phantoms are within 54.7 % and 57.9 % on average. Better agreement was observed between Pat1 and the reference phantoms (RCP-AM and P-RCP-AM) in the absorbed dose coefficients for gonads, prostate, skeleton and colon wall. Absorbed dose coefficients for all organs, except gonads and gall bladder wall agree between Pat1 and Pat1M within 25.0 % (table 8.3).

For Pat2 the differences in the cross-fire absorbed dose coefficients for kidneys, pancreas,

## 8. Developed anatomical models and comparison of their organ doses

	RCP-AM			P-RCP-AM			Pat1M		
	Mean	Min	Max	Mean	Min	Max	Mean	Min	Max
Bladder wall	0.6%	0.3%	0.7%	0.5%	0.3%	0.7%	0.2%	0.1%	0.3%
Prostate	-10.2%	-11.1%	-9.8%	-12.8%	-13.6%	-12.4%	-15.3%	-16.2%	-14.9%
Adrenals	38.7%	31.5%	46.9%	40.1%	32.7%	48.4%	3.3%	-1.9%	11.4%
Gall bladder wall	80.6%	67.8%	88.7%	75.5%	64.4%	83.7%	29.4%	23.2%	35.6%
Colon wall	8.6%	5.8%	10.3%	11.0%	7.2%	13.1%	-17.2%	-18.4%	-16.4%
Pancreas*	32.8%	29.7%	37.2%	32.8%	30.4%	36.8%	-6.5%	-8.7%	-2.9%
Spleen*	39.9%	30.9%	47.3%	43.2%	33.0%	51.7%	6.6%	-0.6%	12.2%
Small intestine wall	57.9%	47.7%	65.8%	45.3%	34.4%	54.2%	14.0%	5.5%	22.9%
Lungs	20.8%	20.1%	21.6%	23.7%	22.2%	25.3%	-3.1%	-4.6%	-1.0%
Stomach wall*	51.4%	49.6%	54.3%	54.7%	52.3%	58.2%	12.4%	9.4%	14.5%
Oesophagus	36.0%	30.1%	44.0%	32.7%	26.4%	40.4%	8.5%	3.8%	12.2%
Liver*	40.9%	39.8%	41.8%	44.3%	43.0%	45.7%	2.2%	0.8%	4.6%
Bone marrow	38.1%	32.7%	46.3%	35.2%	30.2%	43.3%	14.5%	11.4%	19.2%
Kidneys*	37.7%	36.4%	40.0%	41.9%	39.8%	45.0%	4.2%	2.3%	5.9%
Gonads	-20.6%	-26.5%	-18.3%	-20.8%	-26.3%	-18.5%	-28.4%	-34.1%	-26.2%
Skeleton, total	-3.3%	-4.4%	-2.6%	-3.6%	-4.5%	-3.0%	-11.7%	-13.3%	-10.9%
Spinal cord	34.5%	33.4%	36.6%	36.8%	35.3%	39.7%	14.0%	13.5%	15.0%
Heart wall*	42.3%	38.2%	49.7%	41.1%	37.1%	49.2%	8.9%	5.2%	15.0%
Breast, total	0.0%	0.0%	0.0%	4.5%	4.0%	5.5%	-16.4%	-18.1%	-14.1%
Thymus	34.6%	32.5%	38.2%	33.4%	31.2%	35.6%	10.9%	9.6%	12.4%
Muscle tissue	23.1%	22.4%	24.8%	31.7%	29.0%	35.4%	18.5%	16.8%	20.6%
Extrathoracic airways (ET)	19.7%	19.2%	20.7%	25.1%	24.0%	27.9%	3.2%	0.9%	4.5%
Skin, total	12.7%	9.5%	14.6%	11.9%	9.1%	13.3%	-5.7%	-10.9%	-2.8%
Eyes	18.7%	15.9%	20.1%	27.2%	25.0%	28.5%	4.9%	-1.9%	8.4%
Eye lenses	10.3%	7.8%	11.7%	14.4%	8.4%	17.6%	-9.9%	-17.6%	-5.9%
Thyroid*	50.7%	46.8%	57.1%	51.5%	47.3%	58.5%	18.9%	16.8%	21.4%
Brain	29.4%	29.1%	30.3%	31.5%	30.4%	34.2%	11.7%	10.3%	12.4%
Salivary glands*	15.7%	15.5%	16.1%	20.7%	19.8%	22.5%	-9.2%	-10.6%	-8.2%

Table 8.3. Relative differences in the organ absorbed dose coefficients from cross-fire, calculated for three models approximating Pat1, compared to the corresponding doses of Pat1 (five sets of activity data were used).

\*These are the source organs for  $^{18}\text{F}$ -FSPG.

For  $\text{AF} \geq 10^{-4}$  the coefficients of variation were 1.5 % at most, for  $10^{-5} \leq \text{AF} < 10^{-4}$  the coefficients of variation were below 2.5 %. For more information on statistical uncertainties of performed Monte Carlo calculations see section 8.2.

brain, small intestine wall, thymus, and eye lenses relative to the corresponding dose coefficients for Pat2M are approximately lower by a factor of two compared to the differences in the respective dose coefficients between Pat2 and the reference phantoms. As a general finding for all sets of activity data, the relative differences in the absorbed dose coefficients for lungs, stomach wall (cross-fire), adrenals, extrathoracic airways and spinal cord decreased from approximately 30.0 % between RCP-AM, P-RCP-AM and Pat2 to less than 10.0 % between Pat2M and Pat2. The absorbed dose coefficient for eyes and muscles in Pat2M agrees with the corresponding value in Pat2 within 5.6 %. For liver and salivary glands the calculated relative cross-fire dose differences between Pat2M and Pat2 are only one third of those between reference phantoms and Pat2, for skin and eyes only one tenth.

### 8.3. Comparison of organ doses for developed anatomical models

	RCP-AM			P-RCP-AM			Pat2M		
	Mean	Min	Max	Mean	Min	Max	Mean	Min	Max
Bladder wall	-0.9%	-1.1%	-0.5%	-1.0%	-1.2%	-0.5%	-0.4%	-0.5%	-0.2%
Adrenals	-25.4%	-29.4%	-19.8%	-24.7%	-28.7%	-19.0%	-2.8%	-8.0%	3.6%
Gall bladder wall	-8.2%	-13.1%	-3.6%	-11.0%	-15.2%	-7.5%	19.4%	9.9%	23.8%
Pancreas*	-38.1%	-38.7%	-37.1%	-38.1%	-38.9%	-37.3%	-16.9%	-18.2%	-15.8%
Small intestine wall	-29.4%	-33.8%	-24.5%	-34.8%	-38.2%	-30.9%	-18.1%	-22.9%	-13.6%
Spleen*	-21.9%	-26.3%	-18.0%	-20.1%	-25.1%	-16.0%	3.3%	-4.0%	7.8%
Stomach wall*	-29.8%	-31.6%	-24.7%	-28.1%	-29.9%	-22.9%	-6.7%	-8.9%	-0.8%
Colon wall	-15.5%	-17.4%	-13.8%	-13.9%	-16.4%	-12.0%	10.2%	5.9%	12.4%
Liver*	-34.4%	-35.2%	-34.0%	-32.8%	-33.4%	-32.4%	-10.0%	-10.8%	-9.4%
Lungs	-28.0%	-33.5%	-25.1%	-26.5%	-31.5%	-23.9%	-7.2%	-11.0%	-4.7%
Kidneys*	-38.0%	-38.9%	-35.8%	-36.0%	-36.8%	-33.7%	-14.6%	-16.0%	-11.3%
Spinal cord	-25.3%	-28.4%	-22.2%	-24.1%	-26.9%	-21.3%	-7.9%	-9.4%	-5.4%
Oesophagus	-4.7%	-6.5%	-2.8%	-6.9%	-8.3%	-5.4%	17.1%	14.0%	19.0%
Thymus	-26.9%	-29.5%	-23.1%	-27.5%	-29.9%	-23.8%	-12.7%	-16.3%	-8.3%
Bone marrow	0.7%	-2.1%	6.4%	-1.3%	-4.3%	4.3%	17.9%	14.1%	26.3%
Heart wall*	-5.1%	-13.5%	-0.3%	-5.8%	-14.7%	-0.5%	18.5%	8.3%	24.5%
Muscle tissue	-24.7%	-27.7%	-22.2%	-20.2%	-22.3%	-18.8%	-4.2%	-5.0%	-3.5%
Skeleton, total	-8.9%	-10.9%	-6.5%	-9.2%	-11.2%	-6.7%	7.3%	4.6%	12.0%
Breast, total	-7.0%	-9.7%	-3.2%	-3.5%	-6.7%	1.4%	19.2%	13.2%	28.0%
Extrathoracic airways (ET)	-25.5%	-29.9%	-23.3%	-22.7%	-26.3%	-21.0%	-4.8%	-6.2%	-4.1%
Eyes	-27.1%	-32.2%	-24.4%	-22.7%	-27.6%	-20.2%	-2.6%	-5.6%	-1.0%
Eye lenses	-28.4%	-33.7%	-25.6%	-26.2%	-33.3%	-22.4%	-12.4%	-17.6%	-9.5%
Skin, total	-15.5%	-16.9%	-14.5%	-16.3%	-17.4%	-15.6%	-0.9%	-1.6%	0.3%
Brain	-13.4%	-14.4%	-13.0%	-12.4%	-12.4%	-12.3%	6.7%	5.7%	9.2%
Thyroid*	-7.5%	-11.9%	-5.4%	-7.0%	-11.1%	-5.1%	17.5%	14.5%	18.9%
Salivary glands*	-42.1%	-42.6%	-41.6%	-39.7%	-40.9%	-38.1%	-16.3%	-17.9%	-13.9%

Table 8.4. Analogue to table 8.3 the relative differences in the organ absorbed dose coefficients from cross-fire, calculated for three models approximating Pat2, compared to the corresponding doses of Pat2 (five sets of activity data were used).

\*These are the source organs for  $^{18}\text{F}$ -FSPG.

For  $\text{AF} \geq 10^{-4}$  the coefficients of variation were 1.5 % at most,

for  $10^{-5} \leq \text{AF} < 10^{-4}$  the coefficients of variation were below 2.5 %. For more information on statistical uncertainties of performed Monte Carlo calculations see section 8.2.

For the cross-fire absorbed dose coefficients for active bone marrow, breast, oesophagus, thyroid, gall bladder wall and heart wall better agreement was observed between Pat2 and reference phantoms, though. Absorbed-dose coefficients from cross-fire for all considered organs and tissues of Pat2M, except the active bone marrow and breast agree with the ones of Pat2 within 25.0 % (table 8.4). As mentioned in subsection 7.1.2 on page 70, the female individual Pat2 was represented by male anatomy of Pat2M. Despite the gross gender-specific differences between Pat2 and Pat2M, the difference in the organ absorbed dose coefficients from cross-fire were still below 25.0 % for most organs. The gender-specific organs cannot be compared in this case, though.

As expected, for both overweight and slim individuals only minor differences in the absorbed dose coefficients for urinary bladder wall computed for different phantoms were observed. The energy deposited in the urinary bladder wall is almost entirely due to the

activity accumulated in the bladder contents. For the bladder contents – bladder wall source–target pair the same sets of SAFs derived by Andersson et al. [33] were employed for all phantoms. Other source regions, where phantom-specific SAFs were used, did not substantially contribute to the bladder wall absorbed dose coefficients. The computed bladder wall absorbed dose coefficients remained unaffected by them.

Self-absorption is the main contribution to the organ absorbed dose coefficients for most source organs, especially kidneys, pancreas, salivary glands, liver and thyroid. Figure 8.4 shows that the differences in the self-absorption were small. These were the results of the applied mass-correction to the masses of Pat1 or Pat2, as described in subsection 7.4.1 on page 76. Higher differences in the self-absorption dose coefficients between the target patients Pat1 and Pat2 and the models approximating them were observed for heart wall (16–18 %) and stomach wall (4–8 %). The applied mass-scaling of the SAFs might have limitations for walled organs. Additionally, Pat1 and Pat2 do not have the heart wall segmented separately, but only the whole heart instead. This could be another reason for the observed differences for the heart wall, since the self-absorption in the whole heart is expected to be higher than in the heart wall only. For some source organs, e.g. stomach wall and spleen, the absolute contributions to the absorbed dose coefficients from the cross-fire were also substantial due to high activities of some neighboring source organs.

High contribution to the absorbed dose coefficients by the cross-fire from blood was observed for some organs, e.g. lungs, oesophagus, extrathoracic airways, thymus, eyes and eye lenses. The differences in the cross-fire from blood cannot be reduced by the phantom adjustment though. This depends on how blood is attributed to different body organs and tissues in the Monte Carlo calculations. Since individual blood volumes and individual mass fractions of blood in different organs and tissues are usually not available, the cross-fire from blood is a source of uncertainty of the absorbed dose estimation and requires further careful considerations that go beyond the scope of this work.

### 8.4. Synopsis of performed anatomical modeling

The feasibility of reducing the difference between the individual-specific cross-fire and the cross-fire estimated for non-personalized models was shown for most organs. All PET radiopharmaceuticals have the same energy of photon component (annihilation photons of 511 keV each). This is the main contribution to the cross-fire, since  $\beta$ -particles, due to their short range in tissue, influence most the self-absorption. Nonetheless, depending on branching ratio and energies of the emitted  $\beta$ -particles the results might differ for other radiopharmaceuticals, which are based on other radionuclides than  $^{18}\text{F}$  and have other source regions than  $^{18}\text{F}$ -FSPG. Final conclusions are radionuclide-specific and could be drawn if the SAFs evaluated for all source-target pairs of the phantoms were compared. However, such a comparison is practically very difficult because there are too many possible source-target pairs. Additionally, it is not generally obvious how the differences in the SAFs are propagated to the differences in the resulting organ absorbed dose coefficients, since this also depends on the absolute values of SAFs and the absolute values of time-integrated activity coefficients. A considerable methodological limitation of this work is the usage of only two target patients. Pat1 and Pat2 were selected as, respectively, the biggest and the smallest models in the HMGU library. They represent individuals with a pronounced difference in the BMI (31.8 kg/m<sup>2</sup> and 19.2 kg/m<sup>2</sup> for Pat1 and Pat2, respectively). Pat1 and Pat2 also have unique and unrelated organ topology. With the applied relatively simple

adjustments without matching the locations and masses of individual organs to those of Pat1 and Pat2, < 25.0 % agreement in the cross-fire dose coefficients for the two employed target patients was achieved (the corresponding value for most organs of the reference phantoms relative to Pat1 and Pat2 was < 50.0 %). This might not hold true for other individuals, though. To capture the whole range of inter-individual anatomic variability more patients (i.e. individual phantoms) would be required. The results of this test study showed the feasibility of improving the differences in the cross-fire absorbed dose coefficients for both employed models.

The set of adjusted dimensions was selected in a way that they can relatively easily be obtained for the patients. The individual organ masses and positions in Pat1M and Pat2M were not adjusted to match the corresponding values of Pat1 and Pat2. The employed mass-correction of the SAFs described in subsection 7.4.1 is phantom-independent and requires only the masses of the target=source regions. The clinical quantification of the absolute activities in the source regions – which in any case needs to be determined to yield accurate personalized self-absorption doses – implicitly includes the estimation of the source region masses as part of its procedure. The absolute activities are calculated via the multiplication of the activity concentrations, determined from the PET images, and the source region volumes, obtained from registered CT images.

The attempt of this thesis to capture inter-individual anatomic differences for dosimetric calculations showed the potential to improve the dosimetry in nuclear medicine by adjusting P-RCP-AM to the dimensions of an individual. The time required for the scaling of reference polygon-surface phantom, the subsequent voxelization and contouring source organs to obtain their masses is comparable to that needed for an experienced radiologist to contour all regions of interest. Nonetheless, there are several advantages of the proposed method. Since source organs accumulate activity, they are easily detected, and contouring is comparably simple. Accurate segmentation of all regions of interest is, on the contrary, difficult due to poor soft tissues contrast in CT image. The proposed approach can also be useful in those scenarios where tomographic images of sufficient body coverage and resolution are not available. The implementation of the proposed approach could potentially be optimized by developing automatic tools for scaling the reference polygon-surface phantom. This goes beyond the scope of this work, which aimed at evaluating the feasibility to capture inter-individual anatomic differences by phantom scaling. An alternative option could be to increase the diversity of human computational phantoms available for medical dose evaluation, using the set of dimensions adjusted in this thesis, and subsequently select the phantom from a collection of diversified models which best matches the external dimensions of the patient. This would facilitate a fast clinical implementation of the approach proposed and tested in this thesis. The level of personalization of an employed anatomical model should depend on its application. The results of this work suggest that the proposed approach could be sufficiently reliable for most situations involving low to moderate doses (i.e. outside the therapy realm).



## **Part IV.**

# **Uncertainty and sensitivity analysis**



In this part of the thesis global variance-based sensitivity analysis, accompanied by an uncertainty analysis as part of its procedure, was applied to the internal dosimetry in nuclear medicine according to the MIRDO system. The fundamentals of uncertainty and sensitivity analysis, main practical outcomes and general formalism of these procedures are recapitulated in chapter 9. Chapter 10 describes each step of the variance-based sensitivity analysis implemented in this thesis. The results of the uncertainty and sensitivity analysis are presented in chapter 11. Chapter 11, thus, describes the effect of input factors on computed uncertainties of organ dose coefficients, i.e. how these uncertainties are apportioned to the variability of the input factors.



# 9. Fundamentals of uncertainty and sensitivity analysis

In this chapter objectives and commonly used methods of uncertainty and sensitivity analysis are introduced. The purposes of these procedures are described in section 9.1. Section 9.2 presents commonly used basic approaches of uncertainty and sensitivity analysis and an advanced method of sensitivity analysis along with the advantages and drawbacks of these methods.

## 9.1. Objectives of uncertainty and sensitivity analysis

The objective of the uncertainty analysis is to compute and quantify the uncertainty in the model output, caused by the uncertainties of individual input factors of the model. Thus it is a forward process, which propagates the variability in the inputs to the resulting variability of the model.

Sensitivity analysis, denoted as SA from now on, is another key procedure used to assess the quality of a model-based study [20]. It is an evaluation of the relative importance of different input factors on the model output. In other words, SA breaks down the total uncertainty in the model output into the parts caused by different input factors. Thus SA is a backward process, in contrast to uncertainty analysis, because it projects the variability in the model output back to the variability of the input factors.

Knowing the importance of the input factors, two settings are possible: investing efforts in determining more precisely those input factors, which have a high influence on the variability of the model output, and fixing those input factors, which do not affect the model output anywhere in their range of variation. Saltelli et al. [97] denote the above mentioned settings as “factor prioritization” and “factor fixing”, respectively. The important practical outcomes of SA thus include a possibility to reduce the model complexity by applying the “factor fixing” setting and to decrease the variability of the model output in the most effective way by using the “factor prioritization” setting. For the sake of simplicity this thesis will refer to the calculation of organ absorbed dose coefficients as to the model and denote the computed doses as the model output in the following text.

## 9.2. Methods of uncertainty and sensitivity analysis

### 9.2.1. Uncertainty propagation

This commonly used method of error propagation relies on the assumption that a linear approximation of a function  $\mathbb{Y}(X)$  can be used around the mean value  $\bar{X}$  of the input

## 9. Fundamentals of uncertainty and sensitivity analysis

factor  $X$ . Then the change of the function around  $\bar{X}$  can be written as:

$$\mathbb{Y} - \mathbb{Y}(\bar{X}) = \mathbb{Y} - \bar{\mathbb{Y}} \approx \left. \frac{\partial \mathbb{Y}}{\partial X} \right|_{X=\bar{X}} (X - \bar{X}) \quad (9.1)$$

Then, denoting  $X - \bar{X} = \delta X$ , the true value of the output  $\mathbb{Y}$  lies in the interval  $\bar{\mathbb{Y}} \pm \delta \mathbb{Y}$ , where  $\delta \mathbb{Y}$  is:

$$\delta \mathbb{Y} = \left. \frac{\partial \mathbb{Y}}{\partial X} \right|_{X=\bar{X}} \delta X \quad (9.2)$$

In case of a two-dimensional model  $\mathbb{Y}(X_1, X_2)$  for the sake of convenience the mean value of the input is denoted as  $\bar{\mathbf{X}} = (\bar{X}_1, \bar{X}_2)$ . Assuming again that a linear approximation can be used around the mean value  $\bar{\mathbb{Y}} = \mathbb{Y}(\bar{\mathbf{X}})$  it follows:

$$\mathbb{Y} - \bar{\mathbb{Y}} \approx \left. \frac{\partial \mathbb{Y}}{\partial X_1} \right|_{\bar{\mathbf{X}}} (X_1 - \bar{X}_1) + \left. \frac{\partial \mathbb{Y}}{\partial X_2} \right|_{\bar{\mathbf{X}}} (X_2 - \bar{X}_2) \quad (9.3)$$

analogously to equation 9.2 it follows for two input parameters:

$$\delta \mathbb{Y} \approx \left. \frac{\partial \mathbb{Y}}{\partial X_1} \right|_{\bar{\mathbf{X}}} \delta X_1 + \left. \frac{\partial \mathbb{Y}}{\partial X_2} \right|_{\bar{\mathbf{X}}} \delta X_2 \quad (9.4)$$

From equation 9.4 follows that:

$$(\delta \mathbb{Y})^2 \approx \left( \left. \frac{\partial \mathbb{Y}}{\partial X_1} \right|_{\bar{\mathbf{X}}} \delta X_1 \right)^2 + \left( \left. \frac{\partial \mathbb{Y}}{\partial X_2} \right|_{\bar{\mathbf{X}}} \delta X_2 \right)^2 + 2 \left. \frac{\partial \mathbb{Y}}{\partial X_1} \frac{\partial \mathbb{Y}}{\partial X_2} \right|_{\bar{\mathbf{X}}} \delta X_1 \delta X_2 \quad (9.5)$$

Equation 9.5 is the error propagation formula for a two-dimensional model  $\mathbb{Y}(X_1, X_2)$ .

A special case of uncertainty propagation is the Gaussian error propagation. In this case the input parameters  $X_1$  and  $X_2$  of the model  $\mathbb{Y}(X_1, X_2)$  are assumed to be normally distributed. From the definition of the variance  $\sigma^2$  for the case of  $n$  observations, the variance  $\sigma_{\mathbb{Y}}^2$  of  $\mathbb{Y}$  is:

$$\sigma_{\mathbb{Y}}^2 = \frac{1}{n-1} \sum_{j=1}^n (\delta \mathbb{Y}_j)^2 \quad (9.6)$$

From equations 9.5 and 9.6 it follows:

$$\sigma_{\mathbb{Y}}^2 \approx \frac{1}{n-1} \sum_{j=1}^n \left( \left( \left. \frac{\partial \mathbb{Y}}{\partial X_1} \right|_{\bar{\mathbf{X}}} \delta X_{1j} \right)^2 + \left( \left. \frac{\partial \mathbb{Y}}{\partial X_2} \right|_{\bar{\mathbf{X}}} \delta X_{2j} \right)^2 + 2 \left. \frac{\partial \mathbb{Y}}{\partial X_1} \frac{\partial \mathbb{Y}}{\partial X_2} \right|_{\bar{\mathbf{X}}} \delta X_{1j} \delta X_{2j} \right) \quad (9.7)$$

Taking into account that the variances  $\sigma_{X_1}^2$  and  $\sigma_{X_2}^2$  of  $X_1$  and  $X_2$ , respectively, are defined as  $\sigma_{X_1}^2 = \frac{1}{n-1} \sum_{j=1}^n (\delta X_{1j})^2$  and  $\sigma_{X_2}^2 = \frac{1}{n-1} \sum_{j=1}^n (\delta X_{2j})^2$ , equation 9.7 becomes:

$$\sigma_{\mathbb{Y}}^2 \approx \left( \left. \frac{\partial \mathbb{Y}}{\partial X_1} \right|_{\bar{\mathbf{X}}} \right)^2 \sigma_{X_1}^2 + \left( \left. \frac{\partial \mathbb{Y}}{\partial X_2} \right|_{\bar{\mathbf{X}}} \right)^2 \sigma_{X_2}^2 + 2 \left. \frac{\partial \mathbb{Y}}{\partial X_1} \frac{\partial \mathbb{Y}}{\partial X_2} \right|_{\bar{\mathbf{X}}} \sigma_{X_1, X_2} \quad (9.8)$$

where  $\sigma_{X_1, X_2} = \frac{1}{n-1} \sum_{j=1}^n \delta X_{1j} \delta X_{2j}$  is a covariance of  $X_1$  and  $X_2$ . If the input parameters  $X_1$  and  $X_2$  are independent,  $\sigma_{X_1, X_2}$  can be neglected. Therefore for independent  $X_1$  and  $X_2$ :

$$\sigma_{\mathbb{Y}}^2 \approx \left( \left. \frac{\partial \mathbb{Y}}{\partial X_1} \right|_{\bar{\mathbf{X}}} \right)^2 \sigma_{X_1}^2 + \left( \left. \frac{\partial \mathbb{Y}}{\partial X_2} \right|_{\bar{\mathbf{X}}} \right)^2 \sigma_{X_2}^2 \quad (9.9)$$

Equation 9.9 can be generalized for a model  $\mathbb{Y}$  with arbitrary number of independent input parameters  $\mathbb{Y}(X_1, X_2, \dots, X_k)$ :

$$\sigma_{\mathbb{Y}}^2 \approx \sum_{i=1}^k \left( \left. \frac{\partial \mathbb{Y}}{\partial X_i} \right|_{\bar{\mathbf{X}}} \right)^2 \sigma_i^2 \quad (9.10)$$

These error propagation approaches can be applied only to analytical functions. Another substantial drawback of this method is the assumption of a linear approximation to the model  $\mathbb{Y}(\mathbf{X})$  around  $\bar{\mathbf{X}}$ , which does not always hold. These considerably reduce the area of applicability of the error propagation method.

### 9.2.2. Local approach to sensitivity analysis

The local SA is the first historical approach to SA. It evaluates the effect on the model output of small perturbations of the input factors. The values of the inputs are changed around a specific point in the input space, often the mean value. According to this approach the partial derivatives of the model output  $\mathbb{Y}$  at e.g. the mean value of input factors  $\bar{\mathbf{X}}$  are estimated. For instance, a value  $\left( \left. \frac{\partial \mathbb{Y}}{\partial X_i} \right|_{\bar{\mathbf{X}}} \sigma_i \right)^2$  can be considered as a sensitivity index

$S_i$  of the input  $X_i$ . The higher is the term  $S_i = \left( \left. \frac{\partial \mathbb{Y}}{\partial X_i} \right|_{\bar{\mathbf{X}}} \sigma_i \right)^2$ , the higher is the influence of input factor  $X_i$  on the variability of the output  $\mathbb{Y}$ . A substantial disadvantage of this method is the evaluation of sensitivity in one point of the input space only. Additionally, only small perturbations of the inputs are studied in this case. Thus the local approaches do not facilitate the full exploration of the input space. Usually these approaches do not examine the cross-terms (interactions) between different input factors. In SA the input factors “interact”, if the simultaneous change of these factors results in a higher variation of the model output compared to that caused by the separate change of each input factor.

### 9.2.3. “One-factor-at-a-time” sensitivity analysis

One of the simplest SA methods is often called “one-factor-at-a-time”. It is the most frequently used SA approach. Ferretti et al. [98] show in their review of the published academic papers related to the SA that the majority of the papers use “one-factor-at-a-time” SA. It evaluates the effect on the model output of change of one uncertain input at a time around a selected point (often the mean value) while keeping the other inputs constant. After moving one input factor, it is returned to its nominal value. Thereafter the procedure is repeated for other variable input factors in the same fashion. Thus any interactions between the input parameters are ignored in this case, since the simultaneous variation of the inputs is not considered with this approach. Therefore, for reliable and stable results, “one-factor-at-a-time” SA requires linearity and additivity of a model. In an additive model interactions do not occur and the total variation of the model output can be sub-divided into parts caused by different input factors separately. The input space remains not fully explored with the “one-factor-at-a-time” SA. This effect becomes more severe with increasing number of input parameters. Saltelli and Annoni [20] called this effect a “curse of dimensionality” and provided a geometric proof of the inadequacy of “one-factor-at-a-time” SA. Despite the simplicity of this method, it cannot be considered

appropriate for any arbitrary model because of the substantial limitations and the required assumptions mentioned above.

### 9.2.4. Global variance-based sensitivity analysis

In variance-based approaches probability distributions of the input factors are used to obtain the distribution of the model output. The variance of the model output is decomposed into the parts caused by the input factors. Thus the sensitivity measure for input factor  $X_i$  in this case is a fraction of the total variance caused by  $X_i$ . In contrast to “one-factor-at-a-time” SA approaches, global variance-based techniques [97,99–101] are effective and do not require the assumptions of linearity and additivity of a model. They facilitate studying the influence of several input factors on the model output. The basic concepts of the variance-based methods are recapitulated in the following.

Sensitivity indices can be of a different order. The first-order sensitivity indices are also called main effect indices and they indicate an effect of a particular parameter on the model output. Higher-order effect sensitivity indices include interplay effects (combined effects) of several inputs. Total effect indices include the first-order effect and all interactions of a respective input factor [102,103]. It is usually considered that a model can be sufficiently described by two sets of sensitivity indices – the first-order effect and the total effect indices [97,99].

Consider a model  $\mathbb{Y} = f(X_1, X_2, \dots, X_i, \dots, X_n)$  with  $n$  independent uncertain input factors. Denote  $\mathbb{Y}|X_i = x_i^*$  the value of the model  $\mathbb{Y}$  if the input  $X_i$  is fixed to a certain value  $x_i^*$ .  $X_{\sim i}$  is the set of all input factors but  $X_i$ . The mean value of the model  $\mathbb{Y}$  for fixed  $X_i = x_i^*$  but all other inputs  $X_{j \neq i}$  varied is indicated as  $\mathbb{E}_{X_{\sim i}}(\mathbb{Y}|X_i = x_i^*)$ . Then the first-order effect sensitivity index  $S_i$  for the input factor  $X_i$  is defined as follows:

$$S_i = \frac{V_{X_i}(\mathbb{E}_{X_{\sim i}}(\mathbb{Y}|X_i = x_i^*))}{V(\mathbb{Y})} \quad (9.11)$$

where the numerator is variance of  $\mathbb{E}_{X_{\sim i}}(\mathbb{Y}|X_i = x_i^*)$  when varying all possible points  $x_i^*$ .  $V(\mathbb{Y})$  denotes the total unconditional variance of the output.  $V(\mathbb{Y})$  is computed according to its definition:

$$\begin{aligned} V(\mathbb{Y}) &= \mathbb{E}[(\mathbb{Y} - \mathbb{E}(\mathbb{Y}))^2] = \mathbb{E}[\mathbb{Y}^2 - 2\mathbb{Y}\mathbb{E}(\mathbb{Y}) + \mathbb{E}^2(\mathbb{Y})] \\ &= \mathbb{E}[\mathbb{Y}^2] - 2\mathbb{E}[\mathbb{Y}]\mathbb{E}[\mathbb{Y}] + \mathbb{E}^2[\mathbb{Y}] = \mathbb{E}[\mathbb{Y}^2] - \mathbb{E}^2[\mathbb{Y}] \end{aligned} \quad (9.12)$$

A high value of  $S_i$  indicates an important input. A low  $S_i$  does not necessarily mean a non-influential input though, since higher-order effects can occur. To detect them the total effect sensitivity index  $S_{T_i}$  is computed.  $S_{T_i}$  includes  $S_i$  and all interactions of  $X_i$ . Thus the fraction of output variance which is caused by  $X_{\sim i}$  alone needs to be excluded. This fraction is described by the first-order effect sensitivity index for  $X_{\sim i}$ :

$$S_{T_i} = 1 - \frac{V_{X_{\sim i}}(\mathbb{E}_{X_i}(\mathbb{Y}|X_{\sim i} = x_{\sim i}^*))}{V(\mathbb{Y})} \quad (9.13)$$

Analogously to equation 9.11,  $\mathbb{E}_{X_i}(\mathbb{Y}|X_{\sim i} = x_{\sim i}^*)$  is the mean of the model  $\mathbb{Y}$  when  $X_{\sim i} = x_{\sim i}^*$  is fixed, i.e. all input factors except  $X_i$  are kept fixed.  $V_{X_{\sim i}}(\dots)$  is variance of the argument when varying all possible points  $x_{\sim i}^*$ . Considering the law of total variance

$V(\mathbb{Y}) = V[\mathbb{E}(\mathbb{Y}|X)] + \mathbb{E}[V(\mathbb{Y}|X)]$  divided by  $V(\mathbb{Y})$ , equation 9.13 for the total effect sensitivity index  $S_{T_i}$  of input factor  $X_i$  can be written as follows:

$$S_{T_i} = \frac{\mathbb{E}_{X_{\sim i}}(V_{X_i}(\mathbb{Y}|X_{\sim i} = x_{\sim i}^*))}{V(\mathbb{Y})} \quad (9.14)$$

where  $V_{X_i}(\mathbb{Y}|X_{\sim i} = x_{\sim i}^*)$  is the variance over possible  $X_i = x_i^*$  of the model  $\mathbb{Y}$ , while keeping all input factors except  $X_i$  fixed.  $\mathbb{E}_{X_{\sim i}}(\dots)$  is the mean of the argument taken over  $X_{\sim i}$ , i.e. all input factors but  $X_i$ .

Both,  $S_i$  and  $S_{T_i}$  can have non-negative values in the range  $[0, 1]$ , where the importance of the corresponding input factor increases with increasing values of the sensitivity index. For example,  $S_i = 0$  and  $S_{T_i} = 0$  mean, respectively, no main effect influence and no influence of the corresponding input factor on the model output.  $S_i = 1$  means that the variability in the output is solely caused by the variability of the input  $X_i$ . Per definition  $S_{T_i} \geq S_i$ , since the total effect index includes main effect and all interactions of  $X_i$ . According to variance decomposition formula (see reference [97]) for any arbitrary model with independent inputs, the sum of all sensitivity indices of all orders, with each cross-term being considered only once, is always equal to one:  $\sum_i S_i + \sum_i \sum_{j>i} S_{ij} + \sum_i \sum_{j>i} \sum_{l>j} S_{ijl} + \dots + S_{123\dots k} = 1$ . For perfectly additive models, i.e. for models in which no interactions between inputs occur,  $\sum_i S_i = \sum_i S_{T_i} = 1$ . For non-additive models,  $\sum_i S_i < 1$ , since at least one of the higher-order terms  $S_{ij}, S_{ijl}, \dots, S_{123\dots k}$  is nonzero. The sum of all total effect sensitivity indices in a non-additive model is higher than one:  $\sum_i S_{T_i} > 1$ . It follows from the fact that e.g. nonzero cross-term  $S_{jl}$  would be included in  $\sum_i S_{T_i}$  twice – once as part of  $S_{T_j}$  and once as part of  $S_{T_l}$ .

Equations 9.11 and 9.14 present the general formalism of the variance-based SA. To compute the sensitivity measures  $S_i$  and  $S_{T_i}$  according to this formalism, in practice Monte Carlo estimators are used. The latter facilitate the calculation of  $S_i$  and  $S_{T_i}$  from two sets: (1) input factors sampled multiple times from their distributions and (2) corresponding model outputs calculated with each sample of the input factors. This procedure and the Monte Carlo estimators employed in this thesis are discussed later in section 10.3.



# 10. Application of uncertainty and global sensitivity analysis to internal dosimetry

## 10.1. Uncertainties in internal dosimetry

The rationale of reliable internal dosimetry was already discussed in the introduction of this thesis on page 4. As it is shown throughout this thesis, internal dosimetry relies on computational methods, e.g. the MIRDO framework [4] considered here, and on modeling procedures – pharmacokinetic modeling, anatomical modeling and Monte Carlo radiation transport simulations. Each type of the involved modeling is associated with various sources of uncertainty [17, 19]. Therefore the total uncertainty of the computed organ doses can amount to a high value [19]. It follows that the resulting dose estimates are to be provided with the corresponding uncertainties. This is especially important in radionuclide therapy, since the uncertainty in the computed organ doses may influence the decision-making. For instance, the dose in the target that needs to be treated and the dose in the organs at risk are usually two main factors defining an acceptance or a rejection of a treatment plan. The former should be high enough to achieve the therapeutic effect, the latter cannot exceed the highest tolerated dose for the particular organ or tissue. Thus the uncertainties associated with these doses can affect the goodness of the plan and need to be taken into account. Epidemiological studies in nuclear medicine also need to be accompanied by the uncertainty analysis, since the outcome of the study can be affected by uncertainties of the documented doses [18].

Pharmacokinetic modeling involves the uncertainties associated with the model structure, image acquisition and quantification, measurements of activity in collected blood samples etc. Nonetheless, the main source of uncertainty in pharmacokinetic modeling, indicated by Stabin [19], is the goodness of the model predictions for individual patients, i.e. inter-individual differences in the distribution and excretion of an administered substance. The statistical uncertainties of Monte Carlo simulations of radiation transport in a human computational phantom are usually small. Thus the major source of variations in anatomical modeling is the difference between individuals and phantoms used to represent the individuals, as also indicated in reference [19].

The details of uncertainty and sensitivity analysis implemented in this thesis and the considered sources of variability are presented in the following.

## 10.2. Evaluated model and considered sources of uncertainty

Uncertainty and variance-based sensitivity analysis are applied in this thesis to the MIRD model of internal organ dose computation [4]. This model is described in details in chapter 2 on page 23. It is an analytical model defined by equations 2.2, 2.4 and 2.8 on pages 23–24. Moreover, a fixed urinary bladder model for the reference bladder content volume of 200 ml was used to compute the absorbed dose coefficients to urinary bladder wall. For convenience, the main equations of the considered model are repeated below:

$$d(r_T) = \sum_{r_S \neq r_{RoB}} TIAC(r_S) S(r_T \leftarrow r_S) + TIAC(r_{RoB}) \left( \frac{M_{r_{TB}} S(r_T \leftarrow r_{TB}) - \sum_{r_S \neq r_{RoB}} M_{r_S} S(r_T \leftarrow r_S)}{M_{r_{RoB}}} \right) \quad (10.1)$$

where

$$S(r_T \leftarrow r_S) = \begin{cases} \sum_i E_i Y_i SAF(r_T \leftarrow r_S, E_i), & \text{for photons} \\ \int_0^{E_0} P(E) E SAF(r_T \leftarrow r_S, E) dE, & \text{for } \beta\text{-spectrum of electrons} \end{cases} \quad (10.2)$$

The dose-integration period  $T_D$  has been eliminated in equation 10.1 in the arguments of the absorbed dose coefficient  $d(r_T)$  and of the time-integrated activity coefficients  $TIAC(r_S)$ , because it was fixed to  $T_D = 1000$  min (see section 5.1 on page 47). Note that for the sake of simplicity the symbols  $\tilde{a}(r_S)$  and  $\Phi(r_T \leftarrow r_S, E)$  used in equations 2.2, 2.4 and 2.8, are replaced by  $TIAC(r_S)$  and  $SAF(r_T \leftarrow r_S, E)$ , respectively, in equations 10.1 and 10.2 and in the following.

As it can be seen from equations 10.1 and 10.2, the input factors for the model include time-integrated activity coefficients for the source regions  $r_S$  and for the rest of body  $r_{RoB}$  ( $TIAC(r_S)$  and  $TIAC(r_{RoB})$ , respectively),  $S(r_T \leftarrow r_S)$  for all source-target pairs and all considered radiation types,  $S(r_T \leftarrow r_{TB})$ ,  $E_i$ ,  $Y_i$  and the masses of total body and source regions. The latter were taken from the corresponding masses of the employed human computational phantom. The values of  $E_i$ ,  $Y_i$  and the  $\beta$ -spectrum of the considered radiation types were assumed to be constant. Thus the variable input parameters of the model comprise the time-integrated activity coefficients and the specific absorbed fractions. For the sake of convenience they are denoted as TIAC input factors and SAF input factors.

Thus for the output  $\mathbb{Y}$  (the number of outputs is equal to the number of considered target regions  $r_T$ ) it can be written:

$$\mathbb{Y} = f(TIAC_1, TIAC_2, \dots, TIAC_i, \dots, TIAC_k, SAF_1, SAF_2, \dots, SAF_i, \dots, SAF_k) \quad (10.3)$$

with the model  $f$  defined by equations 10.1–10.2 and the number of independent input factors being equal to  $2k$ , where  $k$  is the number of source regions. The model  $f$  was implemented in the scope of this thesis in an in-house MATLAB-based program, which utilizes discrete photon energies and detailed  $\beta$ -spectra from ICRP Publication 107 [55]. The developed program includes the option of mass-correction of the SAFs, as described in

subsection 7.4.1 on page 76. Values denoted as “weighted dose coefficients” in the following were also computed in this thesis. They were calculated as a weighted sum of individual organ absorbed dose coefficients with the tissue weighting factors given in ICRP [34]. The difference between the weighted dose coefficients computed here and the effective dose coefficients defined by ICRP [34] is that the weighted dose coefficients are not sex- and age-averaged and the following organs and tissues were excluded from their calculation: endosteum, lymphatic nodes, oral mucosa, muscle tissue, uterus and prostate. These regions were excluded because they were not present in at least one of the considered phantoms. The employed tissue weighting factors were assumed to be constant.

### 10.3. Monte Carlo approach for variance-based sensitivity analysis

Monte Carlo estimators were used in this thesis to compute the sensitivity indices  $S_i$  and  $S_{T_i}$  given by equations 9.11 and 9.14, respectively. The Monte Carlo estimators were developed by Saltelli et al. [99] for the first-order effect indices  $S_i$  and by Jansen [104] and Saltelli et al. [99] for the total effect indices  $S_{T_i}$  based on the work of Sobol' [100]. These Monte Carlo techniques intrinsically include the uncertainty analysis and, hence, provide both, uncertainty and sensitivity of the model output at once.

According to the implemented Monte Carlo technique, all uncertain input factors are simultaneously sampled from their assigned distributions, providing a vector of inputs  $(X_1, X_2, \dots, X_i, \dots, X_{2k})_1$ . The model output is calculated with the vector of input factors  $(X_1, X_2, \dots, X_i, \dots, X_{2k})_1$  and denoted as  $f(X_1, X_2, \dots, X_i, \dots, X_{2k})_1$ . This procedure is repeated  $N$  times, giving a matrix  $A$  of input factors with a size  $N \times 2k$ , where  $j$ -th row represent  $j$ -th sample of the input factors  $(X_1, X_2, \dots, X_i, \dots, X_{2k})_j$ . The model is executed for each sample of the inputs, providing a vector of outputs  $\mathbb{Y} = f(A)$  of the length  $N$ . In this thesis the SA was implemented in a way that  $S_i$  and  $S_{T_i}$  are computed simultaneously for the output dose coefficients for all target regions  $r_T$ . Thus  $\mathbb{Y} = f(A)$  is not a vector, but a matrix of the size  $N \times$  number of considered  $r_T$ . Each column of this matrix corresponds to a particular  $r_T$  and is a vector. Therefore, for simplicity, the output  $\mathbb{Y}$  is considered to be a vector of length  $N$  in the following. The variability of the output  $\mathbb{Y}$  can be thus evaluated:

$$\sigma_{\mathbb{Y}} = \sqrt{V(\mathbb{Y})} \quad (10.4)$$

Knowing the mean value  $\mathbb{E}(\mathbb{Y})$  of model  $\mathbb{Y}$ , the relative uncertainty is computed as follows:

$$RU = \frac{\sigma_{\mathbb{Y}}}{\mathbb{E}(\mathbb{Y})} \quad (10.5)$$

The generated samples of inputs and the corresponding model outputs are used for the SA. Saltelli et al. [99] proposed the following approach to compute the first-order effect index  $S_i$ :

$$S_i = \frac{\frac{1}{N} \sum_{j=1}^N f(B)_j \left( f(A_B^{(i)})_j - f(A)_j \right)}{V(\mathbb{Y})} \quad (10.6)$$

with  $N$  being a number of model evaluations;  $A$  and  $B$  are independent sampled matrices of input factors with a size of  $N \times 2k$  and are both generated as described above for matrix

$A$  as an example (independence of  $A$  and  $B$  is ensured by an independent sampling of the vectors of input factors  $2N$  times in total);  $A_B^{(i)}$  is equal to the matrix  $A$ , except for the column  $i$ , which is taken from the matrix  $B$ , i.e.  $X_i = \text{const}$  (see equation 9.11 on page 100);  $(A)_j$  and  $(B)_j$  are the  $j$ -th rows of  $A$  and  $B$ , respectively.  $V(\mathbb{Y})$  is computed according to equation 9.12 on page 100 using the outputs  $\mathbb{Y}$  evaluated for both input matrices  $A$  and  $B$ .

The total effect index  $S_{T_i}$  can be computed simultaneously with  $S_i$  according to the method proposed by Jansen [104] and Saltelli et al. [99]:

$$S_{T_i} = \frac{\frac{1}{2N} \sum_{j=1}^N \left( f(A)_j - f(A_B^{(i)})_j \right)^2}{V(\mathbb{Y})} \quad (10.7)$$

An in-house program was developed in the scope of this thesis to compute  $S_i$  and  $S_{T_i}$  according to equations 10.6 and 10.7, respectively. The program was written in MATLAB environment. Various values of the number of model executions  $N$  were used to evaluate and ensure the convergence of the computed SA indices.

## 10.4. Input factors used in sensitivity analysis

As it is described in section 10.2, for each target region  $r_T$  the set of uncertain input factors considered in this work comprised the time-integrated activity coefficients  $\text{TIAC}(r_S)$  for source regions  $r_S$  (and rest of body  $r_{RoB}$ ) and the specific absorbed fractions  $\text{SAF}(r_T \leftarrow r_S, E)$ .

### TIAC input factors

Activity data for radiopharmaceutical  $^{18}\text{F}$ -FSPG derived in part II of this thesis were employed in the sensitivity analysis. The case of blood being a distinct source region was selected, as being more physiologically meaningful. These five sets of activity data are given in table 5.4 on page 49. The 11 source regions for  $^{18}\text{F}$ -FSPG included kidneys, bladder content, heart, thyroid, salivary glands, pancreas, stomach wall, liver, spleen, rest of body and blood. Thus 11 TIAC input factors were considered, i.e. equal to the number of the source regions ( $k=11$  in equation 10.3 on page 104).

### Employed anatomical models and SAF input factors

Six human computational phantoms were considered in the sensitivity analysis of this thesis. These included two reference models – voxel ICRP adult male computational phantom [53] (RCP-AM), polygon-surface ICRP adult male computational phantom [67] (P-RCP-AM); two slim individuals – Irene [65, 72] (= Pat2) and the polygon-surface phantom Pat2M obtained via adjustments of P-RCP-AM to fit selected characteristics of Irene (see chapter 8); and two overweight individuals – Visible Human [65] (= Pat1) and the polygon-surface phantom Pat1M obtained via adjustments of P-RCP-AM to fit selected characteristics of Visible Human (see chapter 8). The description of the reference models is given in section 6.2. The phantoms Visible Human (= Pat1) and Irene (= Pat2) are presented in subsection 7.1.1. The anatomical models Pat1M and Pat2M developed in the scope of this

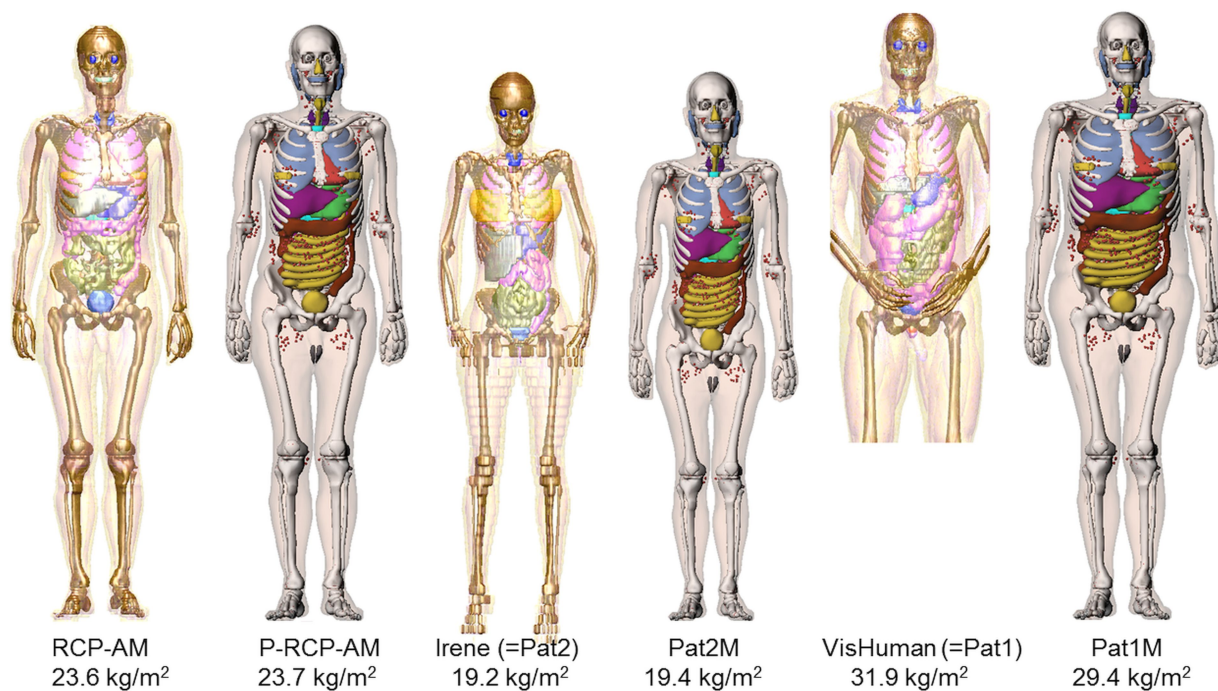


Figure 10.1. Anatomical models of reference (RCP-AM and P-RCP-AM), slim (Irene (= Pat2) and Pat2M) and overweight (VisHuman (= Pat1) and Pat1M) individuals along with their BMI employed in sensitivity analysis.

thesis are described in section 8.1. Figure 10.1 shows the anatomical models employed in the SA along with their body mass index (BMI).

The performed Monte Carlo calculations of the SAF of monoenergetic photon and electron sources are described in sections 7.2 and 8.2. In the computational phantoms Irene and Visible Human heart wall is not segmented, only the whole heart instead. Thus heart wall was surrogated by heart for these two phantoms. Breast of RCP-AM was employed for breast in Visible Human, since the latter is not present. For the urinary bladder dosimetry the SAFs for photon and discrete electron energies computed by Andersson et al. [33] for the bladder content as source and bladder wall as target were employed here for all phantoms. Thus no variability of  $\text{SAF}(UB_{\text{wall}} \leftarrow UB_{\text{cont}})$  among the anatomical models was considered ( $UB_{\text{wall}}$  and  $UB_{\text{cont}}$  stand for urinary bladder wall and urinary bladder content, respectively). The detailed  $\beta$ -spectrum of  $^{18}\text{F}$  from ICRP [55] was considered in this thesis for dose computation. This includes SAFs for various energies of the emitted  $\beta$  component, ranging from zero to the end-point energy  $E_{\text{max}}$  of the  $\beta$ -spectrum (for  $^{18}\text{F}$   $E_{\text{max}} = 633.5$  keV). The SAFs corresponding to the discrete electron energies were not considered as input factors in the sensitivity analysis though. The  $S$  values integrated over all energies of the  $\beta$ -spectrum according to equation 10.2 on page 104 were used instead. Despite this, for the sake of convenience these input factors are denoted SAF input factors, analogously to the photon component. For each radiation type the number of considered sets of the SAFs is equal to the number of source regions for the employed radiopharmaceutical. Thus in the presented study 11 sets of SAFs for photon component and 11 sets of SAFs for electron component were considered.

## 10.5. Sampling of input factors

A truncated normal distribution (without the negative tail) was assigned to the input factors. The negative tails of the distributions were cut, because negative values of TIACs and SAFs are not meaningful. The parameters  $\mu$  and  $\sigma$  (mean and standard deviation, respectively) of the probability density functions were computed from the five volunteer-specific sets of the TIACs for the TIAC input factors and from the phantom-specific sets of the SAFs for the SAF input factors. The parameters  $\mu$  and  $\sigma$  for the TIAC input factors are shown in table 10.1. The mean  $\mu$  and the standard deviation  $\sigma$  calculated for the distributions of the SAF input factors for photons and electrons are given in tables 10.2 and 10.3, respectively.

	Kidneys	Liver	Pancreas	Spleen	St-wall	Thyroid	S-glands	UB-cont	Ht-wall	RoB	Blood
$\mu$	583.6	245.5	134.3	18.5	35.1	4.4	6.1	1175.4	44.3	1885.5	721.7
$\sigma$	79.2	88.2	33.6	9.7	15.2	1.1	1.2	123.2	25.2	392.8	118.5

Table 10.1. Mean  $\mu$  [s] and standard deviation  $\sigma$  [s] of TIAC input factors distributions. St-wall stands for stomach wall, S-glands – for salivary glands, UB-cont – for urinary bladder content, Ht-wall – for heart wall, RoB – for rest of body.

## 10.6. Sobol' low discrepancy sequence

The low-discrepancy (also called quasi-random) sequence developed by Sobol' [105] was used to generate the samples of the independent variable input factors. Such deterministic sequences attempt to minimize the discrepancy, i.e. make the quasi-random points as well spaced as possible in a unit hypercube. Averaged over all projections in a multidimensional unit hypercube, the points in the Sobol' sequence [105] are distributed with a greater uniformity than random (or pseudo-random) numbers and, therefore, provide an accelerated convergence of the computed SA indices. Figure 10.2 shows an example of 128 uniformly distributed points generated with the pseudo-random generator of a personal computer and 128 uniformly distributed points, generated with Sobol' low-discrepancy sequence. To generate Sobol' quasi-random points, the program [106] distributed by the Joint Research Centre of the European Commission (<https://ec.europa.eu/jrc/en>) was employed.

Figure 10.2 shows a two-dimensional case. In panel (a) of figure 10.2 clustering of the points and empty areas can be observed, whereas the points in panel (b) are distributed with much greater uniformity. Note that for a multi-dimensional model it becomes even more difficult to achieve a low discrepancy in the sampled input factors with increasing dimensionality. The Sobol' sequence [105], and low-discrepancy sequences in general, are particularly advantageous for problems with few dimensions and higher sample size. Nonetheless, averaged over all projections, the Sobol' sequence [105] generates points that are considerably better spaced than random numbers. Consequently, it is likely to achieve a faster convergence of the values computed with Monte Carlo methods. However, the convergence is also dependent on the model, and some models will see much more marked improvements from the usage of low-discrepancy sequences than others. Conventional wisdom is to use the Sobol' sequence [105], because it should at least be as good as random sequence, and often is more accurate.

Target regions	Source regions											
	Kidneys	Liver	Pancreas	Spleen	St-wall	Thyroid	S-glands	UB-cont	Ht-wall	RoB	Blood	
Kidneys	$\mu$	2.50E-04	2.20E-05	3.60E-05	3.20E-05	1.70E-05	9.30E-07	3.30E-07	1.60E-06	5.60E-06	4.00E-06	1.60E-05
	$\sigma$	3.80E-06	6.40E-06	1.50E-05	9.90E-06	6.70E-06	1.00E-07	3.50E-08	1.80E-07	1.20E-06	8.50E-07	4.00E-06
Liver	$\mu$	2.20E-05	9.20E-05	3.40E-05	6.70E-06	2.10E-05	2.30E-06	7.40E-07	7.50E-07	1.60E-05	2.50E-06	2.00E-05
	$\sigma$	6.40E-06	9.20E-07	7.20E-06	1.70E-06	4.60E-06	3.10E-07	7.00E-08	1.90E-07	2.70E-06	9.80E-07	4.50E-06
Pancreas	$\mu$	3.60E-05	3.40E-05	4.90E-04	2.00E-05	6.70E-05	1.20E-06	4.20E-07	1.30E-06	1.20E-05	3.80E-06	1.70E-05
	$\sigma$	1.50E-05	7.20E-06	2.30E-05	1.30E-05	3.10E-05	1.30E-07	6.10E-08	3.30E-07	2.40E-06	7.60E-07	4.50E-06
Spleen	$\mu$	3.20E-05	6.70E-06	2.00E-05	4.80E-04	4.30E-05	2.40E-06	7.70E-07	5.30E-07	1.50E-05	3.40E-06	1.70E-05
	$\sigma$	9.90E-06	1.70E-06	1.30E-05	1.30E-05	1.40E-05	3.50E-07	7.10E-08	7.30E-08	4.70E-06	7.70E-07	4.20E-06
St-wall	$\mu$	1.70E-05	2.10E-05	6.70E-05	4.30E-05	2.60E-04	2.00E-06	6.60E-07	7.50E-07	2.90E-05	3.40E-06	1.50E-05
	$\sigma$	6.70E-06	4.60E-06	3.10E-05	1.40E-05	3.20E-05	2.50E-07	1.10E-07	1.70E-07	4.80E-06	7.50E-07	3.40E-06
Thyroid	$\mu$	9.00E-07	2.30E-06	1.20E-06	2.30E-06	1.90E-06	1.50E-03	1.70E-05	4.70E-08	9.90E-06	4.30E-06	7.50E-06
	$\sigma$	1.10E-07	3.20E-07	1.30E-07	3.60E-07	2.30E-07	3.60E-05	2.50E-06	8.50E-09	1.10E-07	8.10E-07	1.70E-06
S-glands	$\mu$	3.10E-07	7.10E-07	3.80E-07	7.30E-07	6.20E-07	1.70E-05	4.60E-04	1.80E-08	1.80E-06	3.80E-06	4.00E-06
	$\sigma$	4.50E-08	6.70E-08	5.90E-08	7.10E-08	1.10E-07	2.50E-06	2.10E-05	2.80E-09	1.50E-07	9.90E-07	9.80E-07
UB-wall	$\mu$	1.50E-06	7.30E-07	1.20E-06	5.10E-07	7.10E-07	4.30E-08	2.00E-08	2.50E-04	2.30E-07	5.40E-06	4.80E-06
	$\sigma$	1.70E-07	2.00E-07	2.70E-07	7.50E-08	1.50E-07	6.10E-09	3.40E-09	0.00E+00	3.70E-08	6.40E-07	1.70E-06
Ht-wall	$\mu$	5.60E-06	1.60E-05	1.20E-05	1.50E-05	2.90E-05	1.00E-05	1.80E-06	2.40E-07	1.60E-04	3.50E-06	2.20E-05
	$\sigma$	1.20E-06	2.70E-06	2.40E-06	4.80E-06	4.80E-06	1.10E-06	1.40E-07	4.70E-08	2.50E-06	8.40E-07	5.80E-06
Red marrow	$\mu$	8.10E-06	6.60E-06	8.30E-06	7.50E-06	5.70E-06	9.60E-06	5.90E-06	9.10E-06	8.00E-06	5.60E-06	7.20E-06
	$\sigma$	1.60E-06	1.20E-06	2.20E-06	1.20E-06	1.30E-06	2.20E-06	1.60E-06	1.30E-06	1.60E-06	9.10E-07	1.80E-06
Colon	$\mu$	1.50E-05	1.00E-05	2.10E-05	9.30E-06	1.80E-05	4.90E-07	1.90E-07	1.60E-05	3.20E-06	5.00E-06	9.70E-06
	$\sigma$	3.20E-06	2.00E-06	6.00E-06	1.70E-06	4.30E-06	1.00E-07	3.40E-08	4.10E-06	6.00E-07	9.40E-07	1.90E-06
Lungs	$\mu$	4.70E-06	1.30E-05	6.80E-06	1.60E-05	1.20E-05	1.50E-05	2.80E-06	1.90E-07	3.30E-05	4.20E-06	1.60E-05
	$\sigma$	8.30E-07	2.00E-06	1.70E-06	3.50E-06	2.00E-06	2.50E-06	3.90E-07	3.40E-08	6.10E-06	7.00E-07	3.50E-06
Oesophagus	$\mu$	5.30E-06	1.30E-05	9.90E-06	1.20E-05	1.80E-05	1.00E-04	7.30E-06	1.80E-07	6.10E-05	4.80E-06	1.70E-05
	$\sigma$	7.00E-07	3.10E-06	1.60E-06	2.30E-06	3.10E-06	2.60E-05	1.30E-06	4.00E-08	1.30E-05	8.70E-07	3.40E-06
Brain	$\mu$	9.90E-08	2.30E-07	1.10E-07	2.40E-07	1.80E-07	2.80E-06	1.60E-05	5.60E-09	4.80E-07	4.60E-06	2.90E-06
	$\sigma$	1.30E-08	1.40E-08	1.80E-08	2.20E-08	3.20E-08	2.30E-07	2.30E-06	1.10E-09	4.50E-08	1.10E-06	7.90E-07
Adrenals	$\mu$	1.10E-04	3.40E-05	7.70E-05	5.60E-05	3.00E-05	1.50E-06	5.10E-07	8.90E-07	1.10E-05	4.40E-06	1.60E-05
	$\sigma$	2.80E-05	6.10E-06	6.90E-05	1.70E-05	1.70E-05	1.60E-07	4.10E-08	1.00E-07	2.50E-06	6.90E-07	4.30E-06
Small intestine	$\mu$	1.40E-05	6.00E-06	2.30E-05	6.00E-06	1.10E-05	3.40E-07	1.30E-07	2.10E-05	2.50E-06	5.50E-06	9.90E-06
	$\sigma$	4.20E-06	8.70E-07	1.00E-05	2.20E-06	3.80E-06	1.20E-07	4.50E-08	1.40E-05	8.60E-07	1.10E-06	1.80E-06

Table 10.2. Mean  $\mu$  [ $\text{g}^{-1}$ ] and standard deviation  $\sigma$  [ $\text{g}^{-1}$ ] of SAF input factors distributions for photons.

St-wall denotes stomach wall, S-glands – salivary glands, UB-wall – urinary bladder wall, Ht-wall – heart wall, UB-cont – urinary bladder content, RoB – rest of body.

Target regions	Source regions											
	Kidneys	Liver	Pancreas	Spleen	St-wall	Thyroid	S-glands	UB-cont	Ht-wall	RoB	Blood	
Kidneys	$\mu$	7.60E-04	6.10E-08	1.40E-07	1.20E-07	5.30E-09	1.20E-10	2.60E-11	2.00E-10	1.20E-09	0.00E+00	2.10E-05
	$\sigma$	1.80E-06	5.60E-08	2.80E-07	2.40E-07	2.50E-09	1.80E-11	4.90E-12	4.10E-11	3.00E-10	0.00E+00	7.70E-06
Liver	$\mu$	6.10E-08	1.30E-04	7.30E-08	1.50E-09	1.80E-07	4.00E-10	8.70E-11	7.70E-11	1.50E-08	0.00E+00	1.90E-05
	$\sigma$	5.60E-08	5.20E-07	7.70E-08	4.80E-10	8.10E-08	6.40E-11	1.10E-11	2.40E-11	1.40E-08	0.00E+00	6.60E-06
Pancreas	$\mu$	1.40E-07	7.30E-08	1.70E-03	6.00E-08	1.70E-06	1.70E-10	4.10E-11	1.70E-10	3.20E-09	2.10E-07	1.30E-05
	$\sigma$	2.80E-07	7.70E-08	9.10E-06	1.20E-07	2.20E-06	2.80E-11	1.50E-11	7.00E-11	7.70E-10	3.10E-07	3.90E-06
Spleen	$\mu$	1.20E-07	1.50E-09	5.90E-08	1.60E-03	2.70E-07	4.20E-10	8.10E-11	4.20E-11	4.70E-09	0.00E+00	2.60E-05
	$\sigma$	2.40E-07	4.90E-10	1.20E-07	7.00E-06	5.10E-07	7.00E-11	1.20E-11	1.10E-11	1.80E-09	0.00E+00	9.00E-06
St-wall	$\mu$	5.30E-09	1.80E-07	1.70E-06	2.70E-07	1.50E-03	3.30E-10	7.20E-11	7.60E-11	4.80E-07	0.00E+00	1.50E-05
	$\sigma$	2.50E-09	8.10E-08	2.20E-06	5.20E-07	2.10E-05	6.10E-11	2.10E-11	2.00E-11	3.70E-07	0.00E+00	4.50E-06
Thyroid	$\mu$	8.30E-11	4.20E-10	1.70E-10	4.40E-10	3.10E-10	1.20E-02	4.30E-09	3.00E-12	2.50E-09	0.00E+00	8.70E-06
	$\sigma$	1.50E-11	9.50E-11	3.50E-11	6.90E-11	6.40E-11	4.80E-05	6.30E-10	4.40E-12	3.90E-10	0.00E+00	2.80E-06
S-glands	$\mu$	2.50E-11	8.50E-11	2.90E-11	8.80E-11	6.30E-11	4.10E-09	2.70E-03	1.60E-13	2.80E-10	4.40E-07	1.00E-05
	$\sigma$	8.90E-12	1.40E-11	5.50E-12	3.00E-11	1.50E-11	7.90E-10	1.40E-05	2.60E-13	4.80E-11	5.20E-07	3.30E-06
UB-wall	$\mu$	1.80E-10	6.60E-11	1.40E-10	4.40E-11	6.80E-11	2.40E-12	7.60E-13	4.80E-05	1.40E-11	3.20E-06	1.30E-06
	$\sigma$	5.30E-11	2.20E-11	4.50E-11	1.40E-11	2.20E-11	2.20E-12	1.10E-12	0.00E+00	8.00E-12	3.60E-07	4.30E-07
Ht-wall	$\mu$	1.20E-09	1.50E-08	3.10E-09	4.70E-09	4.80E-07	2.50E-09	2.90E-10	1.50E-11	5.60E-04	4.60E-08	6.10E-06
	$\sigma$	3.10E-10	1.40E-08	7.20E-10	1.90E-09	3.70E-07	3.20E-10	2.80E-11	4.10E-12	1.90E-04	6.50E-08	5.20E-06
Red marrow	$\mu$	6.40E-09	1.30E-08	1.00E-08	8.60E-09	2.40E-09	3.60E-08	2.40E-08	2.00E-08	6.40E-09	3.40E-07	3.50E-06
	$\sigma$	7.10E-09	1.40E-08	1.70E-08	8.20E-09	1.00E-09	7.40E-08	4.20E-08	3.40E-08	2.40E-09	3.60E-07	2.70E-06
Colon	$\mu$	6.80E-08	4.70E-08	1.80E-08	4.80E-08	1.10E-07	5.40E-11	1.50E-11	1.10E-08	6.70E-10	2.40E-06	1.60E-05
	$\sigma$	1.20E-07	4.50E-08	2.20E-08	8.80E-08	1.40E-07	1.70E-11	4.50E-12	1.10E-08	1.80E-10	3.30E-07	5.30E-06
Lungs	$\mu$	1.00E-09	1.50E-07	1.60E-09	1.90E-07	8.80E-08	4.70E-09	4.60E-10	1.20E-11	4.40E-07	1.60E-06	3.10E-05
	$\sigma$	2.10E-10	1.00E-07	5.10E-10	1.50E-07	1.20E-07	9.50E-10	7.50E-11	2.50E-12	2.70E-07	5.50E-07	1.20E-05
Oesophagus	$\mu$	1.20E-09	3.70E-08	2.90E-09	3.50E-09	1.90E-07	2.50E-06	1.70E-09	1.40E-11	1.40E-06	2.60E-06	1.50E-05
	$\sigma$	2.10E-10	3.80E-08	6.70E-10	8.50E-10	3.80E-07	3.00E-06	4.00E-10	3.30E-12	1.40E-06	3.20E-06	4.60E-06
Brain	$\mu$	4.60E-12	1.50E-11	5.60E-12	1.40E-11	1.10E-11	3.30E-10	3.00E-09	1.60E-13	4.00E-11	3.40E-06	2.70E-06
	$\sigma$	6.40E-13	1.40E-12	1.10E-12	1.20E-12	2.00E-12	2.50E-11	5.30E-10	1.30E-13	4.80E-12	4.10E-07	7.20E-07
Adrenals	$\mu$	7.30E-06	4.40E-07	3.20E-06	7.80E-08	1.10E-08	2.00E-10	3.60E-11	7.20E-11	2.80E-09	2.70E-06	1.30E-05
	$\sigma$	5.10E-06	4.30E-07	5.20E-06	1.20E-07	7.00E-09	3.90E-11	1.30E-11	1.90E-11	7.20E-10	3.30E-07	3.90E-06
Small intestine	$\mu$	2.80E-08	3.40E-09	4.50E-07	6.80E-09	1.00E-07	3.60E-11	7.90E-12	8.20E-08	5.10E-10	2.40E-06	1.60E-05
	$\sigma$	2.80E-08	4.40E-09	6.00E-07	1.20E-08	1.20E-07	1.60E-11	4.00E-12	1.30E-07	2.20E-10	3.20E-07	5.10E-06

Table 10.3. Mean  $\mu$  [MeV  $\cdot$  g<sup>-1</sup>] and standard deviation  $\sigma$  [MeV  $\cdot$  g<sup>-1</sup>] of SAF input factors distributions for electrons. St-wall denotes stomach wall, S-glands – salivary glands, UB-wall – urinary bladder wall, Ht-wall – heart wall, UB-cont – urinary bladder content, RoB – rest of body.

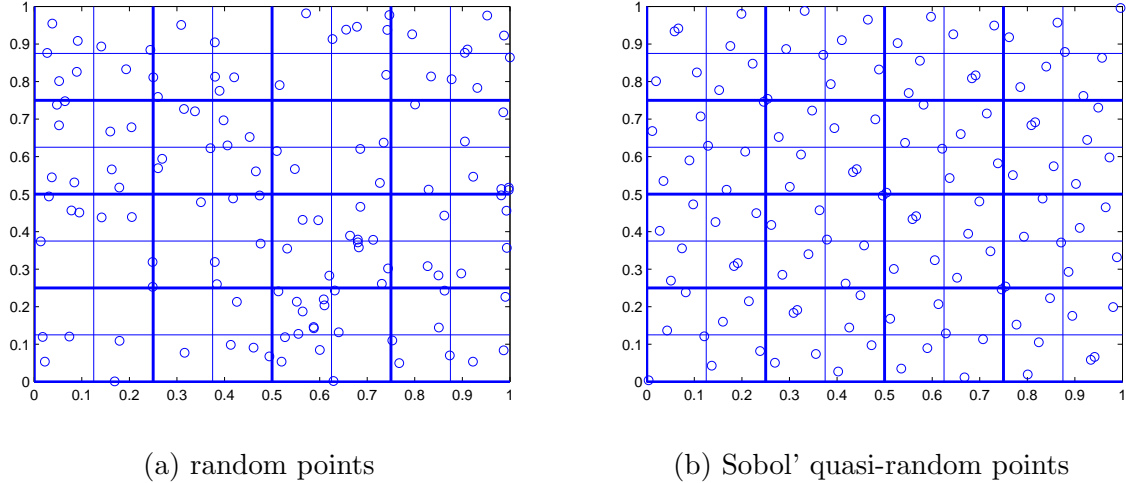


Figure 10.2. (a) 128 points, generated with pseudo-random numbers generator of a personal computer and (b) 128 uniformly distributed quasi-random points, generated with Sobol' low-discrepancy sequence.

As described in section 10.4, the considered model originally included 33 variable input factors: 11 TIACs and 22 SAFs: 11 for photon- and 11 for  $\beta$ -components. For the same source-target pair photon and electron SAFs cannot be considered uncorrelated inputs because they are both dependent on the positions of the source and the target relative to each other. For this reason the same quasi-random numbers were used for sampling the photon and the electron SAFs for the same combination of source and target regions. This decreased the dimensionality of the model from 33 to 22 dimensions.

A MATLAB-based program [106] was employed to generate Sobol' points [105] in a 22-dimensional unit hypercube. These uniformly distributed points were converted to the points from the desired truncated normal distributions with the pre-calculated parameters  $\mu$  and  $\sigma$ , summarized in tables 10.1 – 10.3, using the inverse cumulative density function.

## 10.7. Number of model executions and convergence

An important step, which should be considered in Monte Carlo approaches, is the selection of the sample size. For the purpose of sensitivity analysis the sample size should be high enough to adequately cover the input space and to facilitate the calculation of robust and stable SA indices. At the same time, the number of the sampled input factors defines the number of model executions. Thus, high sample sizes can result in a very computationally intensive SA execution.

In this thesis the number of model runs was set to  $N = 4096$ . Thus  $N = 4096$  Sobol' quasi-random points [105] were generated in a 22-dimensional unit hypercube for each of the independent matrices  $A$  and  $B$  as described in section 10.3. It was verified whether with this sample size the convergence of the computed sensitivity indices  $S_i$  and  $S_{T_i}$  was achieved, i.e. whether  $S_i$  and  $S_{T_i}$  were numerically stable and their values did not change with further increasing the number of model runs. Note that the size of a sample generated with deterministic quasi-random sequences in general and with the Sobol' sequence in particular can be increased if the convergence is not achieved with the originally selected

*10. Application of uncertainty and global sensitivity analysis to internal dosimetry*

number of model executions. The first  $N$  quasi-random (Sobol') numbers (and model executions) in the increased sample remain the same and, thus, they do not require model re-evaluation.

# 11. Effect of input factor variabilities on computed uncertainties of organ dose coefficients

Variance-based global SA was applied in this thesis to internal dosimetry in nuclear medicine, according to the commonly used MIRD system [4]. The effect of changes of all uncertain input factors on the model output was evaluated. The computed uncertainties of the dose coefficients are presented in section 11.1. The convergence of the derived sensitivity indices was verified and the results are shown in section 11.2. Section 11.3 summarizes the results of the SA, i.e. how the variance of the dose coefficients was apportioned to the uncertain input factors.

## 11.1. Uncertainty of computed dose coefficients

The uncertainties in the absorbed dose coefficients for various target regions were computed as part of the Monte Carlo-based SA approach implemented in this thesis. Two sources of uncertainties were investigated: the inter-individual differences in the cumulated activities and the differences between the anatomical models employed in the dosimetry.

The box plot distributions of the computed absorbed dose coefficients and the weighted dose coefficient are presented in figure 11.1. Each sample in figure 11.1 includes  $2N = 8192$  dose coefficients, i.e. model outputs evaluated with two independent matrices  $A$  and  $B$  of sampled input factors (see section 10.3). The boxes comprise 25 and 75 % percentile, the red horizontal lines show the medians of the calculated  $2N = 8192$  dose coefficients. It can be seen in figure 11.1 that no outliers were observed. The red crosses present those 0.7 % of the values that are at the tails of the calculated distributions of absorbed dose coefficients and weighted dose coefficient. Often to describe a spread of values in a sample standard deviation is used, which for normally distributed values includes approximately 68 % of them. The standard deviations of the distributions of the dose coefficients from figure 11.1 are presented in figure 11.2. Figure 11.2 also shows mean values and relative uncertainties of the computed absorbed dose coefficients and the weighted dose coefficient. The relative uncertainty in weighted dose coefficient amounted to approximately 10 %. Since this value effectively averages several absorbed dose coefficients and the variability in the tissue weighting factors was not considered, the expected uncertainty in the weighted dose coefficient is lower than that in the individual absorbed dose coefficients. The computed relative uncertainties in the absorbed dose coefficients were between 10 % for urinary bladder wall and 30 % for heart wall. These uncertainties were caused by inter-individual differences in TIACs and inter-phantom differences in SAFs (as shown in tables 10.1–10.3 on pages 108–110).

The uncertainty in the absorbed dose coefficient for bladder wall was the lowest, since the same values of  $\text{SAF}(UB_{\text{wall}} \leftarrow UB_{\text{cont}})$  calculated by Andersson et al. [33] were used for

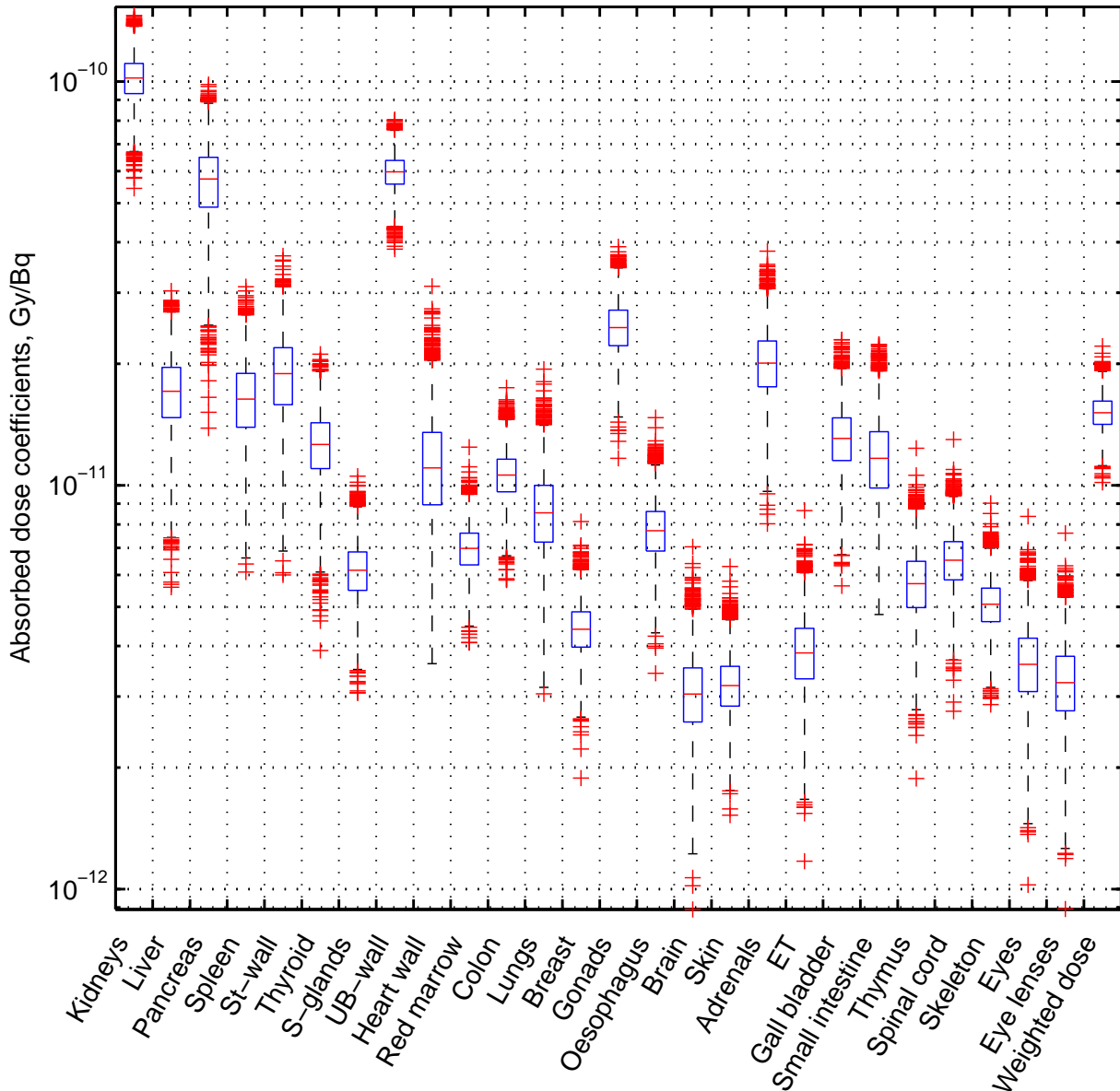


Figure 11.1. Box plot of computed dose coefficients. Each sample includes the results of  $2N = 8192$  model executions. The tops and bottoms of the boxes correspond to 25-th and 75-th percentiles of the samples, respectively. Red horizontal lines are the medians. The ranges of the whiskers include 99.3 % of the points. The points outside these ranges are shown as red crosses. St-wall is stomach wall, S-glands – salivary glands, UB-wall and ET denotes urinary bladder wall and extrathoracic airways, respectively.

all phantoms (see section 10.4). Thus, the variability of the output in this case was caused predominantly by the variability of the cumulated activities in the bladder contents. The utilization of  $\text{SAF}(UB_{\text{wall}} \leftarrow UB_{\text{cont}})$  derived by Andersson et al. [33] was more appropriate here rather than the usage of the corresponding phantom-specific values. For a certain type of radiation and energy, the above mentioned SAFs are dependent on the volumes of the bladder content and the thickness of the bladder wall. Thus, if the phantom-specific values of  $\text{SAF}(UB_{\text{wall}} \leftarrow UB_{\text{cont}})$  were used, the differences in the bladder volumes segmented in

the phantoms and in the thickness of the bladder wall, which is often limited by the voxel size, would introduce additional artificial variation in the SAF input factors. The highest uncertainty was observed for heart wall absorbed dose coefficient. The reason for this was a high inter-individual difference in the TIAC(Heart wall). Additionally, heart wall of two phantoms was surrogated by whole heart. This is another possible reason for the large observed uncertainty for the heart wall dose coefficient.

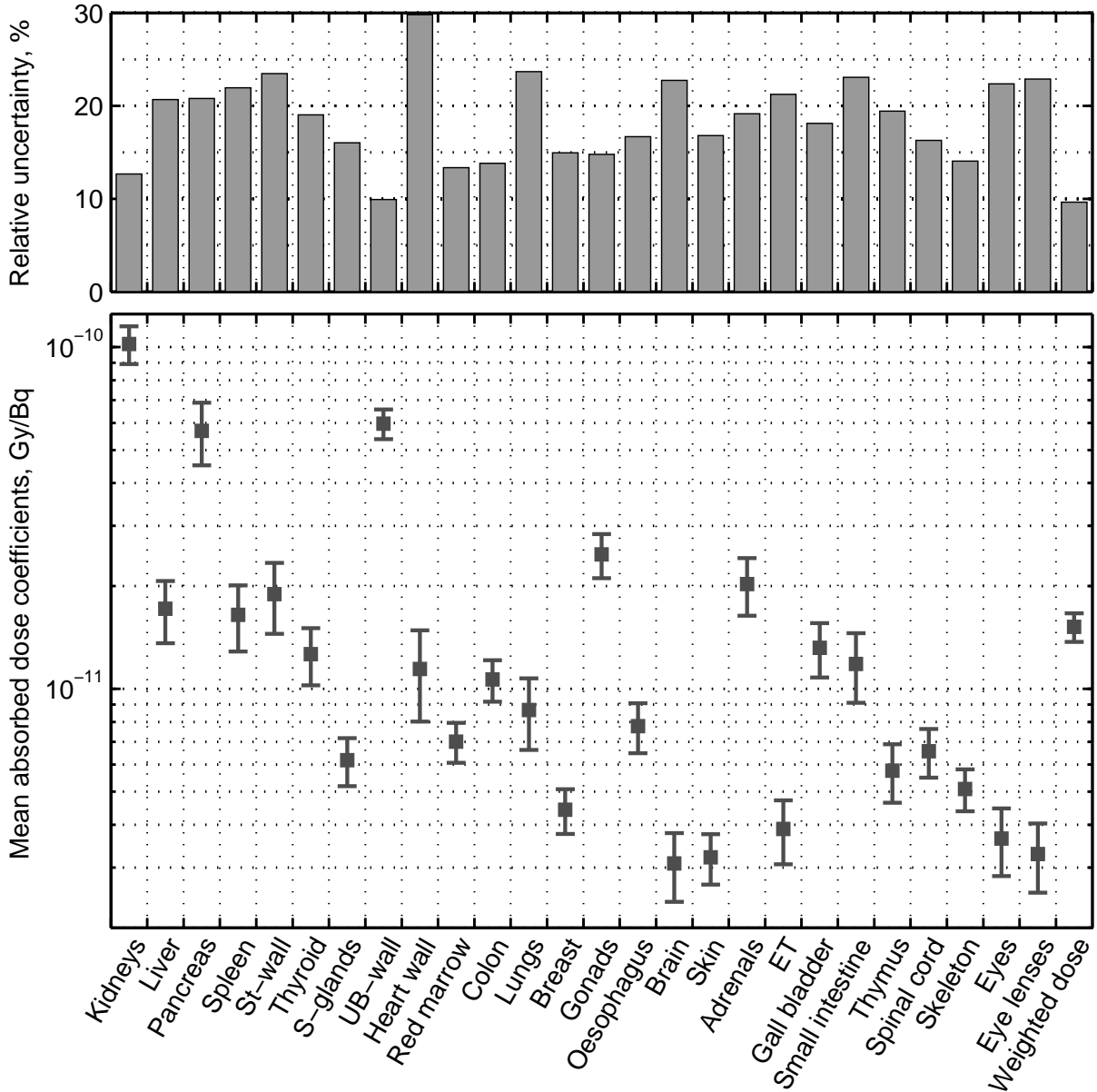


Figure 11.2. Computed dose coefficients along with their uncertainties. Error bars on the lower panel represent standard deviations of the respective dose coefficients. Relative uncertainty on the upper panel is defined as one standard deviation of the respective sample divided by the sample mean (see equation 10.5). The SAFs are mass-scaled to the reference masses of RCP-AM. St-wall denotes stomach wall, S-glands – salivary glands, UB-wall – urinary bladder wall, ET – extrathoracic airways.

The TIACs were computed via integration under the time-activity curves predicted by personalized pharmacokinetic models developed in the scope of this thesis and described in chapter 5. The pharmacokinetic models were assumed to be fixed. Thus, the uncertainties associated with the model structure, image acquisition, activity quantification from PET images and collected blood samples were not a part of the SA in this work. The variability of the tissue weighting factors [34] employed in the computation of weighted dose coefficients was not considered. Xie and Zaidi [107] investigated another source of uncertainty in the computed organ doses associated with respiratory motion. Despite this effect being negligible for most organs considered in the study of Xie and Zaidi [107], the authors showed few cases where it can be perceptible. Including all aforementioned uncertainties into the variance-based SA would be of high interest, however it goes beyond the scope of this thesis.

The applied uncertainty analysis is an intrinsic procedure of the SA implemented in this thesis. It facilitates the computation of variances of the dose coefficients caused by simultaneous changes of all input factors. As suggested by Saltelli et al. [97], Sobol' sequence was employed for the sampling of the input factors, since, as a low-discrepancy sequence, it facilitates good coverage of the input space. Consequently, for the considered input factors and their assigned variability, the possibly full ranges of output variations were computed and shown in e.g. figure 11.1.

## 11.2. Convergence of sensitivity indices

The convergence of the first-order effect sensitivity indices and the total effect sensitivity indices computed with  $N = 4096$  model executions was verified. Figures 11.3 and 11.4 show the calculated SA indices for the absorbed dose coefficient for spleen and brain, respectively, depending on the number of model executions. As it can be seen from these figures, with a small number of model runs the SA indices are not stable and large fluctuations occurred. Nonetheless, both first-order  $S_i$  and total effect  $S_{T_i}$  indices converge relatively fast. For the output absorbed dose coefficient for spleen about 800 model runs were sufficient to achieve the convergence of  $S_i$  and  $S_{T_i}$ . For the output absorbed dose coefficient for brain the convergence of  $S_i$  and  $S_{T_i}$  was achieved later than for spleen. Nonetheless, the used number of model executions  $N = 4096$  was sufficient to ensure the convergence of the SA indices for brain and all other considered outputs.

Figure 11.3 demonstrates that for spleen, which is a source region for the considered radio-pharmaceutical  $^{18}\text{F}$ -FSPG,  $\text{TIAC}(\text{spleen})$  is the most influential parameter for the variability of the absorbed dose coefficient with  $S_i[\text{TIAC}(\text{spleen})] = S_{T_i}[\text{TIAC}(\text{spleen})] = 0.67$ . The influence of  $\text{SAF}(\text{spleen} \leftarrow \text{blood})$  is also shown in figure 11.3 ( $S_i[\text{SAF}(\text{spleen} \leftarrow \text{blood})] = 0.17$  and  $S_{T_i}[\text{SAF}(\text{spleen} \leftarrow \text{blood})] = 0.18$ ). This result is consistent with the fact of spleen being a highly vascularized organ. It can be seen from figure 11.3 that no higher order effects were observed in this case, since the computed total effect SA indices are approximately equal to the respective first-order effect indices (see subsection 9.2.4 on page 101). Brain is not a source region for  $^{18}\text{F}$ -FSPG. Thus the dose absorbed in the brain is due to the energy released by other organs and tissues – source regions. Since brain is located distantly from the local sources, the influential input factors for the variance of the absorbed dose coefficient for brain (figure 11.4) were  $\text{TIAC}(\text{RoB})$  and  $\text{SAF}(\text{brain} \leftarrow \text{RoB})$ .  $S_i[\text{TIAC}(\text{RoB})] = 0.51$ ,  $S_{T_i}[\text{TIAC}(\text{RoB})] = 0.52$ ,  $S_i[\text{SAF}(\text{brain} \leftarrow \text{RoB})] = 0.40$  and  $S_{T_i}[\text{SAF}(\text{brain} \leftarrow \text{RoB})] = 0.41$ .

Fast convergence of the computed sensitivity indices was shown. The considered number

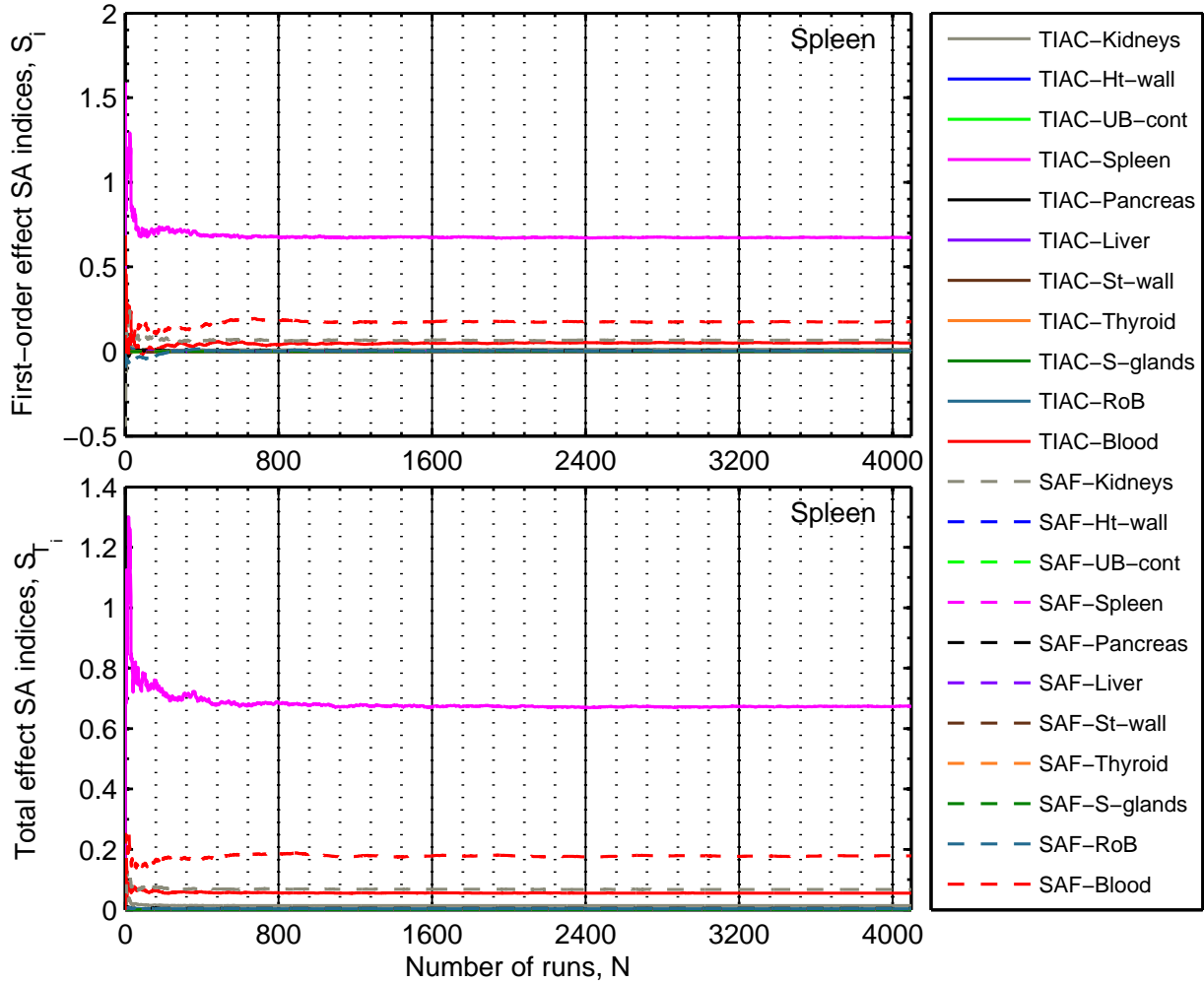


Figure 11.3. Convergence plots for the first-order  $S_i$  (top) and the total effect  $S_{T_i}$  (bottom) SA indices for absorbed dose coefficient for spleen as output. The upper and the lower panels of the plot show the dependence of the computed values of  $S_i$  and  $S_{T_i}$ , respectively, on the number of model runs. Each panel contains 22 convergence curves. Each convergence curve corresponds to one of the 22 considered input factors: 11 TIAC (solid lines) and 11 SAF (dashed lines) input factors. The list of the 22 considered input factors is shown in the rightmost box. Ht-wall stands for heart wall, UB-cont for urinary bladder content, St-wall for stomach wall, S-glands for salivary glands and RoB for rest of body. TIAC(spleen) (magenta solid line) has the highest contribution to the variance of absorbed dose coefficient for spleen, SAF(spleen  $\leftarrow$  blood) (red dashed line) has a notable contribution, whereas the contributions of other inputs are negligibly low. Note that SAF(spleen  $\leftarrow$  spleen) of all phantoms were corrected to correspond to the mass of spleen in RCP-AM.

of model evaluations  $N = 4096$  assured the stability of the presented values  $S_i$  and  $S_{T_i}$ . Due to the relative simplicity of the studied model and the used implementation the pure execution time of the SA with  $N = 4096$  runs on a 3.10 GHz computer was approximately 0.05 seconds.

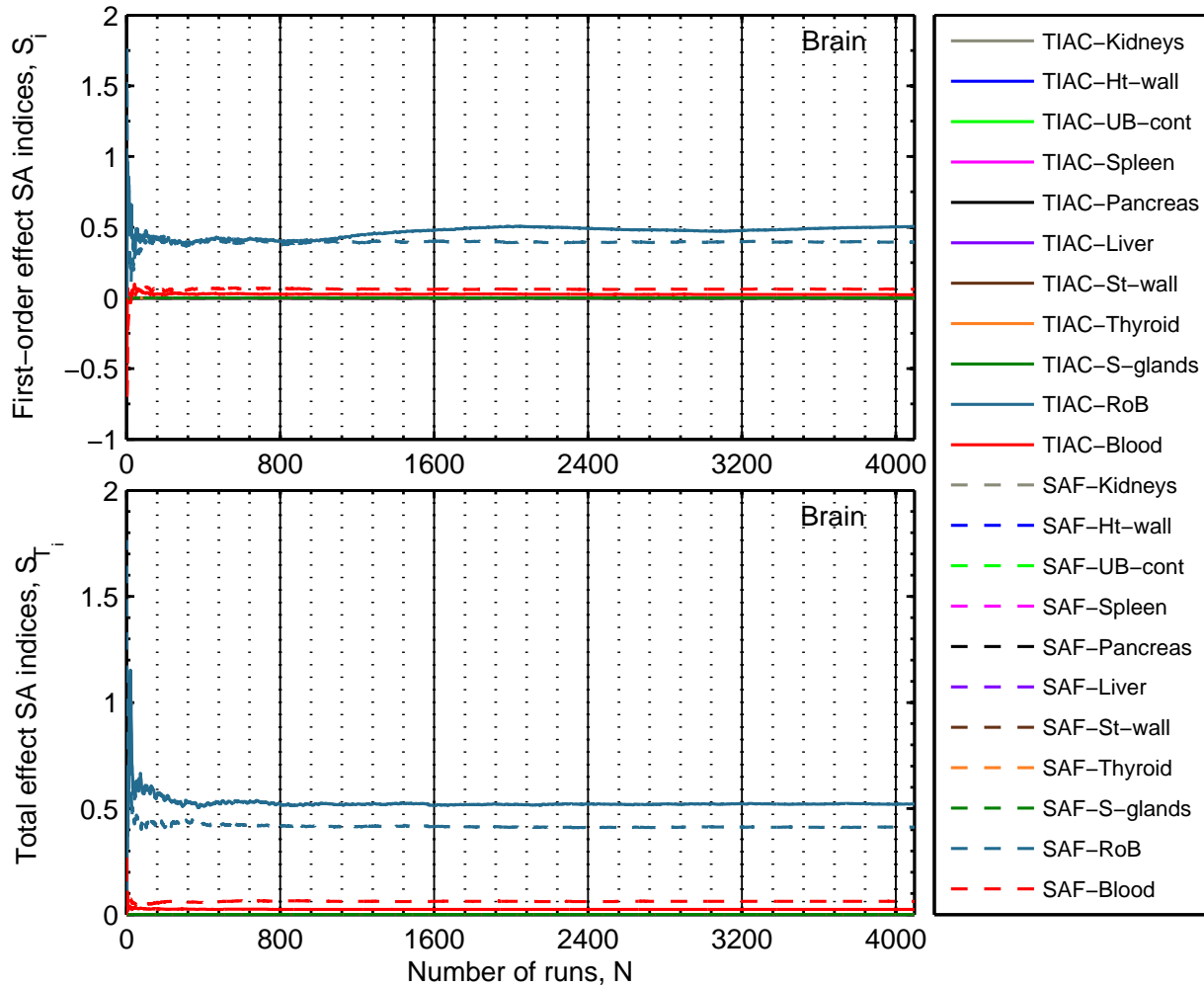


Figure 11.4. Analogue to figure 11.3, convergence plots for the first-order  $S_i$  (top) and the total effect  $S_{T_i}$  (bottom) SA indices for absorbed dose coefficient for brain as output. The rightmost box shows the list of the 22 considered input factors. TIAC(RoB) (turquoise solid line) and SAF(brain  $\leftarrow$  RoB) (turquoise dashed line) are the two influential input factors for the variance of absorbed dose coefficient for brain. The contributions of other inputs are negligibly low.

### 11.3. Effect of input factors on variability of dose coefficients

There are several possible ways to illustrate the sensitivity. One of them is a graphical representation using scatter plots. Each point in a scatter plot represents an output calculated with one sampled vector of input factors. As it is described in sections 10.4–10.6, in this thesis such input vector has the length of 22:  $(TIAC_1, TIAC_2, \dots, TIAC_{11}, SAF_1, SAF_2, \dots, SAF_{11})$ . A subset of scatter plots and the computed respective sensitivity indices for the absorbed dose coefficients for small intestine wall and lungs are presented in figures 11.5 and 11.6, respectively. Each subplot of figure 11.5 and figure 11.6 contains  $N = 4096$  points. If  $S_i = 0$ , it means that there is no main dependence between the respective input variability and the variance of the output. In this case the scatter plot looks like a “cloud” and no correlation

can be observed. The more prominent patterns in the scatter plots correspond to the more influential input factors, making such plots a convenient graphical representation of the sensitivity.

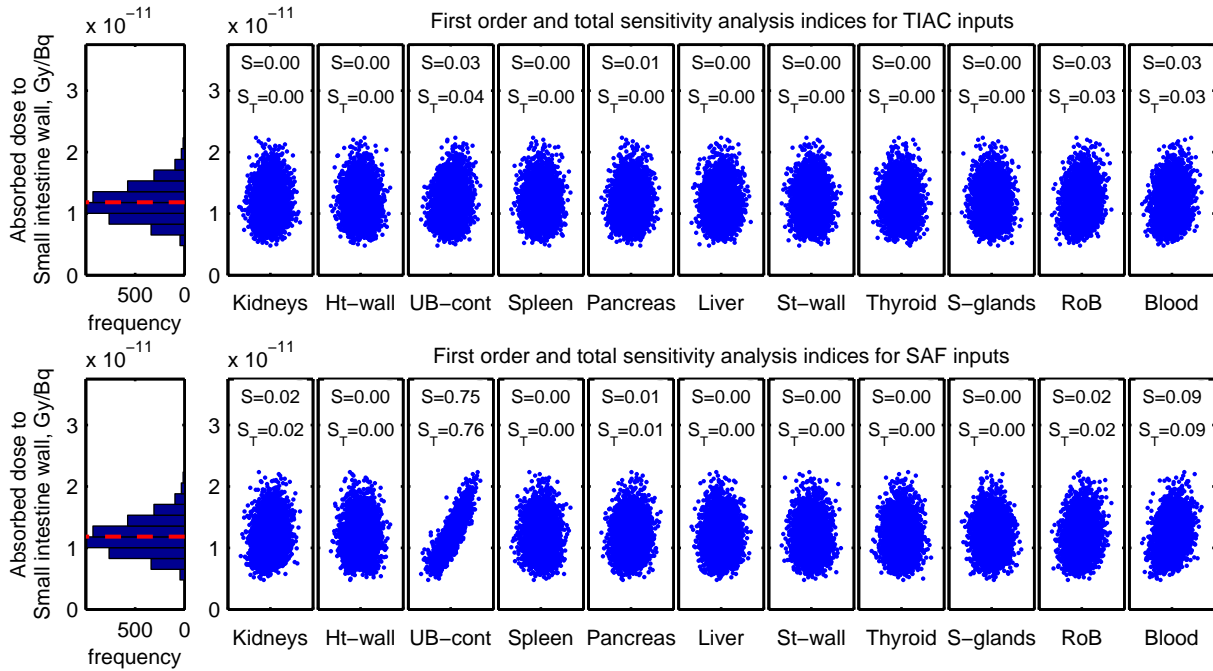


Figure 11.5. Scatter plots, sensitivity indices and distribution of absorbed dose coefficient for small intestine wall. Upper row corresponds to the TIAC inputs, lower row to the SAF inputs. The values  $S$  and  $S_T$  are the first-order and the total effect sensitivity indices, respectively. The histogram displays the distribution of the output dose coefficient. The mean value of the computed absorbed dose coefficient for small intestine wall is marked with red dashed line.

Being target regions and not sources, small intestine wall and lungs receive radiation doses from the cross-fire from other source regions. The example in figure 11.5 shows that the variability of the output is mainly caused by the variability in the cross-fire SAFs from the sources located in the close proximity, e.g. SAF(small intestine  $\leftarrow$  UB<sub>cont</sub>) for absorbed dose coefficient for the small intestine wall, where  $S_i[\text{SAF}(\text{small intestine} \leftarrow \text{UB}_{\text{cont}})] = 0.75$  and the corresponding total effect SA index  $S_{T_i}$  is 0.76. For lungs, as for a target region with substantial mass fraction of blood, notable effect of SAF( $r_T \leftarrow$  blood) and TIAC(blood) is shown and quantitatively expressed via computed  $S_i$  and  $S_{T_i}$  values in figure 11.6:  $S_i[\text{SAF}(r_T \leftarrow \text{blood})] = 0.71$ ,  $S_{T_i}[\text{SAF}(r_T \leftarrow \text{blood})] = 0.73$ ,  $S_i[\text{TIAC}(\text{blood})] = 0.19$  and  $S_{T_i}[\text{TIAC}(\text{blood})] = 0.21$ .

Figure 11.7 shows the scatter plots and the distribution of the absorbed dose coefficient for kidneys. Kidneys are a source region for  $^{18}\text{F}$ -FSPG. SAF(kidneys  $\leftarrow$  kidneys) were mass-scaled (see subsection 7.4.1 on page 76) to the reference mass of kidneys. The variance of the absorbed dose coefficient for kidneys was solely caused by the variability of TIAC(kidneys) with  $S_i[\text{TIAC}(\text{kidneys})] = S_{T_i}[\text{TIAC}(\text{kidneys})] = 0.98$  (see also the prominent pattern in the corresponding scatter plot in figure 11.7).

Figure 11.8 shows the first-order effect sensitivity indices for all considered target regions. Each horizontal line in figure 11.8 contains  $S_i$  in color-codes for all input factors and a

11. Effect of input factor variabilities on computed uncertainties of organ dose coefficients

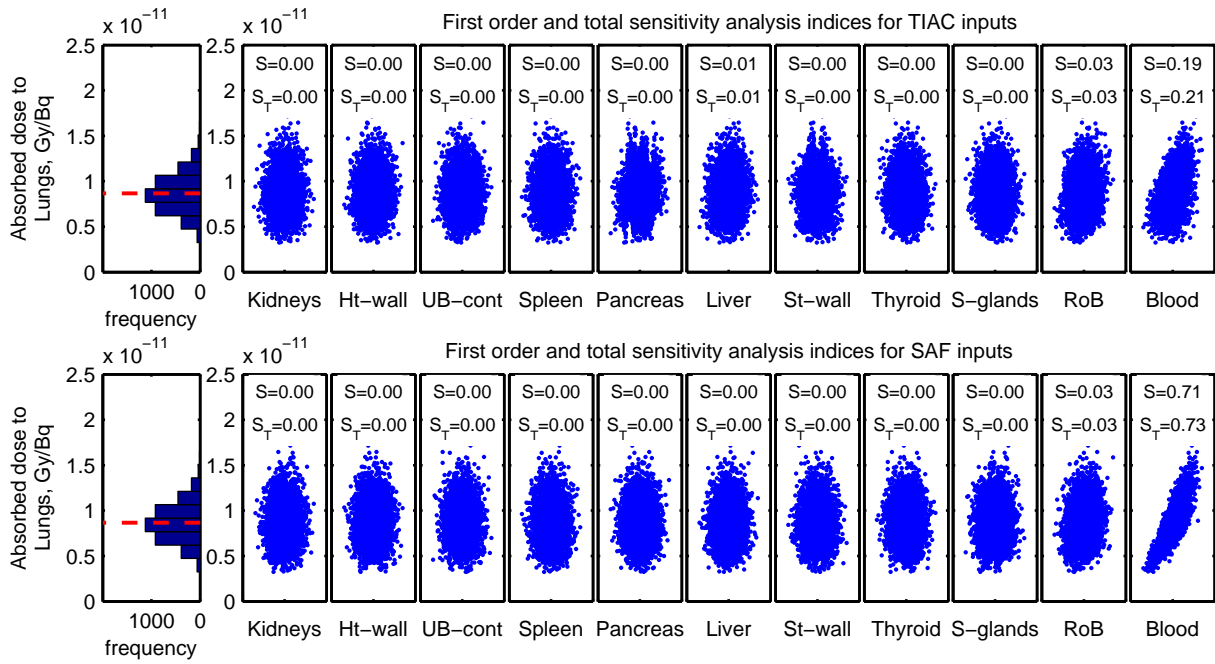


Figure 11.6. Analogue to figure 11.5, scatter plots, sensitivity indices and distribution of absorbed dose coefficient for lungs. The mean value of the computed absorbed dose coefficient for lungs is marked with red dashed line.

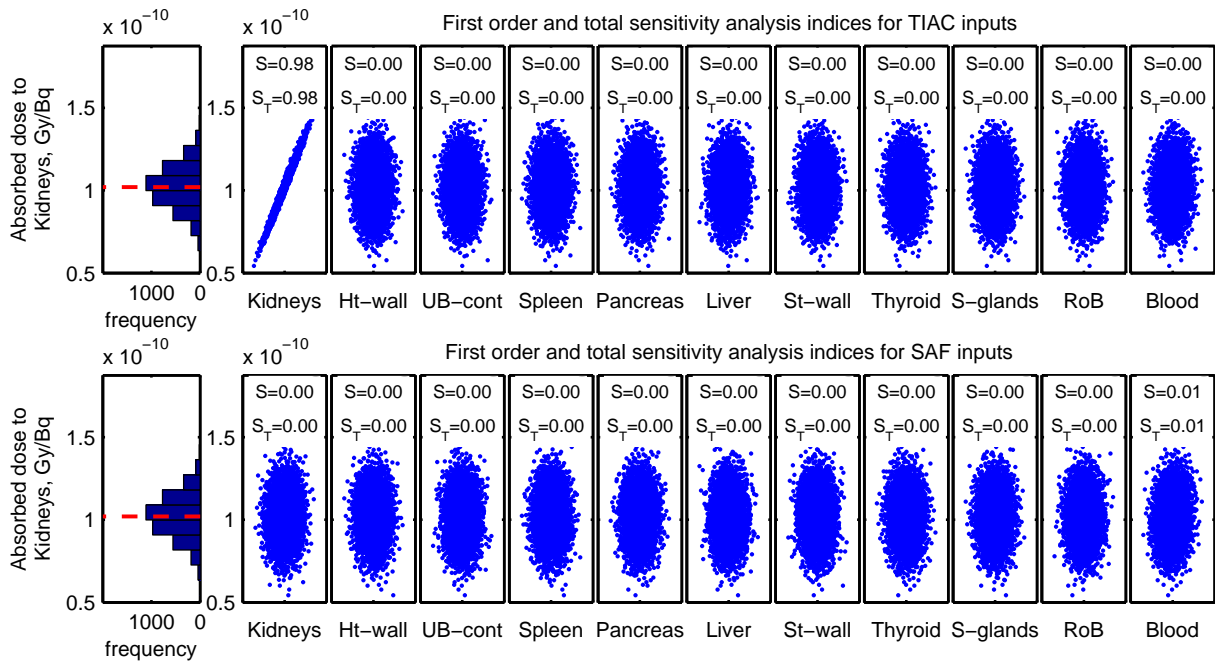


Figure 11.7. Analogue to figure 11.5, scatter plots, sensitivity indices and distribution of absorbed dose coefficient for kidneys. The mean value of the absorbed dose coefficient for kidneys is marked with red dashed line. Note that SAF(kidneys ← kidneys) of all phantoms were corrected to correspond to the mass of kidneys in RCP-AM.

selected output. Figure 11.8 breaks down the uncertainty of each output dose coefficient presented in figure 11.2 on page 115 into parts caused by the variability of each input factor. In figure 11.8 these contributions are numerically expressed by the corresponding  $S_i$ .

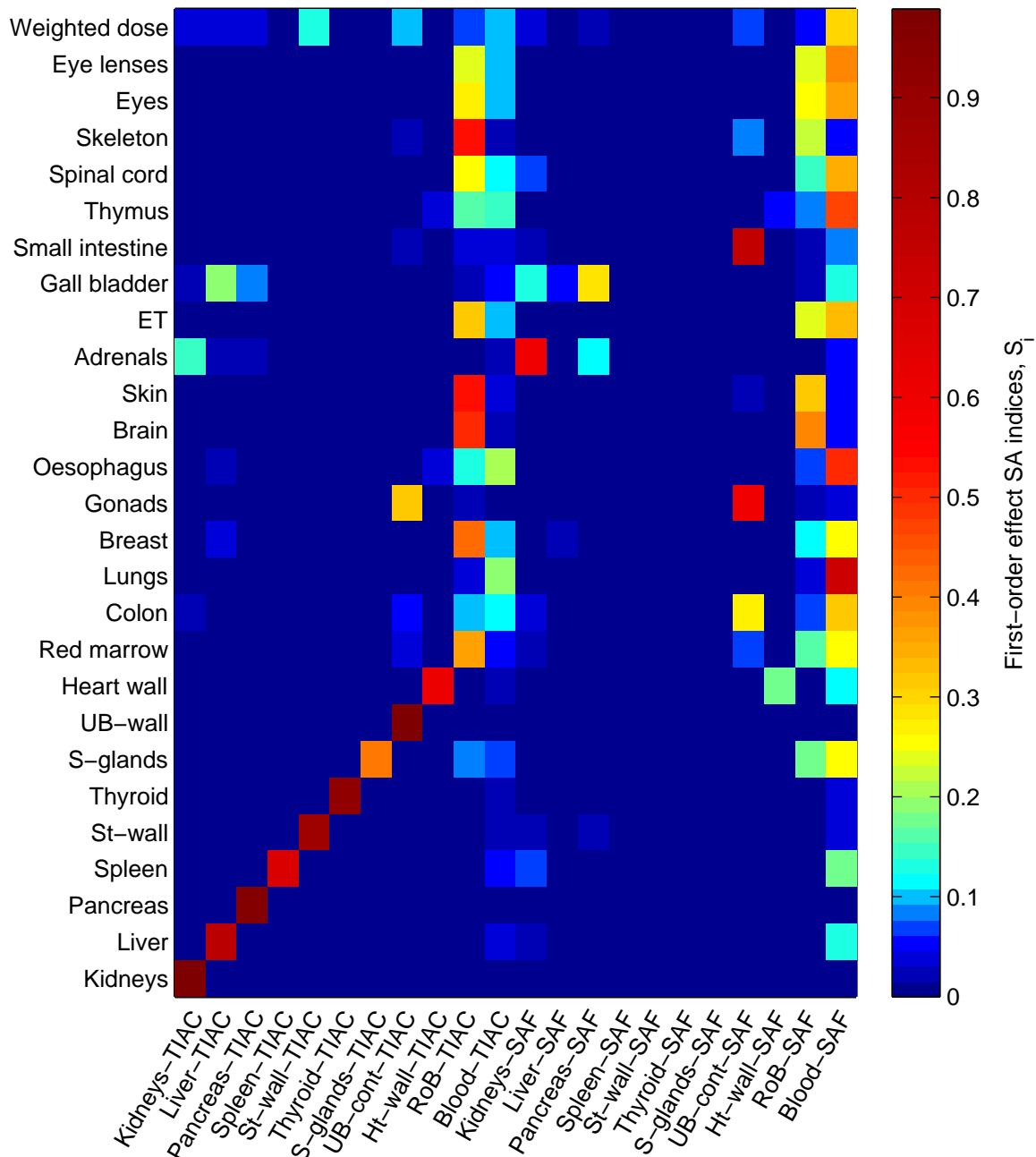


Figure 11.8. First-order effect sensitivity indices for all considered outputs. Each horizontal line in this figure contains  $S_i$  in color-codes for all input factors and a selected output. The input factors are plotted from left to right and the output target regions from bottom to top.  $S_i = 0$  means no main effect of the corresponding input factor.  $S_i = 1$  means that the variability of the output is solely caused by the variability of the corresponding input factor.

The computed total effect sensitivity indices were similar to those of the first-order and, thus, are not presented here but included in appendix B instead. The similarity of main

and total effect sensitivity indices indicates that no substantial higher order effects were observed in the model. Another indication of the absence of notable higher order effects in the studied model is that  $\sum_{i=1}^{2k} S_i \approx 1$ .

Several trends can be seen from figure 11.8. The uncertainty of the computed doses for the source regions is predominated or, in some cases, solely defined by the variability in the activities accumulated in the respective source regions (see the diagonal line of high  $S_i$  in the lower left corner of figure 11.8). For some  $r_T = r_S$ ,  $S_i[\text{TIAC}(r_T=r_S)] \geq 0.9$ . For the considered relatively low energies (511 keV for annihilation photons and, respectively, mean and maximum energies of the  $\beta$ -spectrum of  $^{18}\text{F}$  equal to 249.8 keV and 633.5 keV) the dose absorbed in the source region is mainly due to the self-absorption in this region. The applied mass-scaling of the self-absorption SAF eliminated the inter-phantom differences in these values and thus the variability in the output dose coefficients for the source regions was mainly caused by the variability in the respective TIACs. Thus the accurate determination of the absolute activities in the source regions substantially improves the accuracy of the computed absorbed dose coefficients for the source regions. It also implicitly includes the estimation of the source region masses needed for mass-scaling of the self-absorption SAF.

The results show that for the target regions, which are not sources, the most influential factors for the variability of the computed doses are the cross-fire SAFs from closely located sources. Thus, e.g. the variability in  $\text{SAF}(\text{adrenals} \leftarrow \text{kidneys})$  had the greatest impact on the uncertainty of the absorbed dose coefficient for adrenals ( $S_i[\text{SAF}(\text{adrenals} \leftarrow \text{kidneys})] = 0.6$ ) and the variability in  $\text{SAF}(r_T \leftarrow \text{UB}_{\text{cont}})$  on the absorbed dose coefficients for small intestine ( $S_i[\text{SAF}(\text{small intestine wall} \leftarrow \text{UB}_{\text{cont}})] = 0.75$ ), gonads ( $S_i[\text{SAF}(\text{gonads} \leftarrow \text{UB}_{\text{cont}})] = 0.59$ ) and colon wall ( $S_i[\text{SAF}(\text{colon wall} \leftarrow \text{UB}_{\text{cont}})] = 0.27$ ). To a lesser extent but nonetheless substantial was the influence of the integrated activities accumulated in the source regions located in close proximity, e.g. for adrenals and gonads,  $S_i[\text{TIAC}(\text{kidneys})] = 0.14$  and  $S_i[\text{TIAC}(\text{UB}_{\text{cont}})] = 0.32$ , respectively.

For the targets that do not have high blood contents and are located distantly from the source regions, e.g. eyes, eye lenses, skeleton, skin, extrathoracic airways (ET) or brain, the variability of  $\text{TIAC}(\text{RoB})$  was an important factor, contributing to the uncertainty of the absorbed dose coefficients (see figure 11.8).

For the organs with substantial mass fractions of blood or located very close to highly vascular organs, e.g. lungs, oesophagus, thymus, spinal cord, extrathoracic airways, eye lenses, eyes, colon etc., the sensitivity indices for the input factors  $\text{SAF}(r_T \leftarrow \text{blood})$  and  $\text{TIAC}(\text{blood})$  amount to high values (see figures 11.6 and 11.8). This illustrates the importance of an accurate determination of  $\text{SAF}(r_T \leftarrow \text{blood})$  and the blood activities in dosimetric studies in nuclear medicine. The values of  $\text{SAF}(r_T \leftarrow \text{blood})$  are independent on the relative positions of organs in anatomical models though. They are defined by the blood contents of the respective organs  $r_T$ . This shows that the determination of the individual blood contents of organs has the potential to notably decrease the uncertainty of the computed absorbed doses for highly vascular organs and organs closely located to them.

Each output absorbed dose coefficient had its own set of influential input factors. The sensitivity indices cannot be compared between different outputs though. They allow ranking the input factors according to their effect only on a particular output dose coefficient. Since the absolute values of the absorbed dose coefficients notably vary for different target regions, it is convenient to operate with a value that includes absorbed dose coefficients of various organs and takes into account the differences in the absolute computed dose coefficients. This was the purpose of computing a specific value denoted as weighted dose coefficient

in the text. The SA was also applied to this artificial value to identify the input factors which have the highest effect on the value similar to a risk-weighted average body dose. The computed weighted dose coefficient was an adequate estimate for the effective dose coefficient. Only few target regions were excluded: endosteum, lymphatic nodes, oral mucosa, muscle tissue, prostate and uterus. Since these organs and tissues are not source regions for the considered radiopharmaceutical  $^{18}\text{F}$ -FSPG, the expected absolute absorbed dose coefficients for them are not very high. The corresponding tissue weighting factors are also relatively low (0.01 for endosteum, and the other regions are parts of the reminder tissues). The input factor  $\text{SAF}(r_T \leftarrow \text{blood})$  had the highest effect on the variability of the weighted dose coefficient with  $S_i = S_{T_i} = 0.31$ . Each of the uncertain input factors  $\text{TIAC}(St\text{-wall})$ ,  $\text{TIAC}(UB_{\text{cont}})$ ,  $\text{TIAC}(\text{blood})$ ,  $\text{TIAC}(\text{RoB})$  and  $\text{SAF}(r_T \leftarrow UB_{\text{cont}})$  accounts for approximately 10 % of the variability of the weighted dose coefficient.

Six anatomical models representing slim, reference and overweight individuals were employed in this thesis to construct the distributions of the SAF input factors. The models covered the range in the BMI from 19.2 kg/m<sup>2</sup> to 31.9 kg/m<sup>2</sup>. Although it cannot be claimed that all possible anatomic variations were covered, the considered inter-phantom differences were not limited to the six employed models. The tails of the normal distributions assigned to the input factors covered a broader range of SAFs than that of the six considered phantoms. The Sobol' sequence ensured the sampling of the input factors also from the less probable areas of the input space. The same holds here for the variations of the TIAC input factors, whose distributions were constructed based on the activity data from five volunteers. Thus it is reasonable to assume that the considered differences in the input factors are an adequate estimate for their variability.

It is important to use in the SA computational phantoms with all required regions segmented and blood properly distributed in various body organs. Otherwise additional artificial variations in the SAF input factors could be introduced and lead to different and possibly inadequate results of the SA. For this reason no organ surrogates, besides a whole heart for a heart wall, were used in part IV of this thesis and organs that are not present in one or more phantoms were omitted.

The activity data of a radiopharmaceutical designated for PET diagnosis were employed in this thesis. Since the diagnostic investigations are associated with low to moderate doses, individualized dosimetry is less relevant for this case, compared to therapy. Nonetheless, the applied SA method and the developed framework and computer programs do not depend on the clinical purpose of the radiopharmaceutical and can be applied equally for therapeutic agents.

In this thesis the effect of changes of all uncertain input factors on model output was evaluated by means of variance-based global SA. This method effectively explores the input space and allows studying the interplay effects of any possible simultaneous perturbations of the inputs on the variance of the model output. Additionally, it does not require the studied model to be analytical. Therefore the variance-based global SA is superior compared to more frequently used "one-factor-at-a-time" SA or Gaussian error propagation. The global SA implemented in this thesis is a model-independent method, accompanied by an uncertainty analysis as part of its procedure. All these properties make the variance-based global SA a convenient and powerful procedure used to assess the quality of a model-based study.



## **Part V.**

### **Summary and conclusion**



## 12. Summary

This chapter highlights the motivation and the objective of this thesis, the main developments done in the scope of this thesis and the most important results.

- Personalized internal dosimetry potentially increases the success of radionuclide therapy. In diagnostic nuclear medicine applications, it has a potential to reduce late negative effects of the radiation. Individualized dosimetry is also required for epidemiological studies in nuclear medicine. Theoretically, personalized internal dosimetry is a straight-forward process, since there is a clear formalism of how it is to be done. In practice, it is very difficult to implement, though. Advanced modeling procedures needed for individual dose assessment in nuclear medicine are not viable for each patient, due to high time and effort costs. Consequently, internal doses are estimated for available reference models and these values are applied to individual patients. The accuracy of these estimations is limited.
- A comprehensive analysis was carried out in the scope of this thesis to evaluate the variability in organ doses between reference models and individual patients. To facilitate this analysis, advanced modeling procedures such as pharmacokinetic modeling and anatomical modeling were implemented and evaluated.
- Individual pharmacokinetic models were established for five healthy volunteers administered with a novel diagnostic PET tracer. Based on these models, the inter-individual variability in pharmacokinetics was analyzed and quantified for time-integrated activity coefficients – the first group of input factors required for internal dose calculation.
- One of the important findings of this thesis is that the way how blood is treated in pharmacokinetic modeling and internal dosimetry notably influences the computed organ doses for highly vascular organs, which are not source regions. Blood should be considered as a distinct source region to facilitate more physiologically meaningful modeling and subsequent dosimetry. Therefore, blood samples should be collected and their activity should be measured in all pharmacokinetic and dosimetric studies for radiopharmaceuticals.
- The individual patient anatomy also limits the accuracy of internal dose estimates. To capture the differences in organ doses caused by the inter-individual variations in anatomy, the polygon-surface ICRP adult male model was scaled to fit selected dimensions of patients. These dimensions comprised the distance between the iliac crest and the clavicles, total height, front-to-back distance and width of the rib cage. The implemented scaling requires less effort than is needed for the detailed segmentation of a patient.
- Two computational phantoms were generated with the implemented anatomical modeling: a slim and an overweight individual. These models along with two reference

## 12. Summary

computational phantoms and two other available models of slim and overweight individuals from the HMGU library were used to evaluate and quantify the variability in specific absorbed fractions – the second group of input factors required for internal dosimetry. It was shown that the estimation of individual patient organ doses with the developed scaling is possible within 25 % of error, whereas employing reference phantoms without any scaling applied patient organ doses were estimated with about 50 % relative uncertainty.

- Variance-based sensitivity analysis was implemented in this thesis and applied to dosimetry in nuclear medicine applications for the first time. This approach facilitated an assessment of the variance of dose coefficients caused by inter-individual variations in pharmacokinetics and differences in anatomy. Variance-based sensitivity analysis allowed to break-down the variances of the dose coefficients into fractions caused by different input uncertainties.
- By means of variance-based sensitivity analysis the input factors which have the greatest impact on the variance of dose coefficients were identified in the scope of this thesis. It follows that accurate determination of the time-integrated activity coefficients in the source regions accompanied by the estimation of individual source region masses and the usage of an appropriate blood distribution in a patient's body have the potential to substantially decrease the variance of computed dose coefficients in nuclear medicine. For some organs located in close proximity to the source regions the cross-fire specific absorbed fractions have an impact as well.

The presented work proposes a method of physiologically meaningful modeling of blood activity in pharmacokinetic studies. It shows feasibility of reducing the difference in estimated doses in nuclear medicine caused by anatomical differences between the patient and a reference phantom. The approach proposed for this aim could be a good trade-off between effort and accuracy and has the potential to be directly applicable in medical practice. This thesis provides powerful tools, which facilitate the uncertainty analysis of internal dosimetry and allow ranking the inputs according to their impact on the variance of dose coefficients. The developed methods offer the possibility to reduce the uncertainty of estimated doses in nuclear medicine and, consequently, to provide more reliable dose estimates. Overall these findings give a potential to move from current reference internal dosimetry towards personalized dosimetry in nuclear medicine applications.

## 13. Conclusion

Several advanced modeling procedures were implemented in this thesis to facilitate a comprehensive study on how to decrease the difference between reference internal doses and individual-specific doses in nuclear medicine by practically viable methods. Ways to enhance the reliability of internal dose estimates were studied and led to several recommendations. Due to the demonstrated high impact of blood activity on organ doses, the measurement protocols for pharmacokinetic and dosimetric studies should include the collection of blood samples and the assessment of their activity. Subsequently blood should be considered as a distinct source region. This increases the accuracy of internal dose estimates. Inter-individual differences in anatomy also limit the accuracy of internal dosimetry. These differences can be eliminated by personalized computational phantoms. The segmentation of these data is too time and effort consuming though. The feasibility to capture inter-individual anatomic differences by a less effort-expensive method was shown in the scope of this thesis. The proposed and developed formalism is that a reference polygon-surface phantom is adjusted to fit selected individual external dimensions. The introduced method was tested and evaluated for one slim and for one overweight individual. For both individuals overall reliable dose estimates were achieved (with relative uncertainty  $\leq 25\%$ , compared to that  $\leq 50\%$  for most organs without any scaling applied). Thus, it is possible to improve the estimation of person-specific internal doses with the developed approach. To capture the full range of inter-individual anatomic variability more patients would be required. To facilitate the fast implementation of this approach in clinical practice, the diversity of human computational phantoms available for medical dose evaluation can be increased using the set of dimensions adjusted in this thesis. Subsequently, these dimensions should be considered in selecting the phantom that best matches the individual patient.

The powerful and model-independent variance-based sensitivity analysis was implemented in this thesis and applied to the MIRD system of internal dosimetry for the first time. As an intrinsic part of the sensitivity analysis, the uncertainties of organ dose estimates originating from inter-individual variations in pharmacokinetics and anatomy were computed. The variance-based sensitivity analysis facilitated ranking the input factors according to their impact on the variance of organ doses. Reducing the uncertainty of the highly influential input factors leads to effective gaining accuracy in internal dose estimations.

The accuracy level of internal dosimetry in nuclear medicine depends on the application and on the available resources. When it is not viable to perform patient-specific dose calculations, several steps can be taken to go from reference values to more patient-specific dosimetry. Based on the sensitivity analysis of this thesis, for effective dose coefficients four such steps can be identified. First, the SAFs for the source region total blood need to be determined more accurately, since these SAFs have the highest contribution to the uncertainty of effective dose coefficients. Patient-specific blood contents of organs and tissues are required to increase the accuracy of blood SAFs. Methods to determine patient-specific blood contents need to be evaluated in future studies. Second, self-absorption SAFs are to be scaled to the patient-specific organ masses, since this eliminates the impact of

### 13. Conclusion

these SAFs on the uncertainties of dose coefficients for source regions. Mass-scaling of the SAFs described in this thesis requires the knowledge of individual organ masses, which are relatively easy to determine from tomographic CT or MR images that usually accompany PET or SPECT scans. The next step is the accurate estimation of TIACs. It has been demonstrated in this thesis that the variability in TIACs almost solely defines the variance of absorbed dose coefficients of respective source regions. The uncertainty of effective dose coefficients is influenced by some of the TIACs, e.g. those for stomach wall, bladder content and rest of body for the radiopharmaceutical  $^{18}\text{F}$ -FSPG. Detailed time-resolved activity curves needed for calculations of patient-specific TIACs are usually not obtained in routine clinical practice though. The scaling of reference time-activity curves based on patient-specific activities measured at one or few time points is a possible solution, which could be investigated in future studies. The last step to be taken to improve the accuracy of internal dosimetry is to collect patient blood samples and to measure their activity. This is needed for considering blood as a source region. Additionally, even when blood is a distinct source, approximately 10 % of the variance in effective dose coefficients from  $^{18}\text{F}$ -FSPG is apportioned to the uncertainty of blood TIACs.

To confirm the findings of this thesis regarding the list of influential input factors for doses from radiopharmaceuticals other than  $^{18}\text{F}$ -FSPG, similar studies are to be done for the radiopharmaceuticals of interest. Programs and methods developed in this thesis do not depend on the radiopharmaceutical. Thus they can be applied equally for various radiopharmaceuticals to enhance the accuracy and reliability of internal dosimetry for individual patients in nuclear medicine applications. They provide the potential to move from reference internal dosimetry towards personalized organ dose estimation in medical practice. The viable level of accuracy of internal dosimetry is to be selected according to the resources available in a particular institution.

**Part VI.**  
**Appendix**



# A. Comparison of organ dose coefficients for employed anatomical models

Here organ absorbed dose coefficients computed with four sets of activity data for volunteers 1102/94–1105/94 (see table 5.4 on page 49) are compared between two selected individuals, reference phantoms and the developed matched models. Note that the corresponding comparison for activity dataset 1101/94 is presented in section 8.3. The comparison is done separately for the self-absorption and the cross-fire components of organ absorbed dose coefficients in sections A.1 and A.2, respectively. Figures A.1–A.4 presented in section A.1 are analogues to figure 8.4 on page 85. Figures A.5–A.8 and figures A.9–A.12 in section A.2 are analogues to figures 8.5 (page 86) and 8.6 (page 87) for overweight and slim individuals, respectively.

## A.1. Self-absorption component of absorbed dose coefficients

The calculated absorbed dose coefficients due to the self-absorption along with the deviation in % from the respective values calculated for Pat1 and Pat2 and the absolute contributions of the self-absorption to the total organ absorbed dose coefficients are shown in figures A.1–A.4. Note that for each phantom, i.e. RCP-AM, P-RCP-AM and Pat1M (Pat2M) the relative differences (in %) between the computed self-absorption dose coefficients and the corresponding values for Pat1 (Pat2) are independent of the employed activity. This can be illustrated in the following example for e.g. the relative difference in the self-absorption dose coefficients for kidneys between e.g. RCP-AM and Pat1. In this case the difference is computed as:

$$\text{Diff, \%} = \frac{\tilde{a}(\text{kidneys}) \sum_i E_i Y_i \Phi_{\text{RCP-AM}}(\text{kidneys} \leftarrow \text{kidneys}, E_i) - \tilde{a}(\text{kidneys}) \sum_i E_i Y_i \Phi_{\text{Pat1}}(\text{kidneys} \leftarrow \text{kidneys}, E_i)}{\tilde{a}(\text{kidneys}) \sum_i E_i Y_i \Phi_{\text{Pat1}}(\text{kidneys} \leftarrow \text{kidneys}, E_i)} \cdot 100 \%$$

It follows that the time-integrated activity coefficient for kidneys  $\tilde{a}(\text{kidneys})$  cancels. Hence, the middle panels of figures A.1a–A.4a are identical. The same is applied to the middle panels of figures A.1b–A.4b.

A. Comparison of organ dose coefficients for employed anatomical models

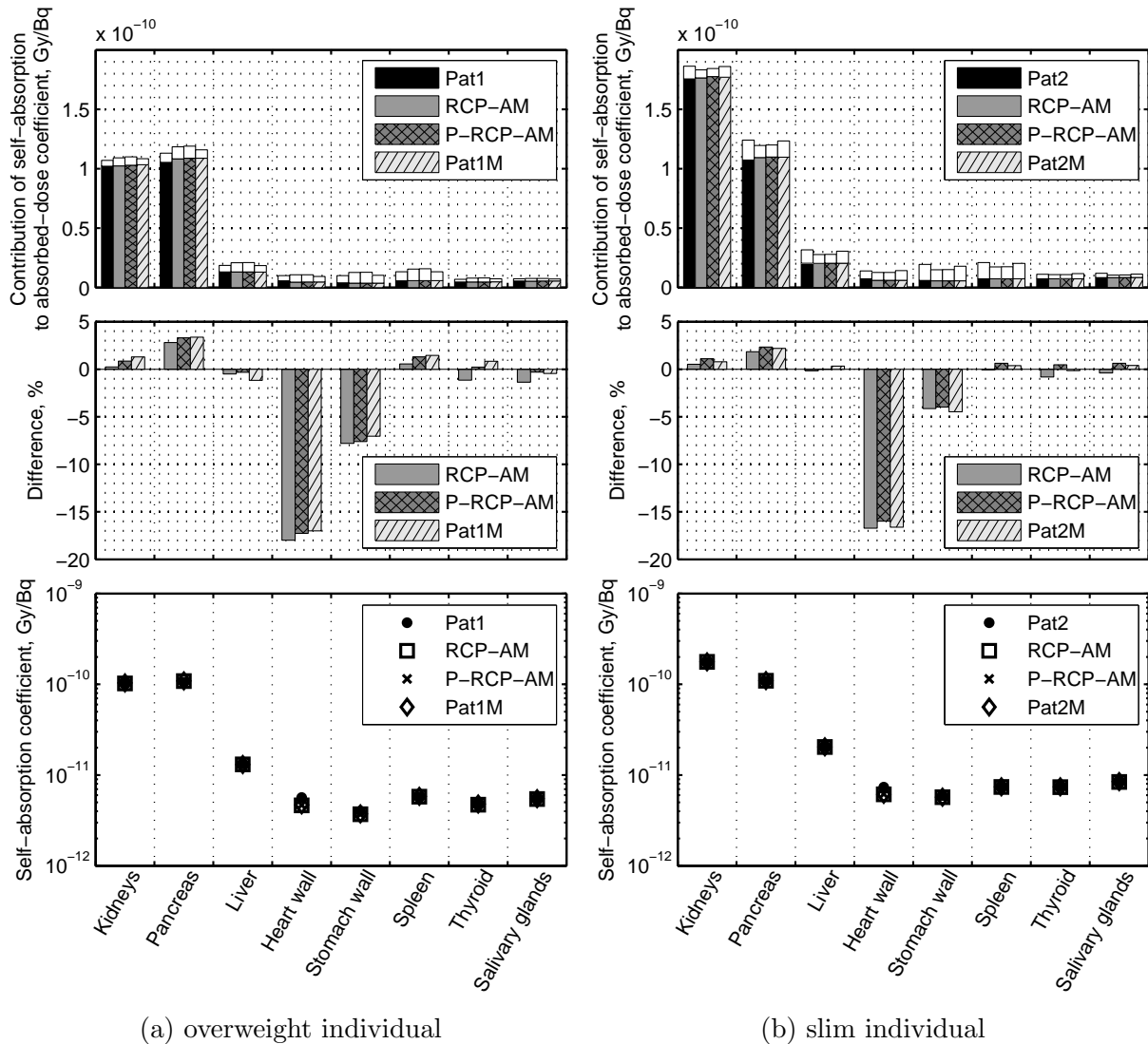
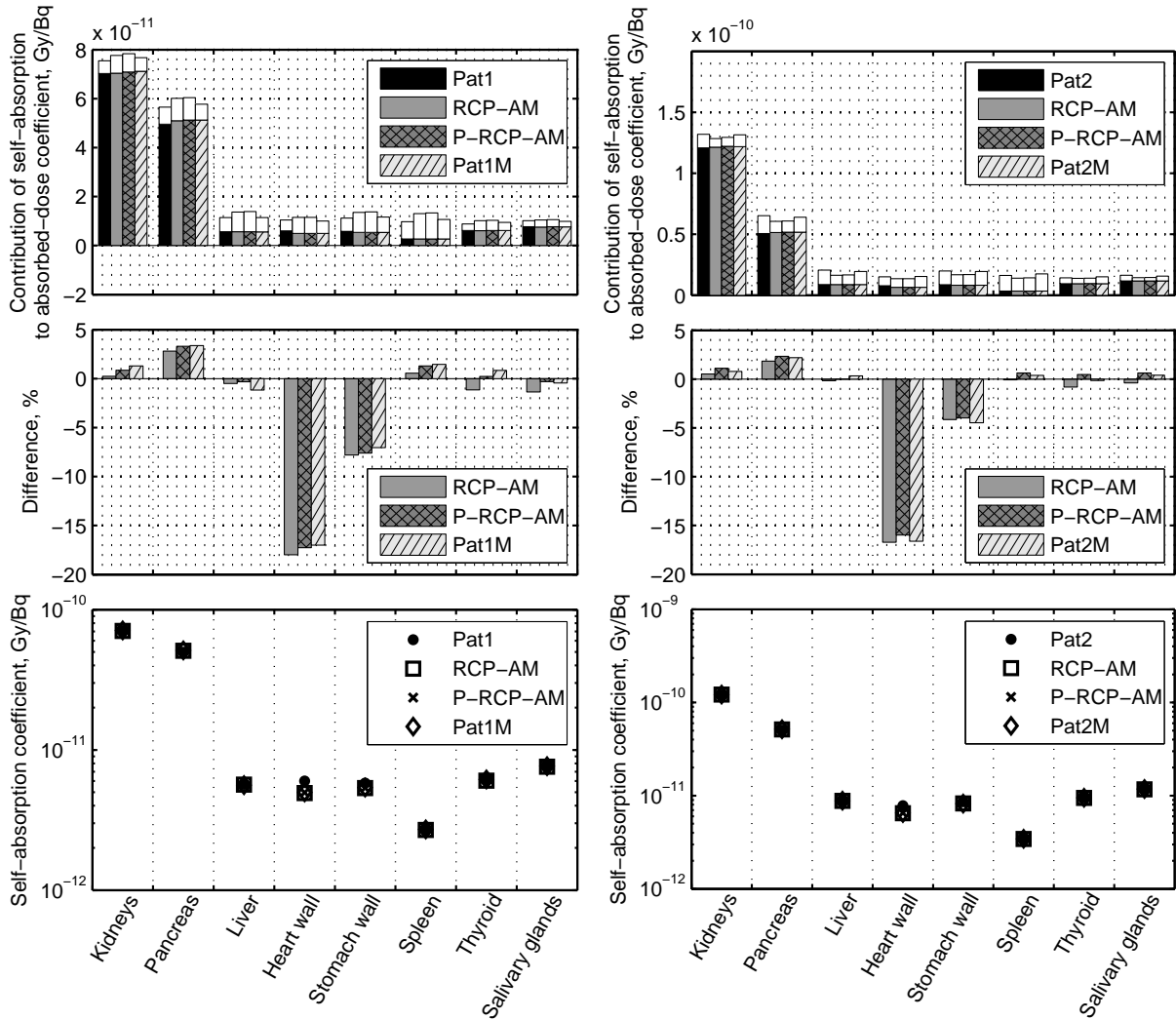


Figure A.1. Calculated self-absorption components of absorbed dose coefficients, differences in % relative to the corresponding values for Pat1 (a) and Pat2 (b) and absolute contributions of the self-absorption to the total absorbed dose coefficients. The total height of the bars on the upper row corresponds to the total organ absorbed dose coefficients, the filled areas to the self-absorption components. The SAFs estimated with RCP-AM, P-RCP-AM and Pat1M (Pat2M) for organs where source is equal to target were adjusted according to the masses of the patient Pat1 (Pat2), as described in subsection 7.4.1. Absorbed dose coefficients were computed with activity dataset 1102/94.

A.1. Self-absorption component of absorbed dose coefficients



(a) overweight individual

(b) slim individual

Figure A.2. Analogue to figure A.1, calculated self-absorption components of absorbed dose coefficients, differences in % relative to the corresponding values for Pat1 (a) and Pat2 (b) and absolute contributions of the self-absorption to the total absorbed dose coefficients. Absorbed dose coefficients were computed with activity dataset 1103/94.

A. Comparison of organ dose coefficients for employed anatomical models

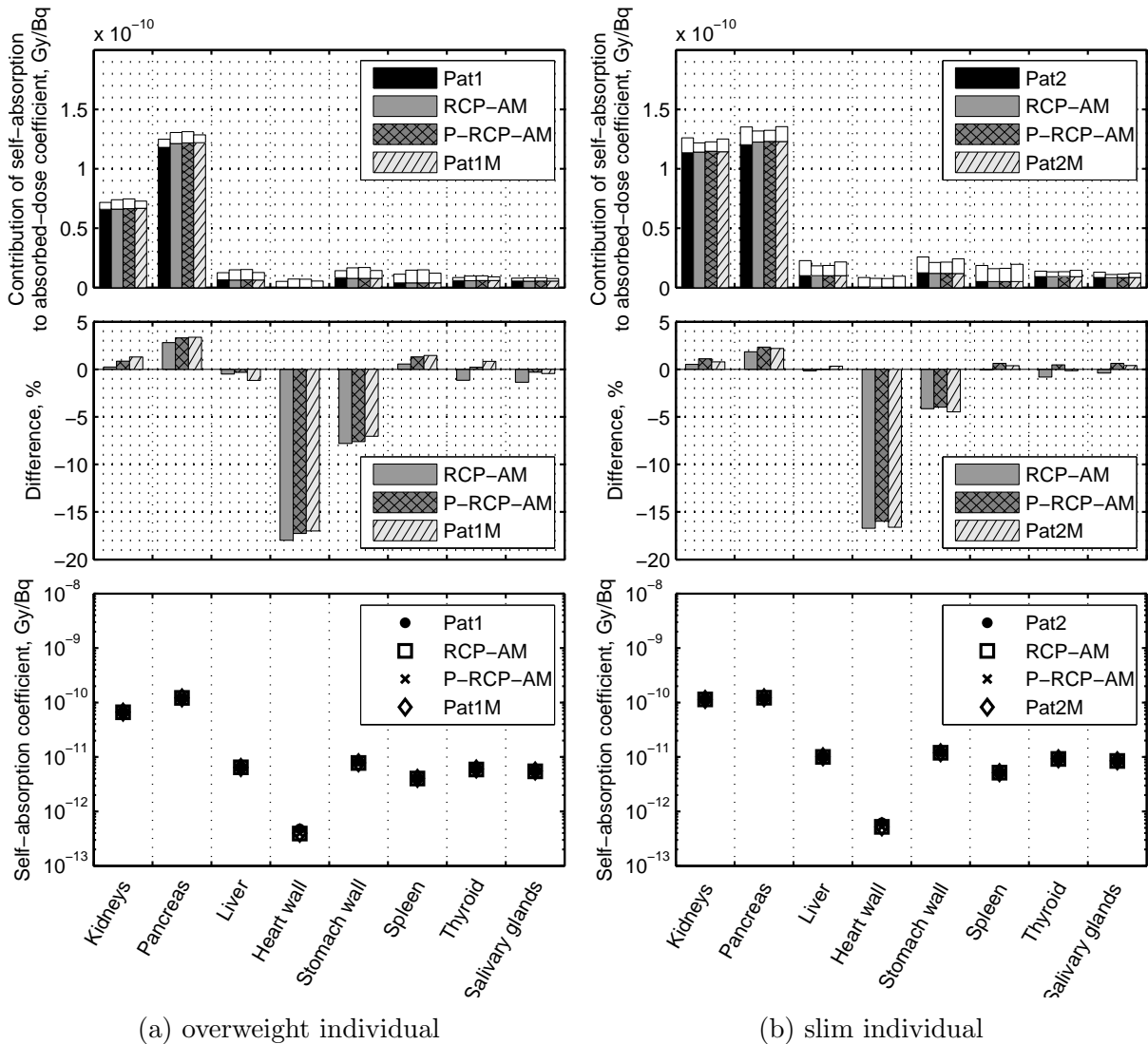


Figure A.3. Analogue to figure A.1, calculated self-absorption components of absorbed dose coefficients, differences in % relative to the corresponding values for Pat1 (a) and Pat2 (b) and absolute contributions of the self-absorption to the total absorbed dose coefficients. Absorbed dose coefficients were computed with activity dataset 1104/94.

A.1. Self-absorption component of absorbed dose coefficients

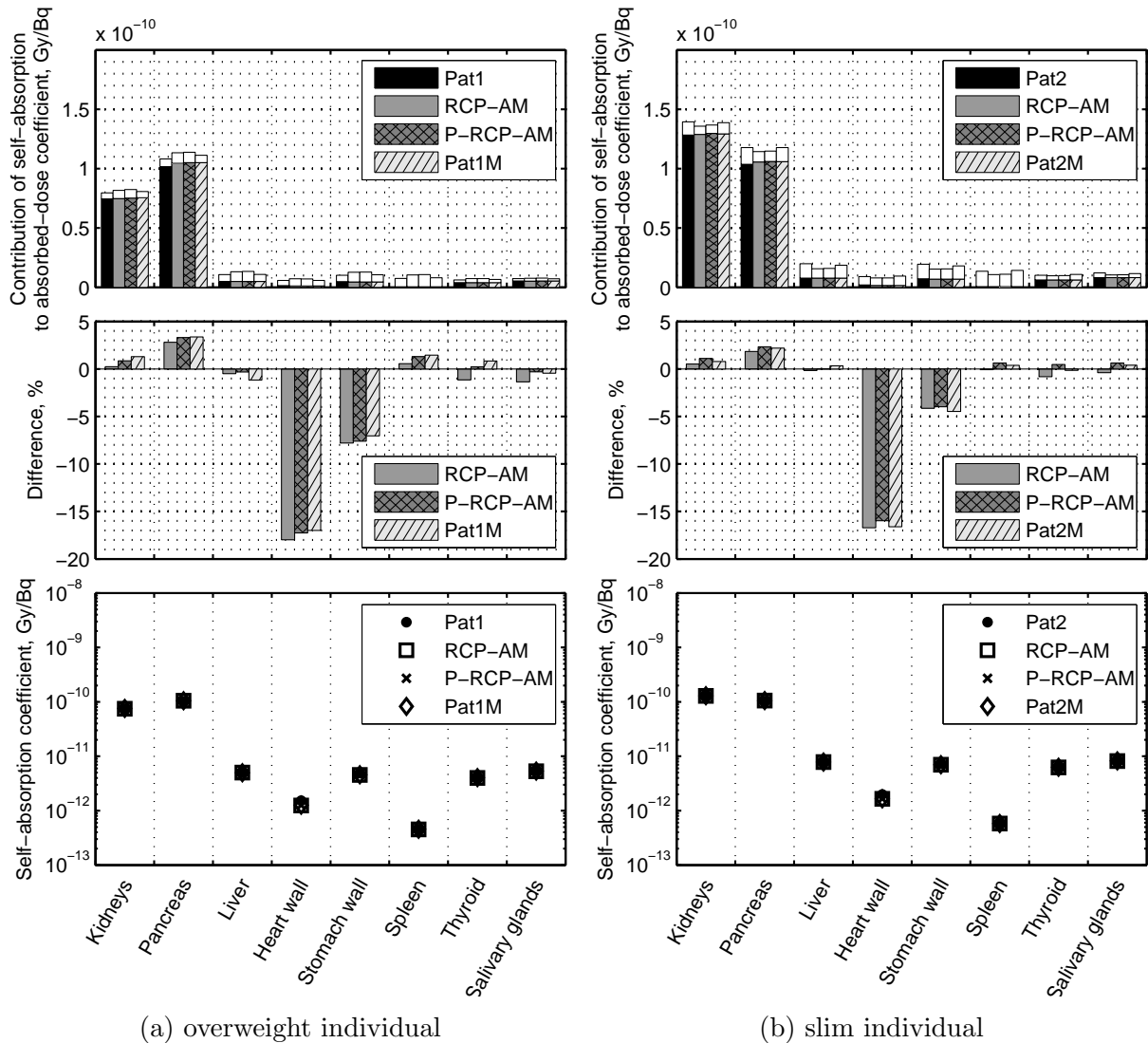


Figure A.4. Analogue to figure A.1, calculated self-absorption components of absorbed dose coefficients, differences in % relative to the corresponding values for Pat1 (a) and Pat2 (b) and absolute contributions of the self-absorption to the total absorbed dose coefficients. Absorbed dose coefficients were computed with activity dataset 1105/94.

## A.2. Cross-fire component of absorbed dose coefficients

The subset of the calculated absorbed dose coefficients from cross-fire along with the deviations in % from those calculated for Pat1 and Pat2 employing four activity datasets (1102/94–1105/94) are presented in figures A.5–A.8 for the overweight individual and in figures A.9–A.12 for the slim individual.

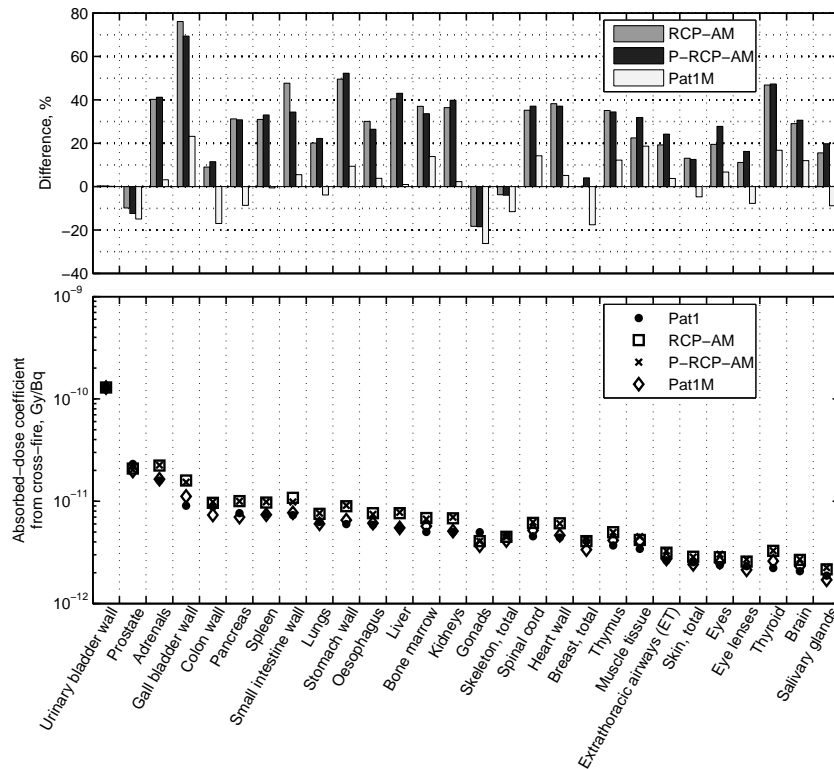


Figure A.5. Calculated with activity dataset 1102/94 cross-fire components of absorbed dose coefficients for Pat1 and models approximating it. The dose differences in the upper panel are given relative to Pat1.

A.2. Cross-fire component of absorbed dose coefficients

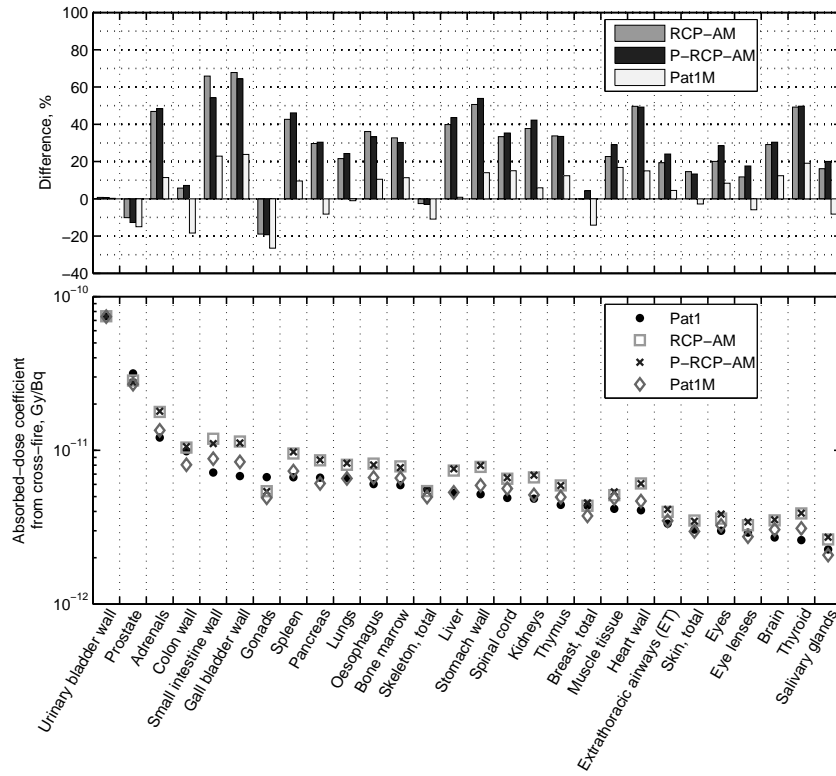


Figure A.6. Analogue to figure A.5, calculated with activity dataset 1103/94 cross-fire components of absorbed dose coefficients.

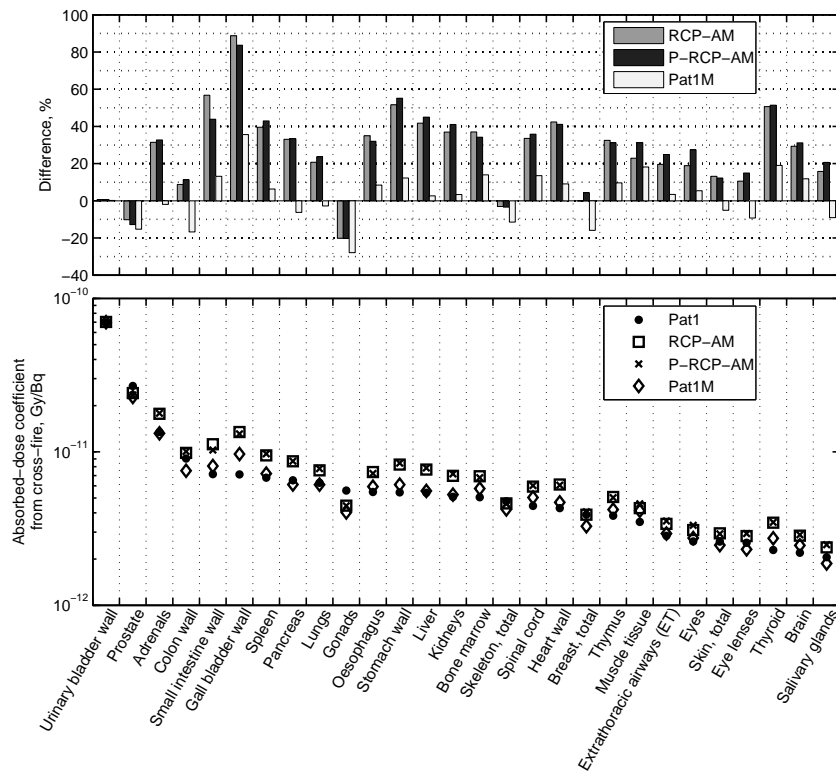


Figure A.7. Analogue to figure A.5, calculated with activity dataset 1104/94 cross-fire components of absorbed dose coefficients.

A. Comparison of organ dose coefficients for employed anatomical models

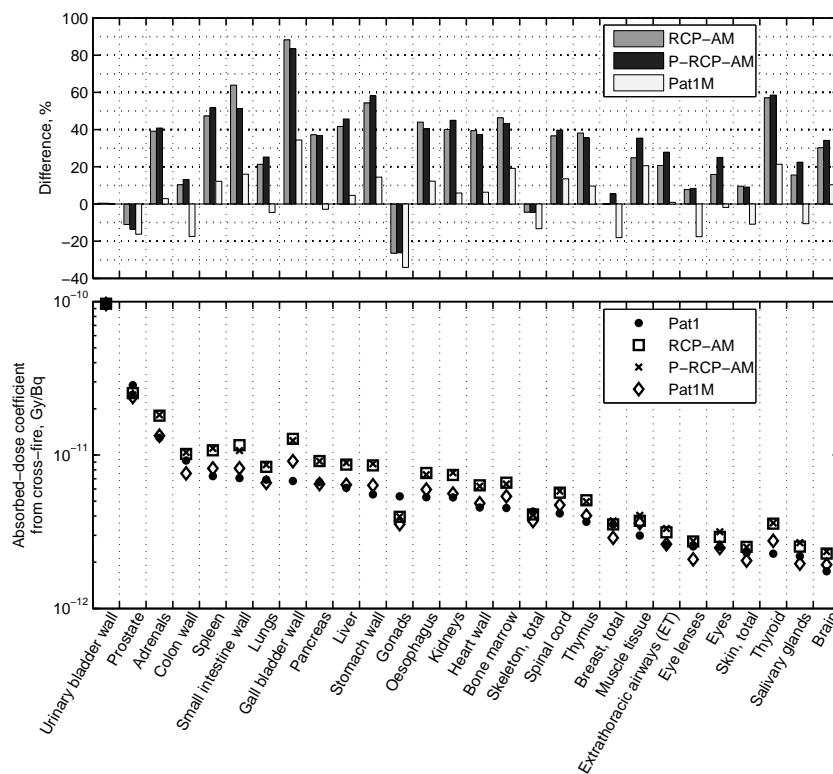


Figure A.8. Analogue to figure A.5, calculated with activity dataset 1105/94 cross-fire components of absorbed dose coefficients.

A.2. Cross-fire component of absorbed dose coefficients

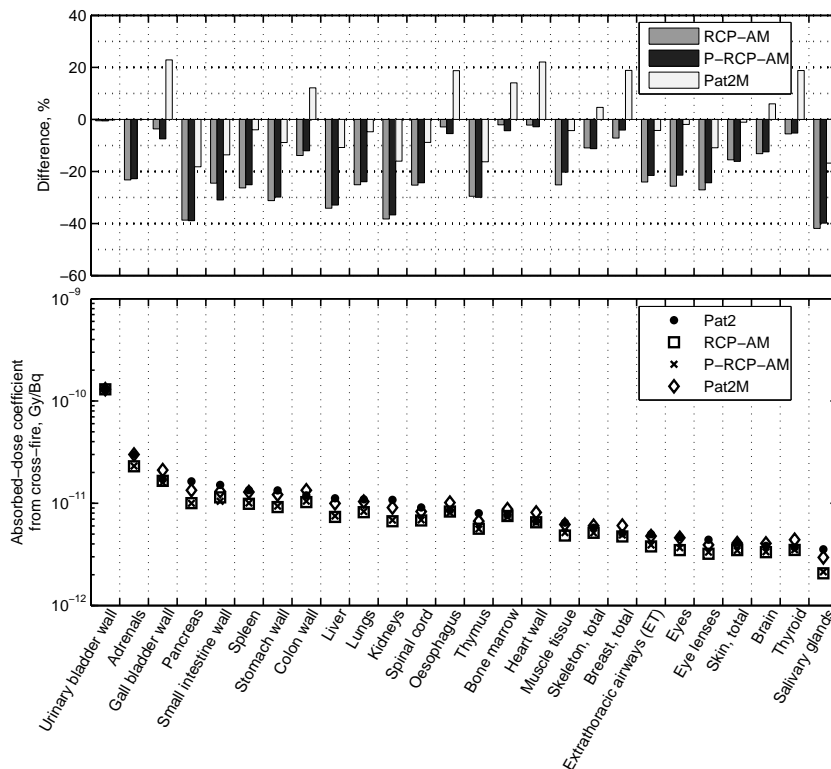


Figure A.9. Calculated with activity dataset 1102/94 cross-fire components of absorbed dose coefficients for Pat2 and models approximating it. The dose differences in the upper panel are given relative to Pat2.

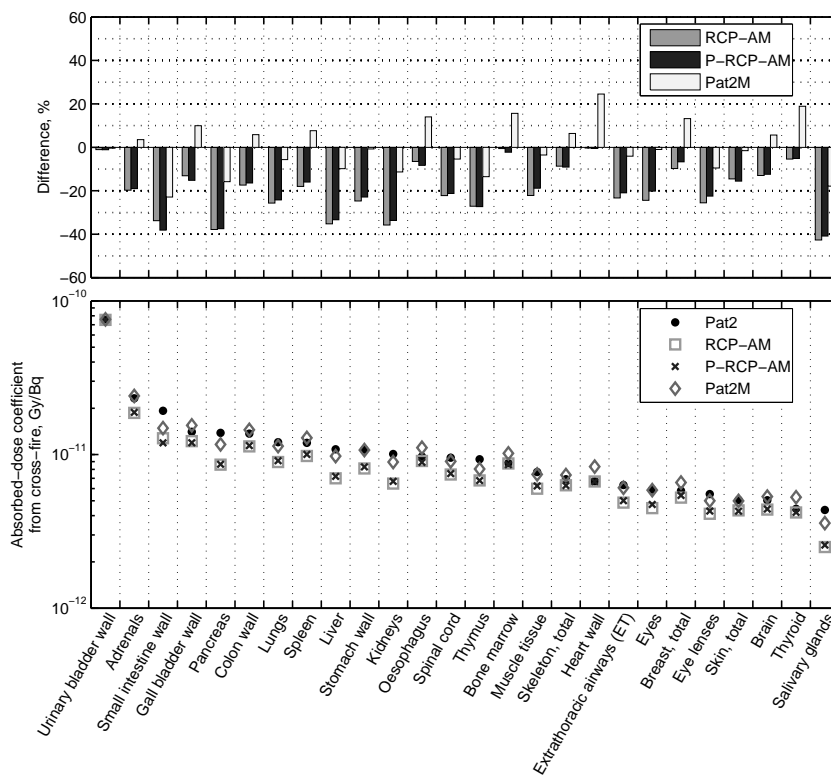


Figure A.10. Analogue to figure A.9, calculated with activity dataset 1103/94 cross-fire components of absorbed dose coefficients.

A. Comparison of organ dose coefficients for employed anatomical models

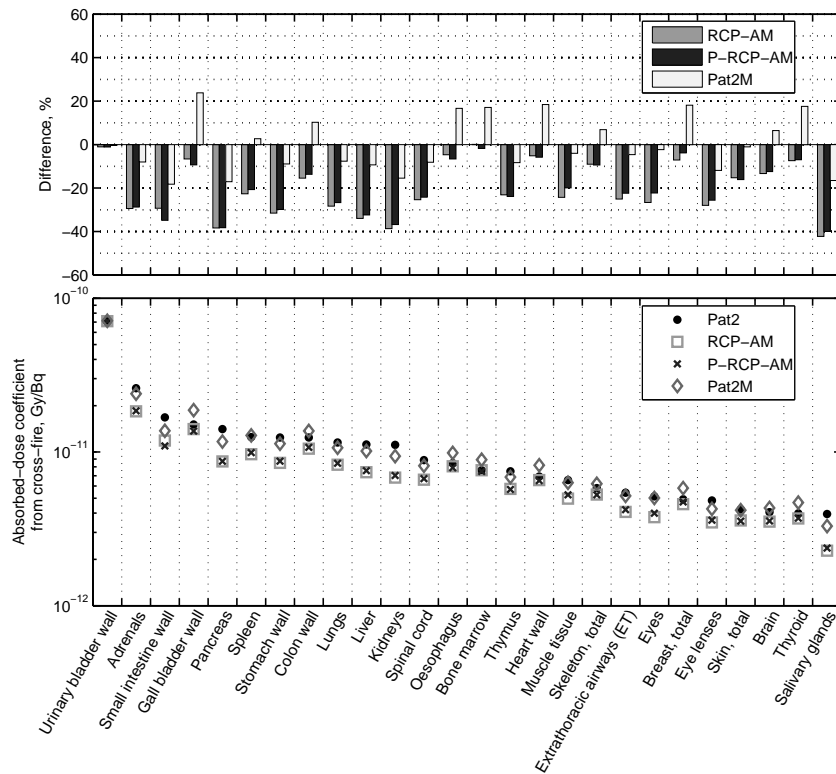


Figure A.11. Analogue to figure A.9, calculated with activity dataset 1104/94 cross-fire components of absorbed dose coefficients.

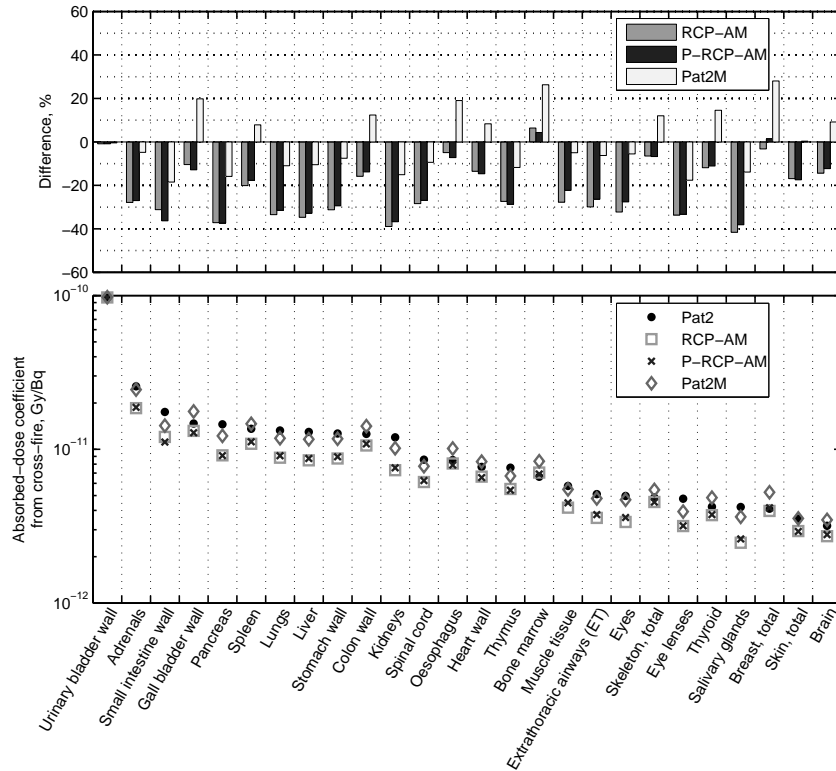


Figure A.12. Analogue to figure A.9, calculated with activity dataset 1105/94 cross-fire components of absorbed dose coefficients.

## B. Total effect sensitivity indices for all considered outputs

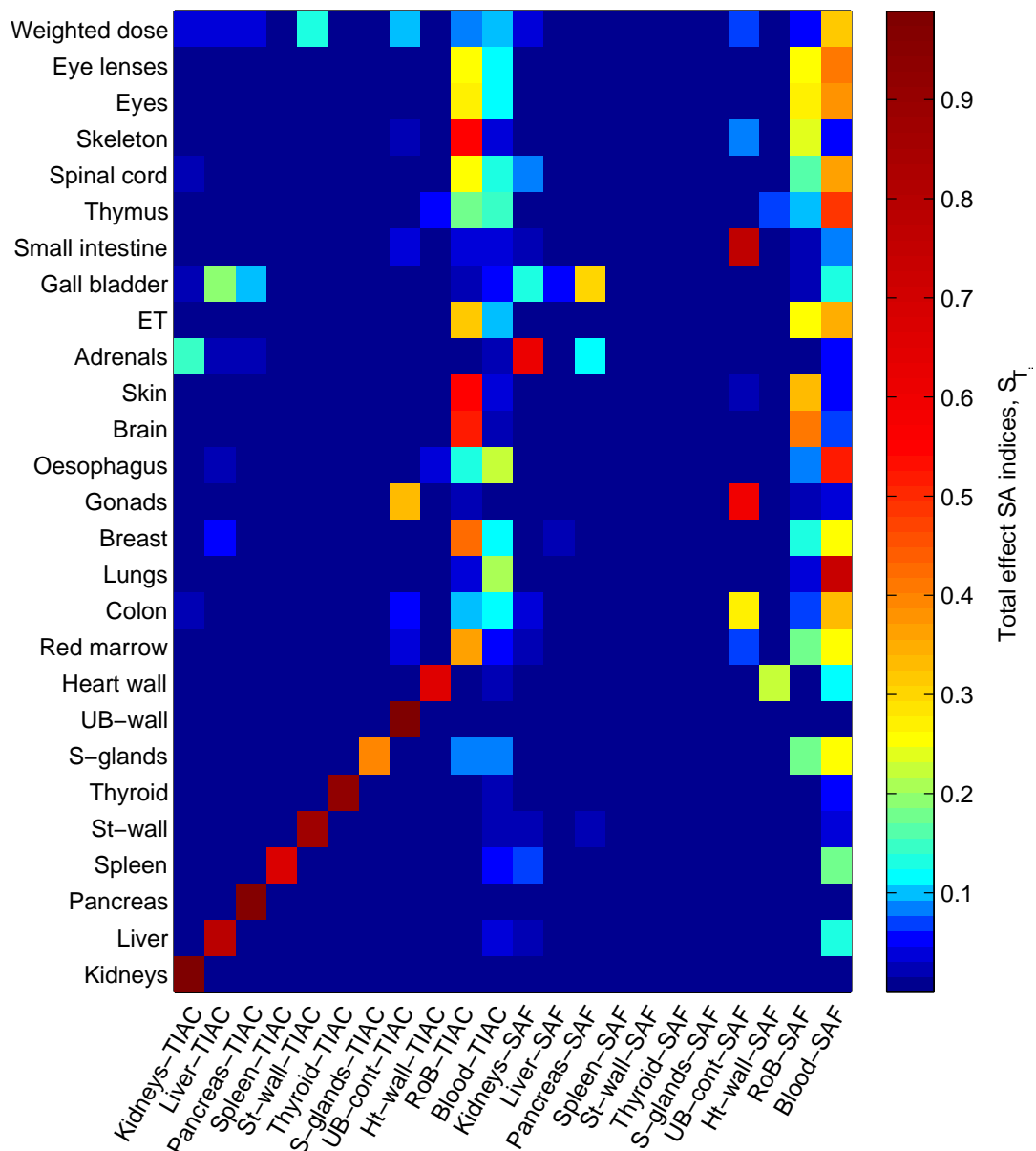


Figure B.1. Total effect sensitivity indices for all considered outputs. Each horizontal line in this figure contains  $S_{T_i}$  in color-codes for all input factors and a selected output. The input factors are plotted from left to right and the output target regions from bottom to top.  $S_{T_i} = 0$  means no effect of the corresponding input factor. The corresponding figure for  $S_i$  (figure 11.8) is shown on page 121.



# List of Figures

1.1. Concept of PET imaging . . . . .	17
1.2. Photon mass attenuation coefficients in water . . . . .	18
4.1. Compartmental pharmacokinetic model structure . . . . .	36
4.2. PET image showing activity of $^{18}\text{F}$ -FSPG in ureter . . . . .	37
4.3. Graphical user interface of SAAM II . . . . .	42
5.1. Compartmental pharmacokinetic model predictions . . . . .	45
5.2. Example of pharmacokinetic model predictions for perfused organs and organ parenchyma . . . . .	46
6.1. MIRDO-5 phantom . . . . .	58
6.2. Voxel phantom of the seven years old female individual “Child” from HMGU library . . . . .	59
6.3. Anterior views of the male and the female 4D XCAT phantoms . . . . .	61
6.4. Triangular torso mesh of a polygon-surface adult male phantom . . . . .	62
6.5. Two reference phantoms of adult male: voxel and polygon-surface . . . . .	64
7.1. Voxel phantoms Visible Human and Irene . . . . .	69
7.2. Adjusted dimensions of reference polygon-surface phantom . . . . .	70
7.3. Three steps of the adjustments of P-RCP-AM to fit selected dimensions of Pat1 . . . . .	71
8.1. P-RCP-AM and the result of its adjustment to Pat1 and Pat2 . . . . .	81
8.2. A subset of four slices of P-RCP-AM . . . . .	82
8.3. Rendered voxelized models P-RCP-AM, Pat1M and Pat2M . . . . .	83
8.4. Calculated self-absorption components of absorbed dose coefficients, differ- ences in % relative to the corresponding values for Pat1 and Pat2 and absolute contributions of the self-absorption to the total absorbed dose coefficients .	85
8.5. Calculated cross-fire components of the organ absorbed dose coefficients for Pat1 and different models approximating it . . . . .	86
8.6. Calculated cross-fire components of the organ absorbed dose coefficients for Pat2 and different models approximating it . . . . .	87
10.1. Anatomical models of reference, slim and overweight individuals employed in sensitivity analysis . . . . .	107
10.2. 128 points generated with uniform random numbers generator and 128 quasi-random points generated with Sobol’ sequence . . . . .	111
11.1. Box plot of computed dose coefficients . . . . .	114
11.2. Computed dose coefficients along with their uncertainties . . . . .	115

11.3. Convergence plots for the first-order and the total effect SA indices for absorbed dose coefficient for spleen . . . . .	117
11.4. Convergence plots for the first-order and the total effect SA indices for absorbed dose coefficient for brain . . . . .	118
11.5. Scatter plots, sensitivity indices and distribution of absorbed dose coefficient for small intestine wall . . . . .	119
11.6. Scatter plots, sensitivity indices and distribution of absorbed dose coefficient for lungs . . . . .	120
11.7. Scatter plots, sensitivity indices and distribution of absorbed dose coefficient for kidneys . . . . .	120
11.8. First-order effect sensitivity indices for all considered outputs . . . . .	121
A.1. Calculated with activity dataset 1102/94 self-absorption components of absorbed dose coefficients, differences in % relative to the corresponding values for Pat1 and Pat2 and absolute contributions of the self-absorption to the total absorbed dose coefficients . . . . .	134
A.2. Calculated with activity dataset 1103/94 self-absorption components of absorbed dose coefficients, differences in % relative to the corresponding values for Pat1 and Pat2 and absolute contributions of the self-absorption to the total absorbed dose coefficients . . . . .	135
A.3. Calculated with activity dataset 1104/94 self-absorption components of absorbed dose coefficients, differences in % relative to the corresponding values for Pat1 and Pat2 and absolute contributions of the self-absorption to the total absorbed dose coefficients . . . . .	136
A.4. Calculated with activity dataset 1105/94 self-absorption components of absorbed dose coefficients, differences in % relative to the corresponding values for Pat1 and Pat2 and absolute contributions of the self-absorption to the total absorbed dose coefficients . . . . .	137
A.5. Calculated with activity dataset 1102/94 cross-fire components of organ absorbed dose coefficients for Pat1 and models approximating it . . . . .	138
A.6. Calculated with activity dataset 1103/94 cross-fire components of organ absorbed dose coefficients for Pat1 and models approximating it . . . . .	139
A.7. Calculated with activity dataset 1104/94 cross-fire components of organ absorbed dose coefficients for Pat1 and models approximating it . . . . .	139
A.8. Calculated with activity dataset 1105/94 cross-fire components of organ absorbed dose coefficients for Pat1 and models approximating it . . . . .	140
A.9. Calculated with activity dataset 1102/94 cross-fire components of organ absorbed dose coefficients for Pat2 and models approximating it . . . . .	141
A.10. Calculated with activity dataset 1103/94 cross-fire components of organ absorbed dose coefficients for Pat2 and models approximating it . . . . .	141
A.11. Calculated with activity dataset 1104/94 cross-fire components of organ absorbed dose coefficients for Pat2 and models approximating it . . . . .	142
A.12. Calculated with activity dataset 1105/94 cross-fire components of organ absorbed dose coefficients for Pat2 and models approximating it . . . . .	142
B.1. Total effect sensitivity indices for all considered outputs . . . . .	143

# List of Tables

4.1. Volunteers details . . . . .	35
4.2. Symbols for mathematical notation of compartmental model of this thesis .	38
4.3. Reference blood contents . . . . .	41
5.1. Estimated model parameters . . . . .	44
5.2. Estimated voiding fractions . . . . .	44
5.3. Time-integrated activity coefficients derived from compartmental pharmacokinetic models . . . . .	48
5.4. Time-integrated activity coefficients used in the dosimetry in concept-1 . .	49
5.5. Time-integrated activity coefficients used in the dosimetry in concept-2 . .	49
5.6. Computed absorbed-dose coefficients and effective-dose coefficients . . . . .	51
7.1. Selected properties of employed individual phantoms . . . . .	69
7.2. Abbreviations used for indicating the computational models in this thesis .	72
7.3. Estimated biologic parameters of dynamic bladder model with $^{18}\text{F}$ -FSPG .	78
7.4. Estimated urine production rates . . . . .	79
8.1. Selected dimensions of Pat1 and Pat2 and the corresponding matched dimensions of Pat1M and Pat2M . . . . .	82
8.2. Selected properties of all considered computational phantoms . . . . .	82
8.3. Relative differences in the organ absorbed dose coefficients from cross-fire, calculated for three models approximating Pat1, compared to the corresponding doses of Pat1 . . . . .	88
8.4. Relative differences in the organ absorbed dose coefficients from cross-fire, calculated for three models approximating Pat2, compared to the corresponding doses of Pat2 . . . . .	89
10.1. Mean and standard deviation of TIAC input factors distributions . . . . .	108
10.2. Mean and standard deviation of SAF input factors distributions for photons	109
10.3. Mean and standard deviation of SAF input factors distributions for electrons	110



# List of Abbreviations and Acronyms

- <sup>18</sup>F-FSPG** (S)-4-(3-<sup>18</sup>F-fluoropropyl)-L-glutamic acid. 35–38, 41–44, 47–52, 74, 78, 84, 88–90, 106, 116, 119, 123, 130
- AF** Absorbed Fraction. 83, 88, 89
- BMI** Body Mass Index. 64, 68, 90, 107, 123
- BREP** Boundary Representation. 57, 60, 62–64, 68
- CSDA** Continuous Slowing Down Approximation. 16, 49
- CT** Computed Tomography. 3, 15, 33, 35, 36, 58, 59, 65, 67, 68, 70, 91, 130
- DAISY** Differential Algebra for Identifiability of SYstems. 43
- HMGU** Helmholtz Zentrum München. 50, 58, 59, 68, 73, 90, 128
- IA** Injected Activity. 35, 40
- ICRP** International Commission on Radiological Protection. 25, 33, 40, 41, 44, 47, 50, 62, 63, 65, 68–70, 72, 74, 76, 81, 104–107, 127
- ICRU** International Commission on Radiation Units and Measurements. 62, 74
- MIRD** Committee on Medical Internal Radiation Dose. 3, 4, 23, 39, 58, 68, 76, 95, 103, 104, 113, 129
- MR** Magnetic Resonance. 58, 59, 67, 70, 130
- NIST** National Institute of Standards and Technology. 49, 73
- NURBS** Non-Uniform Rational B-Spline. 57, 60–62, 72
- OIN** Organ Identification Number. 59
- P-RCP-AM** Polygon-surface ICRP Reference Computational Phantom of Adult Male. 63, 68–72, 74, 76–78, 81–88, 91, 106, 107, 133, 134, 145
- PET** Positron Emission Tomography. 7, 13, 15–17, 20, 21, 31–33, 35–38, 40, 45, 67, 73, 74, 90, 91, 123, 127, 130
- RCP-AM** Voxel ICRP Reference Computational Phantom of Adult Male. 63, 64, 69, 72, 76, 77, 82, 84–88, 106, 107, 115, 117, 133, 134

*List of Abbreviations and Acronyms*

**RoB** Rest of Body. 24, 38, 40, 108–110, 116, 122, 123

**ROI** Region of Interest. 36, 37

**SA** Sensitivity Analysis. 97, 99–101, 105–108, 111, 113, 116–119, 123

**SAAM II** Simulation, Analysis, and Modeling Software II. 32, 33, 40, 41, 43

**SAF** Specific Absorbed Fraction. 3, 23, 73, 74, 76–79, 85, 90, 91, 104, 106–111, 113–120, 122, 123, 129, 130, 134

**SD** Standard Deviation. 44, 48

**SPECT** Single Photon Emission Computed Tomography. 13, 15, 20, 130

**TIAC** Time-Integrated Activity Coefficient. 104, 106, 108, 111, 113, 115–119, 122, 123, 130

# List of Symbols

- $M_{r_S}$  mass of source region. 24, 76
- $M_{r_T}$  mass of target region. 23, 76
- $M_{r_{RoB}}$  mass of rest of body. 24
- $M_{r_{TB}}$  mass of total body. 24, 77
- $N$  number of model evaluations in sensitivity analysis. 105, 106, 111–113, 116–118
- $T_D$  dose-integration period. 23, 47, 104
- $T_{1/2}$  half-life. 36
- $U(t)$  urine production rate. 78, 79
- $V_0$  initial bladder-content volume. 78, 84
- $V_r$  residual bladder-content volume. 78
- $\Phi(r_T \leftarrow r_S, E)$  specific absorbed fraction. 3, 4, 47, 67, 68, 104
- $\lambda$  decay constant. 36, 40
- $\mathbb{E}$  expected value (or mean value). 101
- $\mathbb{Y}$  model output. 100, 101, 104–106
- $\mu$  mean value of distribution. 108–111
- $\mu_{en}/\rho$  mass-energy absorption coefficient. 47, 49
- $\sigma$  standard deviation of distribution. 108–111
- $\tilde{a}(r_S)$  time-integrated activity coefficient. 3, 4, 47, 50, 76, 104
- $r_S$  source region. 3, 4, 23, 43, 77, 104, 106, 122
- $r_T$  target region. 3, 4, 23, 76, 77, 104–106, 122
- $r_{RoB}$  rest of body. 24, 46, 47, 50, 104, 106
- $r_{TB}$  total body. 24, 76, 77
- $S_i$  first-order effect sensitivity index for input factor  $X_i$ . 100, 101, 105, 106, 111, 116–119, 121, 122, 143
- $S_{T_i}$  total effect sensitivity index for input factor  $X_i$ . 100, 101, 105, 106, 111, 116–119, 143

*List of Symbols*

$X_{\sim i}$  all input factors except  $X_i$ . 100, 101

$fr_i$  voiding fraction. 39, 40

# Bibliography

- [1] *Clinical nuclear medicine*. Germany: Springer-Verlag Berlin Heidelberg, 2007.
- [2] B. J. Allen, C. Raja, S. Rizvi, Y. Li, W. Tsui, D. Zhang, E. Song, C. F. Qu, J. Kearsley, P. Graham, and J. Thompson, “Targeted alpha therapy for cancer”, *Phys Med Biol*, vol. 49, no. 16, pp. 3703–12, 2004.
- [3] J. Elgqvist, S. Frost, J. P. Pouget, and P. Albertsson, “The potential and hurdles of targeted alpha therapy - clinical trials and beyond”, *Front Oncol*, vol. 3, p. 324, 2014.
- [4] W. E. Bolch, K. F. Eckerman, G. Sgouros, and S. R. Thomas, “MIRD pamphlet No. 21: a generalized schema for radiopharmaceutical dosimetry—standardization of nomenclature”, *J Nucl Med*, vol. 50, no. 3, pp. 477–84, 2009.
- [5] R. Loevinger, T. Budinger, and E. Watson, “MIRD primer for absorbed dose calculations”, report, Society of Nuclear Medicine, 1988.
- [6] M. Berman, “MIRD pamphlet No. 12: kinetic models for absorbed dose calculations”, New York, N.Y., 1977.
- [7] ICRP, “Radiation dose to patients from radiopharmaceuticals”, ICRP Publication 53, Pergamon, 1988.
- [8] ICRP, “Radiation dose to patients from radiopharmaceuticals: a compendium of current information related to frequently used substances”, ICRP Publication 128, Pergamon, 2015.
- [9] M. G. Stabin, “Update: the case for patient-specific dosimetry in radionuclide therapy”, *Cancer Biother Radiopharm*, vol. 23, no. 3, pp. 273–84, 2008.
- [10] G. Flux, M. Bardies, C. Chiesa, M. Monsieurs, S. Savolainen, S. E. Strand, and M. Lassmann, “Clinical radionuclide therapy dosimetry: the quest for the ”Holy Gray””, *Eur J Nucl Med Mol Imaging*, vol. 34, no. 10, pp. 1699–700, 2007.
- [11] S. Mattsson, “Patient dosimetry in nuclear medicine”, *Radiat Prot Dosimetry*, vol. 165, no. 1-4, pp. 416–23, 2015.
- [12] M. Jamei, G. L. Dickinson, and A. Rostami-Hodjegan, “A framework for assessing inter-individual variability in pharmacokinetics using virtual human populations and integrating general knowledge of physical chemistry, biology, anatomy, physiology and genetics: A tale of ’bottom-up’ vs ’top-down’ recognition of covariates”, *Drug Metab Pharmacokinet*, vol. 24, no. 1, pp. 53–75, 2009.
- [13] W. Bolch, C. Lee, M. Wayson, and P. Johnson, “Hybrid computational phantoms for medical dose reconstruction”, *Radiat Environ Biophys*, vol. 49, no. 2, pp. 155–168, 2010.

- [14] T. Smith, N. Petoussi-Henss, and M. Zankl, “Comparison of internal radiation doses estimated by mird and voxel techniques for a ‘family’ of phantoms”, *Eur J of Nucl Med*, vol. 27, no. 9, pp. 1387–98, 2000.
- [15] M. Zankl, N. Petoussi-Henss, U. Fill, and D. Regulla, “The application of voxel phantoms to the internal dosimetry of radionuclides”, *Radiat Prot Dosimetry*, vol. 105, no. 1-4, pp. 539–48, 2003.
- [16] N. Petoussi-Henss, W. E. Bolch, M. Zankl, G. Sgouros, and B. Wessels, “Patient-specific scaling of reference S-values for cross-organ radionuclide S-values: what is appropriate?”, *Radiat Prot Dosimetry*, vol. 127, no. 1-4, pp. 192–6, 2007.
- [17] F. Paquet, M. R. Bailey, R. W. Leggett, and J. D. Harrison, “Assessment and interpretation of internal doses: uncertainty and variability”, *Ann ICRP*, vol. 45, no. 1 Suppl, pp. 202–14, 2016.
- [18] NCRP, “Uncertainties in internal radiation dose assessment”, Report 164, 2009.
- [19] M. G. Stabin, “Uncertainties in internal dose calculations for radiopharmaceuticals”, *J Nucl Med*, vol. 49, no. 5, pp. 853–60, 2008.
- [20] A. Saltelli and P. Annoni, “How to avoid a perfunctory sensitivity analysis”, *Environ Model Softw*, vol. 25, no. 12, pp. 1508–17, 2010.
- [21] W. B. Li and C. Hoeschen, “Uncertainty and sensitivity analysis of biokinetic models for radiopharmaceuticals used in nuclear medicine”, *Radiat Prot Dosimetry*, vol. 139, no. 1-3, pp. 228–31, 2010.
- [22] S. R. Thomas, M. G. Stabin, C. T. Chen, and R. C. Samaratinga, “MIRD Pamphlet No. 14 revised: a dynamic urinary bladder model for radiation dose calculations”, *J Nucl Med*, vol. 40, no. 4, pp. 102S–23S, 1999.
- [23] Z. Habib, *Quantitative analysis in nuclear medicine imaging*. Singapore: Springer Science & Business Media, 2006.
- [24] G. Gnanasegaran and J. R. Ballinger, “Molecular imaging agents for SPECT (and SPECT/CT)”, *Eur J Nucl Med Mol Imaging*, vol. 41 Suppl 1, pp. S26–35, 2014.
- [25] P. P. Bruyant, “Analytic and iterative reconstruction algorithms in SPECT”, *J Nucl Med*, vol. 43, no. 10, pp. 1343–58, 2002.
- [26] D. L. Bailey and K. P. Willowson, “Quantitative SPECT/CT: SPECT joins PET as a quantitative imaging modality”, *Eur J Nucl Med Mol Imaging*, vol. 41 Suppl 1, pp. S17–S25, 2014.
- [27] M. E. Phelps, ed., *PET: Physics, Instrumentation, and Scanners*. Springer-Verlag New York, 1 ed., 2006.
- [28] P. Zanzonico, “Principles of nuclear medicine imaging: planar, SPECT, PET, multi-modality, and autoradiography systems”, *Radiat Res*, vol. 177, no. 4, pp. 349–64, 2012.

- [29] C. S. Levin and E. J. Hoffman, “Calculation of positron range and its effect on the fundamental limit of positron emission tomography system spatial resolution”, *Phys Med Biol*, vol. 44, no. 3, pp. 781–99, 1999.
- [30] J. Cal-González, J. L. Herraiz, S. España, M. Desco, J. J. Vaquero, and J. M. Udías, “Positron range effects in high resolution 3D PET imaging”, in *Nuclear Science Symposium*, pp. 2788–91, IEEE.
- [31] S. Tavernier, *Experimental techniques in nuclear and particle physics*. Heidelberg; New York: Springer, 2010.
- [32] T. Smith, N. Veall, and R. Wootton, “Bladder wall dose from administered radiopharmaceuticals: the effects of variations in urine flow rate, voiding interval and initial bladder content”, *Radiat Prot Dosimetry*, vol. 2, no. 3, pp. 183–9, 1982.
- [33] M. Andersson, D. Minarik, L. Johansson, S. Mattsson, and S. Leide-Svegborn, “Improved estimates of the radiation absorbed dose to the urinary bladder wall”, *Phys Med Biol*, vol. 59, no. 9, pp. 2173–82, 2014.
- [34] ICRP, “The 2007 recommendations of the International Commission on Radiological Protection”, ICRP Publication 103, Pergamon, 2007.
- [35] A. Zvereva, N. Petoussi-Henss, W. B. Li, H. Schlattl, O. Uwe, M. Zankl, F. P. Graner, C. Hoeschen, S. G. Nekolla, K. Parodi, and M. Schwaiger, “Effect of blood activity on dosimetric calculations for radiopharmaceuticals”, *Phys Med Biol*, vol. 61, no. 21, pp. 7688–703, 2016.
- [36] K. Godfrey, *Compartmental models and their application*. London; New York: Academic Press, 1983.
- [37] M. E. Phelps, J. C. Mazziotta, and H. R. Schelbert, *Positron emission tomography and autoradiography: principles and applications for the brain and heart*. New York: Raven Press, 1986.
- [38] E. R. Carson, C. Cobelli, and L. Finkelstein, *The mathematical modeling of metabolic and endocrine systems: model formulation, identification, and validation*. Biomedical engineering and health systems, New York: John Wiley & Sons, 1983.
- [39] P. H. R. Barrett, B. M. Bell, C. Cobelli, H. Golde, A. Schumitzky, P. Vicini, and D. M. Foster, “SAAM II: simulation, analysis, and modeling software for tracer and pharmacokinetic studies”, *Metabolism*, vol. 47, pp. 484–92, 1998.
- [40] R. W. Legget and L. R. Williams, “A proposed blood circulation model for reference man”, *Health Phys*, vol. 69, pp. 187–201, 1995.
- [41] A. Guyton and J. Hall, *Textbook of medical physiology*. Philadelphia: Elsevier Saunders, 11 ed., 2006.
- [42] G. Sgouros, “Bone marrow dosimetry for radioimmunotherapy: theoretical considerations”, *J Nucl Med*, vol. 34, no. 4, pp. 689–94, 1993.

- [43] R. E. Bigler and G. Sgouros, “Biological analysis and dosimetry for  $^{15}\text{O}$ -labeled  $\text{O}_2$ ,  $\text{CO}_2$ , and  $\text{CO}$  gases administered continuously by inhalation”, *J Nucl Med*, vol. 24, no. 5, pp. 431–7, 1983.
- [44] K. Smolarz, B. J. Krause, F. P. Graner, F. M. Wagner, C. Hultsch, C. Bacher-Stier, R. B. Sparks, S. Ramsay, L. M. Fels, L. M. Dinkelborg, and M. Schwaiger, “(s)-4-(3- $^{18}\text{F}$ -fluoropropyl)-L-glutamic acid: an  $^{18}\text{F}$ -labeled tumor-specific probe for PET/CT imaging–dosimetry”, *J Nucl Med*, vol. 54, no. 6, pp. 861–6, 2013.
- [45] J. Staaf, H. Jacobsson, and A. Sanchez-Crespo, “A revision of the organ radiation doses from 2-fluoro-2-deoxy-d-glucose with reference to tumour presence”, *Radiat Prot Dosimetry*, vol. 151, no. 1, pp. 43–50, 2012.
- [46] A. Challapalli, R. Sharma, W. A. Hallett, K. Kozlowski, L. Carroll, D. Brickute, F. Twyman, A. Al-Nahhas, and E. O. Aboagye, “Biodistribution and radiation dosimetry of deuterium-substituted  $^{18}\text{F}$ -fluoromethyl-[1, 2- $^2\text{H}_4$ ]choline in healthy volunteers”, *J Nucl Med*, vol. 55, no. 2, pp. 256–63, 2014.
- [47] M. G. Stabin, R. B. Sparks, and E. Crowe, “OLINDA/EXM: the second-generation personal computer software for internal dose assessment in nuclear medicine”, *J Nucl Med*, vol. 46, no. 6, pp. 1023–7, 2005.
- [48] ICRP, “Basic anatomical and physiological data for use in radiological protection: reference values”, ICRP Publication 89, Pergamon, 2002.
- [49] G. Bellu, M. P. Saccomani, S. Audoly, and L. D’Angio, “DAISY: a new software tool to test global identifiability of biological and physiological systems”, *Comput Methods Programs Biomed*, vol. 88, no. 1, pp. 52–61, 2007.
- [50] ICRP, “Age-dependent doses to members of the public from intake of radionuclides. Part 2: ingestion dose coefficients”, ICRP Publication 67, Pergamon, 1993.
- [51] A. Giussani, T. Janzen, H. Uusijarvi-Lizana, F. Tavola, M. Zankl, M. Sydoff, A. Bjartell, S. Leide-Svegborn, M. Soderberg, S. Mattsson, C. Hoeschen, and M. C. Cantone, “A compartmental model for biokinetics and dosimetry of  $^{18}\text{F}$ -choline in prostate cancer patients”, *J Nucl Med*, vol. 53, no. 6, pp. 985–93, 2012.
- [52] M. Zankl, H. Schlattl, N. Petoussi-Henss, and C. Hoeschen, “Electron specific absorbed fractions for the adult male and female ICRP/ICRU reference computational phantoms”, *Phys Med Biol*, vol. 57, no. 14, pp. 4501–26, 2012.
- [53] ICRP, “Adult reference computational phantoms”, ICRP Publication 110, Pergamon, 2009.
- [54] L. Hadid, A. Desbrée, H. Schlattl, D. Franck, E. Blanchardon, and M. Zankl, “Application of the ICRP/ICRU reference computational phantoms to internal dosimetry: calculation of specific absorbed fractions of energy for photons and electrons”, *Phys Med Biol*, vol. 55, no. 13, pp. 3631–41, 2010.
- [55] ICRP, “Nuclear decay data for dosimetric calculations”, ICRP Publication 107, Pergamon, 2008.

- [56] X. G. Xu, “An exponential growth of computational phantom research in radiation protection, imaging, and radiotherapy: a review of the fifty-year history”, *Phys Med Biol*, vol. 59, no. 18, pp. R233–R302, 2014.
- [57] W. Snyder, M. Ford, G. Warner, and H. Fisher, “Estimates of absorbed fractions for monoenergetic photon sources uniformly distributed in various organs of a heterogeneous phantom”, MIRDPamphlet 5, Society of Nuclear Medicine, 1969.
- [58] M. Cristy and K. Eckerman, “Specific absorbed fractions of energy at various ages from internal photon sources, Part I: Methods”, ORNL Report TM-8381/V1, Oak Ridge National Laboratory, 1987.
- [59] M. Zankl, R. Veit, G. Williams, K. Schneider, H. Fendel, N. Petoussi, and G. Drexler, “The construction of computer tomographic phantoms and their application in radiology and radiation protection”, *Radiat Environ Biophys*, vol. 27, pp. 153–64, 1988.
- [60] N. Petoussi-Hens, M. Zankl, U. Fill, and D. Regulla, “The GSF family of voxel phantoms”, *Phys Med Biol*, vol. 47, no. 1, pp. 89–106, 2002.
- [61] M. Zankl, *The GSF voxel computational phantom family*, pp. 65–85. Series in Medical Physics and Biomedical Engineering, Boca Raton, London, New York: Taylor & Francis, 2010.
- [62] L. A. Piegl and W. Tiller, *The NURBS book*. Monographs in visual communications, Berlin; New York: Springer, 2nd ed., 1997.
- [63] W. P. Segars, G. Sturgeon, S. Mendonca, J. Grimes, and B. M. Tsui, “4D XCAT phantom for multimodality imaging research”, *Med Phys*, vol. 37, no. 9, pp. 4902–15, 2010.
- [64] M. Zankl, K. F. Eckerman, and W. Bolch, *The ICRP reference computational phantoms*, pp. 377–388. Series in Medical Physics and Biomedical Engineering, Boca Raton, London, New York: Taylor & Francis, 2010.
- [65] M. Zankl, U. Fill, N. Petoussi-Hens, and D. Regulla, “Organ dose conversion coefficients for external photon irradiation of male and female voxel models”, *Phys Med Biol*, vol. 47, no. 14, pp. 2367–85, 2002.
- [66] T. Chao, A. Bozkurt, and X. Xu, “Conversion coefficients based on the vip-man anatomical model and EGS4-VLSI code for external monoenergetic photons from 10 keV to 10 MeV”, *Health Phys*, vol. 81, no. 2, pp. 163–83, 2001.
- [67] Y. S. Yeom, M. C. Han, C. H. Kim, and J. H. Jeong, “Conversion of ICRP male reference phantom to polygon-surface phantom”, *Phys Med Biol*, vol. 58, no. 19, pp. 6985–7007, 2013.
- [68] T. T. Nguyen, Y. S. Yeom, H. S. Kim, Z. J. Wang, M. C. Han, C. H. Kim, J. K. Lee, M. Zankl, N. Petoussi-Hens, W. E. Bolch, C. Lee, and B. S. Chung, “Incorporation of detailed eye model into polygon-mesh versions of ICRP-110 reference phantoms”, *Phys Med Biol*, vol. 60, no. 22, pp. 8695–707, 2015.

- [69] Y. S. Yeom, H. S. Kim, T. T. Nguyen, C. Choi, M. C. Han, C. H. Kim, J. K. Lee, M. Zankl, N. Petoussi-Henss, W. E. Bolch, C. Lee, and B. S. Chung, “New small-intestine modeling method for surface-based computational human phantoms”, *J Radiol Prot*, vol. 36, no. 2, pp. 230–45, 2016.
- [70] Y. S. Yeom, Z. J. Wang, T. T. Nguyen, H. S. Kim, C. Choi, M. C. Han, C. H. Kim, J. K. Lee, B. S. Chung, M. Zankl, N. Petoussi-Henss, W. E. Bolch, and C. Lee, “Development of skeletal system for mesh-type ICRP reference adult phantoms”, *Phys Med Biol*, vol. 61, no. 19, pp. 7054–73, 2016.
- [71] M. Zankl and A. Wittmann, “The adult male voxel model ”Golem” segmented from whole body CT patient data”, *Radiat Environ Biophys*, vol. 40, pp. 153–62, 2001.
- [72] U. A. Fill, M. Zankl, N. Petoussi-Henss, M. Siebert, and D. Regulla, “Adult female voxel models of different stature and photon conversion coefficients for radiation protection”, *Health Phys*, vol. 86, no. 3, pp. 253–72, 2004.
- [73] H. Schlattl, M. Zankl, and N. Petoussi-Henss, “Organ dose conversion coefficients for voxel models of the reference male and female from idealized photon exposures”, *Phys Med Biol*, vol. 52, no. 8, pp. 2123–45, 2007.
- [74] C. Lee, J. L. Williams, C. Lee, and W. E. Bolch, “The UF series of tomographic computational phantoms of pediatric patients”, *Med Phys*, vol. 32, no. 12, pp. 3537–48, 2005.
- [75] C. Lee, C. Lee, J. L. Williams, and W. E. Bolch, “Whole-body voxel phantoms of paediatric patients - UF series b”, *Phys Med Biol*, vol. 51, no. 18, pp. 4649–61, 2006.
- [76] Y. H. Na, B. Q. Zhang, J. Y. Zhang, P. F. Caracappa, and X. G. Xu, “Deformable adult human phantoms for radiation protection dosimetry: anthropometric data representing size distributions of adult worker populations and software algorithms”, *Phys Med Biol*, vol. 55, no. 13, pp. 3789–811, 2010.
- [77] D. Broggio, J. Beurrier, M. Bremaud, A. Desbree, J. Farah, C. Huet, and D. Franck, “Construction of an extended library of adult male 3D models: rationale and results”, *Phys Med Biol*, vol. 56, no. 23, pp. 7659–92, 2011.
- [78] V. F. Cassola, F. M. Milian, R. Kramer, C. A. B. D. Lira, and H. J. Khoury, “Standing adult human phantoms based on 10th, 50th and 90th mass and height percentiles of male and female Caucasian populations”, *Phys Med Biol*, vol. 56, no. 13, pp. 3749–72, 2011.
- [79] A. Ding, M. M. Mille, T. Liu, P. F. Caracappa, and X. G. Xu, “Extension of RPI-adult male and female computational phantoms to obese patients and a Monte Carlo study of the effect on CT imaging dose”, *Phys Med Biol*, vol. 57, no. 9, pp. 2441–59, 2012.
- [80] W. P. Segars, J. Bond, J. Frush, S. Hon, C. Eckersley, C. H. Williams, J. Feng, D. J. Tward, J. T. Ratnanather, M. I. Miller, D. Frush, and E. Samei, “Population of anatomically variable 4D XCAT adult phantoms for imaging research and optimization”, *Med Phys*, vol. 40, no. 4, p. 043701, 2013.

- [81] W. P. Segars, H. Norris, G. M. Sturgeon, Y. Zhang, J. Bond, A. Minhas, D. J. Tward, J. T. Ratnanather, M. I. Miller, D. Frush, and E. Samei, “The development of a population of 4D pediatric XCAT phantoms for imaging research and optimization”, *Med Phys*, vol. 42, no. 8, pp. 4719–26, 2015.
- [82] H. Norris, Y. Zhang, J. Bond, G. M. Sturgeon, A. Minhas, D. J. Tward, J. T. Ratnanather, M. I. Miller, D. Frush, E. Samei, and W. P. Segars, “A set of 4D pediatric XCAT reference phantoms for multimodality research”, *Med Phys*, vol. 41, no. 3, p. 033701, 2014.
- [83] A. M. Geyer, S. O’Reilly, C. Lee, D. J. Long, and W. E. Bolch, “The UF/NCI family of hybrid computational phantoms representing the current US population of male and female children, adolescents, and adults-application to CT dosimetry”, *Phys Med Biol*, vol. 59, no. 18, pp. 5225–42, 2014.
- [84] C. Lee, D. Lodwick, J. Hurtado, D. Pafundi, J. L. Williams, and W. E. Bolch, “The UF family of reference hybrid phantoms for computational radiation dosimetry”, *Phys Med Biol*, vol. 55, no. 2, pp. 339–63, 2010.
- [85] Y. Chen, R. Qiu, C. Li, Z. Wu, and J. Li, “Construction of Chinese adult male phantom library and its application in the virtual calibration of in vivo measurement”, *Phys Med Biol*, vol. 61, no. 5, pp. 2124–44, 2016.
- [86] Y. Zhang, X. Li, W. P. Segars, and E. Samei, “Organ doses, effective doses, and risk indices in adult CT: comparison of four types of reference phantoms across different examination protocols”, *Med Phys*, vol. 39, no. 6, pp. 3404–23, 2012.
- [87] W. Snyder, M. Ford, G. Warner, and E. Watson, ““S” absorbed dose per unit cumulated activity for selected radionuclides and organs”, MIRP Pamphlet 11, Revised, Society of Nuclear Medicine, 1975.
- [88] H. Schlattl, M. Zankl, J. Becker, and C. Hoeschen, “Dose conversion coefficients for CT examinations of adults with automatic tube current modulation”, *Phys Med Biol*, vol. 55, no. 20, pp. 6243–61, 2010.
- [89] I. Kawrakow and D. Rogers, “The EGSnrc code system: Monte Carlo simulation of electron and photon transport”, PIRS Report 701, National Research Council of Canada (NRCC), 2003.
- [90] W. Nelson, H. Hirayama, and D. Rogers, “The EGS4 code system”, SLAC Report 265, Stanford Linear Accelerator Center, 1985.
- [91] I. Kawrakow, “Accurate condensed history monte carlo simulation of electron transport. I. EGSnrc, the new EGS4 version”, *Med Phys*, vol. 27, no. 3, pp. 485–98, 2000.
- [92] M. Berger and J. Hubbell, “XCOM: photon cross sections on a personal computer”, Report NBSIR 87-3597, National Bureau of Standards (former name of NIST), 1987.
- [93] S. B. Nadler, J. H. Hidalgo, and T. Bloch, “Prediction of blood volume in normal human adults”, *Surgery*, vol. 51, no. 2, pp. 224–32, 1962.

- [94] ICRU, “Photon, electron, proton and neutron interaction data for body tissues”, ICRU Report 46, International Commission on Radiation Units and Measurements, 1992.
- [95] F. S. Nooruddin and G. Turk, “Simplification and repair of polygonal models using volumetric techniques”, *IEEE T Vis Comput Gr*, vol. 9, no. 2, pp. 191–205, 2003.
- [96] ICRP, “Limits for intakes of radionuclides by workers. Part 1”, ICRP Publication 30, Pergamon, 1979.
- [97] A. Saltelli, M. Ratto, T. Andres, F. Campolongo, J. Cariboni, D. Gatelli, M. Saisana, and S. Tarantola, *Global sensitivity analysis: the primer*. John Wiley & Sons, 2008.
- [98] F. Ferretti, A. Saltelli, and S. Tarantola, “Trends in sensitivity analysis practice in the last decade”, *Sci Total Environ*, vol. 568, pp. 666–70, 2016.
- [99] A. Saltelli, P. Annoni, I. Azzini, F. Campolongo, M. Ratto, and S. Tarantola, “Variance based sensitivity analysis of model output. Design and estimator for the total sensitivity index”, *Comput Phys Commun*, vol. 181, no. 2, pp. 259–70, 2010.
- [100] I. M. Sobol’, “Sensitivity estimates for nonlinear mathematical models”, *Matematicheskoe Modelirovanie*, vol. 2, no. 1, pp. 112–8, 1990.
- [101] I. M. Sobol’, “Global sensitivity indices for nonlinear mathematical models and their Monte Carlo estimates”, *Math Comput Simul*, vol. 55, no. 1-3, pp. 271–80, 2001.
- [102] T. Homma and A. Saltelli, “Importance measures in global sensitivity analysis of nonlinear models”, *Reliab Eng System Safe*, vol. 52, no. 1, pp. 1–17, 1996.
- [103] A. Saltelli and S. Tarantola, “On the relative importance of input factors in mathematical models: Safety assessment for nuclear waste disposal”, *J Am Stat Assoc*, vol. 97, no. 459, pp. 702–9, 2002.
- [104] M. J. W. Jansen, “Analysis of variance designs for model output”, *Comput Phys Commun*, vol. 117, no. 1-2, pp. 35–43, 1999.
- [105] I. M. Sobol’, “On the distribution of points in a cube and the approximate evaluation of integrals”, *USSR Comput Math & Math Phys*, vol. 7, no. 4, pp. 86–112, 1967.
- [106] I. M. Sobol’, V. I. Turchaninov, Y. L. Levitan, and B. V. Shukhman, “Quasi-random sequence generators”, report, Keldysh Institute of Applied Mathematics, Russian Academy of Sciences, 1992.
- [107] T. Xie and H. Zaidi, “Effect of respiratory motion on internal radiation dosimetry”, *Med Phys*, vol. 41, no. 11, p. 112506, 2014.

# List of Publications

## Peer-reviewed articles

- [A. Zvereva](#), N. Petoussi-Henss, W.B. Li, H. Schlattl, U. Oeh, M. Zankl, F.P. Graner, C. Hoeschen, S.G. Nekolla, K. Parodi, M. Schwaiger, “Effect of blood activity on dosimetric calculations for radiopharmaceuticals”, *Physics in Medicine and Biology*, vol. 61, no. 21, pp. 7688–7703, 2016.
- [A. Zvereva](#), H. Schlattl, M. Zankl, J. Becker, N. Petoussi-Henss, Y.S. Yeom, C.H. Kim, C. Hoeschen, K. Parodi, “Feasibility of reducing differences in estimated doses in nuclear medicine between a patient-specific and a reference phantom”, *Physica Medica: European Journal of Medical Physics*, revised version submitted.
- [A. Zvereva](#), F. Kamp, H. Schlattl, M. Zankl, K. Parodi, “Uncertainty and variance-based sensitivity analysis of organ dose estimates in nuclear medicine”, in preparation.

## Conference contributions and proceedings

- [A. Zvereva](#), W.B. Li, N. Petoussi-Henss, H. Schlattl, U. Oeh, M. Zankl, S.G. Nekolla, C. Hoeschen, K. Parodi, M. Schwaiger, “Personalized compartmental biokinetic modeling and internal dosimetry of two novel radiopharmaceuticals”, *Abstract book of World Congress on Medical Physics and Biomedical Engineering*, pp. 108–109, 2015.

## Publications beyond this work

- S.I. Tkachev, O.P. Trofimova, P.V. Bulychkin, [A.V. Zvereva](#), A.A. Bulanov, “Conformal radiotherapy in the combined chemoradiation therapy of primitive neuroectodermal tumor (case report)”, *Medical Radiology and Radiation Safety (Rus.)*, vol. 57, no. 3, pp. 79–85, 2012.
- [A.V. Zvereva](#), “ESTRO Booklet No. 9 (translation into Russian) review”, *Medical Physics (Rus.)*, no. 2(54), pp. 115–117, 2012.

## Conference contributions and proceedings beyond this work

- C. Borrás, J.D. Bourland, L. Brualla Gonzalez, P. Bulychkin, E. Ford, P. Kazantsev, T. Krylova, A. Lopez Medina, M. Prusova, D. Romanov, J. Roselló Ferrando, T. Willoughby, D. Yan, C. Yu, [A. Zvereva](#), “Medical physics challenges for implementation of new technologies in external beam radiotherapy”, *Medical Physics*, vol. 39, no. 6, p. 3955, 2012.

## Bibliography

- A.V. Zvereva, L.Ya. Klepper, O.P. Trofimova, “Application of NTCP models for quality assurance in radiation therapy”, *Book of extended synopses of International Symposium on Standarts, Applications and Quality Assurance in Medical Radiation Dosimetry*, 2010.
- A.V. Zvereva, “Experience in treatment plans evaluation using NTCP models with focus on breast cancer patients”, *Book of extended synopses of III Eurasian congress on medical physics and engineering “Medical physics - 2010” (Rus.)*, 2010.

# Acknowledgment

This work would not have been possible without many great people who helped and supported me throughout these years. I thank you all for this.

I thank my university supervisor Prof. Dr. Katia Parodi for all the ideas, help, advice and suggestions, for always finding time, for the productive discussions and for giving me the direction and the confidence for accomplishing this work.

I thank Prof. Dr. Werner Rühm for taking time to review this thesis as second referee.

I am very grateful to Dr. Helmut Schlattl, my direct supervisor at the Helmholtz Zentrum München. Thank you for your ideas and support, for the help in all possible matters, for your patience while explaining things and for your door being always open.

I would like to express my gratitude to Maria Zankl and Dr. Augusto Giussani for the suggestions, thoughtful comments and critical contribution to this work.

I am grateful to Dr. Weibo Li and Dr. Matthias Greiter for the fruitful discussions and all the advices they gave me.

I would like to thank Dr. Uwe Oeh for the kind help, friendly discussions and support. Special thank for always motivating me for sport activities.

I thank Tanja Rosentreter and Manuel Kastl for the great friendly atmosphere. Thank you for all the coffees we shared and for all nice and funny moments we had.

I am very thankful to the whole Research Unit Medical Radiation Physics and Diagnostics for being always ready to help, for advices and discussions.

Doktorandeninitiative at Helmholtz Zentrum München (DINI) – I had amazing years with this powerful team. Nirav Florian Chhabra, Tommaso Panni, Meike Köhler, Maria De Vries, Moritz Ludwig and others, I am sincerely thankful to you.

I thank my family in Russia and my family in Germany, especially my mother Marina Zvereva, my sister Polina Zvereva, Ursula Fourier-Kamp and Winfred Kamp for the endless support I received. Finally, I would like to thank Dr. Florian Kamp. Florian, thank you for encouraging me, for supporting me whenever you can, thank you for inspiring and energizing me, thank you for your patience and for being in my life.

This work was supported by the German Bundesministerium für Bildung und Forschung, grant 02NUK026.